Voltage Control of Magnetic Properties in Ferromagnetic Thin Films

Jonathan Mark Wood

A thesis submitted in partial fulfilment of the requirements for the degree of Doctor of Philosophy

Department of Materials Science & Engineering

The University of Sheffield

January 7th 2019

Abstract

Low-power voltage control of magnetic properties of ferromagnetic thin films has long been of interest for many technical applications including magnetic random access memory (MRAM) devices, high-frequency tuneable magnetic devices and magnetic sensors. This research explores novel routes to further develop theses devices.

This thesis presents a study of the variation of magnetic properties of permalloy ($Ni_{80}Fe_{20}$) and Ni thin films when part of an ionic liquid cell via a voltage induced oxidation thinning/thickening of the magnetic film. The cells consisted of a thin ferromagnetic film (<50 nm), the ionic liquid 1-Ethyl-3-methylimidazolium bis(trifluoromethylsulfonyl)imide (EMIMTSFI) and an indium-tin oxide (ITO) coated glass slide.

Magneto-optical Kerr effect (MOKE) magnetometry and vibrating sample magnetometry (VSM) demonstrated drops in coercivity and magnetisation by more than 50%, upon application of low voltages (<4 V), which were partially recovered upon reversal of the voltage polarity.

X-ray photoelectron spectroscopy (XPS) and cyclic voltammetry studies showed a voltage dependent oxidation of the thin films and gave the electrochemical window of the cell to be approximately 4.2 V, with redox peaks at ± 2.5 V.

Ferromagnetic resonance (FMR) spectroscopy demonstrated thickness dependent changes in magnetisation of 5 nm, 10 nm and 50 nm permalloy films, while changes in surface anisotropy and Gilbert damping constant were also observed.

This work hopes to further the understanding of the mechanisms involved in the voltage control of magnetic properties in thin films and advance the technology for future applications.

Publications & Presentations

The work in this thesis has been published and is under preparation for publication in international journals[1,2] and has been presented at international conferences.

[1]J. M. Wood, C. I. Oseghale, O. Cespedes, M. Grell & D. A. Allwood 'Control of ferromagnetic properties of Ni80Fe20 thin films by voltage-induced oxidation', Journal of Applied Physics (Vol.124, Issue 8) DOI: 10.1063/1.5045552

[2]J. M. Wood, M. Sushruth, P. Metaxas, M. Kostylev & D. A. Allwood, 'Ex situ and in situ ferromagnetic spectroscopy of voltage control of magnetisation via oxygen ion migration in thin films' *In preparation*.

[3]Joint European Magnetic Symposia (JEMS), Glasgow, 2016.

[4]Institute of Physics (IOP) Magnetism, Sheffield, 2016.

[5]Institute of Physics (IOP) Magnetism, Leeds, 2015.

[6]Institute of Electrical and Electronics Engineers (IEEE) Magnetic Summer School, Minneapolis, 2015.

Acknowledgements

Contents

1. Introduction

The voltage control of magnetic properties in thin films and nanostructures offers a low power alternative to other current controlled techniques such as current generated magnetic field control[1] and spin-transfer torque[2,3]. Low power switching of magnetic properties could see reduced operating power, improved reliability and wider functionality in magnetic random access (MRAM) devices[4], magnetoelectric sensors[5] and high-frequency tuneable magnetic devices[6].

There is a growing interest in the field of voltage control of magnetic properties, since 2006 the number of papers published per year on the subject has more than tripled[7] (Figure 1.1). Methods of voltage control of magnetism currently receiving a lot of attention include ferromagnetic semiconductors[8] and multiferroic materials[9,10]. However, ferromagnetic semiconductors[11,12] and true (single phase) multiferroics[13] require low operation temperatures and, in the case of true multiferroics, display only weak magnetoelectric coupling, while artificial (composite) multiferroics often have a complex fabrication process[14,15].
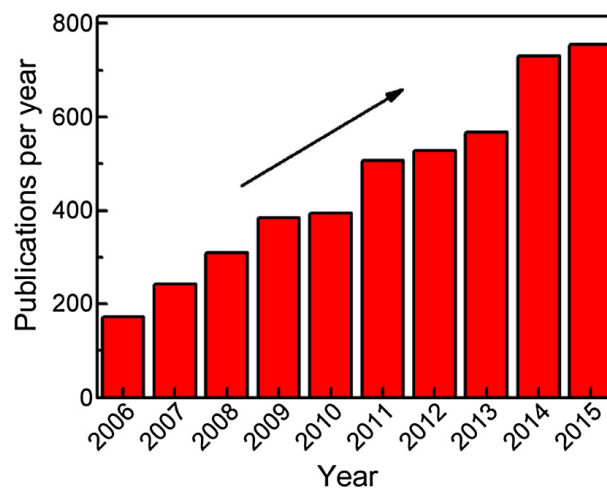
Figure 1.1: Publications per year on voltage control of magnetism[7]

Low power room temperature control of magnetic properties has been demonstrated by using large electric fields to directly alter magnetic properties[16] and in other cases to control oxygen ion transport in magnetic films[17,18]. Weisheit *et al.*[16] added Na^+ ions to propylene carbonate to act as an electrolyte to generate electric fields of up to 4 GVm^{-1} via an electric double layer at the interface with FePt and FePd films. This induced changes of up to 4.5% in coercivity, attributed to a change in unpaired 3d electrons at the interface. While, Bauer *et al.*[17,18] showed that oxygen migration across a perpendicular magnetic anisotropy (PMA) GdO_x/Co interface could be controlled using voltage and heat treatments. This resulted in a significant drop in coercivity and entire loss of PMA after applying -4 V to the oxide layer and complete reversibility after applying +4 V and heating to 100 °C. These effects were attributed to an oxidation-induced change in magnetic anisotropy.

Combining these methods may provide a new approach to further increase the controllability of magnetic properties. In the research described here, a cell was created containing two electrodes, a ferromagnetic film and a transparent indium-tin oxide coated glass layer, separated by an ionic liquid, which are known to generate high electric fields at interfaces. Permalloy films were used here due to its soft magnetic properties[19], high magnetisation[9], ease of patterning[20] and wide use within thin film technology[21]. While Ni films have been previously investigated in multiferroics[22,23], little research has been conducted into the voltage control of magnetic properties of Ni via a redox reaction. A non-volatile chemistry route to controlling magnetic properties of permalloy and Ni could be of interest for tuneable magnetic devices[24].

Applying low-voltages (< |4| V) to this cell resulted in changes in magnetisation, coercivity, magnetic moment, surface anisotropy and Gilbert damping constant in the magnetic film, measured via magneto-optical Kerr effect (MOKE) magnetometry, vibrating sample magnetometry (VSM) and ferromagnetic resonance (FMR)

spectroscopy. X-ray photoelectron spectroscopy (XPS) of the surface of the ferromagnetic films demonstrated a voltage-dependent level of oxidation at the surface of the film, while cyclic voltammetry characterisation of the electrochemical cell identified redox potential voltages where maximum changes in magnetic properties were observed.

The changes in magnetic properties are attributed to a voltage induced redox effect, which caused a thinning/thickening effect of the ferromagnetic film and a change in surface anisotropy. Thicker films (10-50 nm) demonstrated the converse changes in magnetic properties and are attributed to the formation of an iron-rich layer that grew in thickness with positive voltage and to a variation in surface anisotropy. All the variations in magnetic properties presented in this thesis are non-volatile, which is very important for device applications.

1.1 Thesis outline

This thesis consists of eight chapters and an appendix, including this one, as follows:

Chapter 2 introduces the magnetic theory required to understand this research project. This includes origins of magnetism, magnetic energy terms and magnetisation dynamics.

Chapter 3 presents previous work from the literature for the various methods of voltage control of magnetism, highlighting the benefits and drawbacks of each technique.

Chapter 4 details the experimental equipment and methodologies used in the research work. This includes sample preparation and magnetic, surface and electrochemical characterisation.

Chapter 5 presents an investigation of the voltage-controlled magnetic properties of permalloy and Ni films. This includes in situ measurements of hysteresis using an adapted MOKE magnetometer and ex situ VSM measurements of magnetisation.

Chapter 6 presents a study of the surface chemistry of permalloy films due to exposure to the ionic liquid and voltage. Cyclic voltammetry allowed an insight into the electrochemistry of the cells to be gained, while post exposure XPS gave a detailed view of composition of the film surface.

Chapter 7 describes how ferromagnetic resonance (FMR) spectroscopy was used to study 5 nm, 10 nm and 50 nm thick permalloy films in the electrochemical cell. This compliments the experiments in the previous two chapters and allowed magnetisation, surface anisotropy and Gilbert damping to be determined. This gave further insight into the effects of the electrochemical interaction.

Chapter 8 provides a conclusion to the work and suggests future work to be investigated.

An appendix section at the end of the thesis displays all of the XPS data.

1.2 References

1.   Prinz, G. A. Magnetoelectronics. *Science (5394).* **282,** 1660–1663 (1998).

2.   Slonczewski, J. C. Current-driven excitation of magnetic multilayers. *J. Magn. Magn. Mater.* **159,** (1996).

3.   Berger, L. Emission of spin waves by a magnetic multilayer traversed by a current. *Phys. Rev. B* **54,** 9353–9358 (1996).

4.   Apalkov, D., Dieny, B. & Slaughter, J. M. Magnetoresistive Random Access Memory. *Proceedings of the IEEE* **104,** 1796–1830 (2016).

5.   Freitas, P. P., Ferreira, R., Cardoso, S. & Cardoso, F. Magnetoresistive sensors. *J. Physics Condensed Matter* **19,** 165221 (2007).

6.   Kiselev, S. I. *et al.* Microwave oscillations of a nanomagnet driven by a spin-polarized current. *Nature* **425,** 380–383 (2003).

7. Song, C., Cui, B., Li, F., Zhou, X. & Pan, F. Progress in Materials Science Recent progress in voltage control of magnetism : Materials , mechanisms , and performance. *Prog. Mater. Sci.* **87,** 33–82 (2017).

8. MacDonald, A. H., Schiffer, P. & Samarth, N. Ferromagnetic semiconductors: moving beyond (Ga,Mn)As. *Nat. Mater.* **4,** 195–202 (2005).

9. Ramesh, R. & Spaldin, N. A. Multiferroics: progress and prospects in thin films. *Nat. Mater.* **6,** 21–29 (2007).

10. Fiebig, M., Lottermoser, T., Meier, D. & Trassin, M. The evolution of multiferroics. *Nat. Rev. Mater.* 16046 (2016).

11. Chiba, D., Yamanouchi, M., Matsukura, F. & Ohno, H. Electrical manipulation of magnetization reversal in a ferromagnetic semiconductor. *Science* **301,** 943–945 (2003).

12. Chiba, D., Matsukura, F. & Ohno, H. Electric-field control of ferromagnetism in (Ga,Mn)As. *Appl. Phys. Lett.* **89,** 2004–2007 (2006).

13. Tokunaga, Y., Taguchi, Y., Arima, T. & Tokura, Y. Electric-field-induced generation and reversal of ferromagnetic moment in ferrites. *Nat. Phys.* **8,** 838–844 (2012).

14. Heron, J. T. *et al.* Electric-field-induced magnetization reversal in a ferromagnet-multiferroic heterostructure. *Phys. Rev. Lett.* **107,** 1–5 (2011).

15. Lebeugle, D., Mougin, a., Viret, M., Colson, D. & Ranno, L. Electric field switching of the magnetic anisotropy of a ferromagnetic layer exchange coupled to the multiferroic compound BiFeO3. *Phys. Rev. Lett.* **103,** 2–5 (2009).

16. Weisheit, M. *et al.* Electric Field-Induced Modification of Magnetism in Thin-Film

Ferromagnets. *Science,* **315,** 349–351 (2007).

17.   Bauer, U. *et al.* Magneto-ionic control of interfacial magnetism. *Nat. Mater.* **14,** 174–181 (2014).

18.   Bauer, U., Emori, S. & Beach, G. S. D. Electric field control of domain wall propagation in Pt/Co/GdOx films. *Appl. Phys. Lett.* **100,** (2012).

19.   Coey, J. M. D. *Magnetism and Magnetic Materials.* (Cambridge University Press, 2010). doi:10.1017/CBO9780511845000

20.   Cowburn, R. P. Property variation with shape in magnetic nanoelements. *J. Phys. D. Appl. Phys.* **33,** R1–R16 (2000).

21.   Kwiatkowski, W. & Tumański, S. The permalloy magnetoresistive sensors-properties and applications. *J. Phys. E.* **19,** 502–515 (1986).

22.   Weiler, M. *et al.* Voltage controlled inversion of magnetic anisotropy in a ferromagnetic thin film at room temperature. *New J. Phys.* **11,** (2009).

23.   Wu, T. *et al.* Electrical and mechanical manipulation of ferromagnetic properties in polycrystalline nickel thin film. *IEEE Magn. Lett.* **2,** 2–5 (2011).

24.   Vroubel, M., Zhuang, Y., Rejaei, B. & Burghartz, J. N. Integrated tunable magnetic RF inductor. *IEEE Electron Device Lett.* **25,** 787–789 (2004).

2. Origins of magnetic properties

2.1 Introduction

This chapter aims to introduce and explain the physical origins of magnetic moments in atoms and how these moments interact with each other to create magnetic materials. This chapter will help the reader to understand the experimental techniques, experimental data and conclusions presented in later chapters.

Firstly, the origin of the magnetic moment in an atom will be described, followed by how the magnetic moments interact with each other to create the different types of magnetic materials. The magnetic energy terms and the ways in which they compete to define the magnetic properties will then be discussed. Finally, there will be a description of magnetic domains, domain walls and their switching behaviour. This will include an explanation of hysteresis loops, which are an extremely useful tool for characterising magnetic materials.

2.2 Magnetic moments

In 1820 Hans Christian Øersted discovered the phenomenon of electromagnetism, which relates electricity and magnetism. Øersted discovered that a current carrying wire deflects a magnetic compass needle[1]. André-Marie Ampère developed this and formulated an equation (2-1) to relate the magnetic field generated by a current carrying wire[2], where H is the magnetic field, dl is an infinitesimal line element and I is the current. Jean-Baptiste Biot and Félix Savart developed a mathematical description (2-2) of the magnetic field's relationship to current[3], where r is the radial distance from the current carrying wire, δl is an elemental length and $\hat{u}$ is the unit vector along the radial direction. Ampère's law and the Biot-Savart law are equivalent, however in certain geometries one

is preferred over the other. James Clerk Maxwell built on these with his overarching description of electromagnetism[4].

$$\oint \boldsymbol{H} \cdot d\boldsymbol{l} = I \tag{2-1}$$

$$\delta \boldsymbol{H} = \frac{1}{4\pi r^2} I \delta \boldsymbol{l} \times \boldsymbol{\hat{u}} \tag{2-2}$$

Using the discoveries made by these pioneers it is possible to describe the magnetic moment of an electron orbiting a nucleus (Figure 2.1). The orbit of the electron can be thought of as a circulating current that generates a magnetic field perpendicular to the motion of the electron.
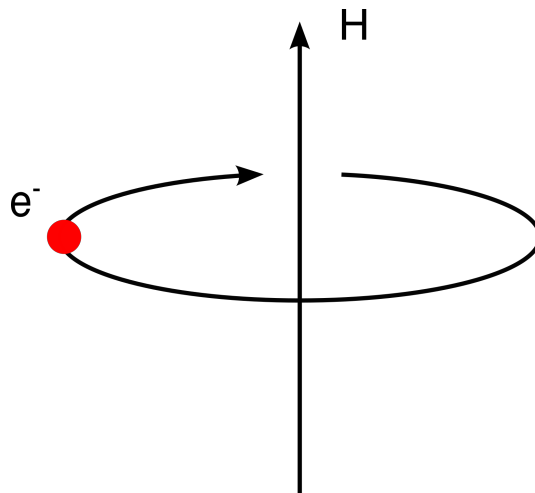
Figure 2.1: Electron, e, orbiting nucleus producing a magnetic field, H, perpendicular to motion.

However, this is a very simplified approach based on a semi-classical description of atomic structure and it is necessary to use quantum mechanics to fully understand the concept. Solving the Schrödinger equation for a free atom gives rise to quantum numbers, which describe the distribution of electrons around the nucleus[5]. The principal quantum number, n, describes the energy level of the electron and can have values equal to 1, 2, 3 ... etc. Each energy level contains n^2 electronic orbitals, which can

contain a maximum of two electrons. The orbital quantum number, l, describes the orbital angular momentum of the electron and can have values equal to 0, 1, 2, 3 …etc. up to n -1. The magnitude of the orbital angular momentum for a single electron, |L|, is given by (2-3).

$$|L| = \sqrt{l(l+1)}\hbar \qquad (2\text{-}3)$$

The orientation of the orbital angular momentum with respect to a magnetic field is described by the magnetic quantum number, m_l, which can take the values of $+l$ to $-l$.

The electron also has an intrinsic spin, s, termed the spin quantum number and has the value of ½. The magnitude of the spin angular momentum for a single electron, |S| is described by (2-4)

$$|S| = \sqrt{s(s+1)}\hbar \qquad (2\text{-}4)$$

Similar to the magnetic quantum number for the total orbital angular momentum, there is a spin magnetic quantum number, m_s, with respect to the magnetic field and has values of +½ and -½. The magnetic moments from the orbital angular momentum and spin angular momentum interact via spin-orbit coupling to give the total angular momentum quantum number, J, described by (2-5).

$$J = L + S \qquad (2\text{-}5)$$

The Pauli exclusion principle and Hund's rules describe how electrons fill atomic orbitals, where orbitals are here termed by s, p, d, f…(synonymous with the allowed values of l). Pauli's exclusion principal states that no two electrons in an atom can have the same quantum numbers, as a result electrons in the same atomic orbital must have opposite spin orientation i.e. antiparallel alignment. Hund's first rule states that electrons maximise the total spin, S. Therefore electrons fill orbitals one by one with the spins

aligned parallel, until orbitals contain one electron each, whereupon electrons fill the orbitals with spins aligned antiparallel. This acts to reduce the Coulomb energy between electrons. Hund's second rule states that total orbital angular momentum, L, is maximised. This leads to electrons orbiting in the same direction thus reducing collisions and therefore Coulomb repulsion. Hund's third rule states that, atoms with less than half-full shells have the lowest energy configuration when J is lowest, while if the shell is more than half full the inverse is true. All of Hund's rules aim to minimise the energy upon filling of electronic orbitals.

An example of how orbitals fill can be seen in figure 2.2 for the Fe 3d orbital. The electrons fill to the 4s orbital, leaving six electrons remaining to fill the 3d orbital. The electrons align parallel in the 3d orbital, until the sixth electron aligns antiparallel, thus summing the m_s values gives the maximum value of $S=2$. The total orbital angular momentum is also maximised, by the sixth electron occupying the $m_l=2$ state. Finally, since the shell is more than half-full J is maximised, therefore inputting the values into equation (2-5) gives $J=4$. This gives a net non-zero angular momentum generating an overall magnetic moment.
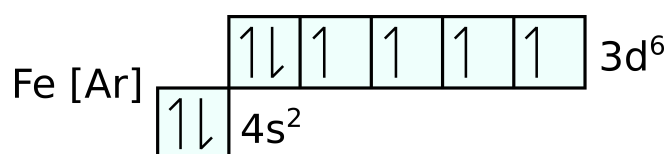
Figure 2.2: Valance electron filling of iron 3d atomic orbital, in line with the Pauli exclusion principle and Hund's rules.

2.3 Types of magnetism

There are several different types of magnetism these include diamagnetism, paramagnetism, ferromagnetism, antiferromagentism and ferrimagnetism. These different effects arise due to the atomic structure and the competing magnetic energy terms within the material. This section aims to explain the features of the different materials and what potential applications they may have.

2.3.1 Diamagnetism

Diamagnetism is a very weak effect that is present in all materials. The weak nature of the effect means materials are only referred to as diamagnetic when other magnetic effects are negligible. Diamagnetism arises when an external magnetic field is applied causing electrons to adjust their orbits in a current-like way to work against the applied field via electromagnetic induction. Lenz's law states that induced currents act to oppose the direction of the applied magnetic field. This results in a larger positive field generating a larger negative magnetisation. In this regard a diamagnetic material has a small and negative susceptibility, χ, which is a measure of how a material's magnetisation varies in response to an applied magnetic field. Values of χ are usually very small except for superconductors[6]. The magnetic susceptibility is described by (2-6) and can be found by reading the gradient of figure 2.3.

$$M = \chi H \qquad (2\text{-}6)$$

On removal of the field the effect is also removed which limits the potential applications of diamagnetic materials. Examples of diamagnetic materials include superconductors[6], pyrolytic carbon[7] and most organic compounds[8].
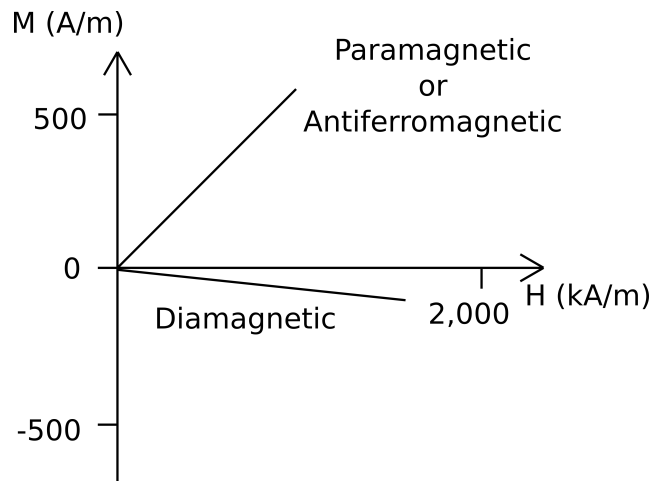
Figure 2.3: Schematic of susceptibility for paramagnetic, antiferromagnetic and diamagnetic materials. Diagram adapted from Spaldin[6].

2.3.2 Paramagnetism

Paramagnetism occurs in materials that contain net magnetic moments with negligible interactions between them. Thermal energy easily overcomes the weak interactions and causes random alignment of magnetic moments. On applying a magnetic field, the moments start to align to the field direction, as show in figure 2.4. However, only a small magnetisation is generated in the material, even for high fields, giving a low susceptibility (Figure 2.3).
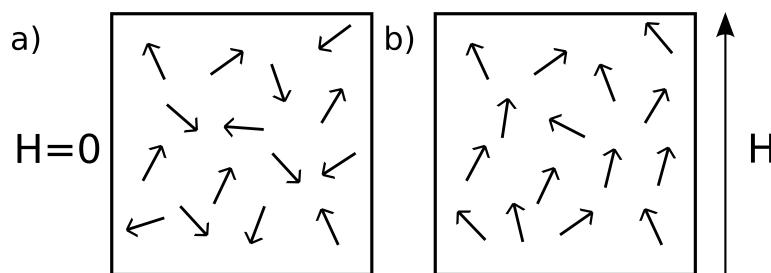
Figure 2.4: Schematic of magnetic moments for a paramagnetic material with zero applied field and with applied field H. Diagram adapted from Spaldin[6].

21

The susceptibility of most paramagnetic materials is inversely proportional to temperature, as described by Curie's law (2-7)[6],

$$\chi = \frac{C}{T} \qquad (2\text{-}7)$$

where T is temperature and C is a constant equal to $Nm^2/3k_B$, N is the total number of magnetic atoms per unit volume, m is the magnetic moment and k_B is the Boltzmann constant. Thus, a lower temperature gives rise to a larger magnetisation for a given field when applied to most paramagnets. Examples of paramagnetic materials include transition metal salts[9] and rare earth salts[10].

2.3.3 Ferromagnetism and exchange energy

Ferromagnetism occurs in materials that contain net magnetic moments that interact strongly with each other to align nearest-neighbour moments (Figure 2.5). This strong interaction arises due to the exchange energy, which is at a minimum when the magnetic moments are aligned. The origin of the exchange energy arises due to the Pauli exclusion principle, which states that two fermions cannot occupy the same quantum state. There is Coulombic repulsion between the neighbouring electrons, which causes the electrons to be in higher energy orbitals because it has a lower energy in comparison to the electrostatic energy. The exchange energy is calculated by summing all the pairs of magnetic moments (2-8).

$$E_{Exchange} = -2J \sum_{ij} \boldsymbol{S}_i \cdot \boldsymbol{Sj} \qquad (2\text{-}8)$$

where $E_{Exchange}$ is the exchange energy, J is the exchange constant and $\boldsymbol{S}_i$ and $\boldsymbol{S}_j$ are spin vectors. When the value of J is positive this gives rise to parallel alignment, creating spontaneous magnetisation and when J is negative there is antiparallel alignment and creates antiferromagnetic and ferrimagnetic materials (see sections 2.3.4 and 2.3.5).
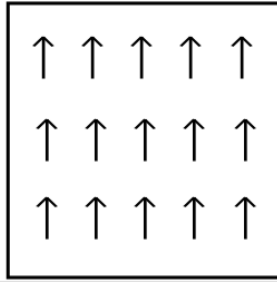
Figure 2.5: Schematic of magnetic moments for a ferromagnetic material.

Above certain temperatures the thermal energy is sufficient to overcome the exchange energy interaction. The magnetic moments become disordered and the material enters the paramagnetic state. This transition temperature is termed the Curie temperature, T_C. The magnetisation decreases as a function of temperature until T_C is reached, where the magnetisation equals zero (Figure 2.6).
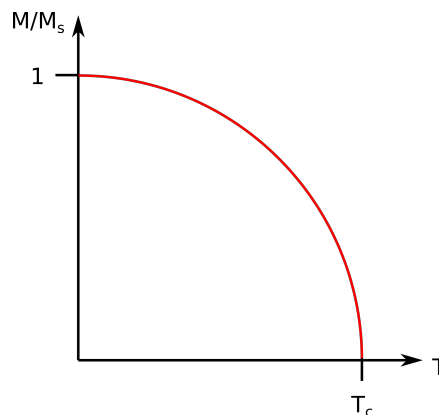
Figure 2.6: Magnetisation as a function of temperature, where T_C is the Curie temperature.

Room temperature ferromagnetic materials include the transition metals nickel, iron and cobalt along with their alloys and also alloys including rare earths[11]. These materials show a broad range of magnetic properties, from 'soft' ferromagnets, in which the magnetisation direction can be easily switched with a low magnetic field, to 'hard' ferromagnets in which a larger magnetic field is required to switch the magnetisation

direction. This is governed by magnetic anisotropy that will be discussed in section 2.4.1.
Both hard and soft magnets each have their own applications and play an important role
in our modern day world[8,12].

2.3.4 Antiferromagnetism

In antiferromagnetic materials neighbouring moments prefer to be aligned in an
antiparallel arrangement, due to a negative exchange constant, J (2-8)[13]. When the
magnetic moments in the material are of equal magnitude the magnetic moments cancel
each other out creating a net zero magnetic moment (Figure 2.7). Antiferromagnetic
materials are often transition metal compounds and are can be used to induce exchange
bias in ferromagnetic materials[14,15].
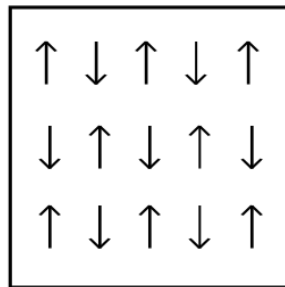
Figure 2.7: Schematic of magnetic moments in an antiferromagnetic
material.

2.3.5 Ferrimagnetism

Ferrimagnetism is very similar to antiferromagnetism and may be considered as a
special case of antiferromagentism. In ferrimagnets, like in antiferromagnets, the nearest
neighbour magnetic moments prefer to align in an antiparallel direction, again due to a
negative exchange constant, J (2-8). However, ferrimagnets are composed of two
lattices of opposite alignment and unequal magnetic moment (Figure 2.8), which creates

an overall magnetic moment. Ferrimagnets also display hysteresis, however, much higher fields are required to reach true saturation, much like antiferromagnetic materials. Examples of ferrimagnetic materials include ferrites[16] and garnets[17].
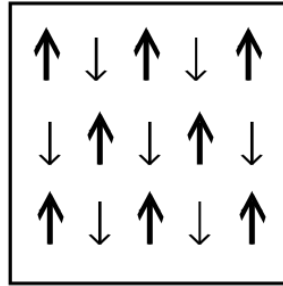
Figure 2.8: Schematic of magnetic moments in ferrimagnetic material.

2.4 Magnetic energy terms

The magnetic materials described in the previous section arise from the magnetic moments and the interactions between them. In the following section the energies that govern how the moments interact with each other will be described. The four main energy terms are: magnetostatic energy, magnetocrystalline anisotropy energy, Zeeman energy and exchange energy (2.3.3).

2.4.1 Magnetocrystalline anisotropy energy

Magnetocrystalline anisotropy is a property that gives a material a preferred direction of magnetisation. The origins of magnetocrystalline anisotropy arise from the spin-orbit coupling interaction, which create a preferred magnetisation direction with the optimal orbital overlap to give the lowest energy. In order to overcome the spin-orbit coupling and align the magnetisation along the hard direction, a large enough magnetic field needs to be applied. In magnetic materials with high spin-orbit coupling, such as rare earth containing materials, the magnetocrystalline anisotropy is high, but for magnetic

transition metal materials the coupling is weaker leading to a lower magnetocrystalline anisotropy. In the case of permalloy, $Ni_{80}Fe_{20}$, there is almost zero magnetocrystalline anisotropy[8].
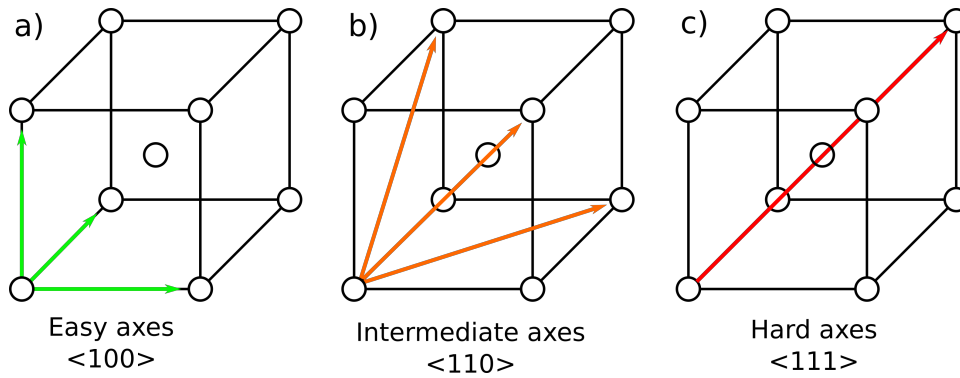
Figure 2.9: Anisotropy axes in BCC Iron a) easy <100>, b) intermediate <110> and c) hard <110>.

This gives rise to easy and hard magnetisation axes, the hard axis requiring a larger magnetic field to reach saturation than the easy axis direction. The magnetocrystalline anisotropy energy (MAE) is the energy difference between the material magnetised along the hard and easy axis. Figure 2.9 shows the easy, intermediate and hard crystallographic axes present in body centred cubic (BCC) iron.

An example of how to calculate the MAE is shown below for Fe, which has a cubic crystal structure (2-9)[6]:

$$E_K = K_1(\alpha_1^2\alpha_2^2 + \alpha_2^2\alpha_3^2 + \alpha_3^2\alpha_1^2) + K_2(\alpha_1^2\alpha_2^2\alpha_3^2) \qquad (2\text{-}9)$$

Where E_K is the magnetocrystalline anisotropy energy in Jm^{-3}, K_1 and K_2 are anisotropy constants and α_i are direction cosines between the magnetisation and the crystal axis.

In thin films surface anisotropy effects are present, which arise due to the broken symmetry at interfaces, this can generate perpendicular magnetic anisotropy (PMA) for

sufficiently thin films. Each anisotropy term, *K,* has contributions from the bulk and the surface and are described by (2-10)

$$K = K_B + \frac{2K_s}{d} \qquad (2\text{-}10)$$

where K_B is the bulk anisotropy term, K_s is the surface anisotropy term and *d* is the film thickness.

A phenomenon that arises due to the anisotropy is magnetostriction, whereby the magnetic material varies in length under the application of a magnetic field. The change in length is small, tens of parts per million, and can be both positive and negative[6]. Magnetostriction arises when an applied field rotates magnetic moments from one crystallographic axis to another. This can cause strain in magnetic domains (see 2.5.1) thus resulting in elongation or contraction of the material. The magnetostrictive effect also works in the inverse manner, whereby applying a strain on a magnetic field induces a change in magnetic anisotropy. This is called the Villari effect[13]. Examples of magnetostrictive materials include Ni and Fe, which demonstrate positive and negative magnetostriction respectively, where positive indicates elongation along magnetic field axis and negative indicates contraction along the magnetic field axis[18].

2.4.2 Magnetostatic energy

The next magnetic energy term to be explained is the magnetostatic energy, which also gives rise to shape anisotropy. Magnetostatic energy arises due to a property called the demagnetising field.

Figure 2.10 shows a magnetised material and the stray magnetic field that emanates from the material. The stray field goes from the north pole (N) to the south pole (S) and acts in the opposite direction to the magnetisation. Inside the magnetic material there is a field that directly opposes the magnetisation; this field is called the demagnetising field, H_d. This field is proportional to the demagnetising factor and the magnetisation of the material (2-11).
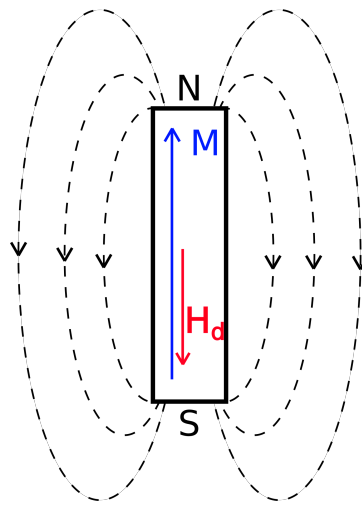
Figure 2.10: Schematic of demagnetising field, H_d, in a material with magnetisation, M.

$$\boldsymbol{H}_d = -N_d\boldsymbol{M} \qquad (2\text{-}11)$$

The demagnetising factor N_d is dependent on the shape of the material, particularly the aspect ratio, which is defined as the ratio of the width to the height. As the aspect ratio of the material becomes greater the demagnetising factor becomes smaller. The energy term associated with the interaction of the demagnetising field with the magnetisation can be seen in (2-12):

$$E_{Mag} = \frac{1}{2}H_dM \qquad (2\text{-}12)$$

where E_{Mag} is the magnetostatic energy per unit volume. For an increasing demagnetising field there is an increase in magnetostatic energy. This creates a shape anisotropy effect, whereby materials are more easily magnetised along their long axis (low H_d value) and much harder to magnetise along their short axis (high H_d value). This creates the so called easy and hard axis magnetisation directions, due to shape anisotropy, ignoring magnetocrystalline anisotropy effects (section 2.4.1). In permalloy, since there is virtually no magnetocrystalline anisotropy, shape anisotropy dominates.

A material reduces the magnetostatic energy by reducing the stray field generated by the magnetisation. The material creates regions of oppositely oriented magnetisation directions called domains to achieve this (Figure 2.11a). The magnetostatic energy directly competes with the exchange energy which aims to have all magnetic moments aligned in the same directions (section 2.3.3). The magnetostatic energy can be reduced even further, by removing all stray fields by creating closure domains that have their magnetisation directed perpendicular to their neighbouring domains. In certain cases this creates the Landau state (Figure.2.11b), which is the arrangement that has the minimum magnetostatic energy.
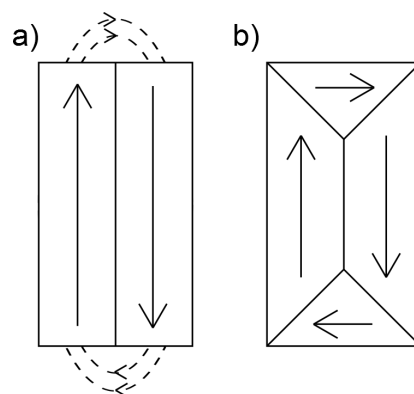
Figure 2.11: Formation of magnetic domains to reduce magnetostatic energy. a) Oppositely oriented domains producing stray fields, b) Landau state with closure domains to reduce stray fields. Diagram adapted from Spaldin[6].

2.4.3 Zeeman energy

The Zeeman energy describes how magnetic moments react to an external magnetic field. When an external field is applied to a magnetic moment, there is a torque exerted on the magnetic moment, which tries to align the magnetic moment to the applied field. The energy associated with this is defined as the dot product between the magnetisation and the applied field (2-13):

$$E_{Zeeman} = -\mu_0 \boldsymbol{M} \cdot \boldsymbol{H} \qquad (2\text{-}13)$$

where E_{Zeeman} is the Zeeman energy in Jm^{-3}, μ_0 is the permeability of free space, $\boldsymbol{M}$ is magnetisation and $\boldsymbol{H}$ is applied field. This gives the lowest Zeeman energy when the moment is aligned to the applied field.

2.5 Magnetic domains and magnetisation dynamics

The previous section described the energy terms involved in magnetics. This section explains how these energy terms compete with each other to form the magnetic domain structure, which is common in magnetic materials. Magnetic hysteresis will be explained and the key properties obtainable from them. In adjoining magnetic domains there exist domain walls, whereby the magnetisation direction changes. This will also be described along with the different types of domain walls that occur. Finally, the concept of ferromagnetic resonance will be explained, which further characterises a material's magnetic properties.

2.5.1 Magnetic Domains

As described in the previous section there are four magnetic energy terms: magnetostatic, magnetocrystalline anisotropy, Zeeman and exchange. The sum of these energy terms gives the total energy of the system (2-14):

$$E_{Total} = E_{Mag} + E_K + E_{Zeeman} + E_{Exchange} \tag{2-14}$$

These energies compete with each other to give lowest energy state for the material. The exchange energy is lowest when the magnetic moments are aligned parallel, hence a single domain. However, a single domain increases the magnetostatic energy, therefore domains are formed with magnetic moments aligned antiparallel (Figure 2.11). The magnetocrystalline anisotropy energy is a minimum with domain magnetisations aligned along the easy axes of the crystal. This often results in a multidomain structure separated by domain walls.

The size of the domain wall is also dominated by the energy terms. The exchange energy is minimised for larger domain walls due to a reduced change in angle between adjacent magnetic moments. Whereas the magnetocrystalline anisotropy is minimised for narrow domain walls, reducing the number of magnetic moments misaligned to the easy axis.
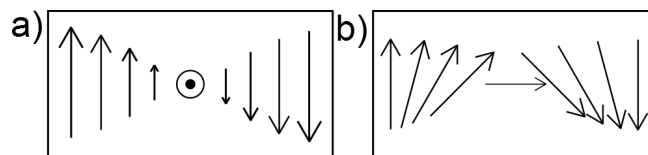
Figure 2.12: Schematics of a) Bloch wall b) Néel Wall.

Two common types of domain walls that occur in magnetic materials are the Bloch wall and the Néel wall[6]. For thin films magnetised in plane, the type of domain wall is governed by the magnetostatic energy. When the film thickness is the same order of magnitude as the domain wall width (< 300 nm), the magnetostatic energy of the domain wall becomes comparable to the exchange and anisotropy terms[18]. This can determine whether a Bloch or Néel wall is formed. Bloch walls change magnetisation direction by rotating the moments out of plane, increasing magnetostatic energy by generating free

poles at the surface (Figure 2.12a). While Néel walls rotate the magnetisation in the plane of the material (Figure 2.12b), thus reducing the magnetostatic energy of the domain wall.

Upon applying a magnetic field the domains with magnetisation aligned parallel to the magnetic field direction start to increase in size by domain wall motion. As domain walls move they may encounter defects in the crystal structure creating pinning sites that require a larger field to overcome. This gives rise to small jumps in magnetisation, termed the Barkhausen effect[19]. At sufficiently large magnetic fields the magnetisation of the material will reach magnetisation saturation, M_S, defined as the magnetisation when all magnetic moments are aligned.
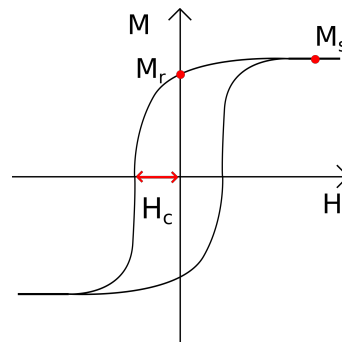
Figure 2.13: Schematic of hysteresis loop for a ferromagnetic material, H is applied field, M is magnetisation, M_S is saturation magnetisation, $M_{r,}$ is remnant magnetisation and H_C is the coercivity.

Removing the magnetic field causes the magnetic moments to rotate back towards the easy axis, thus reducing the magnetisation. However, due to the defects described earlier, the system encounters energy barriers that require further energy to be overcome. This results in a remnant magnetisation, M_r, the magnetisation upon removing magnetic field after saturation. To demagnetise the material (i.e. M=0), a magnetic field in the opposite direction is required, this field is called the coercive field or coercivity, H_C.

Sweeping the magnetic field and measuring the magnetisation generates a hysteresis loop (Figure 2.13), from which the material's magnetic properties can be characterised.

2.5.2 Ferromagnetic Resonance

Ferromagnetic resonance (FMR) is a key property in magnetisation dynamics and enables the magnetisation, gyromagnetic ratio, surface anisotropy and Gilbert damping coefficient to be calculated. As described in section 2.2 a circulating electron generates a magnetic moment perpendicular to its motion. If a magnetic field is then applied to this system, there is a torque that aligns the moment to the field direction (2-15)

$$\boldsymbol{\tau} = \boldsymbol{m} \times \boldsymbol{B} \qquad (2\text{-}15)$$

where $\boldsymbol{\tau}$ is the torque, $\boldsymbol{m}$ is magnetic moment and $\boldsymbol{B}$ is the magnetic field. This torque causes a change in angular momentum and causes the magnet moment to precess around the field direction. This precession is called the Larmor precession, which precesses at the Larmor frequency, given by (2-16)

$$f_L = \frac{\gamma B}{2\pi} \qquad (2\text{-}16)$$

where γ is the gyromagnetic ratio and B is the magnetic field.

These precessing moments couple with the neighbouring moments, creating a spin wave within the material (Figure 2.14). The dynamics of a spin wave are described by the Landau-Lifshitz-Gilbert (LLG) equation (2-17)[20]:

$$\frac{\partial \boldsymbol{M}}{\partial t} = \gamma \left(\boldsymbol{M} \times \boldsymbol{H}_{eff} \right) + \frac{\alpha_G}{M_s} \left(\boldsymbol{M} \times \frac{\partial \boldsymbol{M}}{\partial t} \right) \qquad (2\text{-}17)$$

where γ is the gyromagnetic ratio, $\boldsymbol{H}_{eff}$ is the effective magnetic field and is the total of the applied, dipole and anisotropy fields[13], α_G is the Gilbert damping coefficient and M_s is the saturation magnetisation. The first part of the right hand side of (2-17) represents the

precessional motion of the magnetic moment around the direction of the effective magnetic field as described above. The second part of the right hand side of (2-17) describes damping that causes the magnetic moment to align to the equilibrium position in the direction of the effective field.
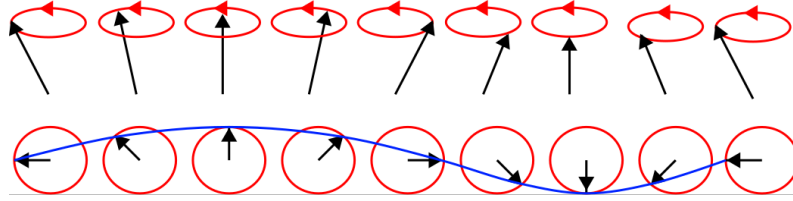
Figure 2.14: Top: schematic of a spin wave Bottom: schematic of spin wave from above with wave drawn in blue. Adapted from[23].

To solve the LLG equation, one can consider a static magnetic field, B_0, applied in the *z* direction to an ellipsoid of ferromagnetic material with demagnetisation factors N_x, N_y and N_z. Thus the components of the internal magnetic fields within the sample are[20]:

$$B_x = B_x^0 - N_x\mu_0 M_x; \; B_x = B_y^0 - N_y\mu_0 M_y; \; B_z = B_z^0 - N_z\mu_0 M_z \qquad (2\text{-}18)$$

The components of the first half of right hand side of the LLG equation then become:

$$\frac{dM_x}{dt} = \gamma M_y \left(B_0 + M(N_y - N_z) \right) \qquad (2\text{-}19)$$

$$\frac{dM_x}{dt} = -\gamma M_x (B_0 + M(N_x - N_z)) \qquad (2\text{-}20)$$

if we set $\frac{dM_z}{dt} = 0$ and $M_z = M$ it is then possible to solve equations (2-19 & 2-20) by using exp(iωt) as the time dependence so that the ferromagnetic resonance is then given by[20]:

$$f^2 = \gamma^2 [B_0 + (N_y - N_z)\mu_0 M][B_0 + (N_x - N_z)\mu_0 M] \qquad (2\text{-}21)$$

This is the Kittel equation that describes the FMR frequency or fundamental mode and is the mode where all the spins precess with the same phase and amplitude over the whole volume of the material. It is possible to obtain the FMR frequency by using a radio frequency (RF) magnetic field and detecting the absorption by the sample (Section 4.3.3). The Kittel equation can be further simplified for the case of thin films magnetized in plane with close to zero anistropy[21]:

$$f^2 = \gamma^2 H_{res}(H_{res} + \mu_0 M_{eff}) \tag{2-22}$$

where f is the resonant frequency, γ is the gyromagnetic ratio and H_{res} is the resonant magnetic field and M_{eff} is the effective magnetisation. Here M_{eff}, is given by (2-23)[22]:

$$M_{eff} = M_S - \frac{2K_S}{\mu_0 M_S d} \tag{2-23}$$

where K_s is the surface anisotropy and d is the film thickness.

As well as the fundamental FMR mode there are also higher order modes, termed standing spin wave modes (SSWMs). SSWM are where the magnetic moments create a standing wave across the film thickness and usually occur at higher frequencies. The in plane SSWMs can be described by a modified Kittel equation (2-24)[23]:

$$f^2 = \gamma^2 (H_{res} + H_{ex})(H_{res} + H_{ex} + \mu_0 M_{eff}) \tag{2-24}$$

where H_{ex} is the exchange field described by (2-25)[23]

$$H_{ex} = Dk^2 \tag{2-25}$$

where D is the exchange stiffness constant and k is the wave vector, $k=n\pi/d$, n is the mode number and d is the film thickness.

2.6 Summary

This chapter has provided the reader with an explanation of the fundamental origins of magnetism, magnetic energy terms, types of magnetic ordering, and ferromagnetic resonance; all with a focus on thin films. The fundamental origins of magnetism are helpful in the understanding of all chapters in this thesis. In particular for chapters 3 & 4 which give a literature review and a description of the characterisation techniques respectively. Magnetization dynamics will help the reader understand the extensive magnetic characterisation data in chapters 5 & 7, with a particular focus on magnetic hysteresis and FMR spectroscopy. Overall this chapter gives the reader a solid basis in magnetism and emerging phenomena. It should enable the reader to understand this research project and the novel contributions made to this are of interest

2.7 References

1. Oersted, H. C. Electricity and magnetic needles. *Philosophy* **16,** 273–276 (1820).

2. Ampere, A.-M. *Memoires de l'academie royale des sciences de l'institut de france* **6,** 175–387 (1823).

3. Biot, J.-B. & Savart, F. Note sur le Magnétisme de la pile de Volta. *Ann. Chim. Phys.* **15,** 222–223 (1820).

4. Maxwell, J. C. A Dynamical Theory of the Electromagnetic Field [J]. *Philos. Trans. R. Soc. London* **155,** 459–512 (1865).

5. Rae, A. I. M. *Quantum Mechanics.* (Taylor & Francis, 2008).

6. Spaldin, N. *Magnetic Materials. Fundamentals and applications*. (Cambridge University Press, 2010). doi:10.2277/0521016584

7.   Fischbach, D. B. Diamagnetic Susceptibility of Pyrolytic Graphite. *Phys. Rev.* **123,** 1613–1614 (1961).

8.   O'Handley, R. C. *Modern Magnetic Materials*. (Wiley, 2000).

9.   Abragam, A. & Bleaney, B. *Electron Paramagnetic Resonance of Transition Ions*. (Oxford University Press, 2012).

10.   Rodden, J. The Paramagnetism of Some Rare Earth Ions. *J. Am. Chem. Soc.* **56,** 648–649 (1934).

11.   Gutfleisch, O. Controlling the properties of high energy density permanent magnetic materials by different processing routes. *J. Phys. D. Appl. Phys.* **33,** R157–R172 (2000).

12.   Coey, J. M. D. Hard magnetic materials: A perspective. *IEEE Trans. Magn.* **47,** 4671–4681 (2011).

13.   Coey, J. M. D. *Magnetism and Magnetic Materials*. (Cambridge University Press, 2010). doi:10.1017/CBO9780511845000

14.   Stamps, R. L. Mechanisms for exchange bias. *J. Phys. D. Appl. Phys.* **34,** 444–444 (2001).

15.   Koon, N. Calculations of Exchange Bias in Thin Films with Ferromagnetic/Antiferromagnetic Interfaces. *Phys. Rev. Lett.* **78,** 4865–4868 (1997).

16.   Pullar, R. C. Hexagonal ferrites: A review of the synthesis, properties and applications of hexaferrite ceramics. *Prog. Mater. Sci.* **57,** 1191–1334 (2012).

17.   Dillon, J. F. Ferrimagnetic Resonance. *Phys. Rev.* **105,** 759 (1957).

18. Cullity, B. D. & Graham, C. D. *Introduction to Magnetic Materials (2nd Edition).* *Materials Today* **12,** (2009).

19. Barkhausen, H. Two phenomena uncovered with the help of new amplifiers. *Physics (College. Park. Md).* (1919).

20. Kittel, C. *Introduction to Solid State Physics.* (Wiley, 1951).

21. Kittel, C. On the theory of ferromagnetic resonance absorption. *Phys. Rev.* **73,** 155–161 (1948).

22. Liu, X., Zhang, W., Carter, M. J. & Xiao, G. Ferromagnetic resonance and damping properties of CoFeB thin films as free layers in MgO-based magnetic tunnel junctions. *J. Appl. Phys.* **110,** (2011).

23. Maksymov, I. S. & Kostylev, M. Broadband stripline ferromagnetic resonance spectroscopy of ferromagnetic films, multilayers and nanostructures. *Phys. E Low-Dimensional Syst. Nanostructures* **69,** 253–293 (2015).

3. Literature Review

3.1 Introduction

This chapter reviews previous research of voltage control of magnetism in thin films and heterostructures. Firstly a description of the typical device configurations will be given to provide the reader with a reference point when reading the research outlined in this literature review. The literature review is divided into different material groups including ferromagnetic semiconductors, multiferroics and bilayer structures, antiferromagnets, ferromagnetic oxides and ultrathin metals. Voltage control of magnetism in these materials is generated by a variety of different mechanisms that include carrier modulation, strain effects, exchange coupling, orbital reconstruction and electrochemical-induced changes. The mechanisms of change will be discussed for each piece of research; occasionally there are multiple mechanisms at play for a given structure leaving the overarching mechanism up for debate. This section will help to introduce potential significance and challenges that need to be overcome in voltage control of magnetism.

3.2 Standard device configurations for voltage control of magnetic properties

In the research area of voltage control of magnetism there are four common device configurations that appear (Figure 3.1). The four device configurations described are field-effect transistor (FET) structure, back gate structure, magnetic tunnel junction (MTJ) structure and nanostructure type. Where possible later in the literature review the specific device structure will be identified and displayed to give the reader a greater understanding of the presented research.

FET configurations consist of three electrodes (gate, source and drain), an insulator and a ferromagnetic film (Figure 3.1a). Where the insulator is sandwiched between the ferromagnetic layer and the gate electrode. Applying gate voltages to the insulator generates electric fields that manipulate ferromagnetic properties of the insulator itself or the ferromagnetic film below[1]. While source and drain electrodes monitor the passage of current through the insulator where necessary. Typical insulators include ferromagnetic semiconductors, oxides, and dielectrics.
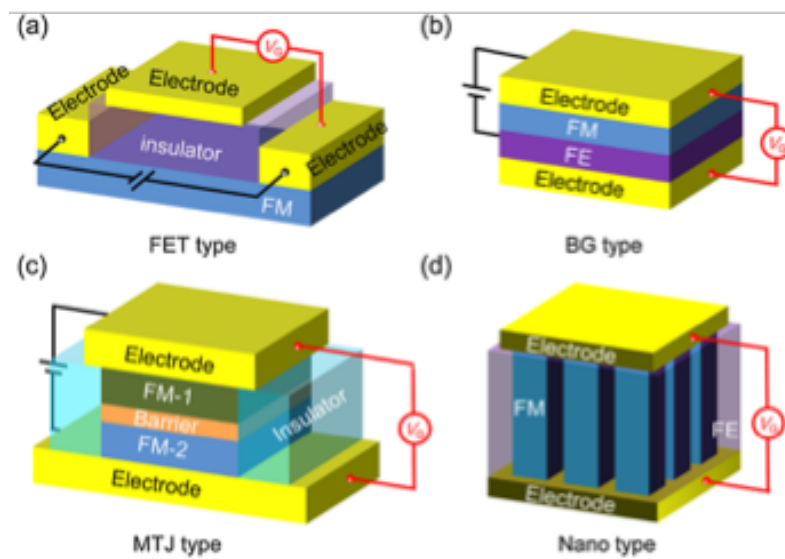

Figure 3.1: Common device configurations in voltage control of magnetism research. (a) Field-effect transistor (FET) structure, (b) back gate structure, (c) magnetic tunnel junction (MTJ) structure and (d) nanostructure.[1]

In back gate structures (Figure 3.1b), the dielectric material lies underneath the ferromagnetic layer. This device structure is common for multiferroic heterostructures or a piezoelectric/ferromagnetic structures, where ferromagnetic properties are controlled by a strain or electric field induced effect across the interface[1]. In MTJ structures (Figure 3.1c) a dielectric separates two ferromagnetic layers and application of a gate voltage manipulates the magnetoresistance across the structure[1]. Finally, nanostructures (Figure

3.1d) are typically composites of ferromagnetic and ferroelectric structures that utilise magnetoelectric coupling to demonstrate voltage control of magnetic properties.
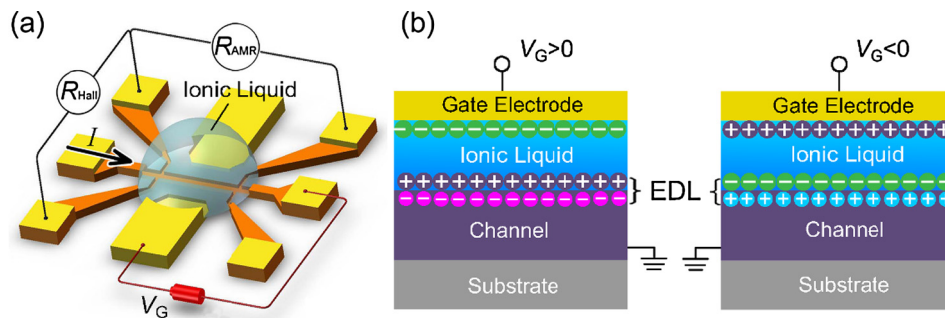

Figure 3.2: (a) Schematic of FET type device structure for voltage control of magnetism with ionic liquid. (b) Schematic of the generation of an electric double layer for a positive (left) and negative (right) gate voltage and the effects on the channel material.[1]

Recently, there has been a lot of interest in ionic liquids as a gating material. This requires innovative device structures to accommodate the liquid substance. A schematic of a device structure containing an ionic liquid is shown in Fig 3.2. The device structure (Figure 3.2a) follows a FET type structure as shown in Figure 3.1a. This allows for a gate voltage to be applied to the ionic liquid, which consequently generates a large electric field by the electric double layer effect at the ionic liquid channel interface (Figure 3.2b). The induced changes in magnetic properties can be measured by monitoring the resistance across the channel.

Throughout this chapter the reader should gain a further understanding of these device structures and the mechanisms behind the voltage control of magnetic properties. Due to the complexity of the mechanisms it is often difficult to identify a sole mechanism behind the change.

3.3 Electric field control of magnetic properties in ferromagnetic semiconductors

In field-effect transistors (FET) an electric field is used to control the passage of current through a semiconductor between source and drain electrodes. In 2000, Ohno *et al.*[2] used the III-V ferromagnetic semiconductor, (In,Mn)As (5 nm), as their channel material in a FET(Figure 3.3 a-c) and demonstrated changes in transition temperature of hole induced ferromagnetism. Applied gate voltages (V_G) of ±125 V across a 0.8 μm thick (E ≈ 1.5 GVcm^{-1}) dielectric polyimide layer (κ = 3.3) varied the Curie temperature (T_C) by 2 K (Figure 3.3d). This occurred due to the gate voltage increasing the charge carrier (holes) concentration due to the manganese ions, which also provide the magnetic moment.
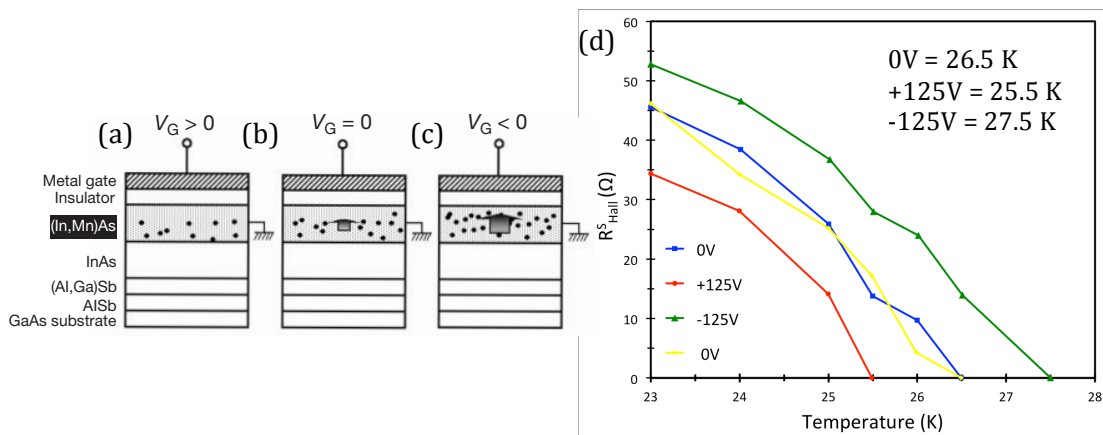

Figure 3.3: Field-effect control of hole induced ferromagnetism in magnetic semiconductor (In,Mn)As field-effect transistors. Parts (a)-(c) show the cross-sections of a metal-insulator- semiconductor structure under different V_G. a) A +V_G results in a decrease in hole concentration and ferromagnetic interaction of Mn ions (filled circles). b) V_G= 0 and c) -V_G both demonstrate an increased hole concentration and increased ferromagnetic interaction. (d) Temperature dependence of R^s_{Hall} (proportional to M_S) with different V_G applied. T_C for the different V_G is displayed in the top right[2].

The same group further investigated using another III-V ferromagnetic semiconductor, (Ga, Mn)As, using a FET structure with a Au electrode, a 40-50 nm HfO_2 dielectric layer (κ = 20) and a 3.5 nm thick film of (Ga, Mn)As[3] (Figure 3.4a). Applying

voltages of 12-15 V generated electric fields of approximately 3-4 GVcm^{-1}. They were able to vary T$_C$ by 16 K at low temperatures (Figure 3.4b), allowing switching between ferromagnetic and paramagnetic behaviour by applying an electric field. This was explained theoretically using the Zener model[4] to calculate T$_C$ for III-V and II-VI semiconductors with respect to varying charge carrier concentration[5]. Figure 3.4c demonstrates the theoretical control of charge carrier concentration through the channel depth of the ferromagnetic layer as a function of V$_G$[6]. This supports a voltage controlled charge carrier concentration induced change in magnetisation phase transition temperature.
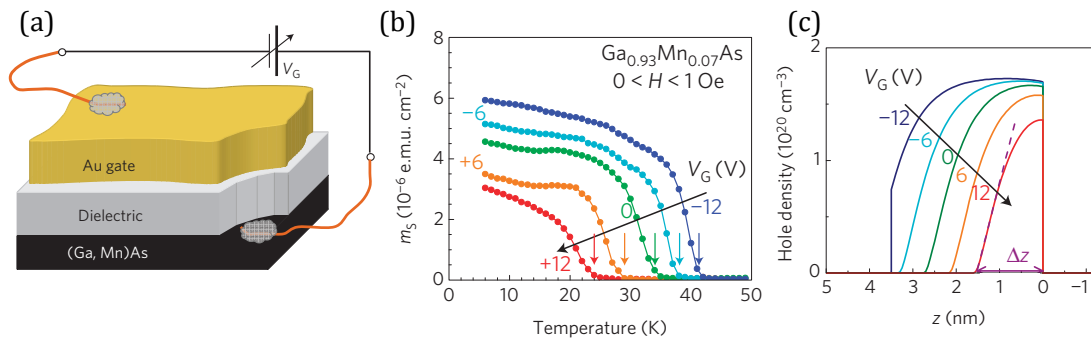

Figure 3.4: (a) Schematic of FET structure, including an Au gate electrode separated from a 3.5 nm (Ga, Mn)As by 40-50 nm HfO$_2$ dielectric. (b) Temperature, T, dependence of spontaneous magnetic moment, m$_s$, for different gate voltages, V$_G$, with the Curie temperature, T$_C$, indicated with arrows (c) Calculated hole concentration using Zener model through thickness, z, of (Ga, Mn) As for different V$_G$. Here the dashed line demonstrates the method used to establish Δz that is used to calculate m$_{sat}$ (not shown here).[3]

Zn, Co)O is a promising II-VI n-type ferromagnetic semiconductor with a similar carrier concentration to the p-type (In, Mn)As. Lee *et al.*[7] used a FET structure (Figure 3.1a) to investigate the change in magnetic properties of (Zn, Co)O upon applying gate voltages (± 70 V) to an 80 nm thick layer of AlO$_x$ to modulate the charge carrier concentration in the ferromagnetic semiconductor channel region. Electric fields of ± 5

GVcm^{-1} switched the magnetisation from ferromagnetic to paramagnetic at temperatures below 10 K[7] (Figure 3.5a & b).
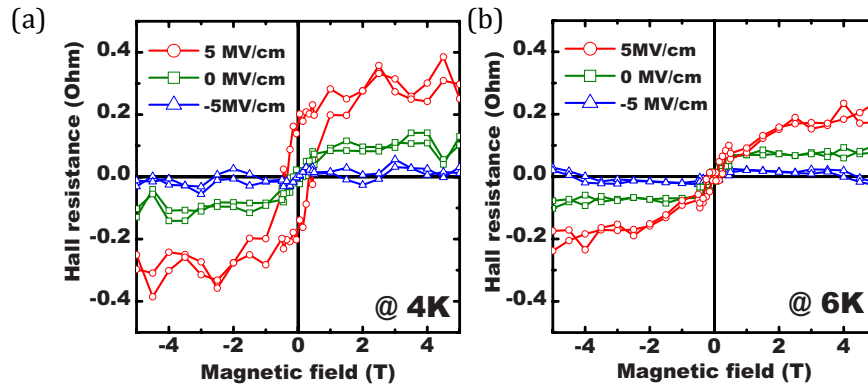

Figure 3.5: Magnetic field dependence of Hall resistance (proportional to M) for gate electric fields +5, 0 and -5 MV/cm[7]. (a) at 4 K, positive gate field electrons accumulate in (Zn, Co)O layer to generate clear hysteresis not present in zero and negative gate field. (b) at 6 K, no hysteresis observed at any gate field.[7]

Finally, research by Park *et al.*[8] demonstrated voltage control of ferromagnetism in a Mn$_x$Ge$_{1-x}$ (group-IV) ferromagnetic semiconductor as part of a FET device (see figure 3.1a). Gate voltages of ± 0.5 V applied to a 1200 Å thick SiN$_x$ insulating film generated electric fields of ± 40 kVcm^{-1} at the ferromagnetic semiconductor/insulator interface. Figure 3.6 shows a decrease (increase) in ferromagnetic ordering on application of a positive (negative) gate voltage at 50 K; this is again attributed to changes in charge carrier (hole) density within the ferromagnetic semiconductor film. Density-functional theory (DFT) in the same study showed that the magnetic moment arose due to hybridization between the Mn 3d states and the Ge p states. Further DFT analysis showed strong antiferromagnetic ordering for nearest neighbour Mn atoms and weak ferromagnetic ordering beyond nearest neighbour atoms, thus giving rise to a magnetic moment.
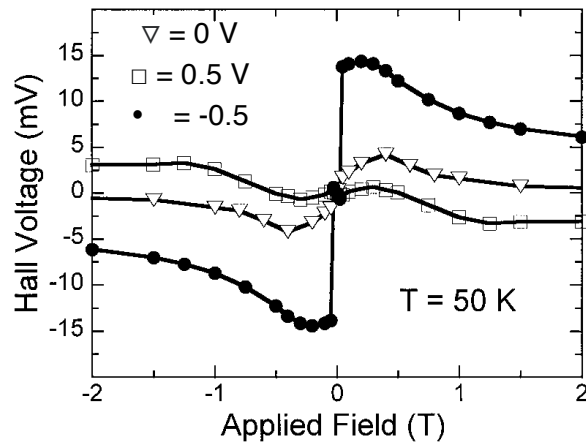
Figure 3.6: Hall voltage (proportional to M) versus applied magnetic field at 50 K with gate voltages 0 V (▽), +0.5 V (□) and -0.5 V (•). V$_G$ varies hole density in MnGe layer generating increase in Hall voltage at small negative voltages.[8]

Although the area of ferromagnetic semiconductors is improving there are still many obstacles that need to be overcome. This chapter indicates there are a large number of different ferromagnetic semiconductor materials being investigated. However, the low temperatures required to demonstrate voltage-controlled effects mean this approach is not currently realistic for device applications and more research is required to increase the operating temperature of these materials. Many of the ferromagnetic semiconductors also require complex, expensive and slow deposition techniques such as molecular beam epitaxy.

3.4 Voltage control of magnetic properties in multiferroic materials

Multiferroics are materials that contain one or more ferroic ordering parameters that couple with each other, such as ferromagnetism, ferroelectricty and ferroelasticity[9] (Figure 3.7). Ferromagnetism has already been described in section 2.3.3; ferroelectrics

and ferroelastics are similar in that they possess a spontaneous electrical and strain polarization, respectively, as opposed to magnetisation in ferromagnetic materials.
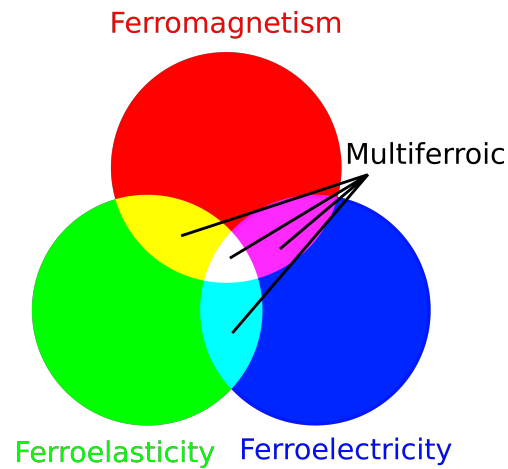

Figure 3.7: Venn diagram showing the overlap of ferroic orders to create multiferroics.

The interesting property of multiferroics for controlling magnetic properties is the ability to apply an electric field or strain field, and not only change the ferroelectric or ferroelastic ordering, but also the ferromagnetic ordering. These two methods to manipulate the ferromagnetic ordering are termed the magnetoelectric effect and the magnetoelastic effect. There are two types of multiferroic materials, true multiferroics and artificial multiferroics. True multiferroics are single-phase materials that contain multiple coupled ferroic properties, while artificial multiferroics are composites of materials with different ferroic ordering that couple with each other. Multiferroics also offer a low power alternative to current based approaches, such as ferromagnetic semiconductors and spin-transfer-torque methods.

3.4.1 True multiferroics

The concept of multiferroics was first introduced by Smolenskii and Ioffe in 1959[10], who suggested inserting magnetic ions into ferroelectric perovskites[11] (Figure 3.8). The first true multiferroic material to be investigated was a boracite material, $Ni_3B_7O_{13}I$ by Ascher

et al[12]., who demonstrated that applying a 5 kVcm⁻¹ electric (6 kOe magnetic) field caused a rotation in the magnetic (electric) polarisation at 56 K.
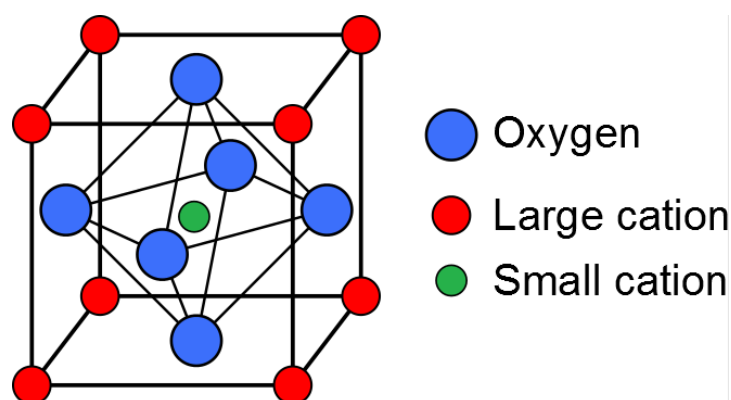

Figure 3.8: Cubic perovskite structure, ABO₃. The octahedron of oxygen anions (blue) contains a small cation (green) that gives rise to multiferroic properties. The large cations (red) occupy unit cell corners. Adapted from Spaldin[13].

In 2000 Hill (now Spaldin)[13] showed that ferroelectricity and ferromagnetism were driven by mutually exclusive properties, ferroelectrics requiring empty outer orbitals while ferromagnetism requiring half-filled outer orbitals. This shifted the paradigm of true multiferroics, suggesting that the atoms that move off centre to generate an electrical dipole moment should be different to the ones generating the magnetic moment[14].Following this revelation, papers were published on various rare earth manganates that showed multiferroic properties, including $TbMnO_3$[15] , $TbMn_2O_5$[16] and $YMnO_3$[17]. Hur *et al.*[16] investigated $TbMn_2O_5$, which has a complex structure with Mn^{4+} ions octahedrally coordinated by oxygen, Mn^{3+} ions at the base centre of a square pyramid and Tb ions surrounded by eight oxygen atoms[18]. Application of large magnetic fields (≈ 8 T), at low temperatures (3 K and 28 K) created changes in dielectric constant of 10-20% and complete reversal of electrical polarization (Figure 3.9). This magnetoelectric coupling was attributed to a magnetic field induced phase transition, tentatively associated with a change in Tb magnetic ordering giving rise to an increased magnetoelectric coupling coefficient.
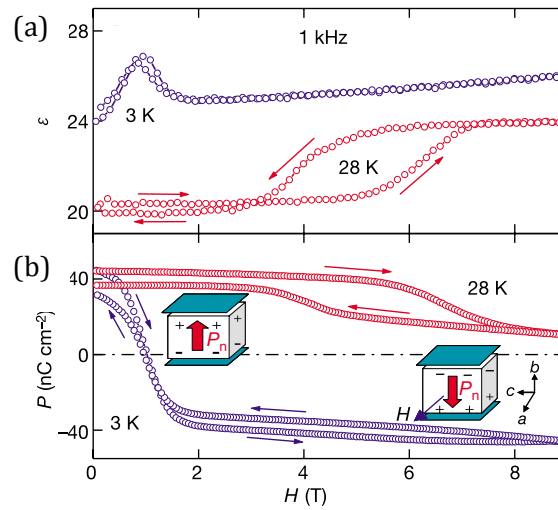
Figure 3.9: Polarisation reversal by magnetic fields. (a) Dielectric constant (measured at 1kHz) versus applied magnetic field at 3 and 28 K. (b) Change of total electric polarization by applied magnetic fields at 3 and 28 K[16].

    Currently rare earth manganates all exhibit multiferroicity well below room temperature. However bismuth ferrite ($BiFeO_3$), does possess multiferroic properties at room temperature and it's perovskite structure is shown in figure 3.6, with large cations of Bi and small cations of Fe. Wang *et al.*[19] successfully demonstrated two ferroic orders, spontaneous electrical polarization of 50-60 μC cm^{-2} and a spontaneous magnetisation of $\approx$ 150 emu cm^{-3} with $BiFeO_3$. This method of multiferroicity is termed the lone-pair mechanism, which arises due to unbound valence electrons around the host ion[20]. For $BiFeO_3$, a lone-pair of 6s valence electrons from the Bi^{3+} ion are not involved in *sp* hybridisation, creating a spontaneous polarisation below the T_C of 1,103 K[21]. The magnetic ordering is antiferromagnetic below the Néel temperature of 643 K[22] and arises due to the FeO_3 octahedra structures[23]. $BiFeO_3$ is the only reported room temperature multiferroic that utilises the lone-pair mechanism. However, the magnetic ordering is antiferromagnetic which means a ferromagnetic layer will be required to couple the two

magnetic orders effectively, which has been achieved successfully[24] and will be discussed below under 'Artificial mutliferroics'.

The lone pair mechanism described above is driven by bond chemistry. Another method of driving ferroelectricity is via geometric constraints that can lead to polar states being formed[25,26]. Some material systems that are known to show geometric ferroelectricity are h-RMnO$_3$ (R= Sc, Y, In or Dy-Lu)[25–28], h-LuFeO$_3$[29] and BaNiF$_4$[30,31]. The h-RMnO$_3$ systems generate a ferroelectric polarisation of up to 5.5 μC cm^{-2} [32] by a buckling of manganate bipyramids at the ferroelectric transition temperature ($\approx$ 1,200 K)[28] to cause a displacement of the R ions[25]. Antiferromagnetic ordering arising from the Mn^{2+} ions has been observed in these systems at temperatures below 130 K[27]. In 1969 Eibschütz et al.[31] demonstrated the ferroelectric properties of BaNiF$_4$. More recently Ederer et al.[30] calculated that this material not only has a small ferroelectric polarisation ($\approx$ 0.01 μC cm^{-2}) but also a weak ferromagnetic moment ($\approx$ 0.1 μ_B). Despite these low ferroic polarisations BaNiF$_4$ is of high interest because there is a direct coupling between ferroelectricity and ferromagnetism.

A strong interest has been shown in LuFe$_2$O$_4$, which exhibits ferroelectricity below 330 K and ferrimagnetism below 250 K[33]. This was thought to arise due to a charge ordering mechanism that generates ferroelectric properties from the formation of a superlattice within the crystal structure that supports an electrical polarization[34]. Here the Fe^{2+}/Fe^{3+} ions were thought to create a frustrated triangular sub lattice with an associated charge, the layer below having the opposite charge creating an electrical dipole between the bilayers creating ferroelectric polarization[33]. However, more recently LuFe$_2$O$_4$ has come under scrutiny with results showing the mechanisms producing ferroelectricty is not from charge ordering[35].

The final method of generating ferroelectric polarization is via spin-driven mechanisms, which are mechanisms furthest removed from the original displacive methods thus fitting the criteria advised by Spaldin[14]. There are three mechanisms that are spin driven. The first and most widely investigated is the inverse Dzyaloshinskii–Moriya (DM) interaction[36]. Which causes a displacement of charges between neighbouring spin states[37,38] and thus generates a reversible electric polarisation upon changing the magnetisation direction. Material systems that show this type of multiferroicity include $CaMn_7O_{12}$[39], Cr_2BeO_4[40] and o-$TbMnO_3$[15], albeit all well below room temperature. The other mechanisms are exchange striction, in which the exchange interaction between neighbouring spins induces striction along a specific crystallographic direction[41], and spin-dependent p-d hybridization, which relies upon spin orbit coupling[20].

In conclusion the mechanisms that generate multiferroicity in a single-phase material are many and varied. The main attraction of true multiferroics is the relative ease of fabrication when compared to artificial multiferroics and lack of interfacial effects. However the overarching drawbacks of true multiferroics are their operating temperature and weak ferroic properties. The only exception to this is $BiFeO_3$, although the magnetism is antiferromagnetic and of more limited use than ferromagnetic equivalents.

3.4.2 Artificial Multiferroics

Artificial multiferroics are composites made up of two or more coupled materials with different ferroic ordering (e.g. ferromagnetic and ferroelectric), termed magnetoelectric coupling when referring to magnetic and electric ordering. Here the coupling occurs by an elastic induced effect between the two ferroic orders. The ferroelectric material in this instance must display piezoelectric properties, whereby an applied electric field produces a mechanical strain in the material. The ferromagnetic material must show magnetostrictive properties, whereby an applied magnetic field causes a mechanical

strain in the material. With these two conditions satisfied, applying an electric field generates a strain in the piezoelectric, which is coupled into the ferromagnetic phase. The induced strain then causes a change in the magnetisation via the inverse magnetostrictive effect; this is described in (3-1a & b). How well the two ferroic orders couple with each other is designated by the magnetoelectric coefficient, α, and has units of V cm^{-1} Oe.

$$ME_H \; effect = \frac{magnetic}{mechanical} \times \frac{mechanical}{electric} \qquad \text{(3-1a)}$$

$$ME_E \; effect = \frac{electric}{mechanical} \times \frac{mechanical}{magnetic} \qquad \text{(3-1b)}$$

Van Suchtelen[42] at Philips Laboratories in the Netherlands first proposed artificial mutliferroics and subsequently managed to demonstrate magnetoelectric coupling in ceramic composites of $BaTiO_3$ – $CoFe_2O_4$[43,44]. Using a complicated process of unidirectional solidification of eutectic compositions, they reached a maximum magnetoelectric coefficient of 0.13 V cm^{-1} Oe, a value 200 times greater than a single crystal multiferroic at room temperature[44] (at time of publication, 1976). Much later further research predicted magnetoelectric effects in sintered composites of ferrites with $BaTiO_3$ or $Pb(ZrTi)O_3$[45], however the magnetoelectric coefficient was lower than previous reports[46]. Then attention turned to terfenol-d, a highly magnetostrictive material[47], coupled to many different piezoelectric layers[47–54]. These composites showed a giant magnetoelectric effect (GME), generating magnetoelectric coefficients of greater than 5 V cm^{-1} Oe[47].
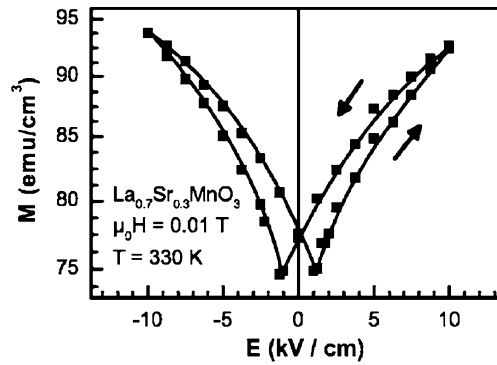
Figure 3.10: Magnetisation [100] as a function of electric field [001] in LSMO/PMN-PT heterostructure at 330 K.[55]

In more recent years a lot of research has gone into thin film heterostructures composed of a ferromagnetic and ferroelectric layer that couple together via the magnetoelectric (ME) effect. For example, Thiele *et al.*[55] successfully demonstrated the control of magnetisation using an electric field in $La_{0.7}S_{0.3}MnO_3$/Pb $(Mg_{0.33}Nb_{0.66})_{0.72}Ti_{0.28}O_3$ (LSMO/PMN-PT) heterostructres (Figure 3.10). In this research film thicknesses were in the range of 20-50 nm and voltages of up to 500 V generated electric fields of up to 12 kV cm^{-1} in the piezoelectric material. These voltages are very high when compared to the ones used in ferromagnetic semiconductors.

Geprägs *et al.*[56] in 2010, demonstrated a reversible 20% manipulation of magnetisation in a Ni/BaTiO$_3$ heterostructure on application of 4 kV cm^{-1} and -0.6 kV cm^{-1} (Figure 3.11). In this work voltages of up to 200 V applied to the BTO piezoelectric produced reversible changes in the in-plane magnetisation and coercivity of 100 nm thick films of Ni. These effects could again be attributed to the electroelastic strain and inverse magnetostrictive effect as outlined earlier.
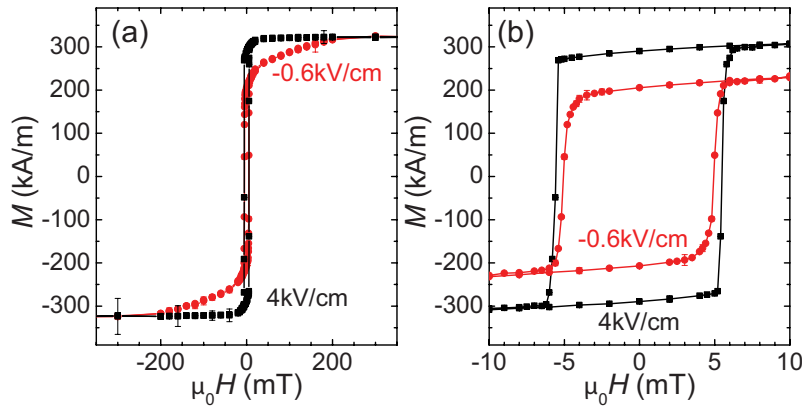
Figure 3.11: In-plane magnetic hysteresis loops M (H) for different electric fields applied across the BTO substrate. (a) Shows hysteresis loops in the ± 400 mT range and (b) in the ± 10 mT range to highlight changes in loop shape.[56]

Zhang *et al.*[57] demonstrated electric field modulated magnetism in CoFeB/PMN-PT heterostuctures via coupling between the ferroelectric domains and the ferromagnetic layer. The sample configuration is shown in fig 3.12a. Applying electric fields of ± 8 kV cm^{-1} to the system drastically manipulated the magnetisation of the film (Figure 3.12b) The peaks in current identify the ferroelectric polarisation switching and coincide with magnetisation switching. This result is particularly impressive because it occurs at room temperature.
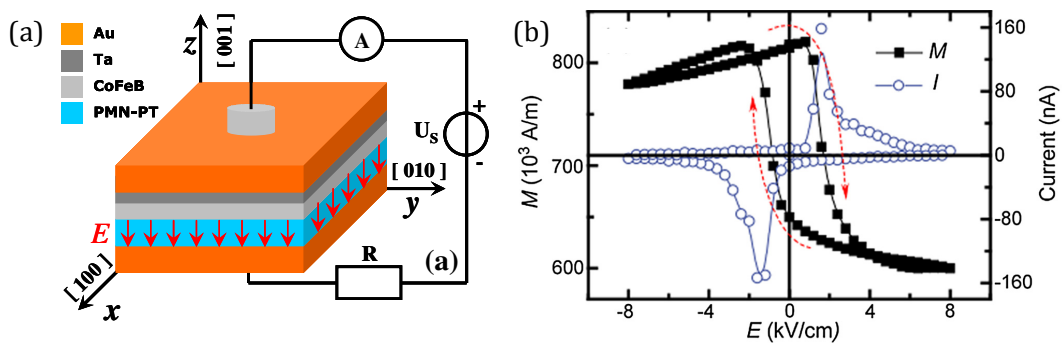

Figure 3.12: (a) Schematic of experimental set-up, Au/Ta/CoFeB/PMN-PT/AU. b) Electric field tuning of in plane magnetisation and polarisation current, recorded simultaneously.

Further to this Liu *et al.*[24] incorporated an antiferromagnetic (AFM) layer into the multiferroic heterostructure, creating a structure of AFM/FM/FE; this caused an exchange bias in the ferromagnetic layer, which is important for magnetoelectric random access memories (MERAM) devices. This study used a lead zinc niobate–lead titanate (PZN-PT) piezoelectric substrate, with a ferromagnetic bilayer, FeGaB (14nm)/NiFe (2nm) coupled to an antiferromagnetic layer of FeMn (15nm) (Figure 3.13a). Applying electric fields of 4-6 kV cm^{-1} drastically altered the coercivity and magnetic remanence of the ferromagnetic layer (Figure 3.13b) in an irreversible manner. This change was attributed to the electric field induced anisotropy and the exchange coupling at the AFM/FM interface[24].
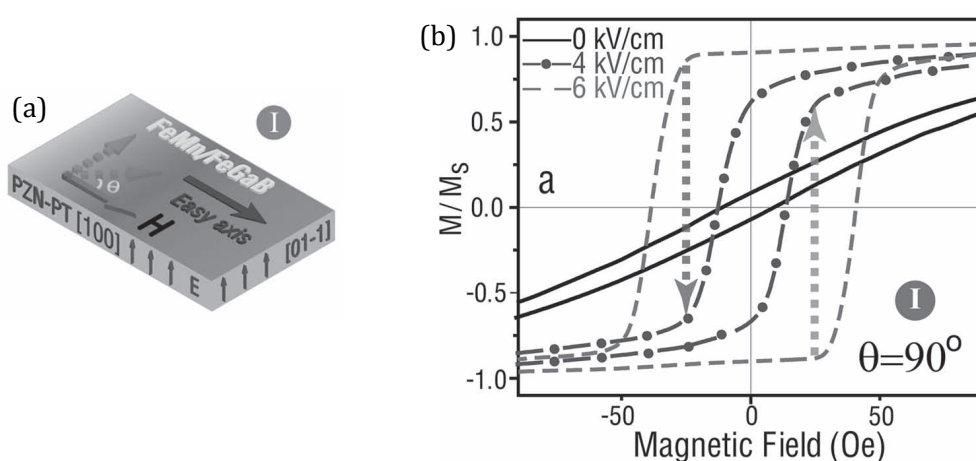

Figure 3.13: a) Schematic of experimental configuration, PZN-PT/FeGaB/NiFe/FeMn, where the FeGaB film was deposited under a bias field to induce an easy axis b) E-field control of coercive field and magnetic anisotropy for h-field along hard axis. Up and down arrow lines display the trends of magnetisation switching by reducing E-field[24].

In the previous examples all the ferromagnetic films have been relatively thick (>10 nm). However when film thickness approach values less than 5 nm interfacial effects start to dominate. At the interface between the ferroelectric and ferromagnetic materials, the ferroelectric polarisation direction has an effect on the electronic structure and when the ferromagnetic film is sufficiently thin the interfacial effects start to

dominate. There are two main origins for this electronic effect on the ferromagnetic properties at the interface: the first is a result of spin-dependent screening[58,59]. The unequal spin-polarization present in ferromagnets causes a different screening of the electric field for opposite spin directions. This generates a change in the electronic density of states (DOS), which determines the magnetic moment.

Niranjan *et al.*[59] used *ab initio* calculations to investigate the interfacial magnetoelectric coupling in $SrRuO_3/BaTiO_3$ heterostructures (Figure 3.14a), where $BaTiO_3$ and $SrRuO_3$ are ferroelectric and ferromagnetic materials. Figure 3.14b shows a clear difference in spin population and thus different magnetic moments at the right and left interfaces as a result of the polarisation direction. The change in exchange splitting originates from the screening of the polarisation of the ferroelectric, which they further consolidate using the Stoner model.[59]
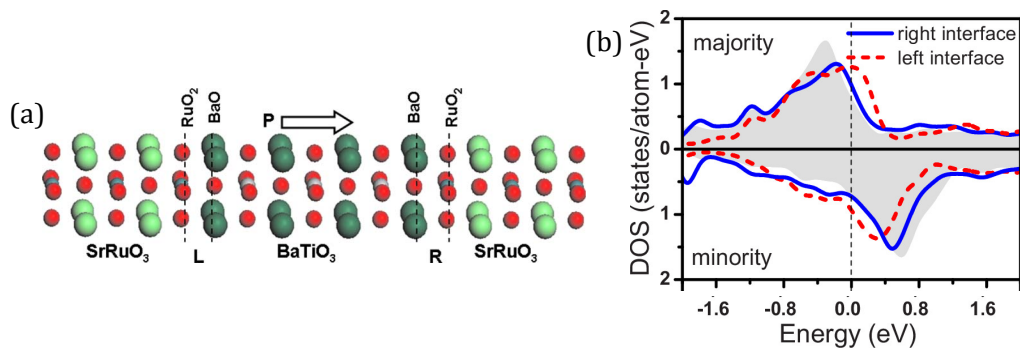

Figure 3.14: (a) The atomic structure of the SrRuO₃/BaTiO₃ (001) interfaces, where P is the ferroelectric polarisation direction and L and R indicate left and right interfaces. (b) Local density of states (DOS) projected onto the Ru 3d orbitals for majority and minority spin states at the left and right interfaces. The grey area represents the Ru 3d density of states in the bulk.[59]

The second origin for this electronic effect for magnetoelectric coupling arises due to the ferroelectric polarisation altering the electron orbital overlap between interfacial atoms of the ferromagnetic and ferroelectric layers. This change in bond chemistry can give rise to changes in interface magnetisation, anisotropy and spin

polarization[58]. Duan *et al.*[60] demonstrated this magnetoelectric effect using first-principles calculations to investigate the Fe(1nm)/BaTiO$_3$(2.5nm) interface (Figure 3.15a), where Fe is ferromagnetic and BaTiO$_3$ is ferroelectric.
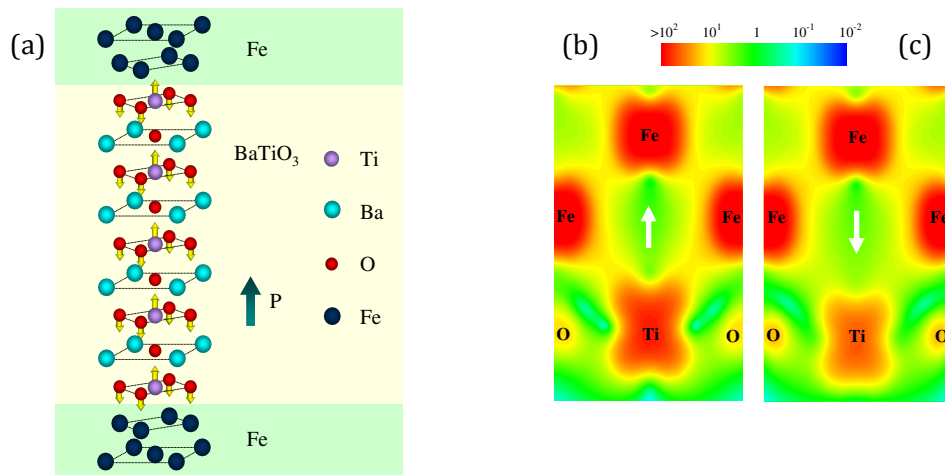

Figure 3.15: (a) Atomic structure of Fe/BaTiO$_3$ multilayer with 4 layers of BaTiO$_3$. The P and associated arrow indicate the polarisation direction, and the arrows on O and Ti atoms indicated atom displacement. b) & c) Minority-spin charge density (arbitrary units) at the Fe/BaTiO$_3$ interface for two opposite polarizations in BaTiO$_3$, (b) net polarisation pointing up (c) net polarisation pointing down.[60]

To illustrate this magnetoelectric effect they calculated the interface electronic charge density for two polarisation directions (Figure 3.15b & c). At the Fe/Ti interface there is a hybridisation of the *d* orbitals of both Fe and Ti items. It is clear from comparing Figure 3.15b & c that there is a clear reduction in orbital overlap when the polarisation points away from the Fe film; indicated by the decrease in charge density. Combining this with density of state calculations confirms the control of magnetic moment via ferroelectric induced change in electron orbital overlap[60].

There is one final mechanism for the magnetoelectric effect in ferromagnetic /ferroelectric heterostructures and that is charge carrier mediated. This effect is similar

to the process as described in 3.2 on ferromagnetic semiconductors above, that is a charge carrier modulation effect but without the semiconductor component. This has been demonstrated by Molegraaf et al.[61] in PZT/LSMO heterostructres, where they show magnetoelectric coupling of 0.8 x10^{-3} Oe cm V^{-1} at 100 K. Figure 3.16 clearly shows electric-field-induced switching of magnetisation. EELS and XANES analysis of LSMO also demonstrate a modification of charge carrier density with electric fields[62,63], further supporting charge carrier mediated changes in magnetic properties. Varying the doping level of LSMO has been highlighted as a way to maximise voltage controlled effects[64].
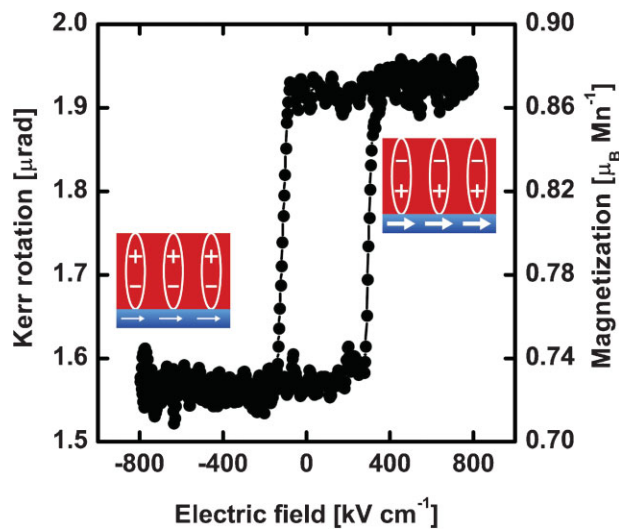

Figure 3.16: Magnetoelectric hysteresis curve at 100 K showing the magnetic response of the PZT/LSMO system as a function of the applied electric field[61].

In conclusion, artificial multiferroics show much greater magnetoelectric coupling between the two ferroic orders, especially at room temperature, which is important for future device applications. However, there are still issues to address, in many of these examples large voltages (>100 V) were required to generate the magnetoelectric coupling, which needs to be greatly reduced for low-power applications. Several

electronic effects have been identified in thin film heterostructures that enhance the magnetoelectric effect, including charge screening, DOS changes and charge carrier density.

3.5 Voltage control of magnetism in antiferromagnetic materials

As described in section 2 antiferromagnetic ordering is such that the magnetic moments align in opposite directions to produce zero net magnetic moment. However, above certain temperatures it is possible for an antiferromagnetic material to exhibit ferromagnetic properties. Antiferromagnetic materials are receiving an increasing amount of interest for applications in AFM spintronics[65]. One of the leading AFM materials receiving the most attention is FeRH, due to its low AFM to FM transition temperature of 350 K and total magnetic moment of 2.9 μ_B [66].
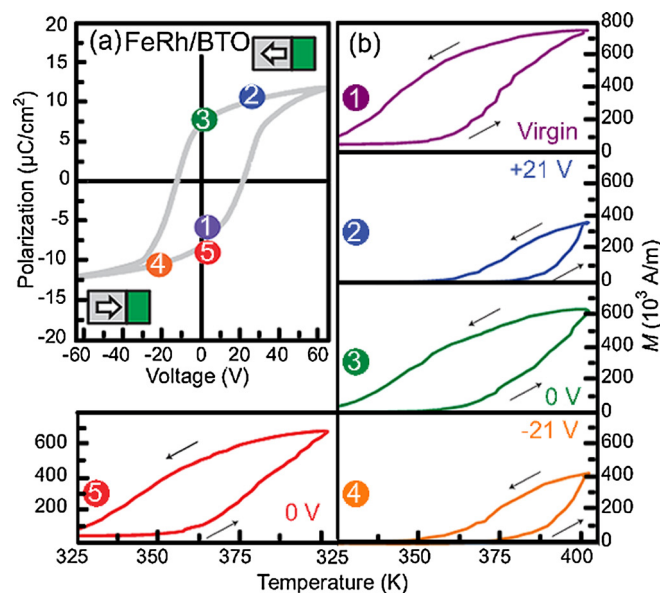

Figure 3.17: (a) Ferroelectric polarisation hysteresis loop for FeRh/BTO system at 300 Hz at RT, with sketches indicating polarisation direction. (b) Temperature variation of magnetisation at 20 kOe for different voltage values[67].

An in-depth report by Cherifi *et al.*[67] recently demonstrated electric field control of magnetic phase transition (AFM to FM) in FeRh films. In this study FeRh films were grown on FE BTO and a voltage applied to Au gate electrode. Applying voltages of ± 21 V generated changes of up to 25 K in transition temperature (figure 3.17). These changes were attributed to a voltage-induced strain effect from BTO to FeRh layer. But authors state it is hard to rule out contributions from charge accumulation and depletion effects. Further investigation into FeRh systems by Lee *et al.*[68]confirmed the strain-induced mechanism by performing *in* situ XRD analysis that indicated large variations in lattice constant with electric field.

3.6 Voltage control of magnetism of ultrathin metal films

This next section investigates the use of high-dielectric layer, ionic liquids and electrolytes to create high electric fields at the ferromagnetic interface, altering electronic configuration and oxidation states giving rise to changes in magnetic properties. The high-electric field generated by ionic liquids arises due to the formation of an electric double layer (EDL). To further understand this phenomenon it is necessary to give a brief description of ionic liquids, their properties and applications.

3.6.1 Ionic liquids & electrolytes

Ionic liquids (ILs), also known as molten salts, are simply salts that are liquid at room temperature[69]. For example sodium chloride becomes an 'ionic liquid' at 1,074 K[70]. This has lead to research into the synthesis of room temperature ionic liquids, for many potential applications including supercapacitors[71,72], field-effect transistors (FET's)[73], batteries[71,74], fuel cells[71,75] and the control of magnetism in thin films[76–82]. ILs are composed of two oppositely charged ions. When ILs replace the dielectric material in a capacitor cell and a voltage applied, the opposing polarity ions are electrostatically attracted to opposite charged plates. The ions form a single molecule layer at electrodes

over which the voltage charges. The small distance of this 'electric double layer' (EDL) causes extremely high electric fields to form (Figure 3.18)[83]. The value of the electric field at the interface is limited by the electrochemical window (ECW), outside of which the IL breaks down. The ECW is the figure of merit for ILs when a high electric field is desired, however even a small voltage of 1V generates an electric field of approximately 1-10 GV m^{-1}, over three orders of magnitude higher than some of the values mentioned earlier in this review generated by far larger voltages[83].
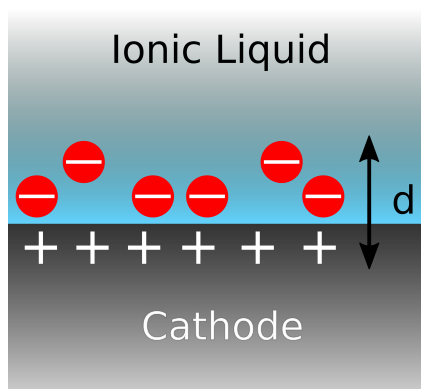

Figure 3.18: Electric double layer (EDL) generated at the ionic liquid (IL) cathode interface separated by d.

Weisheit *et al.*[77] were the first group to control magnetic properties using a liquid electrolyte and an applied voltage. They investigated cells containing Pt electrodes, propylene carbonate with added sodium ions and ultrathin films of FePt and FePd that displayed PMA (Figure 3.19a). Here the propylene carbonate sodium solution is not an ionic liquid but behaves like one by providing two oppositely charged ions, Na$^+$ and OH$^-$. Applying voltages to the electrodes caused the separation of the two oppositely charged ions and formed an EDL at the interface. Relatively low voltages of -0.4 V to -1.0 V decreased the coercivity of the 2 nm FePt films by approximately 4.5%, while the 4 nm films decreased by 1.5% (Figure 3.19b). The decrease in coercivity was attributed to a

decrease in unpaired *d* electrons by 0.015 electrons per unit cell upon application of electric field, thus decreasing the magneto-crystalline anisotropy energy[77]. The variation in coercivity decrease between the two thin film thicknesses was attributed to the difference in the surface to volume ratio.
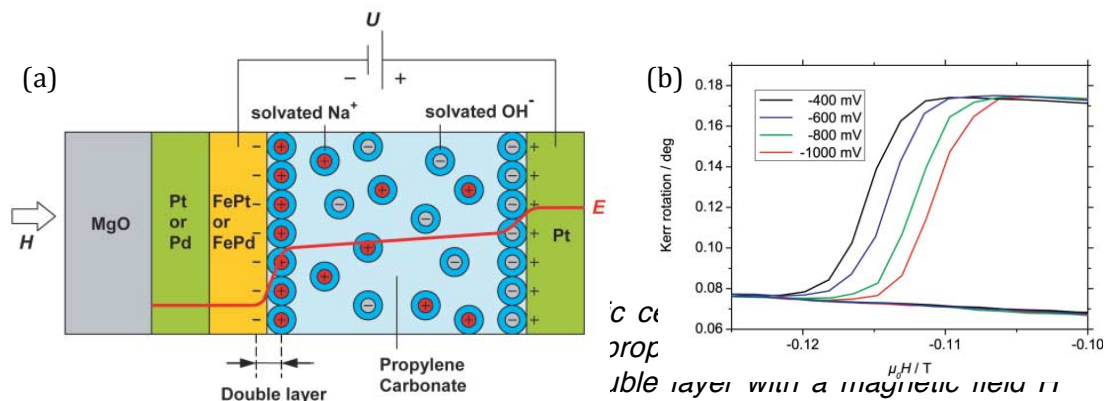
...c ce... ...rop... ...ble layer with a magnetic field H applied. E is the potential profile due to the applied potential U. (b) Magnetisation switching of 2 nm thick FePt films for different U values.

Shimamura *et al.*[81] demonstrated changes in magnetisation, coercivity and Curie temperature of Co thin films in cells containing an ionic liquid. A polymer film containing the ionic liquid ions, 1-ethyl-3-methylimi-dazolium (EMI$^+$) and bis(trifluoromethylsulfonyl)imide (TFSI$^-$), was placed on top of a 0.7 nm thick PMA Co layer and a voltage applied using a Pt gate electrode (Figure 3.20a). In the voltage range of ± 2 V, they successfully manipulated the Curie temperature by 100 K (Figure 3.20b). This was attributed to the formation of an EDL at the IL/Co interface causing a change of ± 0.084 electrons per Co unit cell.
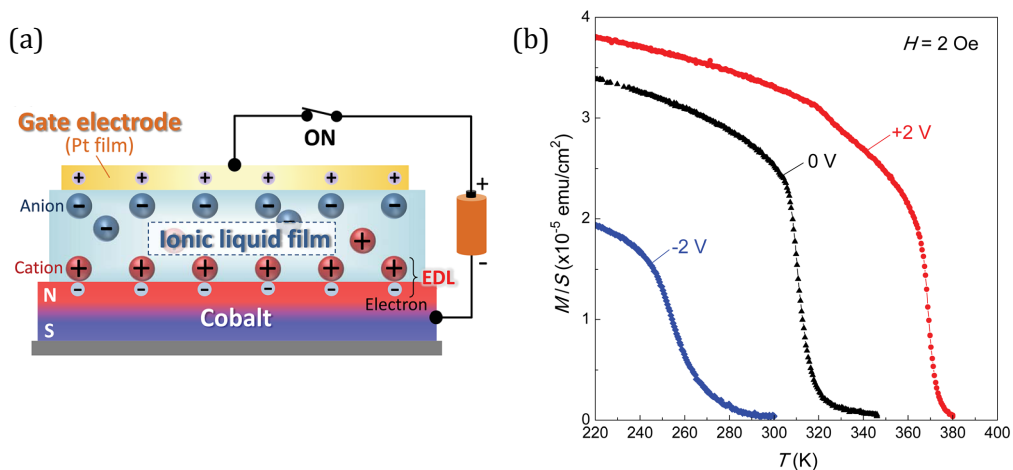
61

Figure 3.20: (a) Schematic of device structure consisting of Co thin film separated from a Pt gate electrode by an ionic liquid film to create electric double layer. (b) Temperature dependence of magnetisation of Co at H = 2 Oe and at gate voltages -2 V, 0 V and +2 V.[81]

Great interest has also been shown in enhancing effects observed in magnetic oxide heterostructures by combining the phenomenon with the large electric fields supplied by ionic liquids. One of the systems to be investigated is an ionic liquid/MgO/magnetic layer. Kawaguchi *et al.*[78] demonstrated this in a cell containing the EMI$^+$ TFSI$^-$ polymer film/MgO(2 nm)/Fe (0.7 nm), applying a voltage of ± 2 V to generate an EDL (Figure 3.21a). The large electric field was calculated to change the electrons per unit cell of Fe by ≈ 0.1, which was demonstrated experimentally by a change of approximately 50% in magnetisation (Figure 3.21b). The authors were also speculative about potential redox reactions taking place at the MgO/Fe interface resulting in changing magnetic properties. Obinata *et al.*[79] investigated a similar structure of an ionic film consisting of N,N,N-trimethyl-N-propylammonium (TMPA$^+$) and bis(trifluoromethylsulfonyl)imide (TFSI$^-$) and a 0.7 nm layer of Pd. The high fields generated from the EDL were successful in changing the electron density of the normally non-ferromagnetic Pd enough to create a ferromagnetic response.
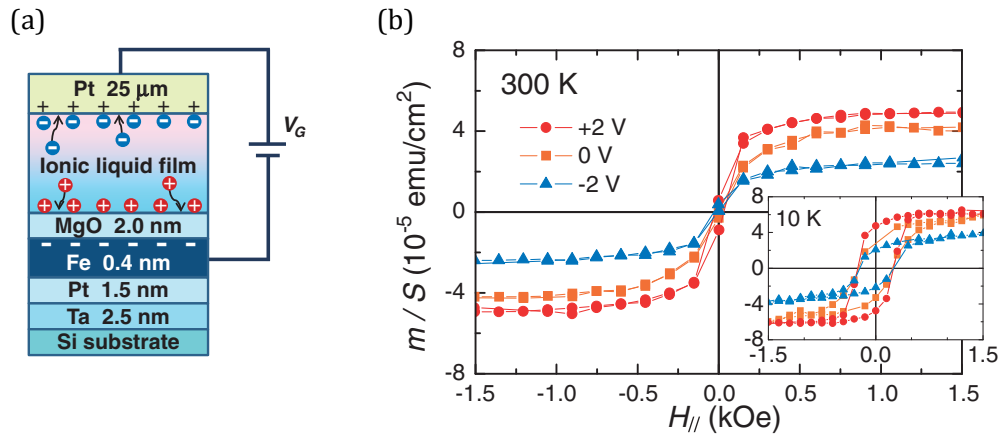
Figure 3.21: (a) Schematic of experimental cell consisting of Fe/MgO multilayer separated from a Pt gate electrode by an ionic liquid film. (b) Magnetisation in thin films of Fe as a function of in-plane magnetic field, H, at gate voltages of +2 V, 0 V and -2 V at 300 K and 10 K (inset)[78].

Another oxide dielectric that has been extensively investigated is HfO_2 in very similar arrangements to the previous experiments. Yan *et al.*[80] successful controlled the magnetisation at 4 K and varied in the Curie temperature in Co/Ni multilayers, using the ionic liquid N,N-diethy1-N-(2-methoxyethy1)-N-methylammonium (DEME$^+$) and bis(trifluoromethylsulfony1)imide (ETFSI$^-$) to create high electric fields. The electric fields were calculated to change the number of electrons per Ni cell by $\pm$ 0.048 on applying voltages of $\pm$ 1.5 V. However, x-ray photoelectron (XPS) spectroscopy revealed reversible oxidation of the thin film, which suggested an electrochemical dependence on magnetism. Zhou *et al.*[82] further investigated this arrangement; they demonstrated a thinning of the magnetic layer by voltage-induced oxidation (Figure 3.22b), which caused the observed changes in magnetic properties (Figure 3.22a & b). The two groups could not confirm that electrochemical effects were the sole origin of the observed effects and could not rule out electric field variation of electron density. Jiang *et al.*[76] used a similar cell to demonstrate voltage-induced ferromagnetism in a usually antiferromagnetic layer

of FeRh. The origins again appear to be a mixture of electric field induced changes of electron density and electrochemical effects.
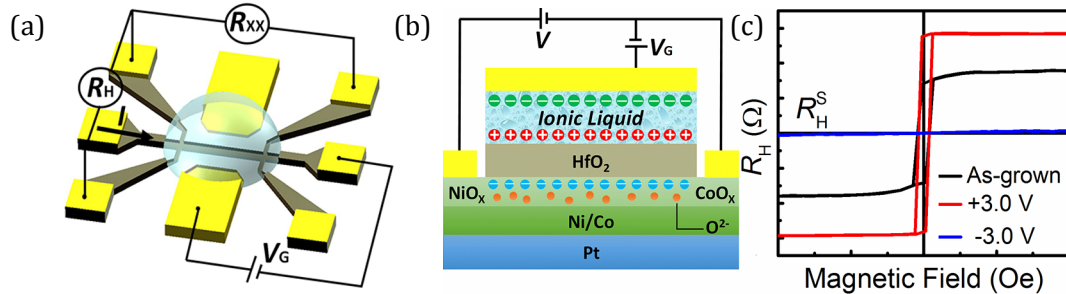

Figure 3.22: (a) Schematic of Hall device with a drop of ionic liquid. (b) EDL structure in Pt/Co/Ni/HfO$_2$ under positive gate voltage with the movement of O^{2-} ions indicated. (c) Magnetic hysteresis loop at gate voltages of +3 V, -3 V and as grown.[82]

Research by Di et al.[84] used a completely electrochemical approach to control the magnetic properties. Here they placed Co thin films in contact with KOH solution and applied a voltage, it is important to note that this is not an ionic liquid but demonstrates electrochemical effects on magnetic properties. Varying the potential reversibly changed the anisotropy from in plane to out of plane as demonstrated by hysteresis data in Figure 3.23a. This was attributed to OH and H groups at the surface of the film, indicated by current peaks A and C in Figure 3.23a, while changes in reflectivity also indicate changes in surface chemistry (Figure 3.23b).
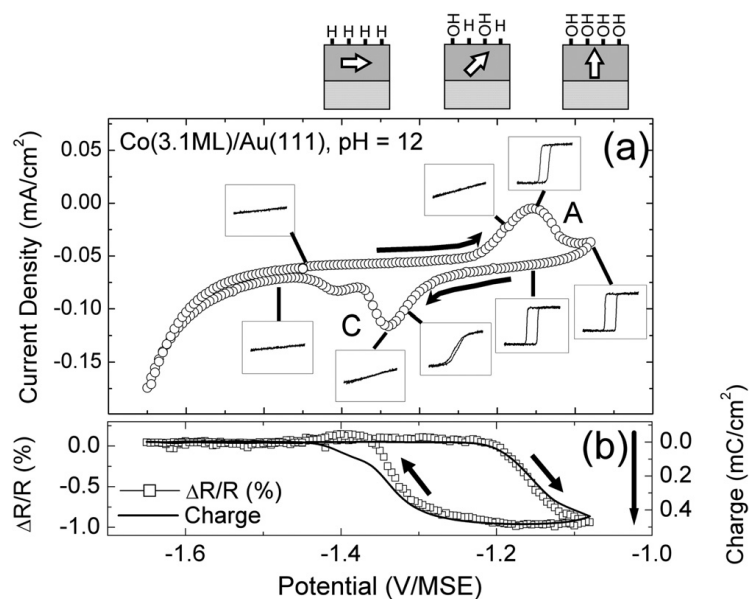
Figure 3.23: (a) Cyclic voltammagram of Co/Au/KOH cell at pH = 12, with magnetic hysteresis loops shown inset. Points A & C correspond to the first Co oxidation/ reduction steps. (b) Relative reflectivity of sample with varying voltage and right axis the charge (calculated by integrating the electrochemical current with the baseline corrected for water decomposition). Above shows surface oxidation of sample. Arrows on a) & b) indicate sweep direction.[84]

In conclusion, ionic liquids show a huge potential in the field of voltage control of magnetic properties. It has been demonstrated in this chapter that ionic liquids can generate extraordinarily high electric fields and have an unprecedented effect on the materials magnetic properties. However, the origin of the magnetic changes is currently unclear. The opposing arguments are an electrochemical change or an electric field control of electronic configuration or both. Therefore more research is required to fully understand the observed phenomena.

3.6.2 Dielectric Oxides

This next section discusses the progress in the area of dielectric oxides and the use of oxygen ions to control magnetic properties in ultrathin films. Whereas in ferromagnetic semiconductors and multiferroics where the magnetic changes are mediated by a

change in charge carriers or strain induced, here the majority of changes are generated

by the presence of oxygen ions, which change the electronic orbital arrangement of
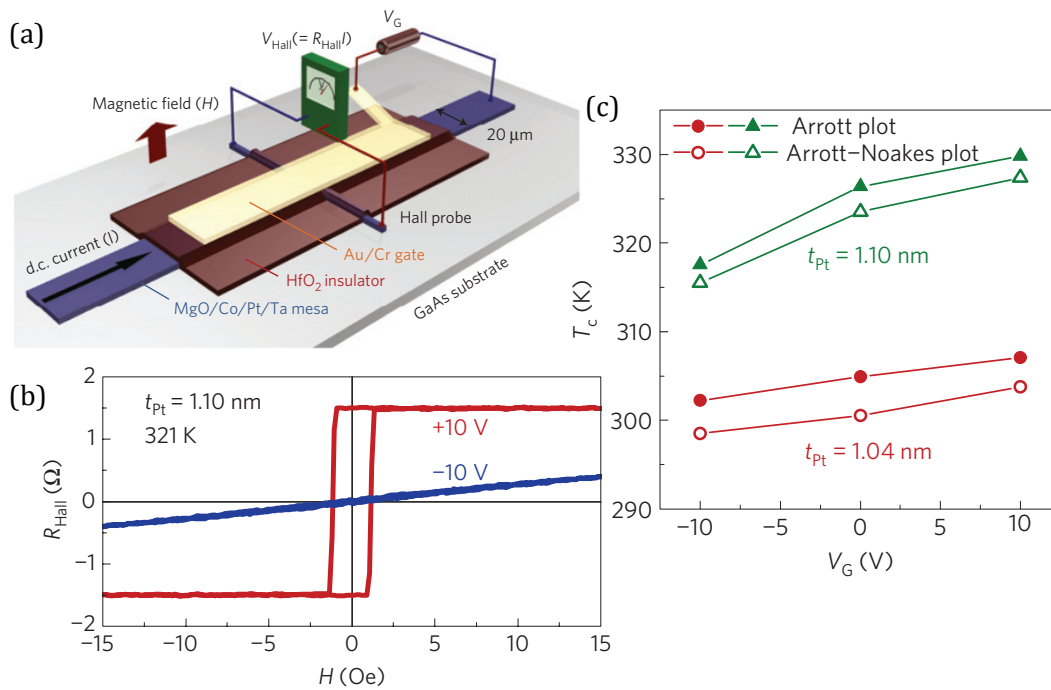
ferromagnetic atoms.

Figure 3.24: (a) Schematic of experimental set-up and sample structure, Au/Cr(gate electrode)/HfO$_2$(dielectric)/MgO/Co/Pt/Ta mesa. (b) hysteresis curves for sample with Pt thickness 1.10 nm ± 10Vat 321 K. (c) Curie temperature as a function of V$_G$ for Pt thickness, calculated using Arrot and Arrot-Noakes fitting[86].

Chiba et al.[85] demonstrated changes in coercivity and Curie temperature in

ultrathin Co/Pt films after applying a voltage to a HfO$_2$ dielectric layer. Au contacts were

used as a gate electrode, which was separated from the Co layer by a 50 nm HfO$_2$ layer

(Figure 3.24a). Applying gate voltages of ± 10 V generated changes in Curie temperature

of 12 K (Figure 3.24b & c). The mechanism behind these changes could be due to a

change in electrons per Co atom upon voltage application or due to mixing between the

Co and Pt layer. Further analysis by fitting models to experimental data, demonstrated

the Co/Pt film showed magnetically 2D characteristics, further supporting changes in

number of electrons as the dominant mechanism behind observed changes in magnetic

properties.

In 2013 Lin *et al.*[86] demonstrated irreversible increases in coercivity in thin heterostructures of Fe/ZnO (Figure 3.25a) upon application of a voltage. Using Au contacts the group applied voltages to the heterostructure and measured coercivity, current, resistance and temperature (Figure 3.25 b-e). Under applied voltages greater than +5 V the coercivity of a 5 nm thick Fe film increased from 100 Oe to 250 Oe (Figure 3.25b). X-ray photoelectron spectroscopy (XPS) detected Fe oxidation at the Fe/ZnO interface above +5V. The change in coercivity was attributed to direct current heating induced Fe oxidation, supported by Figure 3.25 b-e. The level of oxidation in the Fe is restricted by the ZnO thickness and the oxygen diffusion lengths[86].
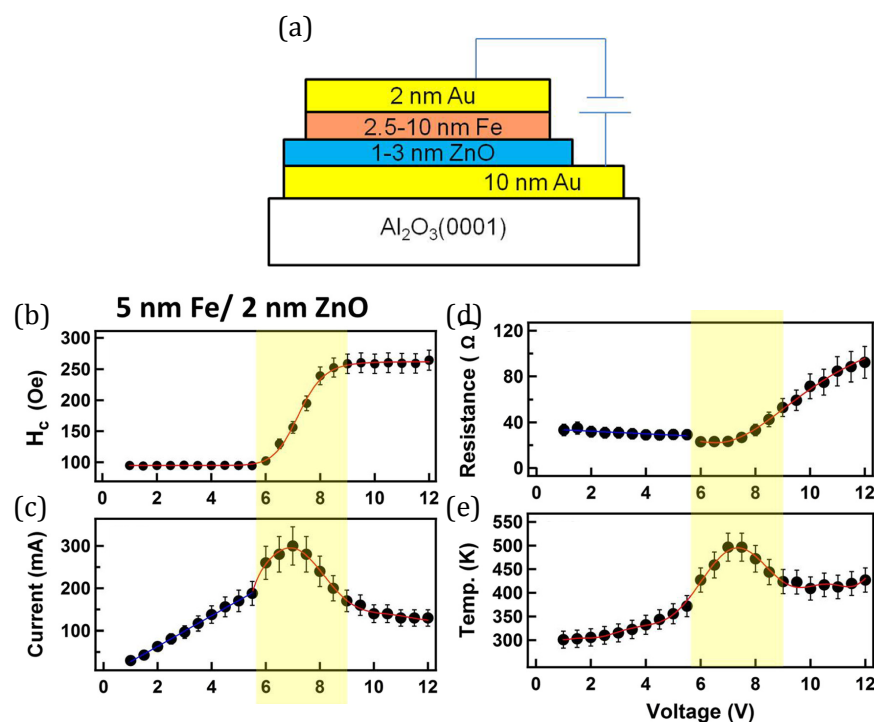

Figure 3.25: (a) Schematic of experimental cell Au(gate electrode)/Fe/ZnO/Au/Al$_2$O$_3$. Change of (b) coercivity (c) current (d) resistance (e) temperature with voltage for Fe/Zno heterostructure[86].
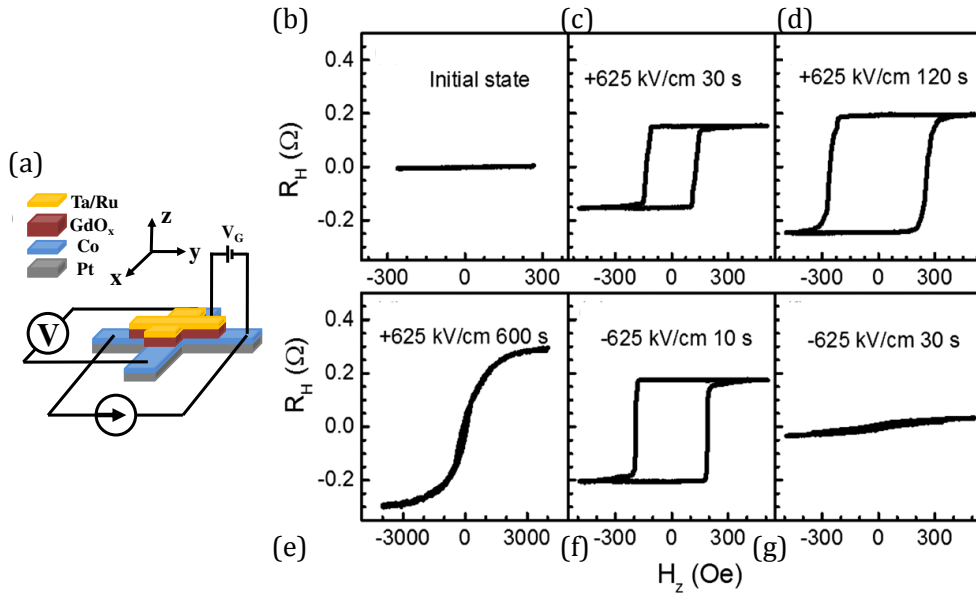
Figure 3.26: Schematic of the sample and experimental cell, Ta/Ru/GdOx/Co/Pt. Electric field induced evolution of magnetism of 0.7nm Co. (a) -625 kV cm^{-1} (b) +625 kV cm^{-1}, 30s (c) +625 kV cm^{-1}, 120s (d) +625 kV cm^{-1}, 600 s (e) -625 kV cm^{-1} 10 s and (f) -625 kV cm^{-1}, 30 s (g).[87]

Another ultrathin magnetic oxide heterostructure was investigated by Bi *et al.*[87], which showed large changes in coercivity and an unprecedented change in magnetic anisotropy upon applying low voltages (Figure 3.26). The system investigated was a Co(0.7 nm)/GdO$_x$(80 nm) heterostructures (Figure 3.26a), which possess a strong perpendicular magnetic anisotropy (PMA) due to hybridisation of Co 3d orbitals and O 2p orbitals at the interface[87]. The authors achieve this result thanks to large electric fields generated at the interface and the high mobility of O^{2-} ion mobility in the oxide layer. Applying voltages of ± 5 V generated electric fields of ± 625 kV cm^{-1} at the interface at 533 K; they show a two-fold increase in coercivity after 120 s (Figure 3.26d) and removal of PMA after 600 s (Figure 3.26e), which was subsequently restored on reversing the field polarity (Figure 3.26f). Combining this with x-ray absorption spectroscopy (XAS) and x-ray magnetic circular dichroism (XMCD) they demonstrated that positive fields drive out O^{2-} ions making almost pure Co. The removal of oxygen ions increased the magnetic

moment and removed the hybridisation of between 3d and 2p orbitals, thus removing the

PMA. On the other hand negative electric fields quickly oxidised the Co completely

removing all magnetic properties until a positive electric field was applied again. One

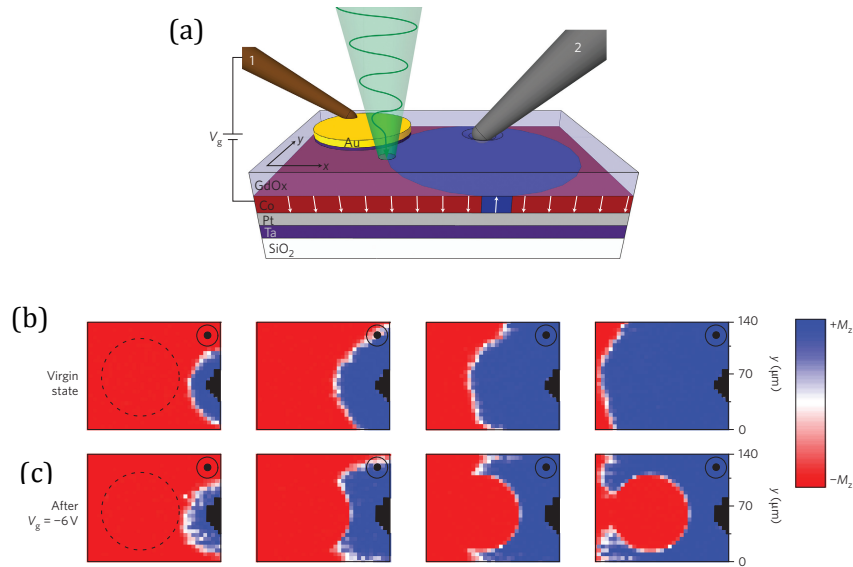drawback of this approach is that it appears that heat is required to assist the observed

effects.

Figure 3.27: (a) Schematic showing the Ta/Pt/GdOx structure, where 1 is a microprobe for voltage application and 2 is a probe to create nucleation sites, the green cone is the incoming MOKE signal. Space- and time-resolved domain expansion, where dashed circle is area underneath electrode and the black area is the mechanical probe. (a) shows DW expansion passing under electrode unaffected (b) shows DW being trapped in area underneath electrode area[89].

Bauer *et al*. carried out further research into Co/GdOx systems, where they

successfully controlled domain wall (DW) propagation in Co thin films by varying the

oxygen presence with a voltage (Figure 3.27a-c)[88,89]. They demonstrated that applying -6

V to a Co(0. 9nm)/GdOx (3 nm) (Figure 3.27a) drives oxygen ions to the interface, the

increased oxygen presence decreases the PMA and creates a local energy barrier[89].

Creating local nucleation sites with a mechanical probe, DW's propagated towards the

area under the electrode, which past straight through after 0 V was applied, but the DW

underneath the electrode area remained trapped after -6V (Figure 3.27b & c). This

phenomenon was used to create a three-bit register, which demonstrated the feasibility for voltage controlled memory devices for the future.
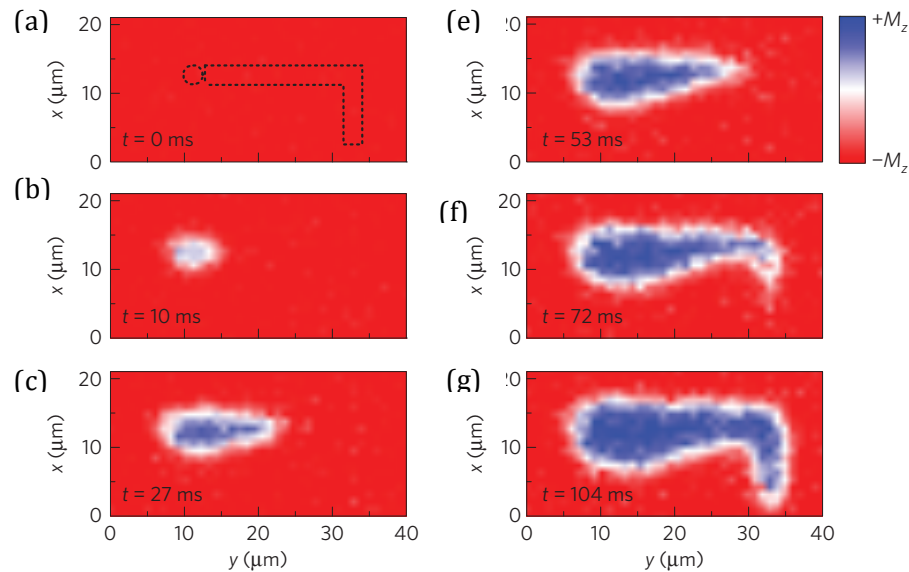

Figure 3.28: Laser-defined anisotropy patterns and DW conduits. Time resolved MOKE of DW expansion with increasing time after exposure to 10 mW with a driving magnetic field, H = 42 Oe. (a) Area outlined by 10 mW laser at V_G = -3 V, with dashed circle exposed for 100 s and L shape scanned in 1.25 µm steps with 65 s exposure at each point. All maps acquired at zero bias voltage. (b) 10 ms (c)27 ms (d) 53 ms (e) 72 ms and (f) 104 ms.[91]

Using the same material system the same group further investigated the controllable magnetic properties by using laser light to locally heat areas of the sample[90]. Building on the previous work they used *in situ* transmission electron microscopy (TEM) and high-resolution electron emission loss spectroscopy (EELS) to directly observe oxygen migration into the magnetic layer upon application of a negative voltage, which was subsequently removed on reversing the voltage polarity. The group further demonstrated that increasing the temperature and voltage magnitude significantly increased switching speed. They used a 10 mW laser to locally increase the temperature by 20 K, which gave sufficient energy to locally induce oxygen ion migration[90]. Scanning the laser across the sample allows 2-D patterning of different magnetic anisotropy

regions (Figure 3.28). This was a significant step in low power control of magnetic properties and opens up possibilities of reconfigurable patterned magnetic devices.

Maruyama et al.[91] used a polyimide/MgO/Fe multilayer stack (Figure 3.29a & b) to demonstrate voltage control of magnetic anisotropy. Applying voltages of ± 200 V they successfully toggled the magnetic easy axis between in plane and out of plane (Figure 3.29c), which was attributed to a field induced change in the overlap of the d orbitals. However, it is hard to rule out the effect of oxygen ion migration across the MgO/Fe interface.
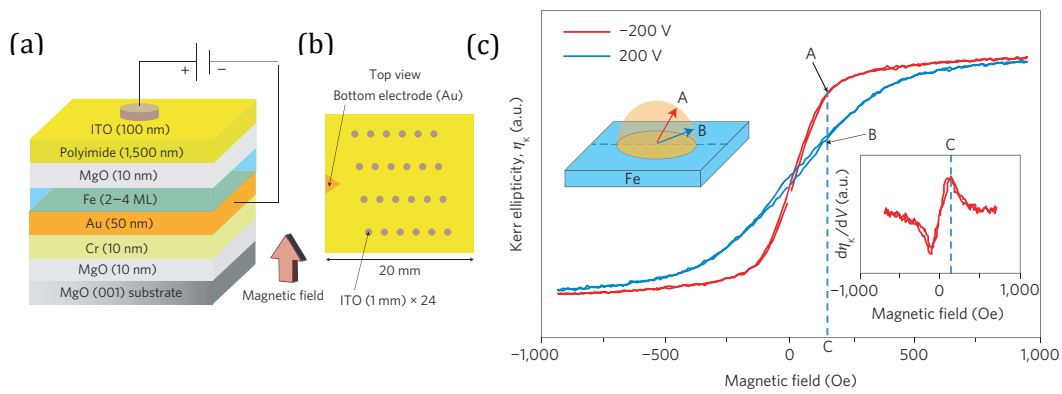
Figure 3.29: Schematic of sample arrangement (a) side view and (b) top view.(c) Magneto-optical Kerr ellipticity, η_k, for -200 V and +200 V applied as a function of field. The left inset shows the magnetisation direction at points A (-200 V) and B (+200 V) in hysteresis loops. The right inset shows the voltage modulation response of the Kerr ellipticity, where C represents the maximum $d\eta_k/dV$, which corresponds to the maximum difference between the two hysteresis loops.[91]

Finally, Chiba et al. utilised an HfO_2/MgO/Co/Pt multilayer which possesses PMA properties to demonstrate changes in ferromagnetic transition temperatures. Applying voltages of ± 10 V successfully transitioned between ferromagnetic behaviour and non-ferromagnetic behaviour. This drastic change is attributed to a change in MAE by voltage-induced changes of carrier density and electron occupancy.

In conclusion ultrathin magnetic oxide heterostructures show very promising progress in the field of low power voltage control of magnetic properties, with steps taken towards creating devices. The main positives over other approaches are the room temperature operation of the observed effects and the large magneto-ionic coupling effects of anisotropy.

3.7 Summary

In summary there are many different methods for controlling magnetic properties with voltage. With some techniques such as a multiferroics and ferromagnetic semiconductors, where the processes involved are well known, and others such as oxygen ion migration and electric field control of electronic configuration. The recent emergence of IL cells to support voltage-control of magnetic properties offers a high degree of flexibility and relatively simple arrangements as well as changes that remain upon removal of the voltage, which is of interest for low power applications.

3.8 References

1.   Song, C., Cui, B., Li, F., Zhou, X. & Pan, F. Progress in Materials Science Recent progress in voltage control of magnetism : Materials , mechanisms , and performance. *Prog. Mater. Sci.* **87,** 33–82 (2017).

2.   Ohno, H. *et al.* Electric-field control of ferromagnetism. *Nature* **408,** 944–946 (2000).

3.   Sawicki, M. *et al.* Experimental probing of the interplay between ferromagnetism and localisation in (Ga,Mn)As. *Nat. Phys.* **6,** 8 (2009).

4.   Zener, C. Interaction between the d-shells in the transition metals. III. Calculation of the Weiss factors in Fe, Co, and Ni. *Phys. Rev.* **83,** 299–301 (1951).

5.   Dietl, T., Ohno, H. & Matsukura, F. Hole-mediated ferromagnetism in tetrahedrally coordinated semiconductors. *Phys. Rev. B* **63,** 195205 (2000).

6.   Matsukura, F., Tokura, Y. & Ohno, H. Control of magnetism by electric fields. *Nat. Nanotechnol.* **10,** 209–220 (2015).

7.   Lee, H.-J., Helgren, E. & Hellman, F. Gate-controlled magnetic properties of the magnetic semiconductor (Zn,Co)O. *Appl. Phys. Lett.* **94,** 212106 (2009).

8.   Park, Y. D. *et al.* A Group-IV Ferromagnetic Semiconductor : MnxGe1-x. **295,** 651–654 (2002).

9.   Martin, L. W. & Ramesh, R. Multiferroic and magnetoelectric heterostructures. *Acta Mater.* **60,** 2449–2470 (2012).

10. Smolenskii, G. A., Isupov, V. A. & Agronovskaya, A. . New ferroelectrics of complex composition of the type A22 + (BI3 + BII5 +)O6. *Sov. Physics, Solid State* **1,** 150–151 (1959).

11. Spaldin, N. *Magnetic Materials. Fundamentals and applications*. (Cambridge University Press, 2010). doi:10.2277/0521016584

12. Ascher, E., Rieder, H., Schmid, H. & Stössel, H. Some properties of ferromagnetoelectric nickel-iodine boracite, Ni 3B7O13I. *J. Appl. Phys.* **37,** 1404–1405 (1966).

13. Hill, N. A. Why Are There so Few Magnetic Ferroelectrics? 6694–6709 (2000). doi:10.1021/jp000114x

14. Ramesh, R. & Spaldin, N. A. Multiferroics: progress and prospects in thin films. *Nat. Mater.* **6,** 21–29 (2007).

15. Kimura, T. *et al.* Magnetic control of ferroelectric polarization. *Nature* **426,** 55–58

(2003).

16.   Hur, N. *et al.* Electric polarization reversal and memory in a multiferroic material

        induced by magnetic fields. *Nature* **429,** 392–395 (2004).

17.   Fiebig, M., Lottermoser, T., Fröhlich, D., Goltsev, a V & Pisarev, R. V.

        Observation of coupled magnetic and electric domains. *Nature* **419,** 818–820

        (2002).

18.   Saito, K. & Kohn, K. Magnetoelectric effect and low-temperature phase transitions

        of TbMn2Os. Phys. Condens. Matter 7**,** 2855–2863 (1995).

19.   Wang, J. *et al.* Epitaxial BiFeO3 multiferroic thin film heterostructures. *Science*

        299, 1719–1722 (2003).

20.   Fiebig, M., Lottermoser, T., Meier, D. & Trassin, M. The evolution of multiferroics.

        Nat. Rev. Mater. 16046 (2016). doi:10.1038/natrevmats.2016.46

21.   Moreau, J. M., Michel, C., Gerson, R. & James, W. J. Ferroelectric BiFeO3 X-Ray

        and Neutron Diffraction Study. *J. Phys. Chem. C* **32,** 1315–1320 (1971).

22.   Kiselev, S. V., Ozerov, R. P. & Zhdanov, G. S. Detection of Magnetic Order in

        Ferroelectric BiFeO3 by Neutron Diffraction. *Sov. Phys. Dokl.* **7,** 742 (1963).

23.   Ederer, C. & Spaldin, N. A. Weak ferromagnetism and magnetoelectric coupling in

        bismuth ferrite. *Phys. Rev. B - Condens. Matter Mater. Phys.* **71,** 1–4 (2005).

24.   Liu, M., Lou, J., Li, S. & Sun, N. X. E-field control of exchange bias and

        deterministic magnetization switching in AFM/FM/FE multiferroic heterostructures.

        Adv. Funct. Mater. **21,** 2593–2598 (2011).

25.   Van Aken, B. B., Palstra, T. T. M., Filippetti, A. & Spaldin, N. a. The origin of

        ferroelectricity in magnetoelectric YMnO3. *Nat. Mater.* **3,** 164–170 (2004).

26. Fennie, C. J. & Rabe, K. M. Ferroelectric transition in YMnO3 from first principles. *Phys. Rev. B - Condens. Matter Mater. Phys.* **72,** 1–4 (2005).

27. Fiebig, M. *et al.* Determination of the magnetic symmetry of hexagonal manganites by second harmonic generation. *Phys. Rev. Lett.* **84,** 5620–5623 (2000).

28. Lilienblum, M. *et al.* Ferroelectricity in the multiferroic hexagonal manganites. *Nat. Phys.* **11**, pages 1070–1073, (2015).

29. Wang, W. *et al.* Room-temperature multiferroic hexagonal LuFeO3 films. *Phys. Rev. Lett.* **110,** 1–5 (2013).

30. Ederer, C. & Spaldin, N. A. Electric-field-switchable magnets: The case of BaNiF4. *Phys. Rev. B - Condens. Matter Mater. Phys.* **74,** 1–4 (2006).

31. Eibschütz, M., Guggenheim, H. J., Wemple, S. H., Camlibel, I. & DiDomenico, M. Ferroelectricity in BaM2+F4. *Phys. Lett. A* **29,** 409–410 (1969).

32. Fujimura, N., Ishida, T., Yoshimura, T. & Ito, T. Epitaxially grown YMnO3 film: New candidate for nonvolatile memory devices. *Appl. Phys. Lett.* **69,** 1011–1013 (1996).

33. van den Brink, J. & Khomskii, D. I. Multiferroicity due to charge ordering. *J. Phys. Condens. Matter* **20,** 434217 (2008).

34. Ikeda, N. *et al.* Ferroelectricity from iron valence ordering in the charge-frustrated system LuFe2O4. *Nature* **436,** 1136–1138 (2005).

35. De Groot, J. *et al.* Charge order in LuFe 2O 4: An unlikely route to ferroelectricity. *Phys. Rev. Lett.* **108,** 1–5 (2012).

36. Sergienko, I. A. & Dagotto, E. Role of the Dzyaloshinskii-Moriya interaction in

multiferroic perovskites. *Phys. Rev. B - Condens. Matter Mater. Phys.* **73,** 1–5 (2006).

37. Mostovoy, M. Ferroelectricity in spiral magnets. *Phys. Rev. Lett.* **96,** 1–4 (2006).

38. Katsura, H., Nagaosa, N. & Balatsky, A. V. Spin current and magnetoelectric effect in noncollinear magnets. *Phys. Rev. Lett.* **95,** 1–4 (2005).

39. Johnson, R. D. *et al.* Giant improper ferroelectricity in the ferroaxial magnet CaMn 7O 12. *Phys. Rev. Lett.* **108,** 2–5 (2012).

40. Newnham, R. E., Kramer, J. J., Schulze, W. A. & Cross, L. E. Magnetoferroelectricity in Cr2BeO4. *J. Appl. Phys.* **49,** 6088–6091 (1978).

41. Tokura, Y., Seki, S. & Nagaosa, N. Multiferroics of spin origin. *Rep. Prog. Phys.* **77,** 076501 (2014).

42. van Suchtelen, Product Properties: A New Application of Composite Materials J. *Philips Research Report.* Vol. 27, No. 1, 1972, pp. 28-37, (1972).

43. Van Run, A. M. J. G., Terrell, D. R. & Scholing, J. H. An in situ grown eutectic magnetoelectric composite material. *J. Mater. Sci.* **9,** 1710–1714 (1974).

44. Van Den Boomgaard, J., Van Run, A. M. J. G. & Suchtelen, J. Van. Magnetoelectricity in piezoelectric-magnetostrictive composites. *Ferroelectrics* **10,** 295–298 (1976).

45. Harshe, G., Dougherty, J. P. & Newnham, R. E. Magnetoelectric effect in composite materials. in **1919,** 224–235 (1993).

46. Lopatin, S., Lopatina, I. & Lisnevskaya, I. Magnetoelectric PZT/ferrite composite material. *Ferroelectrics* **162,** 63–68 (1994).

47.   Dong, S. *et al.* Circumferential-mode, quasi-ring-type, magnetoelectric laminate composite-a highly sensitive electric current andor vortex magnetic field sensor. *Appl. Phys. Lett.* **86,** 1–3 (2005).

48.   Dong, S., Li, J. F. & Viehland, D. Ultrahigh magnetic field sensitivity in laminates of TERFENOL-D and Pb(Mg1/3Nb2/3)O3-PbTiO3 crystals. *Appl. Phys. Lett.* **83,** 2265–2267 (2003).

49.   Dong, S., Zhai, J., Li, J. & Viehland, D. Small dc magnetic field response of magnetoelectric laminate composites. *Appl. Phys. Lett.* **88,** 166–168 (2006).

50.   Dong, S., Zhai, J., Li, J.-F. & Viehland, D. Magnetoelectric effect in Terfenol-D∕Pb(Zr,TiO)[sub 3]∕µ-metal laminate composites. *Appl. Phys. Lett.* **89,** 122903 (2006).

51.   Zhai, J., Li, J., Dong, S., Viehland, D. & Bichurin, M. I. A quasi(unidirectional) Tellegen gyrator. *J. Appl. Phys.* **100,** 2004–2007 (2006).

52.   Dong, S., Zhai, J., Li, J. & Viehland, D. Enhanced magnetoelectric effect in three-phase MnZnFe2O4/Tb1-xDyxFe2-y/Pb(Zr,Ti)O3 composites. *J. Appl. Phys.* **100,** 124108/1-124108/4 (2006).

53.   Dong, S., Zhai, J., Li, J. F., Viehland, D. & Bichurin, M. I. Magnetoelectric gyration effect in Tb1-xDyxFe 2-yPb (Zr,Ti)O3 laminated composites at the electromechanical resonance. *Appl. Phys. Lett.* **89,** (2006).

54.   Dong, S., Zhai, J., Li, J. & Viehland, D. Near-ideal magnetoelectricity in high-permeability magnetostrictive/ piezofiber laminates with a (2-1) connectivity. *Appl. Phys. Lett.* **89,** 3–6 (2006).

55.   Thiele, C., Dörr, K., Bilani, O., Rödel, J. & Schultz, L. Influence of strain on

magnetization and magnetoelectric effect in La0.7A0.3MnO3 / PMN-PT(001) (A = Sr; Ca). *Phys. Rev. B* **75,** 054408 (2007).

56. Geprägs, S., Brandlmaier, A., Opel, M., Gross, R. & Goennenwein, S. T. B. Electric field controlled manipulation of the magnetization in Ni/ BaTiO3 hybrid structures. *Appl. Phys. Lett.* **96,** 13–16 (2010).

57. Zhang, S. *et al.* Electric-Field Control of Nonvolatile Magnetization in Co40Fe40B20/Pb(Mg1/3Nb2/3)0.7Ti0.3O3 Structure at Room Temperature. Phys Rev Lett. **137203,** 1–5 (2012).

58. Garcia, V., Bibes, M. & Barthélémy, A. Artificial multiferroic heterostructures for an electric control of magnetic properties. *Comptes Rendus Phys.* **16,** 168–181 (2015).

59. Niranjan, M. K., Burton, J. D., Velev, J. P., Jaswal, S. S. & Tsymbal, E. Y. Magnetoelectric effect at the SrRuO3/BaTiO3 (001) interface: An ab initio study. *Appl. Phys. Lett.* **95,** 1–4 (2009).

60. Duan, C. G., Jaswal, S. S. & Tsymbal, E. Y. Predicted magnetoelectric effect in Fe/BaTiO3 multilayers: Ferroelectric control of magnetism. *Phys. Rev. Lett.* **97,** 13–16 (2006).

61. Molegraaf, H. J. A. *et al.* Magnetoelectric effects in complex oxides with competing ground states. *Adv. Mater.* **21,** 1–5 (2009).

62. Vaz, C. A. F. *et al.* Origin of the Magnetoelectric Coupling Effect in Pb(Zr0.2Ti0.8)O/La0.8Sr0.2MnO3 Multiferroic Heterostructures, *Physical Review Letters*, 104, 127202 (2010).

63. Spurgeon, S. R. *et al.* Polarization screening-induced magnetic phase gradients at

complex oxide interfaces. *Nat. Commun.* **6,** 1–11 (2015).

64. Jiang, L. *et al.* Tunneling Electroresistance Induced by Interfacial Phase Transitions in Ultrathin Oxide Heterostructures. (2013). doi:10.1021/nl4025598

65. Moriyama, T. Antiferromagnetic spintronics. *Rev. Mod. Phys.* **90,** 15005 (2018).

66. Zakharov, A. I. et al. Magnetic and magnetoelastic properties of a metamagnetic iron-rhodium alloy. 19, 1348–1353 (2010)

67. Cherifi, R. O. *et al.* Electric-field control of magnetic order above room temperature. **13,** 345–351 (2014).

68. Lee, Y. et al. Large resistivity modulation in mixed-phase metallic systems. 1– 7, Nature comms. (2015)

69. Liaw, B. Y. *Electrochemical Aspects of Ionic Solids. Key Engineering Materials* **125–126,** (1997).

70. Haynes, William M*., CRC Handbook of Chemistry and Physics (92nd ed.), CRC Press. ISBN 978-1439855119, (2011).*

71. Armand, M., Endres, F., MacFarlane, D. R., Ohno, H. & Scrosati, B. Ionic-liquid materials for the electrochemical challenges of the future. *Nat. Mater.* **8,** 621–9 (2009).

72. Balducci, A., Bardi, U., Caporali, S., Mastragostino, M. & Soavi, F. Ionic liquids for hybrid supercapacitors. *Electrochem. commun.* **6,** 566–570 (2004).

73. Kim, S. H. *et al.* Electrolyte-gated transistors for organic and printed electronics. *Adv. Mater.* **25,** 1822–1846 (2013).

74. Lewandowski, A. & Świderska-Mocek, A. Ionic liquids as electrolytes for Li-ion

batteries-An overview of electrochemical studies. *J. Power Sources* **194,** 601–609 (2009).

75.   Díaz, M., Ortiz, A. & Ortiz, I. Progress in the use of ionic liquids as electrolyte membranes in fuel cells. *J. Memb. Sci.* **469,** 379–396 (2014).

76.   Jiang, M. *et al.* Electrochemical control of the phase transition of ultrathin FeRh films. *Appl. Phys. Lett.* **108,** 202404 (2016).

77.   Weisheit, M. *et al.* Electric Field-Induced Modification of Magnetism in Thin-Film Ferromagnets. *Science (80-.).* **315,** 349–351 (2007).

78.   Kawaguchi, M. *et al.* Electric field effect on magnetization of an Fe ultrathin film. *Appl. Phys. Express* **5,** 6–9 (2012).

79.   Aya Obinata *et al.* Electric-field control of magnetic moment in Pd. *Sci. Rep.* **5,** 14303 (2015).

80.   Yan, Y. N. *et al.* Electrical control of Co/Ni magnetism adjacent to gate oxides with low oxygen ion mobility. *Appl. Phys. Lett.* **107,** (2015).

81.   Shimamura, K. *et al.* Electrical control of Curie temperature in cobalt using an ionic liquid film. *Appl. Phys. Lett.* **100,** (2012).

82.   Zhou, X. *et al.* Role of oxygen ion migration in the electrical control of magnetism in Pt/Co/Ni/HfO2 films. *J. Phys. Chem. C* **120,** 1633–1639 (2016).

83.   Fujimoto, T. & Awaga, K. Electric-double-layer field-effect transistors with ionic liquids. *Phys. Chem. Chem. Phys.* **15,** 8983–9006 (2013).

84.   Di, N. *et al.* Influence of controlled surface oxidation on the magnetic anisotropy of Co ultrathin films. *Appl. Phys. Lett.* **106,** 122405 (2015).

85.   Chiba, D. *et al.* Electrical control of the ferromagnetic phase transition in cobalt at room temperature. *Nat. Mater.* **10,** 853–856 (2011).

86.   Lin, W. C., Chang, P. C., Tsai, C. J., Hsieh, T. C. & Lo, F. Y. Magnetism modulation of Fe/ZnO heterostructure by interface oxidation. *Appl. Phys. Lett.* **103,** 1–6 (2013).

87.   Bi, C. *et al.* Reversible control of Co magnetism by voltage-induced oxidation. *Phys. Rev. Lett.* **113,** 1–5 (2014).

88.   Bauer, U., Emori, S. & Beach, G. S. D. Electric field control of domain wall propagation in Pt/Co/GdOx films. *Appl. Phys. Lett.* **100,** (2012).

89.   Bauer, U., Emori, S. & Beach, G. S. D. Voltage-controlled domain wall traps in ferromagnetic nanowires. *Nat. Nanotechnol.* **8,** 411–6 (2013).

90.   Bauer, U. *et al.* Magneto-ionic control of interfacial magnetism. *Nat. Mater.* **14,** 174–181 (2014).

91.   Maruyama, T. *et al.* Large voltage-induced magnetic anisotropy change in a few atomic layers of iron. *Nat. Nanotechnol.* **4,** 158–161 (2009).

4. Experimental methods

4.1 Introduction

This chapter aims to give the reader an in depth understanding of the techniques used throughout this research project. This will include sample preparation, growth techniques, magnetic characterisation methods, surface analysis and ionic liquid characterisation. All the methods used in this project are widely used in the research community and are well understood.

4.2 Sample preparation

4.2.1 Substrate preparation

The substrate material used for the majority of this work was Si (100), and unless stated otherwise the reader can assume that is has been used for all of the presented work. Si was chosen because it is cheap, very flat and widely used within the electronics industry. The Si wafers were cut using a diamond scribe, to the desired size for the experiment. The substrates were then washed in an ultrasonic bath in isopropanol (IPA) to remove any debris that may be on the surface.

4.2.2 Thermal evaporation

Thermal evaporation is a technique for depositing thin films of material, metallic or organic, onto a given substrate. The films can be deposited with sub-nanometre thickness precision and hundreds of micrometres depending on the exposure time. For this project thicknesses of 1 to 50 nm were of interest. At these thicknesses thermal

evaporation was an ideal process for providing flat uniform thin films. The thermal

Figure 4.1: Photograph of Wordentec thermal evaporator used to deposit permalloy and Ni films.

evaporator used in this research was custom built by Wordentec[1] (Figure 4.1).

The thermal evaporator consists of an alumina-coated tungsten crucible for storing and heating the material, a shutter to control the flow of the evaporated material, a sample holder with five sample positions and a rate monitor that measures the thickness of the deposited material (Figure 4.2). Power is passed through the crucible heating up the material until it starts to evaporate and deposit on the sample at the top of the chamber. The sample holder is faced downwards to allow the evaporated material to be deposited on the correct side of the substrate. The rate monitor measures the deposition rate using a quartz crystal that has a variable resonant frequency that changes depending on the amount of material deposited. This requires a previous

calibration step to calculate a tooling factor for each material, which can be achieved by atomic force microscopy (AFM).
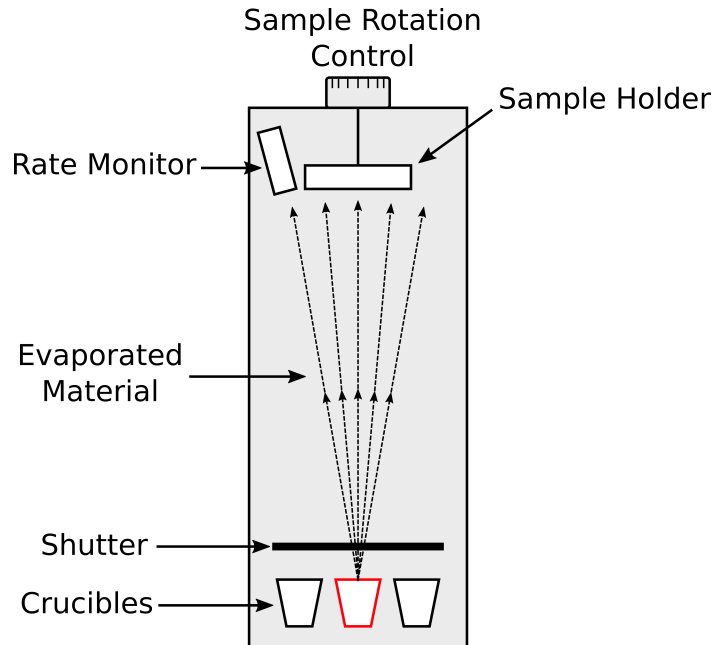
Figure 4.2: Schematic of thermal evaporator used to deposit permalloy and Ni films.

The evaporated deposition geometry follows a line of sight description, outlined in (4-1)[2]:

$$\frac{d\bar{M}_s}{dA_s} = \frac{\bar{M}_e(n+1)cos^n\phi\,\cos\theta}{2\pi r^2}, \quad n \geq 0 \tag{4-1}$$

where $\frac{d\bar{M}_s}{dA_s}$ is the mass of the evaporated material deposited on the substrate area, $\bar{M}_e$ is the total mass of evaporated material, n is related to the geometry of the crucible, ϕ is the emission angle from normal vector, θ is the receiving angle of substrate and r is the distance from the crucible to the substrate. For the Wordentec evaporator both ϕ and θ are close to 0 due to the rotational control and r is approximately 0.5 m. This results in a highly uniform thin film across the surface area of the substrate.

After preparing the substrates as described in section 4.2.1, the samples were then adhered to a substrate holder, using poly(methyl methacrylate) (PMMA), in one of the five sample positions. The sample holder could also be used as a mask to create large features on the substrate during deposition.

Once the PMMA has dried the holder can then be loaded into the evaporation chamber. In the lower part of the chamber there were three different alumina-coated tungsten crucibles, which contain different powder materials to be evaporated. This enables multilayers to be made without removing the substrate from the chamber, which is useful for preparing seed and capping layers.

Once the crucibles were filled and the samples loaded, the chamber was then pumped down to approximately 1×10^{-7} mbar. A bake out procedure was used before growth to reduce volatile impurities. This process was initiated by increasing the electrical power to the desired crucible in increments every two minutes. This gradual ramping rate was required to prevent the crucible from being damaged by thermal shock. The shutter was open during this process but the sample holder position ensured no deposition onto substrates. The power was increased until a steady rate of deposition was obtained, the value of which depending on the material. The material typically used in this research was Ni and Ni-Fe. The bake out was complete when approximately 10 nm of material had been evaporated. The power was then decreased gradually and the chamber left to pump down to 1×10^{-7} mbar.

A similar process was used for the growth stage of the evaporation. The power was increased in the same manner as the bake out stage, until a steady deposition rate of 0.2-0.4 Å/s was reached. The sample stage was then rotated to expose the desired substrate and the appropriate amount of material deposited. After removal from the

cooled chamber, samples were washed using acetone and ultrasonicated to remove any excess PMMA. An IPA rinse was then used to remove any acetone residue.

4.2.3 Ionic liquid cell

Ionic liquid cells consist of two electrodes separated by an ionic liquid that generate large electric fields at the interface via an electric double layer (EDL) upon voltage application[3]. These high electric fields have been shown to manipulate magnetic properties in ferromagnetic electrodes, as discussed in section 3.6.1, and is therefore of use in voltage control of magnetism.
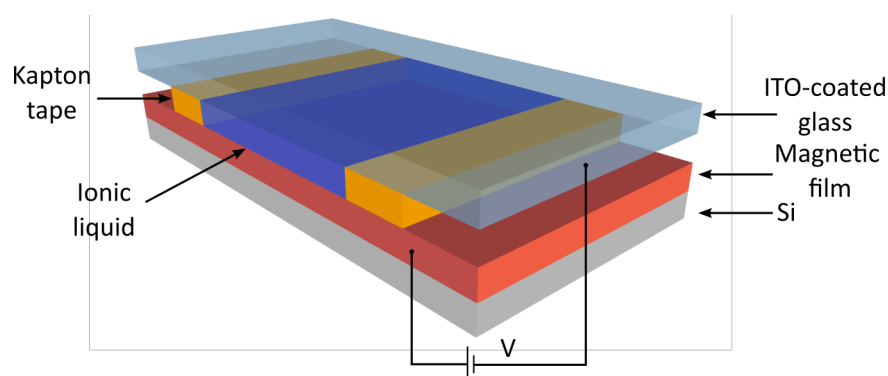
Figure 4.3: Schematic of ionic liquid cell, consisting of the ionic liquid sandwiched between ITO coated glass and permalloy film deposited on a Si wafer.

Following the sample preparation techniques described earlier, the ionic liquid cell was then prepared. The ionic liquid cell consisted of the magnetic thin film, two strips of Kapton tape, an indium tin oxide (ITO) coated glass slide (Sigma-Aldrich, surface resistivity 70-100 Ω/sq, ITO thickness is 150 Å – 300 Å) and the ionic liquid, which in this case was 1-Ethyl-3-methylimidazolium bis(trifluoromethylsulfonyl)imide (EMIMTSFI)(IO-LI-TEC, 99%)(Figure. 4.3). ITO coated glass was used because it is conductive and

transparent, which is necessary for electrical contacting and magneto-optical Kerr effect (MOKE) magnetometry measurements.

The magnetic film and ITO coated glass act as the two electrodes of the cell. Electrical contacts were attached to the magnetic film and the conductive ITO coated glass outside of the cell region using silver conductive paint. Two strips of Kapton tape, approximately 10 mm x 1 mm x 0.3 mm, were placed on top of the magnetic film, separated by approximately 10 mm. The Kapton tape acted as a non-conductive spacer layer between the two electrodes. Approximately 10 μL of EMIMTSFI was deposited between the two strips of Kapton tape using 10 μL syringes (Fisher Scientific). The ITO coated glass was then placed on top of the EMIMTSFI droplet, spreading the liquid out and holding the ITO coated glass in place via surface tension.

4.3 Magnetic Characterisation

Knowledge of a material's magnetic properties is of fundamental importance when designing functional devices that use magnetic materials. There are many properties that can be used to define a magnetic material, as described in chapter 2. Likewise there are many methods to measure these magnetic properties. The methods used in this research will be described in the following sections.

4.3.1 Magneto-optical Kerr Effect Magnetometry

Magneto-optical Kerr effect (MOKE) magnetometry is a quick, surface sensitive technique for measuring the hysteresis loops of thin films. MOKE was discovered in 1877 by John Kerr[4] and is now a standard measurement technique of thin films and nanostructures in the magnetic research community. MOKE is a phenomenon whereby the plane of polarization of incident linearly polarised light is rotated upon reflection from a magnetized surface. The polarization is rotated in opposite directions depending on the

orientation of the magnetisation. Monitoring this polarisation while varying the magnetic field applied to a sample allows a hysteresis loop to be extracted.
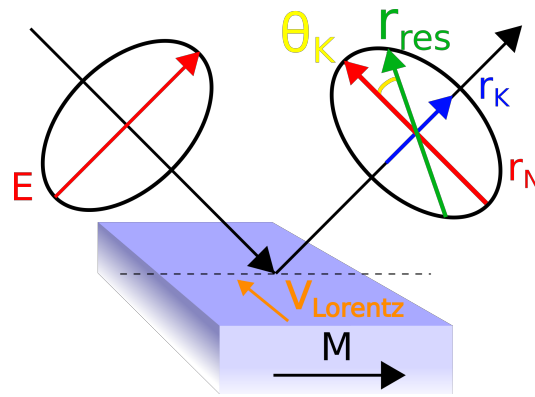
There are three configurations of MOKE magnetometry. These include: polar MOKE, where the magnetisation is normal to the film surface; transverse, where the magne*Figure 4.4: Schematic of longitudinal MOKE, where E is electric field, θ_k* ; and *Kerr rotation, r_{res} is resultant reflection, r_K is the Kerr reflection, r_N is the* longitu*normal reflection, $V_{Lorentz}$ is the Lorentz motion and M is the magnetisation.* ane of incidence[5,6] (Figure 4.4).

In longitudinal MOKE incident polarised light is reflected off the magnetised surface. The polarized light causes the electrons to oscillate in the plane of the polarization. The light is reflected with amplitude, r_N, in the optical plane of incidence. However, there is also the effect of the Lorentz force, which generates a component perpendicular to the polarisation and magnetisation direction[6], r_K, that is proportional to the magnetisation of the film. The reflected light thus becomes elliptically polarised by

the Lorentz force. The resultant change in overall polarisation gives the Kerr rotation θ_K of the polarisation. Using a quarter wave plate to convert any ellipticity to linear polarised light and an analyser to convert polarisation rotation to intensity change allowing Kerr signal detection with a photodetector. Reversing the magnetic field generates the opposite Kerr rotation and thus a hysteresis loop.

The longitudinal MOKE geometry was used throughout this project. The following set-up was constructed to allow MOKE measurements to be made on the cell described in section 4.2.3. The use of a liquid component required the cell to be flat. This also required an electromagnet to be set up for horizontal (in-plane) fields and mirrors to redirect the laser from the horizontal plane.
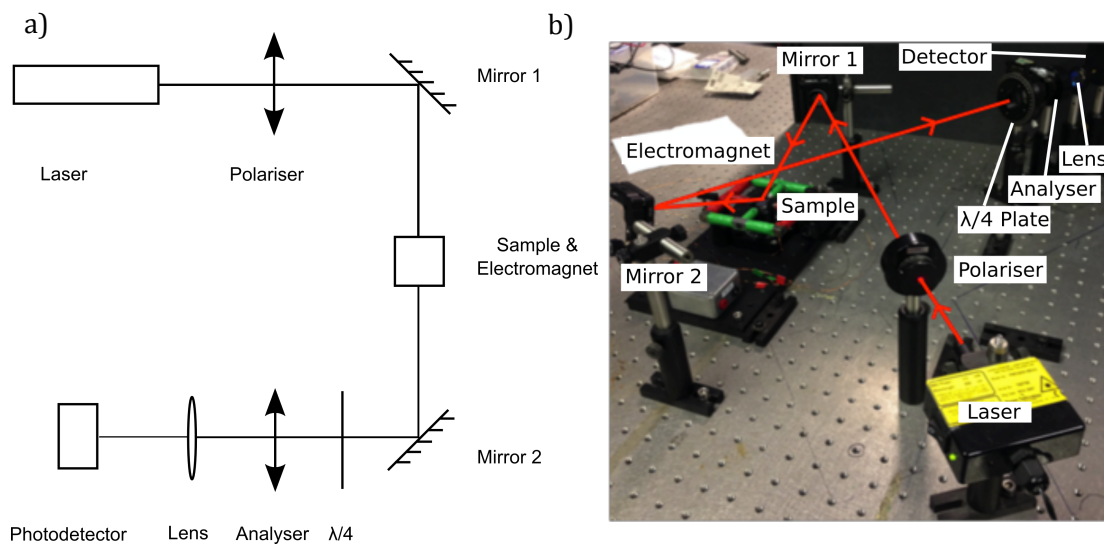
Figure 4.5: a) Schematic of optical arrangement of MOKE magnetometer b) Photograph of MOKE magnetometer, with the optical instruments and laser path displayed

The optical arrangement can be seen in Fig. 4.5a. The laser (632nm wavelength, 3 mW, spot size $\approx$ 1 mm) first passed through a linear polariser and was reflected down onto the sample (Figure 4.5b). On reflection, the polarisation modified, the light was

incident on a second mirror and directed towards the photodetector. Before reaching the photodetector the beam passed through a quarter wave plate, second polariser, the analyser and a lens to focus the light on the photodetector where the Kerr signal was detected.

The electromagnet was powered using a bipolar power amplifier (Kepco, BOP 20-10M) that was controlled by a LabVIEW script. The script output a sinusoidal wave to the power supply via a digital-to-analogue converter (DAC), which supplied the current to the electromagnet at a frequency of 6 Hz. The field of the electromagnet was detected using a pick-up coil around the pole piece. The pick-up coil signal was integrated to provide a measurement of magnetic field. The magnetic field and the Kerr voltage were then displayed on an associated computer via the DAC, from which a hysteresis loop could be generated. Typically loops were obtained with 500 cycle averages and with 10,000 data points. The averaged hysteresis loops were then processed in a MATLAB script file that normalised the Kerr signal values and calculated the coercivity of the sample under test.

4.3.2 Vibrating Sample Magnetometry

Vibrating sample magnetometry (VSM) is a magnetic induction technique that can measure magnetic moment, as a function of magnetising field, temperature and crystallographic orientation. VSM uses pick-up coils to detect changes in magnetic field induced by the dipole field of a magnetised sample oscillating perpendicular to an applied magnetic field[7].
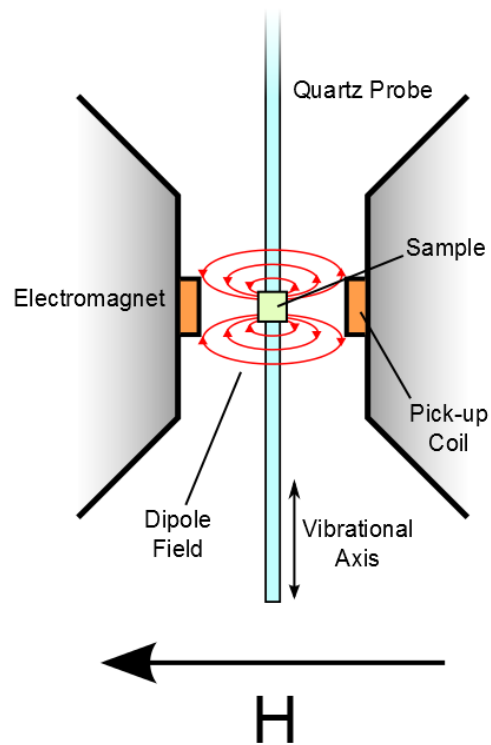
Figure 4.6: Schematic of VSM apparatus, with H displaying the magnetic field direction and the read lines indicating the dipole field.

VSM consists of a quartz probe, an electromagnet and two pick-up coils (Figure 4.6). The electromagnet generates a highly homogenous magnetic field that magnetises the sample and creates a dipole field. The quartz probe oscillates the sample along the vertical axis and creates a change in magnetic flux inducing a voltage in the pick-up coils via Faraday's law (4-2).

$$\varepsilon = -N\frac{d\phi}{dt} \qquad (4\text{-}2)$$

where ε is electromotive force in Volts, N is the number of turns and ϕ is the magnetic flux. Here the pick-up coil voltage is proportional to the magnetic moment of the sample.

The magnetic moment can be found by equating the magnetic flux produced by a magnetic moment to the magnetic induction produced by a current carrying wire, giving (4-3)[8]

$$B \cdot m = I\phi \tag{4-3}$$

where B is the magnetic induction, m is the magnetic dipole moment, I is the current in the detection coils and ϕ is the magnetic flux produced by m. Assuming that the sample undergoes simple harmonic motion (4-4)

$$\frac{dz}{dt} = A\omega cos(\omega t) \tag{4-4}$$

where A is amplitude and ω is frequency. Combining equations (4-2), (4-3) and (4-4) gives (4-5)

$$V = \frac{d\phi}{dz} \cdot \frac{dz}{dt} = GmA\omega \cos(\omega t) \tag{4-5}$$

where V is pick-up coil voltage and G is a geometrical factor. Using a ferromagnetic sample of known magnetic moment it is possible to obtain a conversion factor between the pick-up coil voltage and magnetic moment[8]. In this research a 30 nm thick permalloy sausage-shaped (i.e. rectangular with rounded ends) sample approximately 1 mm x 3 mm was used. This standard was used to reduce demagnetising effects and size factors that can affect the calibration process for thin films[9].

In this research the VSM used was a MPMS 3 SQUID-VSM (SVSM) from Quantum Design, housed at the University of Leeds where Dr. Oscar Cespedes supervised the research. Before carrying out the measurements samples had to be cut down to a 3 mm x 3 mm square or less, to ensure they would fit into the VSM chamber. The samples were stuck to the quartz probe to ensure the sample did not come loose upon vibration.

Once the sample had been secured the probe was loaded into the VSM. The apparatus was purged upon loading and unloading the probe. To find the operating frequency of the probe and to ensure the sample was centred in the middle of the pick-

up coils, a frequency sweep was carried out and the resonant frequency obtained. Various parameters such as temperature, number of data points, time between data points, field increments could be set with the control software. Once these values are inputted the experiment is ran.

The static magnetic field perpendicular to the probe was then applied, the maximum applied field used in this research was 100 kA/m but the apparatus is capable of reaching 4,000 kA/m. The probe was set to vibrate along the z-axis at a frequency of approximately 12-15 Hz. The induced pick-up coil voltage was then interpreted by VSM software to output magnetic moment. This process was then repeated at new static fields until a hysteresis loop was formed.

Due to the complexity of the VSM apparatus it was not possible to measure the magnetic moment of the cell whilst applying the voltage in situ. This meant the samples had to be measured post exposure to the ionic liquid and voltage.

4.3.3 Ferromagnetic Resonance Spectroscopy

Ferromagnetic resonance (FMR) spectroscopy utilises the FMR of ferromagnetic materials to extract key magnetic properties including magnetisation, gyromagnetic ratio and the Gilbert damping factor. As explained in section 2.5.2, all ferromagnetic materials have a defined FMR frequency, at which all the spins within the material precess resonantly with the same amplitude and phase.

Static applied field (Oe)
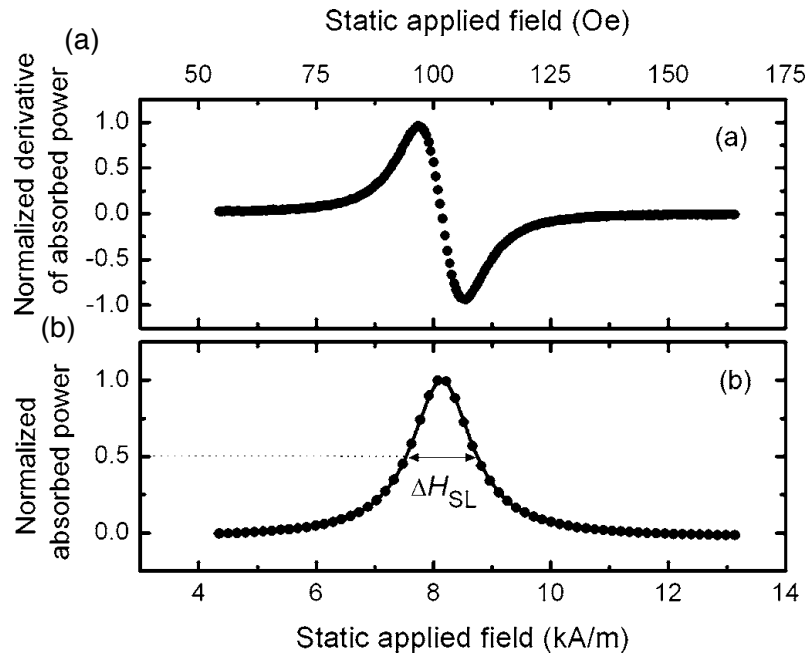
Figure 4.7: Example FMR trace for 50 nm permalloy film at 3 GHZ from ref Kalarickal[22]

FMR spectroscopy measures the absorption of high frequency microwaves by a ferromagnetic sample under the influence of an external DC magnetic field. A FMR spectrometer typically consists of an electromagnet, microwave frequency source, a transmission line (stripline or cavity) and a detector. When a high frequency microwave is passed through the transmission line and a DC magnetic field applied, some of the microwave power is absorbed by the ferromagnetic sample. When the microwave frequency is equal to the FMR frequency of the sample there is maximum power absorption. There are two methods for obtaining an FMR spectrum, sweeping the DC magnetic field while keeping the microwave frequency constant or sweeping the microwave frequency while keeping the DC magnetic field constant. The change in absorbed power can then be detected; plotting this against applied magnetic field or microwave frequency gives an FMR spectrum. Figure 4.7 shows stripline FMR (SL-FMR) data by Kalarickal *et al.*[10] for 50 nm samples of permalloy, with a constant 3 GHz excitation field while sweeping the magnetic field. Part (a) shows the measured

absorption derivative, while (b) shows the normalised integrated data, with the resonant frequency, H_{Res} = 8.08 kA/m, along with the linewidth, ΔH_{SL} = 1.5 kA/m.

To acquire magnetic data it is necessary to take FMR traces at a number of different frequencies. The DC magnetic field at which the sample resonated can be found by the intercept through the x-axis. These data can then be fit to the Kittel equation (4-6)[10] that describes the frequency of the FMR mode in an ellipsoid when magnetised in z-direction

$$f^2 = \gamma^2 (H_{res} + (N_{xx} - N_{zz}))(H_{res} + (N_{yy} - N_{zz})) \tag{4-6}$$

where f is the resonant frequency, γ is the gyromagnetic ratio, H_{res} is the applied (DC) magnetic field at which the sample resonates and N_{xx}, N_{yy}, N_{zz} are demagnetising factors. This equation can be simplified for low anisotropy thin films magnetised in plane (4-7)[11]

$$f^2 = \gamma^2 H_{res}(H_{res} + 4\pi M_{eff}) \tag{4-7}$$

where M_{eff} is the magnetisation. Plotting f^2/H_{res} against H_{res}, allows the extraction of γ from the gradient and M_{eff} from the y intercept. Where M_{eff} is described by (4-8)[12]:

$$M_{eff} = M_S - \frac{2K_S}{\mu_0 M_s d} \tag{4-8}$$

where K_s is the surface anisotropy, μ_0 is the permeability of free space and d is the film thickness. By measuring the FMR at a range of thicknesses it is possible to calculate the magnetisation saturation, $M_{S,}$ and surface anisotropy, K_s, of films.

Furthermore, the Gilbert damping constant can be calculated for ferromagnetic films by plotting the FMR linewidth against resonant frequency and thus fitting to (4-9)[13]:

$$\Delta H = \Delta H_{in} + \frac{f\alpha}{\gamma} \qquad (4\text{-}9)$$

where ΔH is the FMR linewidth, ΔH_{in} is the inhomogeneous contribution to the linewidth and α is the effect Gilbert damping. Here the Gilbert damping constant can be further separated into surface and bulk contributions by fitting to equation (4-10)[14]:

$$\alpha = \alpha_B + \frac{\alpha_S}{d} \qquad (4\text{-}10)$$

where α_B is the bulk damping term and α_S is the surface damping term.

There are several types of FMR spectroscopy techniques. These include, vector network analyser (VNA) FMR, pulse inductive microwave magnetometry (PIMM) and broadband ferromagnetic resonance (BFMR)[11]. These techniques each have their drawbacks and benefits. For this research project a BFMR set-up and the University of Western Australia (UWA) was used under the supervision of Professor Mikhail Kostylev.
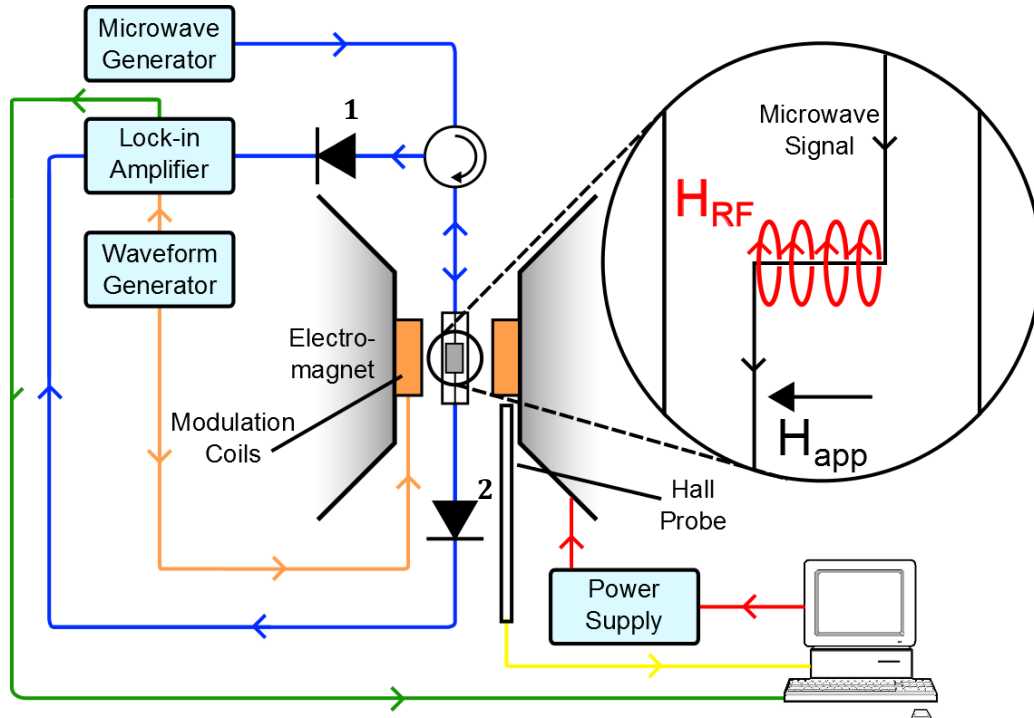
Figure 4.8: Schematic of broadband stripline ferromagnetic resonance (BFMR), where H_{app} & H_{RF} shows the applied external field and RF excitation field respectively

A schematic of the BFMR set-up used at UWA can be seen in figure 4.8. The BFMR consists of a microwave frequency generator to output high frequency electromagnetic waves, a circulator and two diodes to control the flow of the microwaves, a stripline to bridge between sample and microwaves and a lock-in amplifier to measure absorbed power. There was also an electromagnet to magnetise the sample, a Hall probe to measure magnetic field, modulation coils and waveform generator to allow detection from lock-in amplifier. This set-up was controlled using a computer and LabVIEW script. Firstly a microwave generator (HP 8350B RF source) was programmed to a specific frequency in the GHz range. This microwave passed through a circulator allowing the reflected power from the sample to be measured after passing diode 1. The microwave signal that was transmitted through the stripline is absorbed by the sample. The transmitted signal then passed through diode 2 and to the lock-in amplifier (EG&G Lock-In Amplifier Model 5207). A 220 Hz sinusoidal wave from the waveform generator (Agilent 33220A) was transmitted to the lock-in and the modulation coils. This enabled lock-in amplifier detection which improved the signal-to-noise ratio[15]. This signal was proportional to the derivative of the imaginary part of the magnetic susceptibility[16]. The signal was then amplified and recorded by the computer.

This process was then repeated as a function of DC field, which was increased in 2.4 kA/m increments approximately. Once a suitable field range had been measured an FMR trace was obtained. The resulting data was passed through a MathCAD script written by Professor Mikhail Kostylev, which calculated the FMR, linewidth and also removed the background and symmetrized the data using a Lorentzian fit.

4.4 Surface and Structural Characterisation

This section describes the techniques used to investigate the morphology and elemental structure of samples and how these properties vary after being exposed to various

conditions. These measurements were pivotal in improving the understanding of the processes and mechanisms involved in causing the observed changes in magnetic properties.

4.4.1 X-ray Photoelectron Spectroscopy

X-ray photoelectron spectroscopy (XPS) is a surface sensitive technique that can provide elemental analysis of thin films and powders[17]. It is also sensitive to surface chemistry and enables the identification of the oxidation state of materials.

XPS is based on the photoelectric effect, which was explained by Albert Einstein earning him the Nobel Prize in 1921. The photoelectric effect describes the absorption of a photon by a material causing an electron to be emitted from the surface, provided the energy of the incident photon is higher than the binding energy of the electron. The surplus energy transferred from the photon is converted into kinetic energy of the emitted electron. The photoelectric effect is described by (4-11):

$$E_{KE} = hf - E_B \qquad \text{(4-11)}$$

where E_{KE} is the kinetic energy of the emitted electron, h is Planck's constant, f is the frequency of the incident photon and E_B is the binding energy of the electron.

A schematic of the XPS spectrometer can be seen in figure 4.9, displaying the incoming photon, γ, the emitted photoelectron, a retarding plate to reduce the velocity of the electron, negative and positive electrodes control the passage of the electron through the hemisphere and a detector to detect incoming electrons. The incident photon emits a photoelectron, which passes through a retarding plate that slows down the photoelectrons by varying the negative voltage applied to it. The photoelectron then passes through an electrostatic energy analyser, which depending on the kinetic energy of the photon will either be attracted to the positive electrode (low energy, red), will

collide with the negative electrode (high energy, green) or a third option whereby the photoelectron passes to the detector (pass energy, blue). By varying the voltage applied to the retarding plate photoelectrons of different kinetic energy are able to reach the detector, thus creating a spectrum.
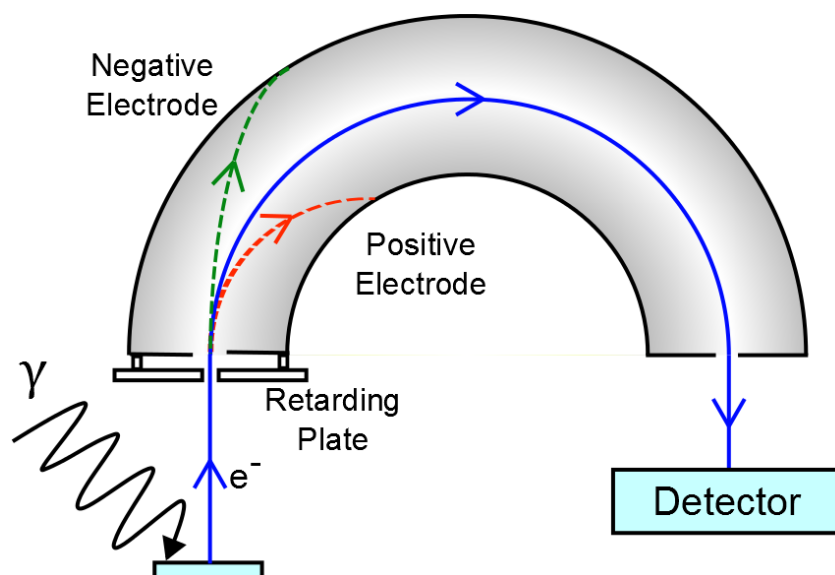
Figure 4.9: Schematic of key components of an X-ray photoelectron spectrometer, where Υ is an incoming photon and e⁻ is the emitted photoelectron

The kinetic energy of the photoelectrons acts as an atomic fingerprint of the different energy levels. This allows the user to determine the elemental composition of the sample; this includes oxidation states and chemical bonds present in organic molecules. This is due to the small energy difference for different oxide materials and chemical bonds that are detectable by highly sensitive XPS measurements. The kinetic energies are normally converted to binding energies, using equation (4-9).

The instrument used in this research was a Thermo K-alpha, which uses a micro-focused monochromatic Al Kα source (3 mA, 12 kV) with a spot size of 400 x 800 μm. For the survey spectra a 200 eV pass energy was used and 30 scans acquired, while for the high-resolution spectra a 40 eV pass energy was used and 10 scans acquired. The

XPS measurements were made at room temperature in three positions on each sample and averaged.

To assist in obtaining an accurate chemical analysis of sample surfaces, CasaXPS was used, an XPS analysis software. CasaXPS has an extensive library of energy values associated to different elements to help identify peaks, it allows the creation of a background to improve fitting and also provides an analysis report. In this research a standard fitting protocol was followed in order to ensure consistency within the results. A general guideline to the fitting process is outlined below and specific details will be given in section 6.4.
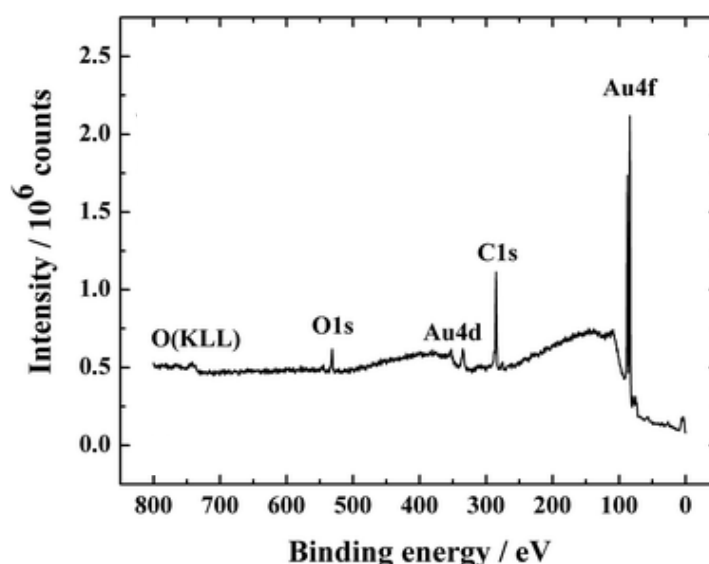
Figure 4.10: Example XPS Survey Spectrum of Gold displaying Au, C & O peaks from Mooste[18]

In a typical XPS analysis there are two types of spectra obtained: survey spectra (Figure 4.10) and high-resolution spectra. The survey spectra have a wide binding energy range and provide an overview of the chemicals present at the sample surface. High-resolution spectra have a shorter binding energy range but contain more data points; this can allow for the identification of particular oxides present on the sample

surface. Survey spectra are usually taken prior to high-resolution spectra to identify the binding energies that would be of interest to the user.

An example XPS survey spectrum from a Au thin film can be seen in figure 4.10[18], here the peaks have been identified by the CasaXPS library. The Au 4f peak corresponds to the photoelectrons emitted from the 4f energy level of gold and the low binding energy of these electrons is because they lie furthest from the nucleus. This binding energy is only found for electrons from the 4f energy level of gold and from no other element. There is further evidence of gold from the Au 4d peak. The oxygen and carbon peaks in the spectrum are a common feature and correspond to atmospheric CO_2, which may have become adsorbed onto the sample surface. Also shown in figure 4.10 is the peak O KLL, this corresponds to an oxygen Auger peak. Auger peaks arise when an x-ray removes a core electron creating a hole and leaving the atom in an excited state. A higher energy electron then relaxes to fill this hole to stabilise the atom, this energy is transferred to a further electron, which leaves the atom with a defined kinetic energy that is converted to a binding energy to generate an Auger peak.

Once all peaks in a survey spectrum have been identified, high-resolution spectra can be taken to allow a more rigorous analysis of the elements present on the sample surface. Prior to analysis of high-resolution spectra, an energy calibration is made. There is often an energy shift in XPS spectra due to sample charging, this can result in incorrectly identified peaks. In this research the spectra was calibrated to the C 1s peak (Figure 4.11) because the binding energy is accurately known and is often present. The spectra is shifted by the difference between the measured and the data book value for the binding energy of C 1s, for example, measured value is 285.3 eV and data book value is 284.8 eV, spectra shifted by –0.5 eV. This calibration can then be applied to the other high-resolution spectra.
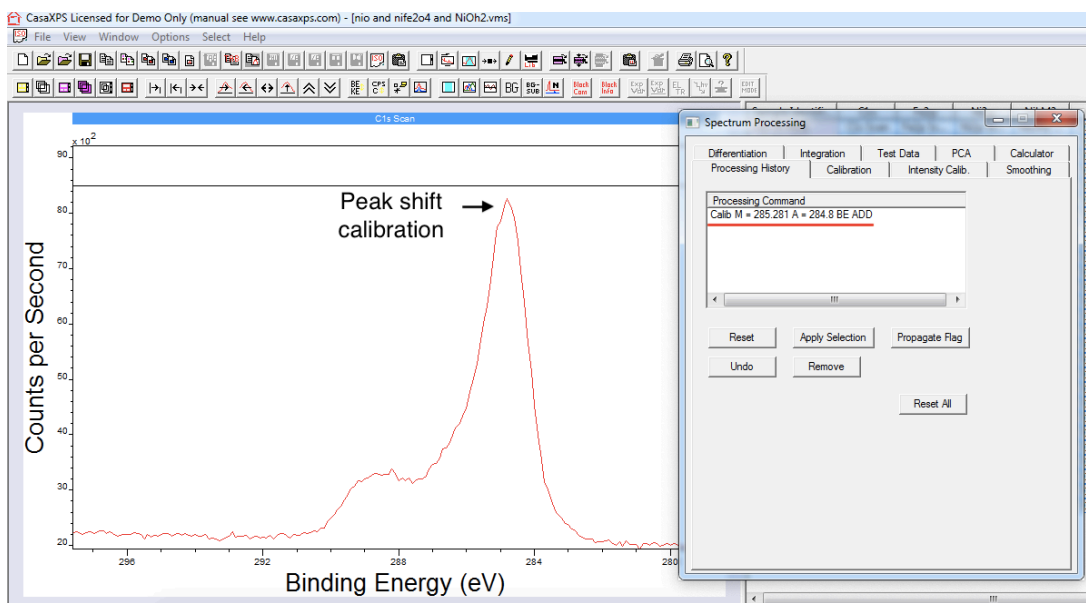
Figure 4.11: Screenshot of CasaXPS software demonstrating peak shift calibration for C 1s peak, from 285.28 eV to 284.8 eV

Following the energy calibration, a quantification region and a suitable background should be defined; this gives a defined area of interest and helps to provide accurate peak intensity data. Continuing from the example shown previously, the region was first defined between approximately 291-280 eV, either side of which, the counts per second is relatively flat (figure 4.12). In this example, a linear background was applied, because there is not a large difference in background signal before and after the quantification region. There are other more complex background types including Shirley and Tougaard, which may be better suited to other spectra.

It is now possible to resolve the peaks, which can often be a complex process, where there are overlapping peaks making it hard to deconvolute. To assist in the peak deconvolution it is necessary to consult the literature to obtain key parameters such as peak position, full width half maxima (FWHM), line shape, and relative peak intensity for standard samples of elements that are suspected to be present. Components can then

be added to the high-resolution spectra, along with certain constraints. A residual can then calculated by CasaXPS to provide a measure of fit to the data.
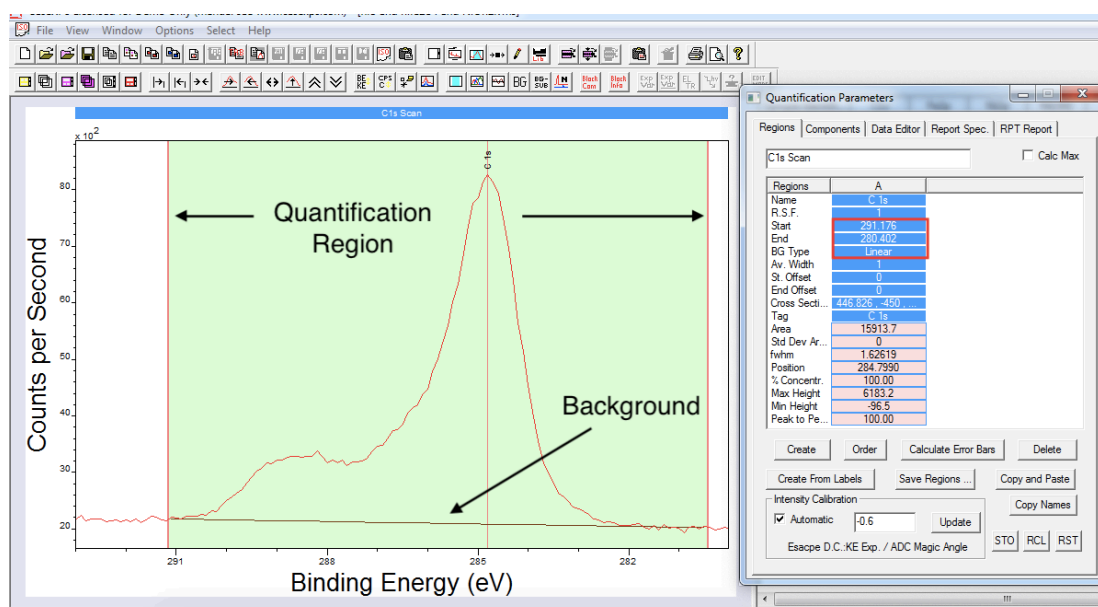
Figure 4.12: Screenshot of CasaXPS software demonstrating the quantification region and the background selection for a C 1s spectrum.

Once again continuing with the Carbon 1s example, from Biesinger *et al.*[19] standard fitting parameters for various carbon systems such as alkyls, alcohols, esters etc can be obtained. These parameters include the line shape, which in this case is a mixture of Gaussian and Lorenztian (70% and 30%) and the peak position as mentioned earlier 284.8 eV. The secondary components are constrained in relation to the primary component (C-C, C-H), by peak position and FHWM. These constraints can then be added to the quantification parameters and the components adjusted to fit the data (figure 4.13). Further, there is a "Fit Components" function, which is based on a non-linear least squares model that helps to fine tune the fit while taking into account the constraints. It is important not to add too many constraints or over confine the

constraints, as this will restrict the peak deconvoluton process. Once the fit has been optimised, it is then possible to gain information regarding the amount of each element as percentage.
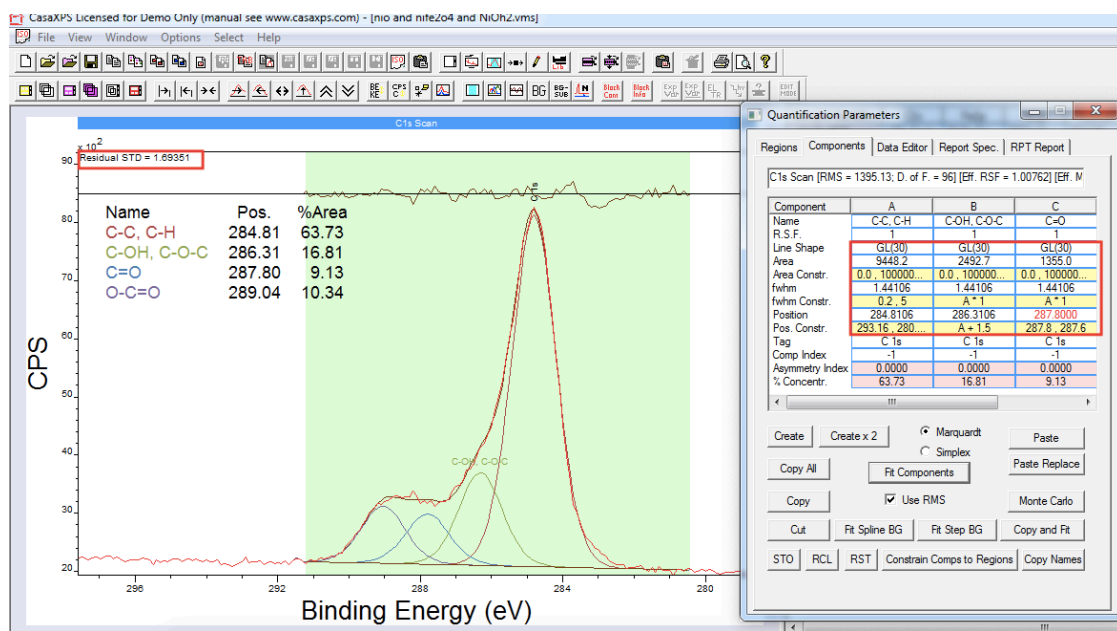
Figure 4.13: Screenshot of CasaXPS software demonstrating the components and constraints applied to a C 1s spectrum, including analysis report.

Following this same protocol it is possible to repeat this process for all elements to provide a deep understanding of the surface composition of materials. It is hoped that this section provides an introduction to XPS analysis and the CasaXPS software to allow the reader to understand the more complex data presented in chapter 6. However, further information will be provided where necessary to describe further intricacies to XPS analysis.

4.5 Ionic Liquid Characterisation

This section describes the techniques used to characterise ionic liquids. There is currently a lot of interest in ionic liquids for a broad range of applications[20]. One of the

main areas under investigation is using ionic liquids in super capacitors[21]. The primary measurement technique for characterisation of ionic liquids is cyclic voltammetry, which will be described in the following section.

4.5.1 Cyclic Voltammetry

Cyclic voltammetry measures the current through a cell as a function of applied voltage, where a cell consists of two electrodes separated by an ionic liquid. The voltage is applied to the cell in incremental steps of 0.5 mV, while the current passing through the cell is simultaneously measured. The voltage is cycled between positive and negative voltages to create a cyclic voltammogram, from which the electrochemical window can be found. This is the voltage range within which the cell can operate in without becoming damaged.
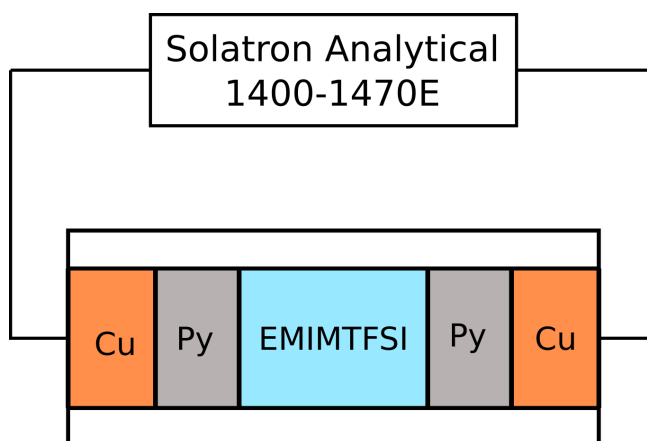
Figure 4.14: Schematic of ionic liquid cell structure, permalloy coated copper discs sandwiching filter paper soaked in ionic liquid, connected to the Solatron Analytical 1400-1470E

Before the cyclic voltammetry measurements could be made a suitable cell had to be built. The cell is held in place by Swagelok components, which restricted the lateral size of the cell, to a circle of 1.2 cm diameter. This constraint caused a slight change in the cell components described in section 4.2.3. To adhere to the size constraint the

magnetic material was deposited onto 1.2 mm radius copper disks. However, it is not possible to deposit ITO in our research facilities. As a result the cell consisted of magnetic material/ionic liquid/ magnetic material. A 1.2 cm diameter disk of filter paper was saturated by the ionic liquid and sandwiched in between the two copper disks (figure 4.14). The cell was also wrapped in polythene sheet to enclose the cell and prevent any shortages.

With the cell made a voltage can then be applied in defined increments and the current through the cell sensed. The cyclic voltammetry measurements were made using a Solartron Analytical 1400-1470E, which is a multichannel potentiostat designed for DC characterisation of energy storage devices. Here it has been employed to characterise the ionic liquid cell. Voltage is then plotted against current and a voltammogram can be made, see figure 4.15 for an example. When the current values are virtually zero, this is defined as the electrochemical window. Current peaks can be seen at approximately -2.5V and +2.5, which correspond to the reduction and oxidation of the electrode, respectively. Therefore it is important to operate the cell within these voltage ranges.
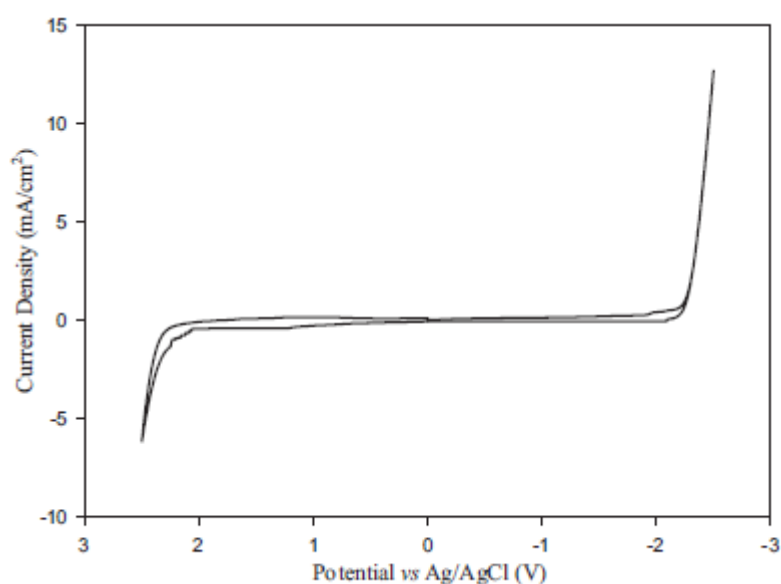
Figure 4.15: Example of cyclic voltammogram for EMIMTFSII
using a glassy carbon marcroelectrode [23]

4.6 Summary

This chapter provides the reader with a detailed understanding of the experimental techniques used throughout this research project. This includes sample preparation, magnetic characterisation, surface characterisation and electrochemical analysis. Further details are given about the sample dimensions and the ionic liquid cell used in the majority of this research project. Where necessary explanations on how to interpret and analyse the data have been given. After reading this section the reader should understand how the data has been obtained and how to interpret the data presented in the later results chapters 5, 6 & 7.

4.7 References

1.   http://www.wordentec.com (accessed 6/01/19 at 9:15).

2.   Ohring, M. *Material Science of Thin Films*. (Academic Press, 2002).

3.   Fujimoto, T. & Awaga, K. Electric-double-layer field-effect transistors with ionic liquids. *Phys. Chem. Chem. Phys.* **15,** 8983–9006 (2013).

4.   Kerr, J. On Rotation of the Plane of Polarization by Reflection from the Pole of a Magnet. *Philos. Mag.* **3,** 321 (1877).

5.   Coey, J. M. D. *Magnetism and Magnetic Materials*. (Cambridge University Press, 2010). doi:10.1017/CBO9780511845000

6.   Hubert, A. & Schäfer, R. *Magnetic Domains The Analysis of Magnetic Microstructures*. (1998).

7.   Foner, S. Versatile and sensitive vibrating-sample magnetometer. *Rev. Sci.*

Instrum. **30,** 548–557 (1959).

8.   Zieba, A. & Foner, S. Detection coil, sensitivity function, and sample geometry effects for vibrating sample magnetometers. *Rev. Sci. Instrum.* **53,** 1344–1354 (1982).

9.   Lindemuth, J., Krause, J. & Dodrill, B. Finite sample size effects on the calibration of vibrating sample magnetometer. *IEEE Trans. Magn.* **37,** 2752–2754 (2001).

10. Kittel, C. *Introduction to Solid State Physics*. (Wiley, 1951).

11. Maksymov, I. S. & Kostylev, M. Broadband stripline ferromagnetic resonance spectroscopy of ferromagnetic films, multilayers and nanostructures. *Phys. E Low-Dimensional Syst. Nanostructures* **69,** 253–293 (2015).

12. Chen, Y.-C. *et al.* Ferromagnetic resonance study of thickness-dependent magnetization precession in Ni80Fe20 films. *J. Appl. Phys.* **101,** 09C104 (2007).

13. Liu, X., Zhang, W., Carter, M. J. & Xiao, G. Ferromagnetic resonance and damping properties of CoFeB thin films as free layers in MgO-based magnetic tunnel junctions. *J. Appl. Phys.* **110,** (2011).

14. Zhao, Y. *et al.* Experimental Investigation of Temperature-Dependent Gilbert Damping in Permalloy Thin Films. *Sci. Rep.* **6,** 22890 (2016).

15. Camley, R., Celinski, Z. & Stamps, R. *Magnetism of Surfaces, Interfaces, and Nanoscale Materials, 1st Edition*. (Elsevier, 2015).

16. Belmeguenai, M. *et al.* Microstrip line ferromagnetic resonance and Brillouin light scattering investigations of magnetic properties of Co2MnGe Heusler thin films. *Phys. Rev. B - Condens. Matter Mater. Phys.* **79,** 1–9 (2009).

17. Attard, G. & Barnes, C. *Surfaces*. Oxford Chemistry Primers (1998).

18. Mooste, M., Marandi, M., Matisen, L., Sammelselg, V. & Tammeveski, K. Electrochemical properties of gold and glassy carbon electrodes electrografted with. 1–10 (2016). doi:10.1039/C6RA05609A

19. Biesinger, M. C., Payne, B. P., Lau, L. W. M., St, R. & Smart, C. X-ray photoelectron spectroscopic chemical state quantification of mixed nickel metal , oxide and hydroxide systems. 324–332 (2009). doi:10.1002/sia.3026

20. Vekariya, R. L. A review of ionic liquids: Applications towards catalytic organic transformations. *J. Mol. Liq.* **227,** 40 (2017).

21. Brandt, a., Pohlmann, S., Varzi, A., Balducci, A. & Passerini, S. Ionic liquids in supercapacitors. *MRS Bull.* **38,** 554–559 (2013).

22. Kalarickal, S. S. *et al.* Ferromagnetic resonance linewidth in metallic thin films: Comparison of measurement methods. *J. Appl. Phys.* **99,** 1–7 (2006).

23. Hayyan, M., Mjalli, F. S., Hashim, M. A., AlNashef, I. M. & Mei, T. X. Investigating the electrochemical windows of ionic liquids. *J. Ind. Eng. Chem.* **19,** 106–112 (2013).

5. Voltage control of magnetic properties in Ni$_{80}$Fe$_{20}$ & Ni thin films

5.1 Introduction

This chapter describes an investigation of the variation of magnetic properties of Ni$_{80}$Fe$_{20}$ (permalloy) and Ni upon application of a voltage to a ferromagnetic/ionic liquid interface. Permalloy was chosen due to its soft magnetic properties[1], high magnetisation (860 kA/m)[2], ease of patterning[3] and wide use in thin film technology[4]. The ionic liquid in this research is 1-Ethyl-3-methylimidazolium (EMIM$^+$) bis(trifluoromethylsulfonyl)imide (TFSI$^-$), EMIMTFSI was selected due to its large electrochemical window (ECW)[5] and its high air stability[6]. The applied voltage to the ferromagnet/EMITSFI was varied and the changes in hysteresis loop observed by magneto-optical Kerr effect (MOKE) magnetometry. Reversible changes of up to 80% were observed in the permalloy thin films and 90% changes in Ni films. Vibrating sample magnetometry (VSM) measurements demonstrated a variation in magnetic moment for permalloy films. The changes in magnetic properties were attributed to a thinning/thickening of the ferromagnetic films.

5.2 Sample preparation and characterisation process

Permalloy and Ni samples for MOKE magnetometry were prepared by thermal evaporation on Si wafers, 2 cm x 1 cm, at thicknesses ranging from 1 – 50 nm. The thicknesses of the films had been calibrated previously using an atomic force magnetometer (AFM) and a tooling factor calculated for a quartz crystal within the thermal evaporator.

5.3 MOKE magnetometry of ferromagnetic properties of Ni$_{80}$Fe$_{20}$ thin films

The magnetic properties of the as-deposited films were characterised to obtain an understanding of the coercivity dependence on thickness. The literature survey (Chapter 3) showed that thinner magnetic materials showed larger observed changes in magnetic properties[7]. However, reducing the thickness will eventually create a discontinuous film and might also challenge the sensitivity of magnetometry measurements.

To investigate this, samples of permalloy thicknesses of 1 nm, 2 nm, 3 nm, 4 nm, 5 nm and 7 nm were deposited onto Si substrates and then measured using longitudinal MOKE magnetometry (section 4.3.1). A 6 Hz AC magnetic field was applied and the hysteresis loops averaged over 500 cycles for the different sample thicknesses (Figure 5.1). Below 3 nm no Kerr signal was detected and are therefore not shown in the figure. This may be due to complete oxidation of the film making it no longer ferromagnetic, the sensitivity of the MOKE magnetometer has been reached or the thinnest films may be superparamagnetic. MOKE magnetometer measurements from several locations on each sample were unchanged, thus ruling out the formation of non-continuous films i.e. island formation. The 3 nm hysteresis loop displays a poor signal-to-noise ratio, while 4 nm and thicker show clear loops with much reduced noise.
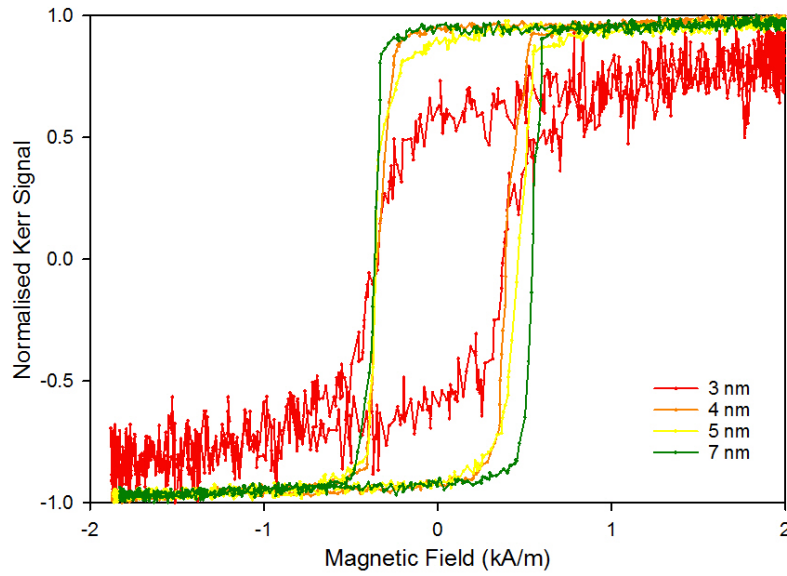
Figure 5.1: Magnetic hysteresis loops with increasing Py film thickness of 3, 4, 5 & 7nm.
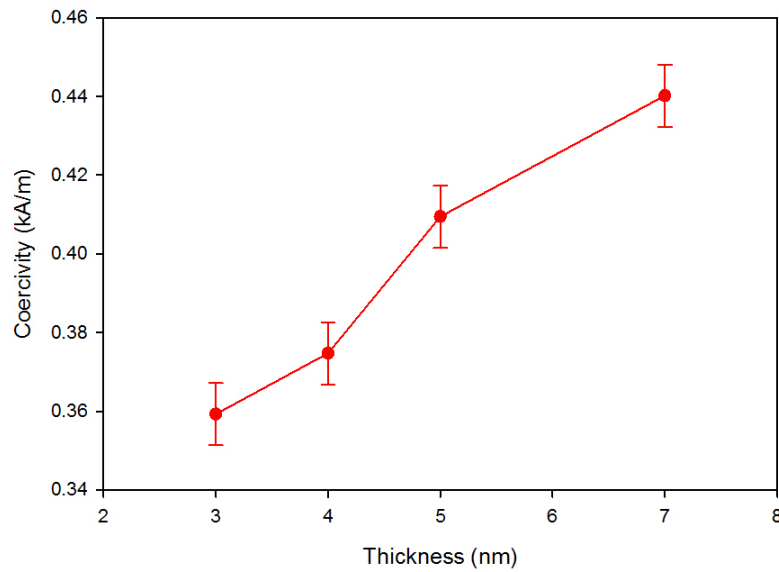
Figure 5.2: Coercivity as a function of thickness for permalloy films.

From the data in figure 5.1 the values of the coercivity were extracted and are shown in figure 5.2. There is a clear trend in coercivity with film thickness, namely the thicker the film the larger the coercivity, this agrees well with previous research on permalloy[8]. Like in the entire MOKE data presented here the error in field arises from the

accuracy of the Hall probe. The MOKE data was also averaged over 500 loops, which reduces the effect of random measurement errors. In Figure 5.1 there is a noticeable offset in the hysteresis loops, this is due to a remanent magnetisation in the iron core of the magnet. Applying a demagnetising field to the electromagnet before each measurement later rectified this problem. This does not affect the data presented in figure 5.1 and 5.2, which demonstrate significant changes in coercivity with film thickness.
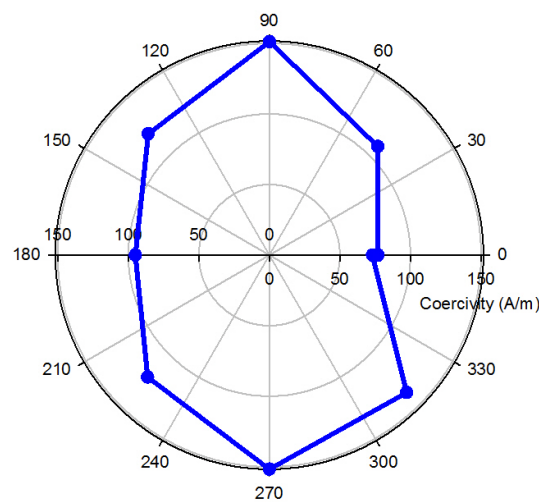
Figure 5.3: Coercivity with rotation away from the samples long axis for 5nm permalloy films.

Permalloy shows almost zero magnetocrystalline anisotropy[9] and therefore switching properties are strongly governed by shape anisotropy. In thin films of permalloy the magnetic easy axis is in-plane, while the hard axis is out-of-plane. This property of permalloy films has been utilised in numerous proposed nanotechnology applications[10]. The anisotropy of 5 nm permalloy films was investigated by rotating the permalloy sample in 45-degree increments and measuring magnetic hysteresis loops. Figure 5.3 demonstrates almost no change in the coercivity upon rotation from the long axis, which suggests that the film is isotropic. The small increases in coercivity at 90° and 270° have

been attributed to a negligible anisotropy induced by small external magnetic fields in the growth process.

These preliminary measurements show that film thicknesses of 5 nm or greater can be reliably produced and the magnetic properties measured consistently. The magnetic measurements show the permalloy films to be a soft magnetic material and display no preferred in-plane easy axis. These data agree well with the literature values and set a solid basis for the untreated films to draw a comparison.

5.4 In situ MOKE magnetometry of voltage control of ferromagnetic properties of $Ni_{80}Fe_{20}$ films

The magnetic properties of 5 nm permalloy films sufficiently characterised, the next step was characterising the magnetic films under an applied voltage. The ferromagnetic film/ionic liquid cell was set-up as described in section 4.2.3, with a 5 nm permalloy film. A slight excess of ionic liquid was used, which created enough surface tension in order to avoid the indium-tin oxide (ITO) coated glass from flipping over during measurements. Silver conducting paste was added to both electrodes to assist in a creating a good electrical contact; this reduced the resistance variation for different sample connections. Multiple laser spots were observed upon reflection from the experimental cell, however only one of these was discovered to be from the ferromagnetic film

First of all positive voltages were applied, from 0 V to +4 V, where the positive voltage is applied to the permalloy film and the negative voltage to the ITO coated glass. Successive voltages were applied for approximately 5 minutes before each hysteresis loop was obtained (Figure 5.4). The coercivity decreased steadily with increasing applied voltage, although hysteresis loops remained similar in shape. Upon removal of the applied voltage the hysteresis loop remained unchanged, demonstrating non-volatile changes in coercivity.
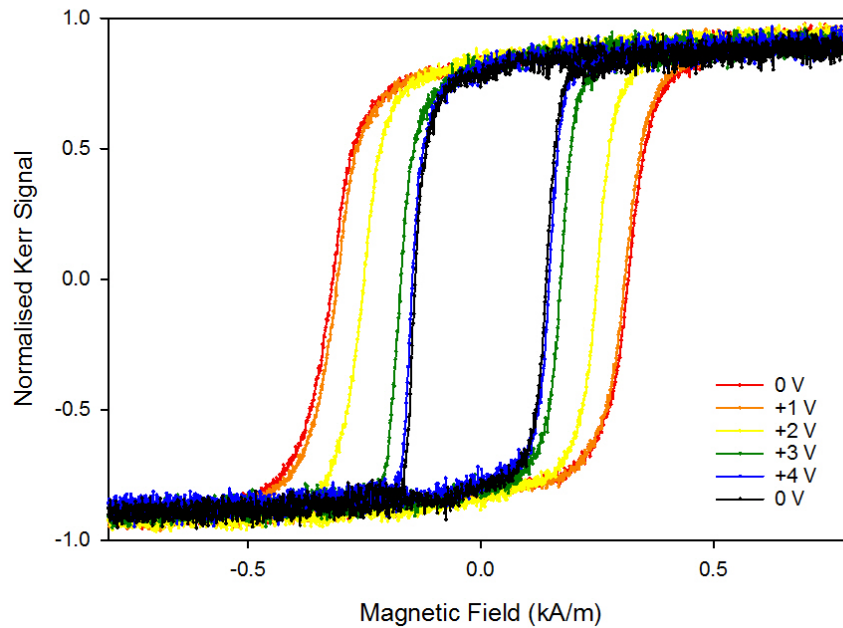
Figure 5.4: Magnetic hysteresis loops upon application of a positive voltage to a 5nm permalloy film.

Figure 5.5 shows the coercivity dependence on applied voltage directly. Over the voltage range investigated, the coercivity drops from approximately 320 A/m to less than 160 A/m, a decrease of over 50%. Also shown for each voltage is the fractional Kerr signal, $\Delta K/K_{ave}$, which is proportional to magnetic moment and therefore allows identification of qualitative changes in relative magnetic moment between voltages.[11] Here ΔK is the difference in Kerr signal at the maximum positive and negative applied fields (i.e. K_{max}- K_{min}) and K_{ave} is the average Kerr signal in each hysteresis loop. $\Delta K/K_{ave}$ (taken from the non-normalised data) was observed to follow a similar decrease with applied voltage as seen with coercivity (Figure 5.5), implying a decrease in the film's magnetic moment. The decrease in both coercivity and magnetic moment is consistent with a thickness decrease. The value of $\Delta K/K_{ave}$ at 0 V is not shown because the MOKE magnetometer was realigned between measurements.
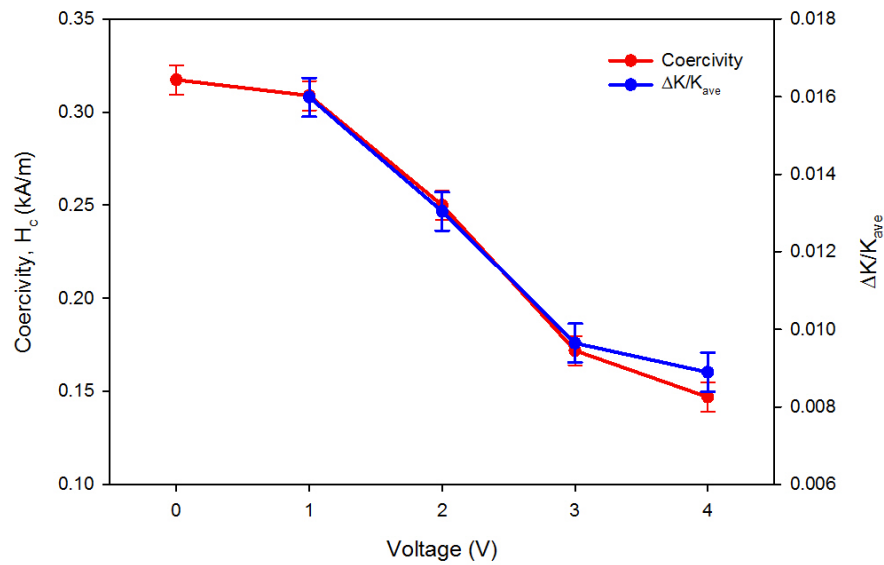
Figure 5.5: Coercivity, H_c, and ΔK/K_ave with increasing positive voltage applied to a 5nm permalloy film.

To further investigate the voltage control of ferromagnetic properties time-dependent measurements were carried out. First of all the cell was prepared as previously and no voltage applied to ensure there were no chemical reactions taking place on the film surface. As shown in figure 5.6 there is very little change in hysteresis upon exposure to the ionic liquid with no voltage applied. This identifies the voltage as the cause of the change in magnetic properties.
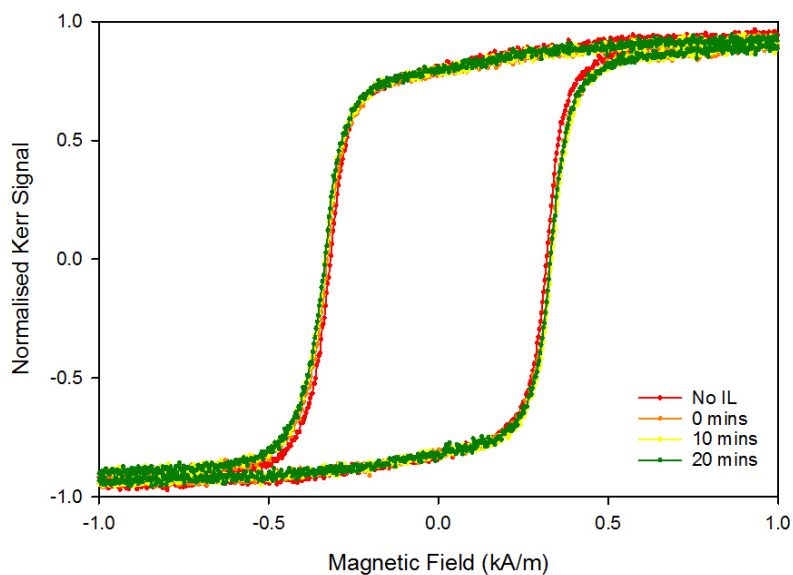
Figure 5.6: Magnetic hysteresis with time after exposure of 5nm permalloy film to ionic liquid at 0 V.

Time dependent measurements with a voltage applied were then investigated. Voltages of +1 V, +2 V, +3 V and +4 V were applied and hysteresis loops measured at 2-minute intervals (Figure 5.7). The coercivity at +1 V decreases only slightly over a 40-minute measurement, while +2 V shows an initial decrease before levelling off. At the higher positive voltages, +3 V and +4 V, there is a much more pronounced decrease in coercivity displaying an almost linear response with time. After applying +4 V for 15 minutes a magnetic signal could no longer be detected by the MOKE magnetometer, suggesting the thin film was no longer magnetic. The sharp initial decrease at +3 V and +4 V is not fully understood and further work is required to understand this process. Fitting linearly to the +3 V and +4 V plots gives decreases in coercivity of 4 A/m/minute and 14 A/m/minute, respectively. This means that voltage and exposure time to applied potentials both control the films' properties.
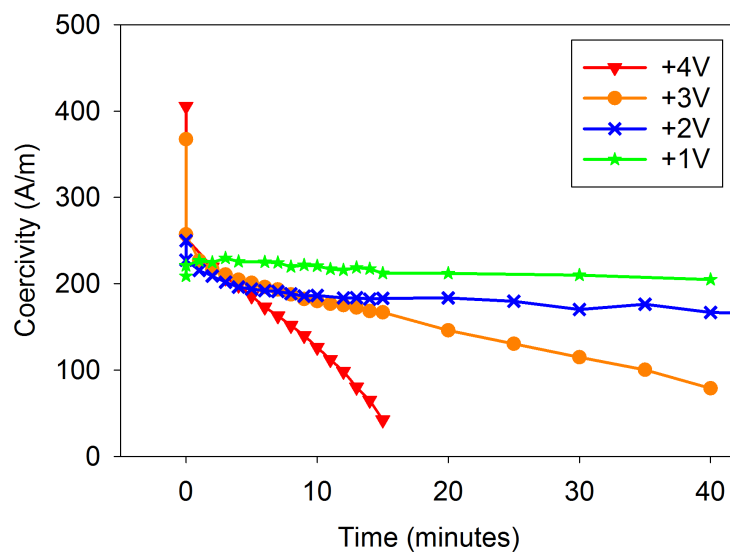
Figure 5.7: Coercivity with respect to time for increasing voltages +1 V, +2V, +3 V, and +4 V applied to a 5nm permalloy film.

The $\Delta K/K_{ave}$ values were calculated for the same data set (Figure 5.8). At all voltages the $\Delta K/K_{ave}$ signal decreases, indicating a decrease in magnetisation and film thickness. At lower voltages, +1 V and +2 V, the decrease is small and the rate of decrease slower, while at higher voltages, +3 V and +4 V, the magnetisation decrease is larger and more rapid. The slight increase at 20 minutes for +1 V is attributed to MOKE magnetometer realignment.
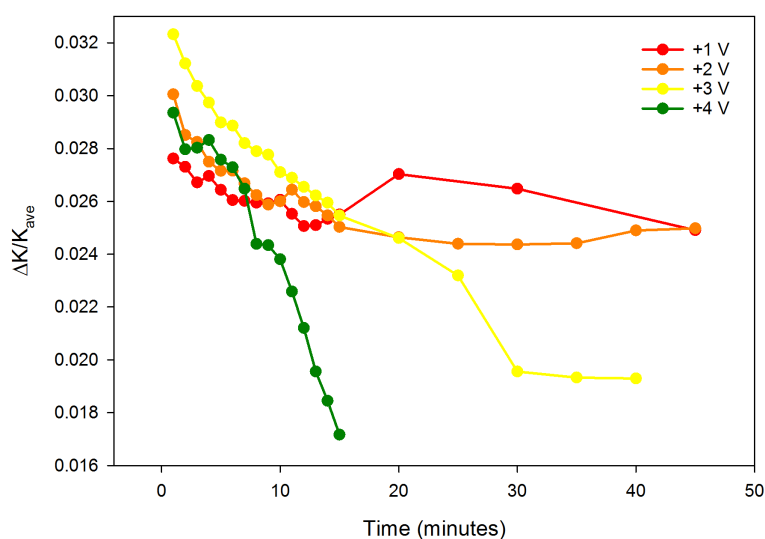
Figure 5.8: $\Delta K/K_{ave}$ with time for increasing positive voltage, +1 V, +2 V, +3 V and +4V applied to a 5nm permalloy film.

Using a fresh 5nm permalloy sample the experiment was repeated, but with voltage cycled from 0 V to +4 V to -4 V followed by a subsequent cycle of +3 V to -4 V. A multimeter was placed in series to measure current passing through the cell; this provided an overview of electrochemical processes and verified the electrical contact connection. The voltage was increased in 1 V steps and was maintained at the defined voltages for 5 minutes before MOKE measurement. Example hysteresis loops are shown in figure 6.9. From 0 V to +4 V (a → b) there is a similar drop in coercivity as shown above, accompanied by a slight increase in noise due to a reduction in Kerr signal. The coercivity continued to decrease upon reducing the voltage back to 0 V (b → c), this is

due to the exposure time effect displayed earlier. Reversing the voltage polarity to -4 V remarkably increased the coercivity by 59% from the value at 0 V (c → d).
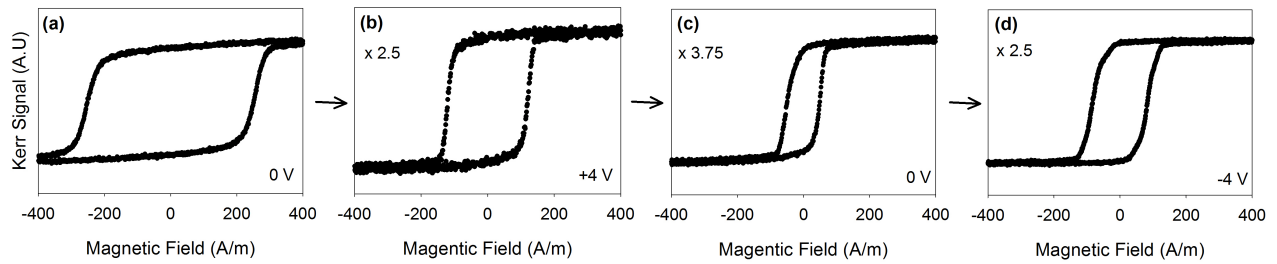
Figure 5.9: Magnetic hysteresis loops of 5 nm permalloy film under a sequence of voltages 0 V → +4 V → 0 V → -4 V, (a → d).

Plotting the coercivity data from the experiment (Figure 5.10) further demonstrates the steady decrease in coercivity on application of a positive voltage (0 V → 4 V). While reducing the positive voltage the coercivity continued to decrease as demonstrated in figure 5.9, however at a much slower rate that in the previous +4 V regime. Once the voltage reached -4 V the coercivity started to increase, upon leaving the voltage at -4 V for a further 4 minutes the coercivity continued to increase. This effect is very similar to the time exposure measurements in figure 5.7, however this time the coercivity is increasing. Cycling the voltage back to 0 V the coercivity ceased to increase.
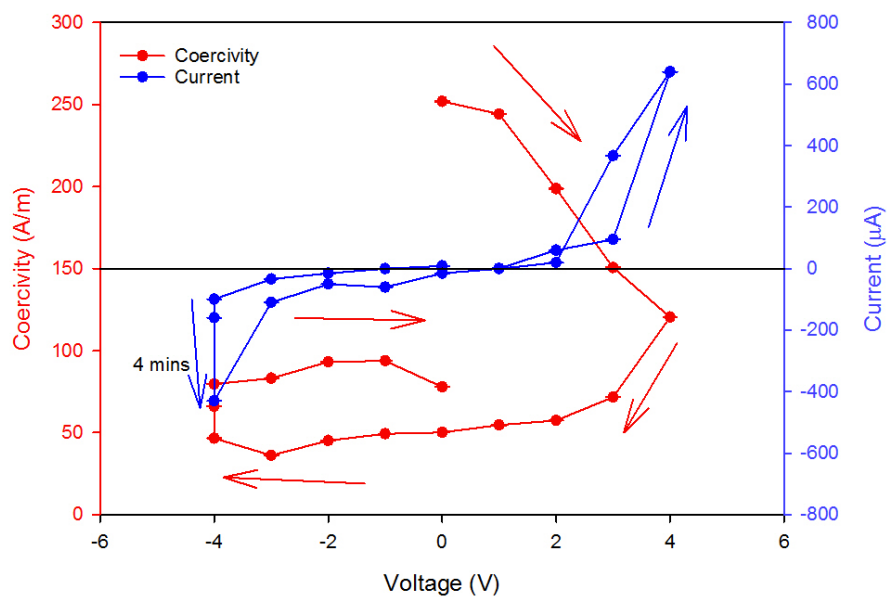
Figure 5.10: Coercivity of 5 nm permalloy film and current through cell for a sequence of voltages, 0 V → +4 V → -4 V → 0 V, with an extended exposure of 4 more minutes at -4V.

The current plot on figure 5.10 displays large current peaks at voltage values of +4 V and -4 V, which are the voltages at which the largest changes in coercivity are observed. The current peaks indicate the passage of charge, which could be via oxidation or reduction of the permalloy film. This gives a useful insight into the potential mechanisms involved in the observed changes in magnetic properties. However a more in depth analysis into the electrochemical nature of the cell will be required, along with surface characterisation.
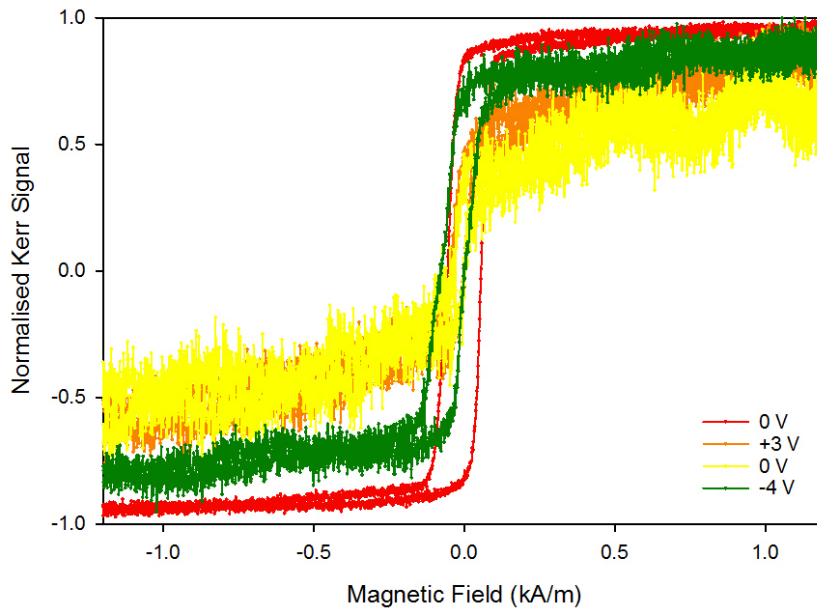
Figure 5.11: 2nd cycle of 5nm permalloy ionic liquid cell from 0 V → +3 V → 0 V → -4 V, after previous exposure to +4 V and -4 V.

After cycling the cell through 0 V → +4 V → -4 V → 0 V, the sample was further cycled through 0 V → +3 V → 0 V → -4 V. The immense changes observed on this secondary cycle are displayed in figure 5.11. The 0 V hysteresis loop shows low noise and clear coercivity, applying a positive voltage created a lot of noise which continued upon reduction to 0 V. For these positive voltages there was a large uncertainty in coercivity and the Kerr signal was much reduced. Upon reducing the voltage to -4 V there is a marked improvement of magnetic hysteresis loop quality, with a clear measurable coercivity and much less noise. This further demonstrates the control and reversibility of ferromagnetic properties displayed in the first cycle.
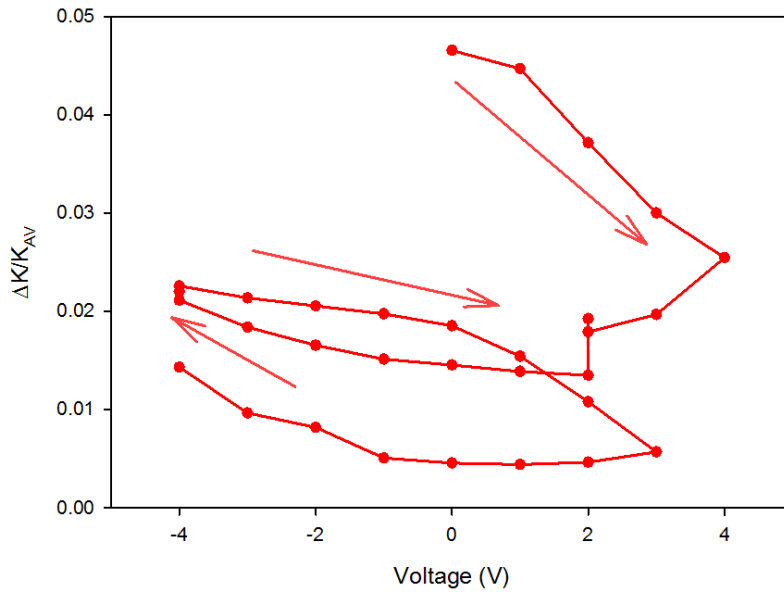
Figure 5.12: ΔK/K$_{ave}$ of 5nm permalloy film upon cycling the voltage 0 V → +4 V → -4 V → +3 V → -4 V.

The ΔK/K$_{ave}$ data was again extracted from non-normalised data to observe the relative changes in magnetisation of the (originally) 5 nm permalloy film (Figure 5.12). As previously, ΔK/K$_{ave}$ steadily dropped upon applying a positive voltage but reversing the polarity on the first cycle steadily increased the ΔK/K$_{ave}$ ratio and continued increasing with time. The second cycle again displayed a decrease upon application of a positive voltage with the negative voltage then restoring the ferromagnetic properties somewhat.

To characterise the cell further, a fresh 5 nm permalloy cell was prepared and a negative voltage applied first, followed by a positive voltage. The results plotted in figure 5.13, show that from 0 V to -3 V there was no distinct change in coercivity or hysteresis loop shape. At -4 V the hysteresis loop becomes much more square and the coercivity decreased by a significant amount. This result is a great contrast to earlier experiments where upon applying a negative voltage the coercivity increased and the hysteresis shape stayed relatively similar. The change in hysteresis loop shape implies a change in the switching mechanism, which in addition could vary the coercivity.
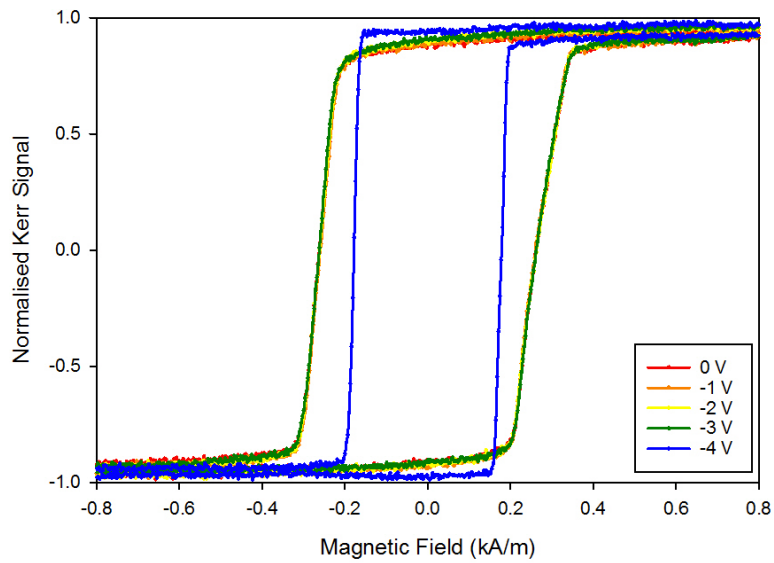
Figure 5.13: Magnetic hysteresis in 5 nm of permalloy thin film upon application of a negative voltage.

The voltage applied to this sample was then reduced to 0 V and positive voltages applied (Figure 5.14). On returning the voltage back to 0 V the coercivity steadily increased. Applying a positive voltage the coercivity continued to increase and the hysteresis loop started to resemble the shape of the virgin state sample at 0 V. Increasing the voltage to +3 V removed the Kerr signal and no hysteresis was observed. The cause of these changes is difficult to understand from magnetic measurements alone but it is clear that the process involved upon applying a negative voltage is reversed upon applying a subsequent positive voltage.
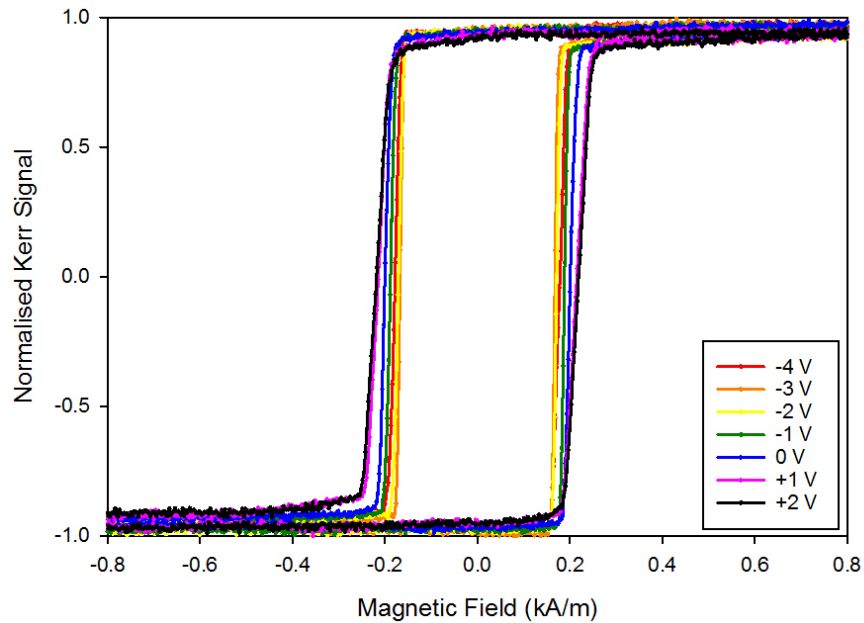
Figure 5.14: Magnetic hysteresis of 5 nm permalloy film upon decreasing negative voltages and switching the voltage polarity after previous exposure to -4 V.

Extracting the Kerr signal from the raw data and calculating the fractional MOKE signal reveals data related to the relative magnetisation. The data for the fractional Kerr signal (Figure 5.15) showed an increase for negative voltages, a relative increase in magnetic moment, which agrees with the previous demonstration. The relative magnetic moment then decreased upon reducing the voltage and applying a positive voltage, this again agrees with the data shown previously. The coercivity data however displays the opposite trend to that observed previously. The inconsistencies in the coercivity trends suggest a slightly more complex process than originally anticipated.
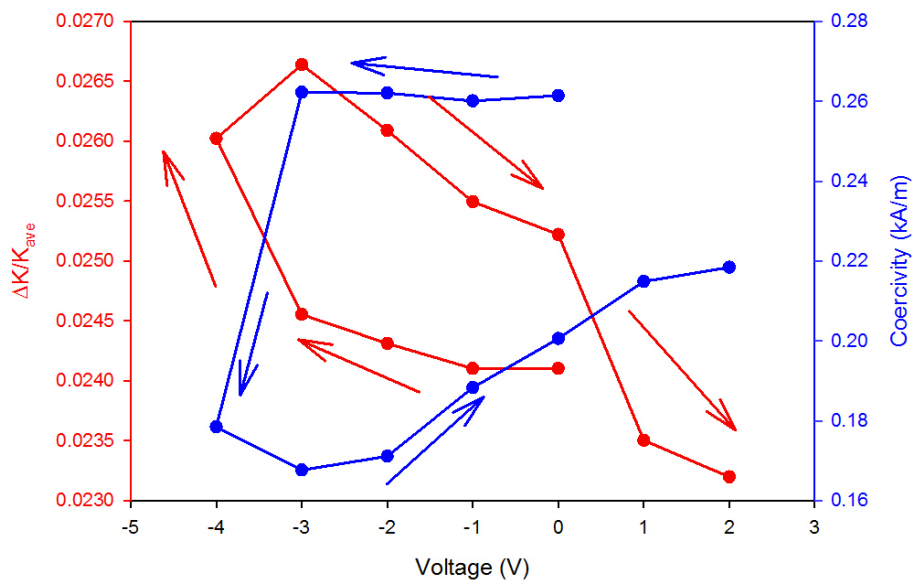
Figure 5.15: Fractional Kerr signal and coercivity for sequence of voltages applied to a 5nm permalloy film, 0 V → -4 V → +2V.

The kinetics of this process were investigated by applying -4 V to a fresh 5 nm permalloy film and measuring hysteresis loops at regular intervals along with a measure of the current passing through the cell. The coercivity dropped immediately upon application of -4 V but then remained approximately constant for over an hour (Figure 5.16). Once the voltage was removed the coercivity returned to close to the original value indicating a volatile effect. This suggests a different process is behind the changes and could be related to the positive ionic liquid ions causing an alternative effect than the negative ions. This result is in stark contrast to the time course measurements at +4 V where the coercivity quickly reduced and after 20 minutes there was no magnetic signal remaining (Figure 5.7 & 5.8). These results demonstrate the importance of the sequence of the applied voltages and the polarity and could open further opportunities for voltage control of magnetic properties.
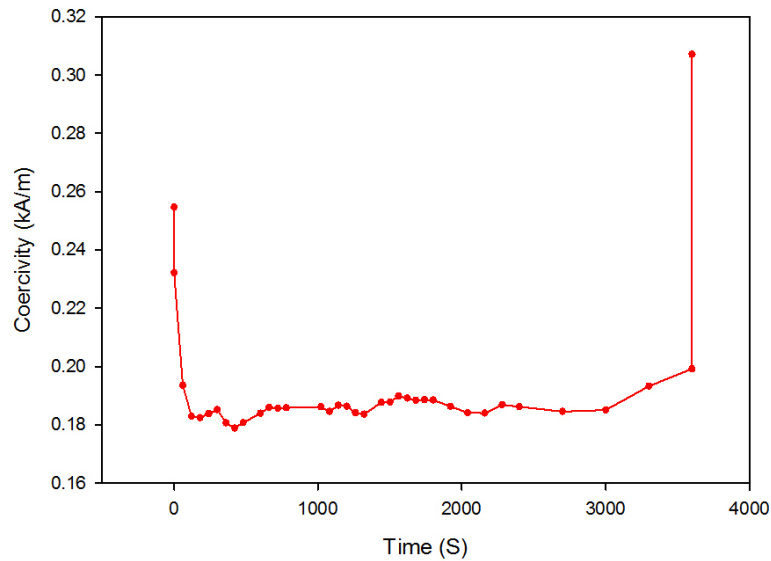
Figure 5.16: Coercivity of 5nm permalloy film upon application of -4 V for an increasing length of time, the final data point is after the voltage was removed and the sample had been washed and replaced.

5.5 Vibrating sample magnetometry of Ni$_{80}$Fe$_{20}$ films

Vibrating sample magnetometry (VSM) measurements were performed on 5 nm permalloy films previously exposed to a sequence of voltages. The VSM characterisation and sample preparation is described in detail in section 4.3.2. VSM is a key technique that provides a measurement of the magnetic moment and is widely used in magnetic characterisation of thin films.

In these experiments each sample was left at voltages for 10 minutes before increasing the voltage or terminating the experiment. For all of these results the magnetisation was divided by the sample volume to give magnetisation per unit volume. Upon increasing the voltage to +3 V the magnetisation was decreased by approximately 35% of the value at 0 V (Figure 5.17). The magnetisation value at 0 V is approximately 25% lower than the value of data book values for permalloy.

Upon reversing the voltage to negative voltages the magnetisation continues to decrease until -4 V is reached, whereby the magnetisation increases by 120% of the value at -3 V. The continual substantial decreases in magnetic moment up to -3 V is in contrast with the MOKE data (Figure 5.12) which showed an unchanged magnetisation between 0 V and -3 V. The VSM and MOKE data do agree upon a strong increase in magnetic moment and magnetisation at -4 V.
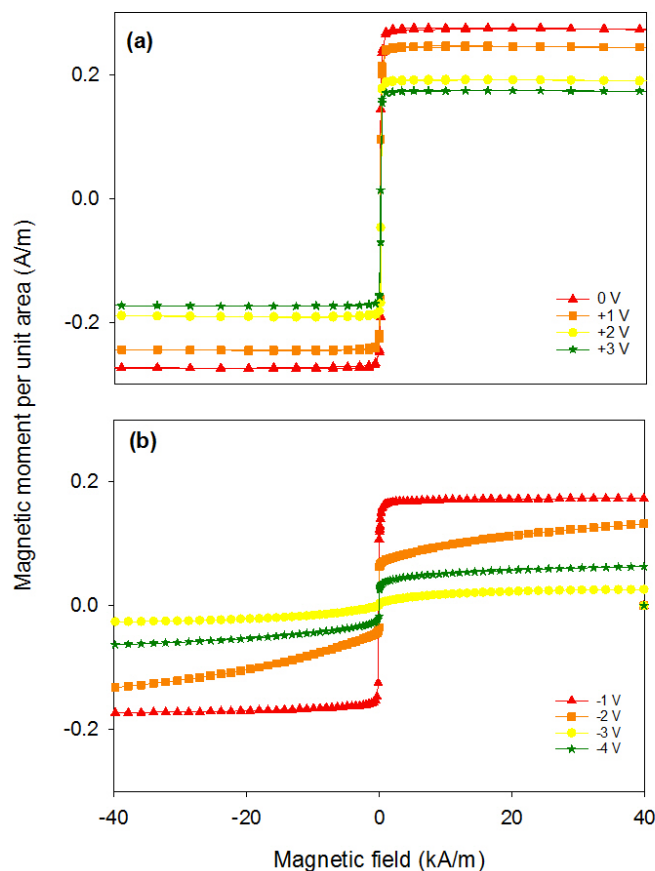
Figure 5.17: VSM generated hysteresis loops showing magnetic moment per unit area of permalloy film as a function of applied field after exposure to a sequence of voltages while part of a permalloy/EMIMTFSI/ITO cell; all cells were dismantled and all films washed in IPA prior to VSM characterisation. The voltage sequence passed from (a) 0 V to +3 V and subsequently to (b) -4 V; all negative voltages had prior exposure to +3 V for 5 minutes.

A potential cause for the changes in magnetisation is a thinning/thickening of the permalloy layer by oxidation driven redox reactions. In the calculation of the magnetisation of these films the thickness is assumed to be a constant 5 nm, however

this may not be the case as permalloy is prone to oxidation upon exposure to the atmosphere. It is possible to estimate the permalloy thickness of the films under test by dividing the raw magnetisation data by the area of the permalloy and permalloy magnetisation of 830 kA/m.[1] The results of this calculation are shown in figure 5.18. This shows the permalloy thickness decreasing with increasing positive voltage and a subsequent increase in permalloy thickness upon reversing the polarity to -4 V. The results show a decreased thickness even at no exposure, suggesting the films become oxidised upon removal form the evaporation chamber. These results agree with the trends demonstrated in the earlier MOKE measurements and clearly show a permalloy thinning/thickening via a voltage induced redox effect.
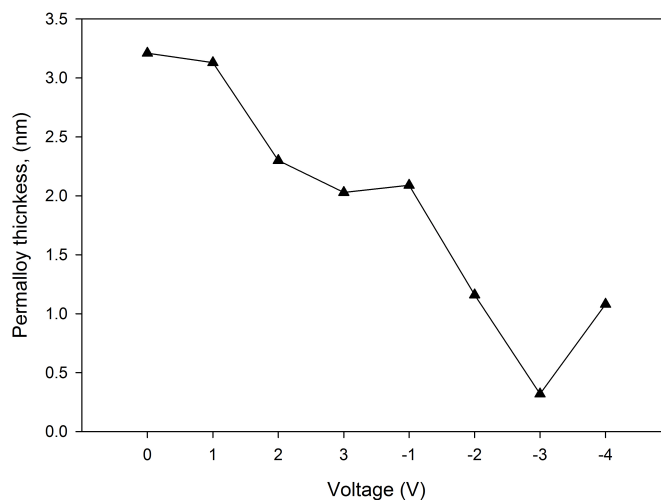
Figure 5.18: Calculated permalloy thickness as a function of voltage using VSM data

Although great care was taken to ensure that the films were exposed for the same durations of time, it may be that there was some slight variation. As demonstrated in figures 5.7 & 5.8, exposure time has a strong effect on magnetic properties, particularly at larger voltage magnitudes.

5.6 In situ MOKE magnetometry of voltage control of magnetic properties of Ni films

This section describes the variation of magnetic properties of thin films of Ni upon application of a voltage to a Ni/ionic liquid interface. The experiments are similar to those discussed in the previous section with the $Ni_{80}Fe_{20}$ switched for a Ni film and were carried out to compare the changes in magnetic properties of the two materials.

The voltage control of magnetic properties in Ni films has been demonstrated previously using magnetoelastic coupling between a ferromagnetic film and piezoelectric film[12,13]. However, little research has been conducted into the voltage control of magnetic properties of Ni via a redox reaction

The Ni thin films were grown using the same evaporation technique. Film thicknesses of 2 nm, 3 nm, 4 nm, 5 nm and 6 nm were grown and characterised magnetically using MOKE magnetometry.

Figure 5.19-5.23 shows MOKE hysteresis loops for films of different thicknesses. There is a clear magnetic hysteresis at thicknesses of 6nm and 5nm (Figure 5.19 & 5.20). However, below 5nm there is almost no magnetic signal detected by the MOKE magnetometer. It is possible that below 5nm there is no longer a continuous film and therefore a much reduced Kerr signal. Similar thickness limitations were demonstrated for permalloy films earlier chapter 5. The following data therefore focus on 5nm thick Ni films in an effort to increase surface effects and obtain larger changes in magnetic properties.
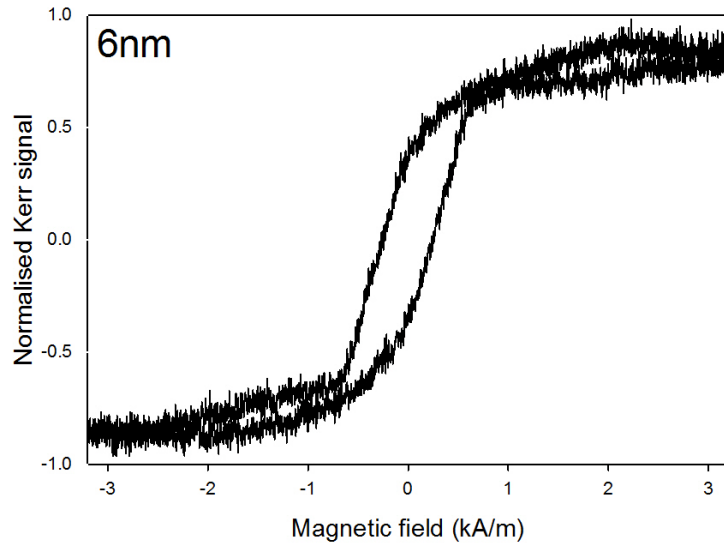
Figure 5.19: Magnetic hysteresis of 6 nm Ni film.
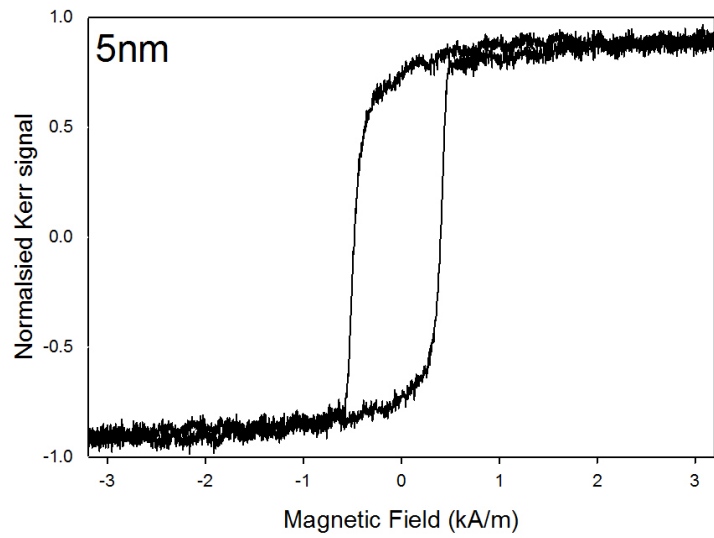
Figure 5.20: Magnetic hysteresis of 5 nm Ni film.
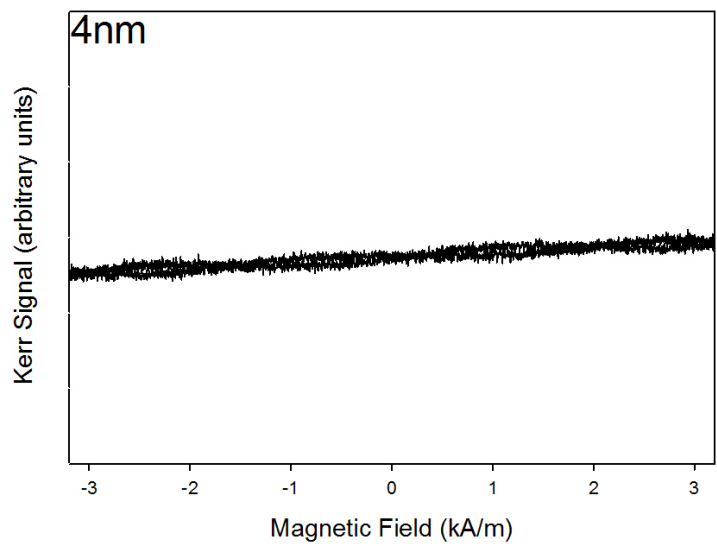
Figure 5.21: Magnetic hysteresis of 4 nm Ni film.
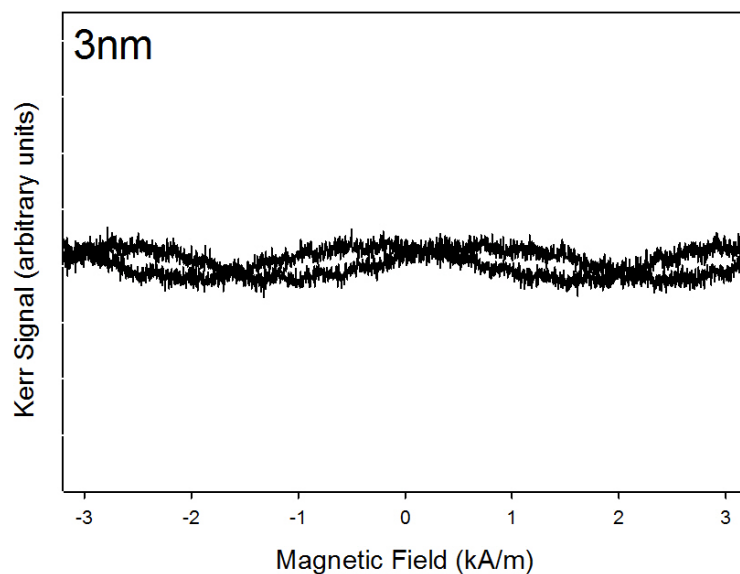
Figure 5.22: Magnetic hysteresis of 3 nm Ni film.
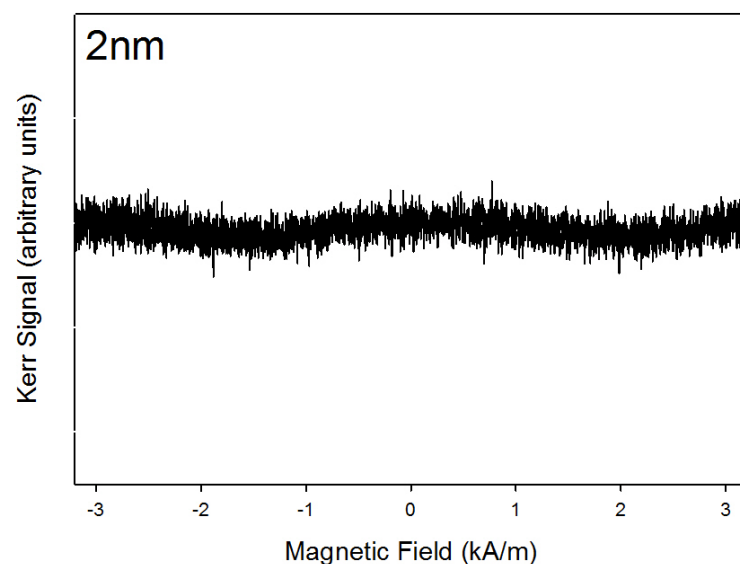
Figure 5.23: Magnetic hysteresis of 2 nm Ni film.

The ionic liquid cell was created using the same method described in section 4.2.3. The voltage applied to the electrochemical cell increased in steps of 0.2 V up to +3.2 V, and left at each voltage for 2-3 minutes. The coercivity of the Ni film decreased with increasing applied voltage (Figure 5.24 & 5.25) and was reduced by 90% for an applied voltage of +3.2V from its initial value. Above potentials of +3.2 V the MOKE magnetometer could no longer detect a magnetic response from the film.
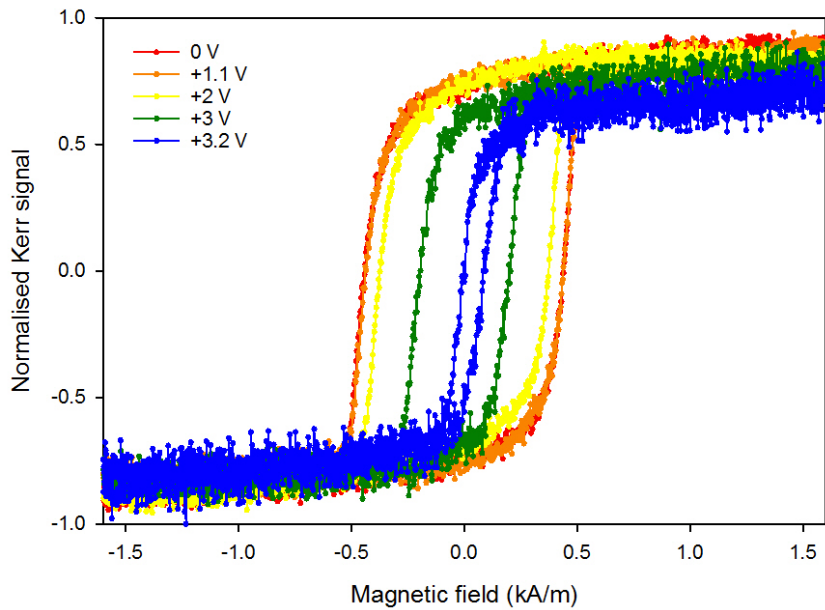
Figure 5.24: Magnetic hysteresis loops of 5nm Ni film within EMITSFI electrochemical cell as a function of applied voltage.
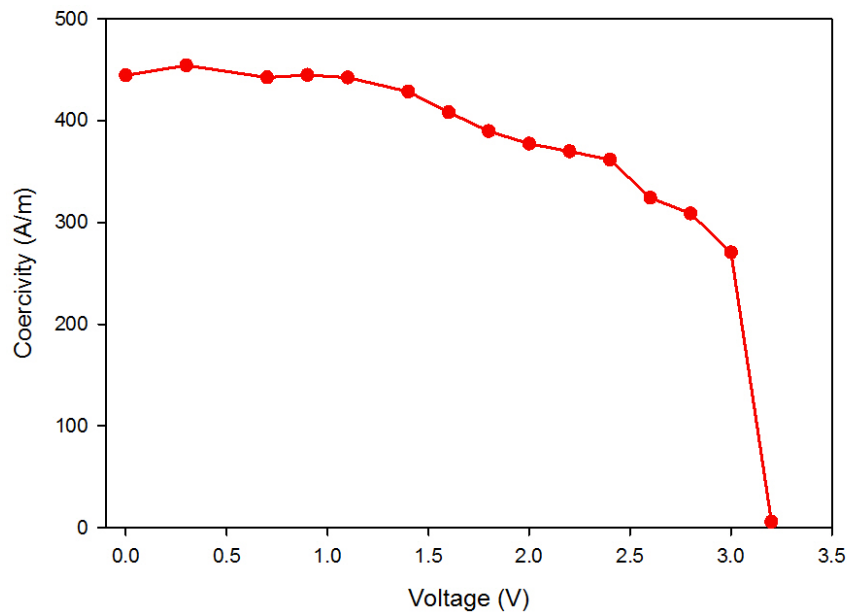
Figure 5.25: Coercivity of 5nm Ni film within EMITSFI electrochemical cell as a function of applied voltage.

Using the raw Kerr voltage data it was possible to calculate the fractional Kerr signal, as in section 5.4 for permalloy (Figure 5.26). The fractional Kerr signal gives a relative measurement of magnetisation between samples. Ni has a lower magnetisation than permalloy and this is demonstrated by the lower fractional Kerr signal. The relative

magnetisation of the Ni film started to decrease at +2 V until +3.2 V where there largest decrease took place. The low value of fractional Kerr signal at 0 V is attributed to a change in MOKE magnetometer alignment. The changes in fractional Kerr signal and coercivity show significant correlation and suggest the two changes are related.
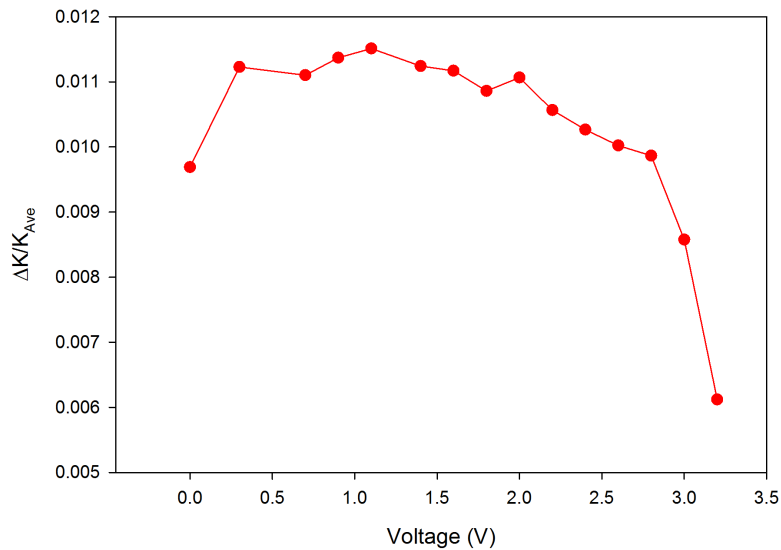
Figure 5.26: Fractional Kerr signal as a function of voltage.

The experiment was repeated using fresh samples with the maximum positive voltage reduced to +2.4 V to maintain a reasonable coercivity in the Ni film, and the voltage subsequently reduced to 0 V (Figure 5.27). The results again showed a steady decrease in coercivity with increasing positive voltage, decreasing by 20% over the voltage range used. Upon reducing the voltage the coercivity continued to decrease until the voltage was lower than +2 V, at which point the coercivity remained approximately constant.
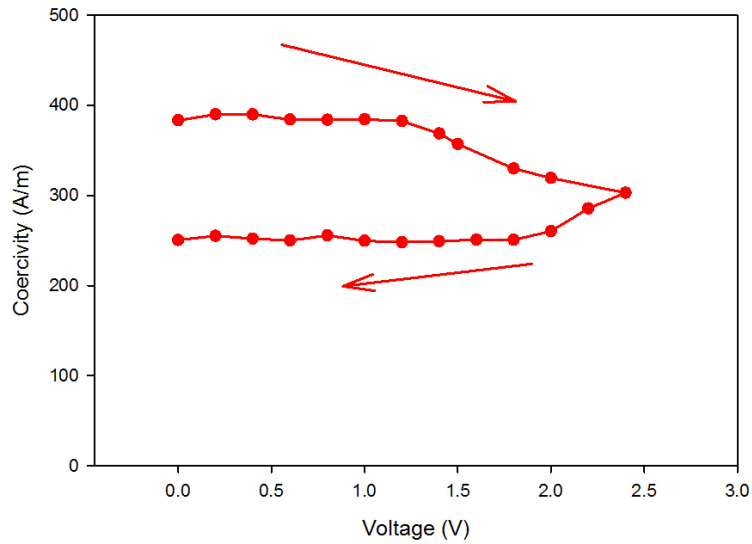
Figure 5.27: Coercivity of 5 nm Ni as applied voltage is increased to +2.4 V and then returned to 0 V.

Using a fresh 5 nm thick Ni film in a new cell, the voltage was increased to +2 V and reversed to -2 V and then repeated, with the cell left at each voltage for approximately 5 minutes. Increasing the voltage to +2 V again reduced the coercivity (Fig. 5.28) but here reduced by 57% from the initial value due to the longer exposure time used here, previously 2-3 minutes. Reversing the voltage polarity to -2 V subsequently increased the coercivity, which continued to increase at 0 V. This partially restored the coercivity by 32% at 0 V. Once the voltage had reached +2 V the coercivity decreased again. Repeating the voltage cycle saw further reductions in coercivity, although far less significantly than in the initial cycle.
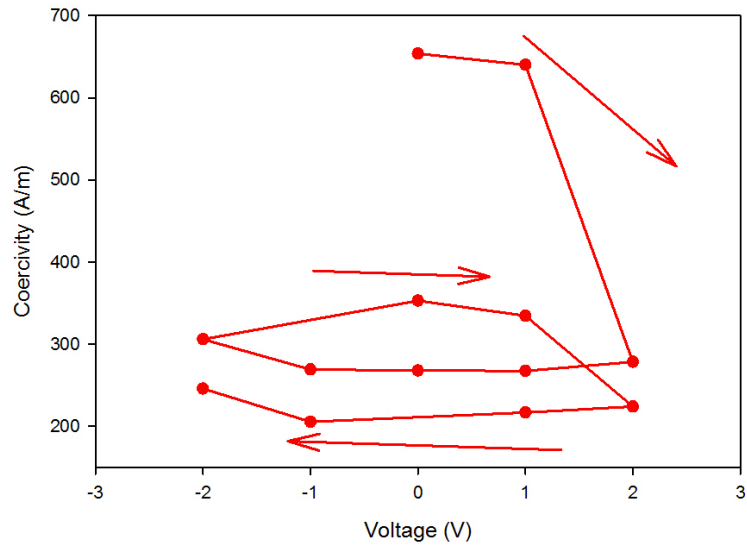
Figure 5.28: Magnetic coercivity of 5nm Ni films within EMITSFI electrochemical cell as a function of applied the voltage.

The time dependence of the electrochemical change in Ni was investigated by applying +2 V to the test cell and MOKE hysteresis loops obtained at 2-minute intervals for 20 minutes. A sharp decrease in coercivity to 90 % of its original value occurred over the first 6 minutes. After which the hysteresis loops greatly deteriorated and gave unreliable coercivities (Fig. 5.29). The low initial coercivity of this data is attributed to a variation in the sample shape.
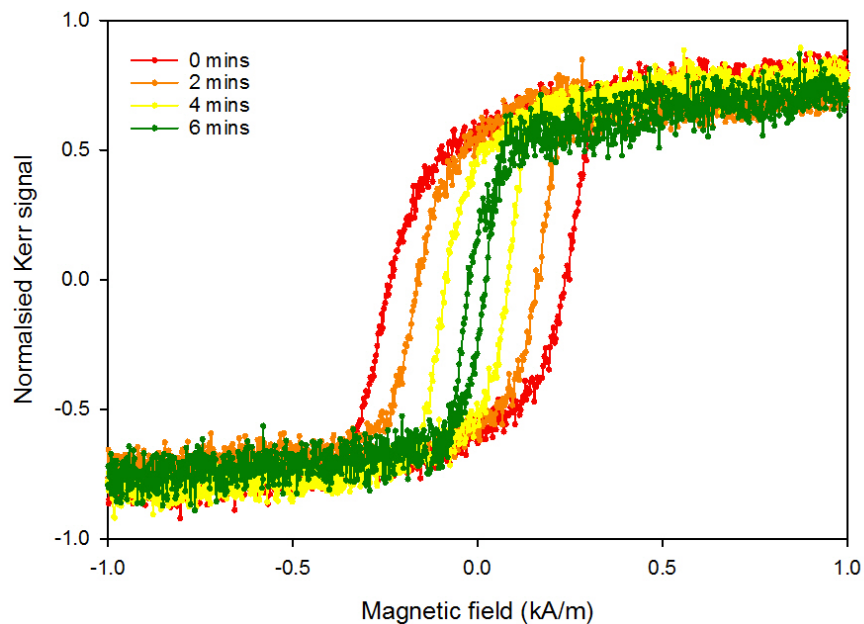
Figure 5.29: Time-dependent hysteresis loops of 5nm Ni film held at +2 V within EMITSFI electrochemical cell.

Using 7 nm and 9 nm thick Ni films allowed the influence of initial film thickness on the magnetic response of films in the electrochemical cell to be investigated. The 7 nm thick film (Fig. 5.30) showed a similar response to the 5 nm films (Fig. 5.25), with a gradual decrease in coercivity with increasing positive voltage until it dropped away sharply with no magnetic response observed for +4 V. This is a higher voltage than that at which magnetic properties were removed in the 5 nm thick Ni (Fig. 5.25). The coercivity of the 9 nm thick film (Fig. 5.31) changed little up to applied voltages of +3 V but, again, no magnetic response was observed for applied voltages of +4 V. This response of the thicker film demonstrates a reduced sensitivity to the electrochemically-induced changes in effective magnetic thickness up until a voltage when the entire film (or vast majority of it) is oxidised.
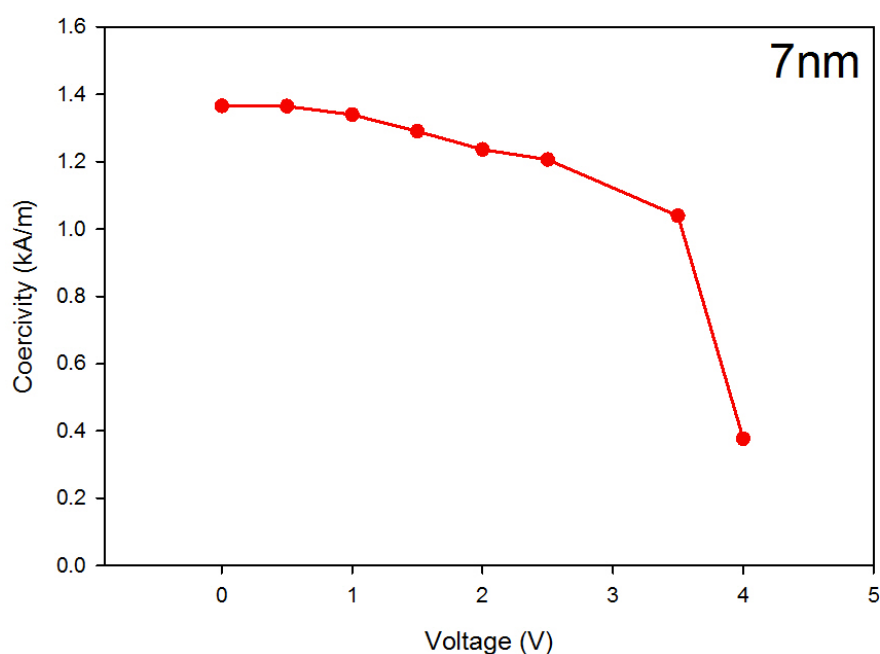
Figure 5.30. Coercivity as a function of voltage for Ni cells with a thickness of 7 nm.
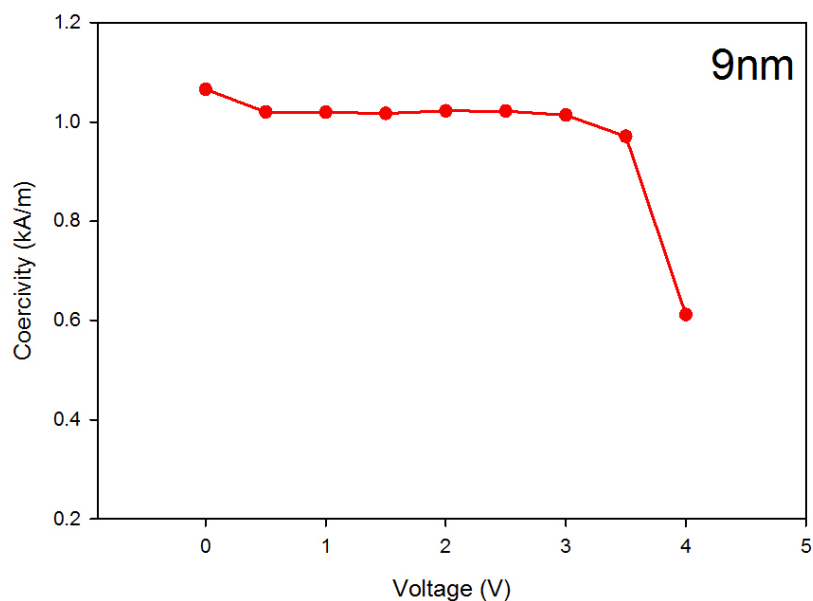
Figure 5.31. Coercivity as a function of voltage for Ni cells with a thickness of 9 nm.

5.7 Conclusion

This chapter has demonstrated and explored the tuning of magnetic properties of permalloy and Ni films. Upon application of low voltages to a ferromagnetic/ionic liquid cell interface, large relative changes in coercivity and magnetisation of the ferromagnetic films were observed. These changes could be partially reversed upon reversing the voltage polarity. It was also found that exposure time had a strong influence on the change in coercivity. VSM measurements demonstrated a variation in magnetisation of permalloy films after voltage application, calculations also showed a decreased permalloy thickness that further decreased upon application of a positive voltage. Reversing the voltage polarity consequently increased the permalloy thickness. These results confirmed a non-volatile effect, an important property for potential applications.

The magnetic data also showed that the magnitude of the voltage increased the rate of decrease in magnetic properties. This is attributed to the voltage magnitude

increasing the oxidation/reduction rate of the cell. Further, when the cell was first exposed to a negative voltage a sharp switching field was observed. This is thought to be caused by a reduction reaction causing oxygen impurities in the film to be removed and thus removing potential pinning sites. Future experiments will be required to fully characterise this phenomenon. The permalloy and Ni data demonstrate similar results which is to be expected due to the composition of permalloy. Controlling magnetic properties of thin films allows scope for use in tuneable magnetic devices. This result provides a demonstration of this and hopes to provide an insight into the mechanisms behind this process.

5.8 References

1.   Coey, J. M. D. *Magnetism and Magnetic Materials*. (Cambridge University Press, 2010). doi:10.1017/CBO9780511845000

2.   Spaldin, N. *Magnetic Materials. Fundamentals and applications*. (Cambridge University Press, 2010). doi:10.2277/0521016584

3.   Cowburn, R. P. Property variation with shape in magnetic nanoelements. *J. Phys. D. Appl. Phys.* **33,** R1–R16 (2000).

4.   Kwiatkowski, W. & Tumański, S. The permalloy magnetoresistive sensors-properties and applications. *J. Phys. E.* **19,** 502–515 (1986).

5.   Hayyan, M., Mjalli, F. S., Hashim, M. A., AlNashef, I. M. & Mei, T. X. Investigating the electrochemical windows of ionic liquids. *J. Ind. Eng. Chem.* **19,** 106–112 (2013).

6.   Hagiwara, R. & Ito, Y. Room temperature ionic liquids of alkylimidazolium cations and fluoroanions. *J. Fluor. Chem.* **105,** 221–227 (2000).

7.   Weisheit, M. *et al.* Electric Field-Induced Modification of Magnetism in Thin-Film Ferromagnets. *Science (80-.).* **315,** 349–351 (2007).

8.   Akhter, M. A., Mapps, D. J., Tan, Y. Q. M., Petford-Long, A. & Doole, R. Thickness and grain-size dependence of the coercivity in permalloy thin films. *J. Appl. Phys.* **81,** 4122–4124 (1997).

9.   O'Handley, R. C. *Modern Magnetic Materials*. (Wiley, 2000).

10.   Atkinson, D. *et al.* Magnetic domain-wall dynamics in a submicrometre ferromagnetic structure. *Nat. Mater.* **2,** 85–7 (2003).

11.   Allwood, D. A., Xiong, G., Cooke, M. D. & Cowburn, R. P. Magneto-optical Kerr effect analysis of magnetic nanostructures. *J. Phys. D Appl. Phys.* **36,** 2175–2182 (2003).

12.   Weiler, M. *et al.* Voltage controlled inversion of magnetic anisotropy in a ferromagnetic thin film at room temperature. *New J. Phys.* **11,** (2009).

13.   Wu, T. *et al.* Electrical and mechanical manipulation of ferromagnetic properties in polycrystalline nickel thin film. *IEEE Magn. Lett.* **2,** 2–5 (2011).

6. X-ray photoelectron spectroscopy (XPS) &

cyclic voltammetry of $Ni_{80}Fe_{20}$ & Ni thin films

6.1 Introduction

To understand the mechanisms behind the observed changes in magnetic properties reported in the previous chapter, X-ray photoelectron spectroscopy (XPS) and cyclic voltammetry measurements were carried out. XPS provides an elemental analysis for depth ranges of 5-10 nm. Other techniques such as scanning electron microscope (SEM) and energy-dispersive X-ray spectroscopy (EDX) were attempted but signals were impossible to distinguish over that of the silicon substrate.

Prior to XPS analysis the 5 nm pemalloy samples were exposed to a variety of voltages and were washed in isopropanol to remove any remaining ionic liquid. The samples were then measured using XPS in three separate locations to remove the effect of random defects. XPS spectra were obtained from samples exposed to 0 V to +3 V, and from -1 V to -4 V after having previously been exposed to +3 V, all in the presence of the ionic liquid. The reader is referred to section 4.4 for instrument and measurement details. The data were analysed using CASAXPS software, the high-resolution peaks were deconvoluted with guidance from peak fitting parameters from the literature[1–4]. In this results chapter the fitting protocol and parameters will be explained in more detail for each high-resolution spectra data set. In this chapter only the key XPS spectra are presented, while all XPS spectra are shown in the appendix. When a figure is referred to that is located in the appendix the notation used will be Figure A1.1 for example, which will refer to appendix section one figure 1.

Cyclic voltammetry measurements characterised the ferromagnetic ionic liquid cell and provided key information such as the electrochemical window of the cell and redox potentials for both permalloy and Ni ionic liquid cells.

6.2 Survey spectra

The survey spectra displayed in this section were fit using the Element Library in the CasaXPS software. In the first example, Figure 6.1 shows a 0 – 1400 eV survey spectrum for a permalloy film at 0 V with the peaks identified. The spectrum shows clear Ni peaks, with the lower binding energy peaks corresponding to Ni 3s and Ni 3p, and higher binding energy peaks corresponding to Ni 2s and Ni 2p, where Db corresponds to an energy doublet. There is also an Auger peak, Ni LMM, which further confirms the presence of Ni. The spectrum shows that Fe peaks are also present, demonstrated by the Fe 2s and Fe 2p peaks and again by the Fe LMM Auger peak. The Fe peaks are not as intense as the Ni peaks due to the atomic ratio of Ni to Fe in permalloy (80:20). Indeed, calculation of the sample stoichiometry gave a Ni:Fe ratio close to 80:20.
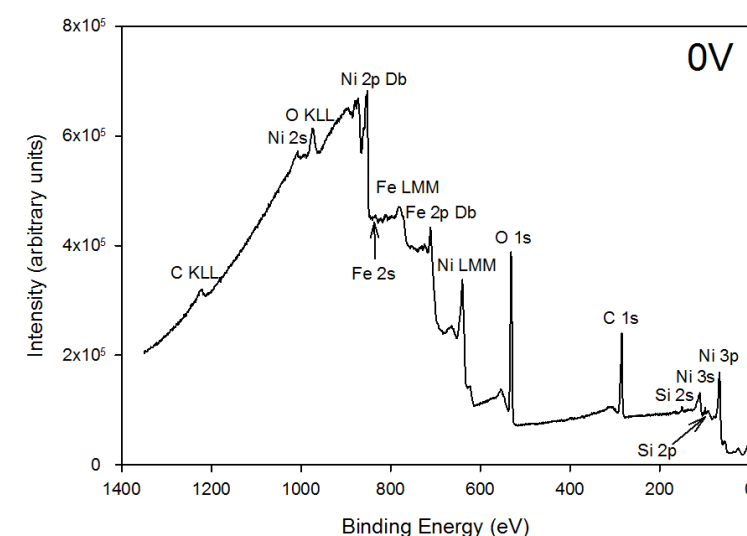
Figure 6.1: XPS survey spectrum of 0 V sample with peaks identified by the CasaXPS element library and Fe & Ni LMM and O KLL represent Auger peaks.

Figure 6.1 shows high intensity peaks for O and C; these peaks are common in XPS analysis and correspond to adventitious carbon contamination from exposure to the atmosphere[5]. The adventitious material is made up of carbon bonded to oxygen and is reported to have a thickness of 0.6 ± 0.2nm[6], which is a substantial proportion of the samples being analysed (12 %). XPS is extremely surface sensitive and therefore will show strong signal intensity for the adventitious carbon.

Another set of peaks in the spectra are Si peaks identified at low binding energies and generated from the Si substrate underneath the permalloy film. Finally, it is possible to see some secondary peaks, most noticeably after the C 1s and O 1s peak; these are known as loss peaks and are not to be confused with elemental data. The peaks displayed at the very low binding energies correspond to the same elements already mentioned and have not been identified on the figure for clarity.

Upon increasing the positive voltage the survey spectra show the clear appearance of fluorine, sulphur and nitrogen peaks, indicated by F 1s, S 2s, S 2p, N 1s and a N Auger peaks at a higher binding energy (Figures A1.1-4 & Figure 6.2). The appearance of these elements comes from the negative ion of the EMIMTFSI ionic liquid that contains fluorine, sulphur and nitrogen. This demonstrates that the ionic liquid cannot be completely removed from the surface by washing with isopropanol for a 15-minute period. The increase in relative intensity of F, S and N at +3 V suggests that these elements are penetrating further into the film and occupy a higher percentage of the film resulting in an increase in peak intensity. The increased penetration could be explained due to the larger electrostatic field generated at the interface. From the survey spectrum it is difficult to see whether the ionic liquid is adsorbed onto the surface or alternatively that it is mixing with the permalloy film. The O 1s and C 1s peaks showed minimal change with increasing positive voltage. At +3 V (Figure 6.2) the C peak

appeared to increase in relative intensity compared to the O peak; this could be due to the ionic liquid presence.

The Ni LMM, Ni 2p doublet and Fe 2p doublet peaks showed a decreasing intensity for increasing positive voltage. The largest reduction in relative intensity compared to the 0 V spectrum was at +3 V, where the most marked changes in magnetic properties were also observed (e.g. Figure 5.4).
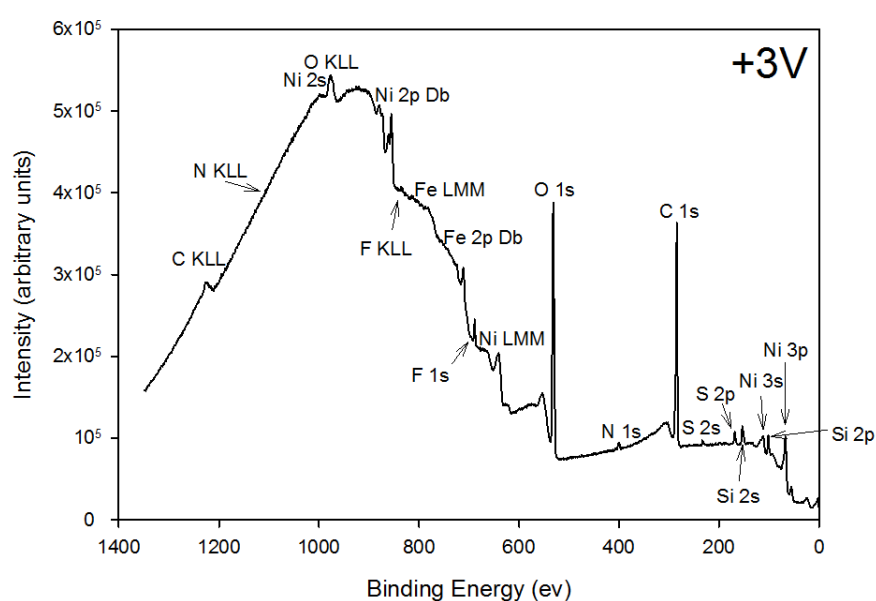
Figure 6.2: XPS Survey spectrum of +3 V sample, which displays the additional peaks of F, N & S.

The following negative voltage samples have all previously been exposed to +3 V and should therefore be compared in relation to Figure 6.2. Upon application of a negative voltage the elements from the negative ions in the ionic liquid (N, F, S) appeared to show a small decrease in intensity, this is thought to be due to the reversal of the electric field at the interface causing the negative ions to move to the positive

indium-tin oxide (ITO) electrode (Figures A1.5-8) & 6.3). At -3 V and -4 V In appeared in the spectrum, which has been deposited from the ITO electrode (Figure 6.3).

At low negative voltages of -1 V and -2 V (Figures A1-.5 & 1.6) the O 1s and C 1s peaks showed a ratio close to 2:1, in contrast to the 1:1 ratio displayed at +3 V (Figure 6.2). At larger negative voltages of -3 V and -4 V the O 1s and C 1s peaks return closer to a 1:1 ratio (Figure A1.7 & 6.3). It is unclear from the survey spectra what could be the cause for these changes; it is unlikely that the adventitious material would change by such a significant amount from sample to sample. The high-resolution spectra will help in explaining this result.

The Ni and Fe peaks showed little change upon switching the voltage polarity, apart from -3 V and -4 V, where In has been deposited on the surface and thus reduced the Ni and Fe signal.
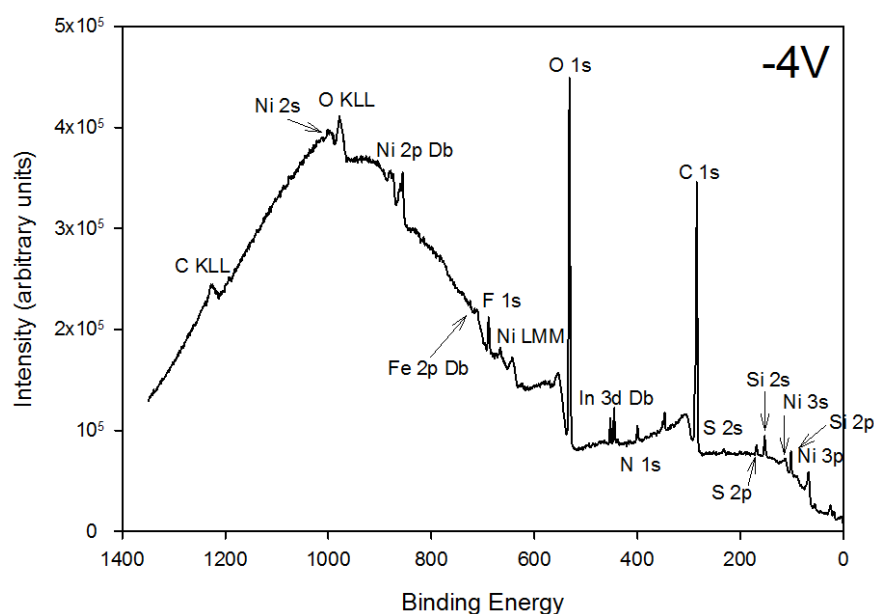
Figure 6.3: XPS Survey spectrum of -4 V sample, which displays the additional peaks of In from the Indium-Tin Oxide coated glass.

The survey spectra give an approximate idea of the atomic percentage of elements present at the surface of the film. The atomic percentage is calculated by dividing the peak area of a region by the relative sensitivity factor (RSF), which is then compared to other peaks in the spectrum. The RSF is specific to transitions within the electronic structure and has been adapted when investigating regions concerning doublets or singlet peaks. The atomic percentage was calculated in three different places on the sample and the results averaged for each voltage.
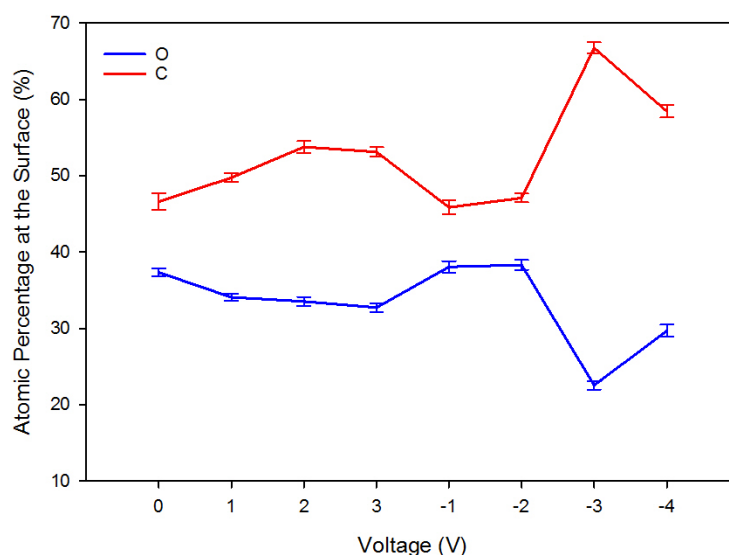
Figure 6.4: Atomic percentage at the surface of 5 nm permalloy film with applied voltage.

The variation in atomic percentage was plotted against voltage and can be see in figure 6.4 for carbon and oxygen. The atomic percentage of C increases with positive voltage, while the atomic percentage of O decreased. On applying a negative voltage the C and O atomic percentages returned close the values at 0 V, while further increasing the voltage magnitude to -3 V and -4 V created large variation in atomic percentage. These changes could be due to variations in adventitious carbon species or a chemical change happening at the surface. It appears that the C atomic percentage is dependent on the O atomic percentage, with an increase in C linked with a decrease in O. The

errors bars presented on this graph were calculated from the standard deviation generated by the CasaXPS software.
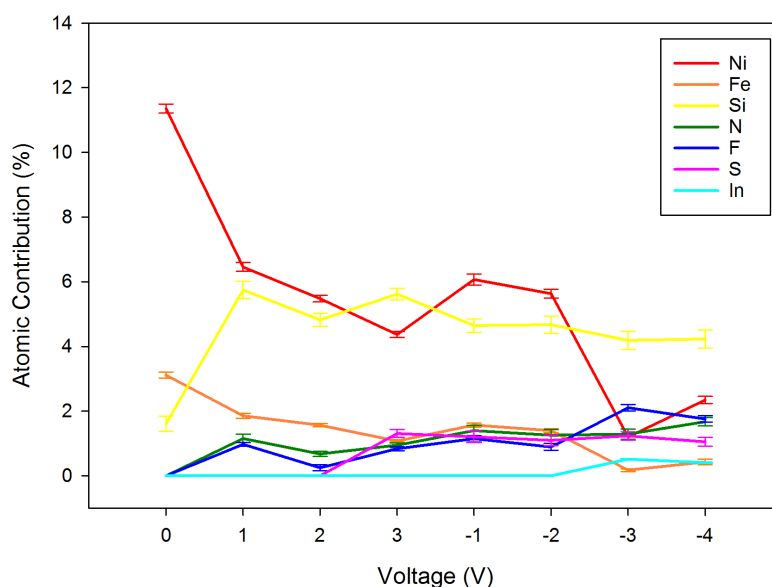
Figure 6.5: Atomic percentage at the surface of 5 nm permalloy film with applied voltage, for the elements Ni, Fe, Si, N, F, S & In.

The data in figure 6.5 shows the variation in atomic percentage for the other elements present at the film surface, including Ni, Fe, N, F, Si, S and In. On applying +1 V there was a sharp decrease atomic percentage of Ni and a sharp increase in Si, this may indicate a thinning of the permalloy film. The Ni then showed an increase in atomic percentage at the surface on application of a negative voltage, which then plummeted after -3 V and -4 V with the presence of In on the film. It is important to mention that it is likely that these films are inhomogeneous with the formation of oxides and adventitious carbon; this has a large effect on the RSF, which can lead to inaccurate atomic percentage values. In addition, the significant overlap of peaks around the Ni 2p energy range make it difficult to identify a suitable background, which can also lead to errors in atomic percentage. The difficulty in using a suitable background will be further explored in the Ni 2p energy range section of this chapter. The Fe atomic percentage mimics the

behaviour of the Ni data, this agrees well with the atomic ratio of the permalloy (80:20). The remaining elements show little change throughout voltage exposure.

The atomic percentage values displayed in the survey scans are approximate due to the changes in RSF from the inhomogeneity of films analysed. Subsequent high-resolution narrow XPS scans present a more accurate representation of the films and are shown in the following sections. The high-resolution narrow scan spectra allow a more thorough analysis of the film surface, providing bond chemistry and oxidation chemistry.

6.3 High-resolution spectra fitting of O 1s, Ni 2p and Fe 2p energy range

Analysis of the O 1s, Ni 2p and Fe 2p energy range spectra provides a strong insight into the oxidation at the film surface; this can help to explain the observed changes in magnetic properties. The fitting process of the spectra for each of these three elements is combined in the following sub sections to give the reader a greater insight into the complexities of the fitting process and an explanation for how the conclusions were reached.

The 0 V spectra presented in this section were fit using the preliminary description provided in section 4.4.1, including the initial calibration of the carbon 1s peak applied to the rest of the spectra and the setting up of a quantification region including background. Following this general initial step, an element specific fit was made for each high-resolution energy spectra and this then propagated for all voltage values. Where the fit is more complex, for example Ni spectra, greater detail will be given of the fitting process.

6.3.1 Fitting analysis of O 1s high-resolution spectra

The first spectra to be analysed is the O 1s spectra at 0 V. An initial assessment of the O

1s spectra clearly shows two peaks at approximately 529.5 eV and at 531.5 eV. Using the CasaXPS element library the large peak at 531.5 eV was identified as a hydroxide or lattice oxide peak, where lattice oxides are metals with periodic oxygen impurities. A limitation of the CasaXPS element library is the lack of data for fitting oxides peaks; therefore a literature search was carried out for XPS analysis of Nickel-Iron films. Biesinger et $al.$[2] used XPS to analyse high-purity powder and metal samples of Ni, NiO, $NiFe_2O_4$, $Ni(OH)_2$ and Fe. Using the research paper as a guideline, it was possible to identify the peak at 529.5 eV as a lattice oxide and an initial fit was attempted. However, the fit did not match the spectra because there remained a feature unaccounted for around 532.8 eV, which is linked to water and other organic species. With all the peaks identified it is then necessary to apply constraints to the fit, such as line shape peak position and FWHM. The line shape used was GL (30) (Gaussian and Lorenztian (70% and 30%)); it can be assumed that this line shape was used for all spectra unless specified otherwise. The fitting parameters used throughout this chapter for O 1s peaks can be seen in Table 6.1. The "Fit Components" function of CasaXPS can also be used to improve the fit using a least squares fitting approach, this reduces the residual to close to unity for each fit, while remaining within the applied constraints.

The constraints described in table 6.1 allow for variation to account for the different oxide materials present and a less restrictive fitting process. The O 1s data in figure 6.6a for the 0 V sample shows the three main peaks, attributed to lattice oxides, hydroxides/lattice defects and water/organic species. Literature from similar systems suggest the lattice oxides could be NiO, FeO, Fe_2O_3, $NiFe_2O_4$ or Ni_2O_3, the hydroxide material could be $Ni(OH)_2$, $Fe(OH)_2$, $Fe(OH)_3$, $Ni_3O_2(OH)_4$ or $Fe_2O_3.xH_2O$[1,2,4].

Lattice oxide		Hydroxide, hydrated or defective oxide		Water or organic oxygen	
Peak Position (eV)	FWHM	Peak Position (eV)	FWHM	Peak Position (eV)	FWHM
529.6 - 529.4	0.8 - 1.3	531.1 - 531.8	1.5 - 2.3	533.5 - 532.9	1.2 - 2.0

Table 1: O 1s fitting parameters for XPS spectra, including peak position range and FWHM for lattice oxides, hydroxide, hydrated or defective oxide and water or organic oxygen.

6.3.2 Fitting analysis of Ni 2p high-resolution spectra

The information learnt from the O 1s spectra can now be utilised in the fitting process of the metallic spectra, for example metallic oxides and hydroxides can be expected. When analysing the Ni 2p energy range, only the Ni $2p_{3/2}$ feature was inspected to reduce the complexity of the deconvolution (figure 6.6b); the relative sensitivity factor was altered to reflect this. However, when selecting a quantification region the whole Ni 2p range was considered, this allowed the whole $2p_{3/2}$ spectra to be analysed. In this case a Shirley background was used, including an offset at the start of the spectra, initially set to 6 x 10^3 counts per second[2]. The Shirley background is where the background signal is proportional to the total peak area above the background in the lower binding peak energy range.

First of all the prominent peak at 852.3 eV was identified as Ni metal by the CasaXPS element library. Following consultation of the XPS analysis of standard Ni metal samples, plasmon loss and satellite peaks were identified at approximately 855.9 eV and 858.3 eV respectively and the identified constraints applied. The constraints applied here include peak position, FWHM, line shape (L. Sh) and percentage area. For Ni metal the line shape was chosen as LA(1.1,2.2,10) in line with research on standard

metal samples. LA(1.1,2.2,10) describes an asymmetric line in the form, LA (α,β,m), where α and β describe the spread of the tail either side of the Lorentzian component, while m describes the width of the Gaussian used to convolute the Lorentzian curve[1]. Plasmon peaks occur due to a specific loss of energy from an interaction between emitted photoelectrons and conduction band electrons, while satellite peaks occur due to the emission of photoelectrons from an excited state within the material system.

The initial fit of the spectrum clearly showed unidentified peaks at approximately 856 eV and 861 eV. The O 1s spectra clearly identified a lattice oxide on the sample surface. After searching the literature for oxidation of permalloy films NiO and $NiFe_2O_4$ were identified as typical metallic oxides found on permalloy films[4]. These lattice oxides also have binding energies close to those identified earlier. The fitting parameters for these lattice oxides were then added to the Ni 2p spectrum, along with the appropriate constraints from standard high purity samples as identified by Biesinger *et al*[1]. Applying these components and constraints greatly improved the fit to the spectra, as demonstrated by a marked reduction in the residual. This suggests that during growth a NiO layer is created above the permalloy layer due to oxygen in the air. This leaves a Fe rich layer underneath the NiO, which generates the $NiFe_2O_4$ at the expense of the permalloy. This would reduce the permalloy film thickness and therefore reduce the expected magnetisation, showing further evidence for the thinning effect observed in chapter 5.

However, there were still areas in the spectra that were left unaccounted for where the residual was much larger than unity. Again, from the O 1s spectrum, which the main peak was identified as hydroxide and defect oxides, which could refer to the defect lattice oxides already identified or also $Ni(OH)_2$. This nickel hydroxide could be attributed to contributions from the surrounding water in the air[4]. Once these components along with their constraints had been applied to the Ni 2p spectrum, the fit closely matched the

data as demonstrated by a much-reduced residual that approached unity. All of the fitting parameters used for the Ni 2p spectrum can be seen below in table 2. These fitting parameters were then propagated to all the Ni 2p spectra. There are some variations in FWHM between Biesinger *et al.*[2] and the parameters here due to the difference in pass energy.

Compound	Peak 1 (eV)	Percentage of total area (%)	Peak 1 FWHM (eV)	Δ Peak 2 – Peak 1 (eV)	Percentage of total area (%)	Peak 2 FWHM (eV)	Δ Peak 3 – Peak 1 (eV)	Percentage of total area (%)	Peak 3 FWHM (eV)
Ni Metal	852.25	81.2	1.03	3.65	6.3	2.0	6.03	12.5	3.48
NiFe$_2$O$_4$	854.90	17.3	1.85	1.52	38.2	3.5	6.93	38.5	5.0
NiO	853.8	14.3	0.8	1.71	44.2	3.3	7.15	34.0	3.3
Ni(OH)$_2$	854.4	7.4	1.0	0.77	45.3	2.38	2.79	3	2.1

Compound	Δ Peak 4 – Peak 1 (eV)	Percentage of total area (%)	Peak 4 FWHM (eV)	Δ Peak 5 – Peak 1 (eV)	Percentage of total area (%)	Peak 5 FWHM (eV)
NiFe$_2$O$_4$	10.22	2.8	3.5	12.49	3.2	3.1
NiO	10.25	3.6	2.9	12.63	3.9	3.0
Ni(OH)$_2$	6.58	39.2	5.0	11.54	3.7	3.5

Table 2: Ni 2p$_{3/2}$ fitting parameters for XPS spectra for Ni metal, NiFe$_2$O$_4$, NiO and Ni(OH)$_2$, where percentage of total area is related to the specified compound and ΔPeak changes are the difference in subsequent peak binding energies in eV.

6.3.3 Fitting analysis of Fe 2p high-resolution spectra

Finally, the fitting analysis of the Fe 2p spectra can be investigated. Once again only the Fe $2p_{3/2}$ spectra was analysed to reduce the complexity in the peak deconvolution. Similarly to the Ni 2p spectra, a Shirley background type was used and a quantification region defined. Initially, the CasaXPS library identifies the Fe 2p peak at 706.6 eV, which is so small due to the ratio of Fe to Ni in permally (20:80). The line shape used for this metal peak was (LA(1.2,4.8,3), as identified from a high-purity sample analysed by Biesinger *et al.*[1]. Utilising the knowledge from the previous peak fitting of O 1s and Ni 2p spectra, the $NiFe_2O_4$ peak components can be added to the Fe 2p spectra. Once these two components were identified in the spectra, the residual fit was close to unity. The fitting parameters used for fitting the Fe 2p spectra can be seen in Table 3. Once again these fitting parameters were applied to all of the Fe 2p spectra and there is variation in FWHM due to the difference in pass energy used.

Compound	Peak 1 (eV)	Percentage of total area (%)	Peak 1 FWHM (eV)	Δ Peak 2 – Peak 1 (eV)	Percentage of total area (%)	Peak 2 FWHM (eV)	Δ Peak 3 – Peak 1 (eV)	Percentage of total area (%)	Peak 3 FWHM (eV)
Fe Metal	706.6	100	1.28	-	-	-	-	-	-
$NiFe_2O_4$	709.8	34.1	2.5	1.3	33.2	2.08	2.7	22.3	1.84

Compound	Δ Peak 4 – Peak 1 (eV)	Percentage of total area (%)	Peak 4 FWHM (eV)
$NiFe_2O_4$	4.3	10.4	2.28

Table 3: Fe 2p$_{3/2}$ fitting parameters for XPS spectra for Fe metal and $NiFe_2O_4$, where percentage of total area is related to the specified compound and ΔPeak changes are the difference in subsequent peak binding energies in eV.

6.4 XPS analysis of O 1s, Ni 2p and Fe 2p spectra

Using the fitting parameters described in the previous section the O 1s, Ni 2p and Fe 2p spectra could then be deconvoluted and the sample surface described. The C 1s data can be found in the appendix, along with all of the XPS data.

The initial spectra at 0 V show a large amount of hydroxide/defect lattice oxide peaks from the O 1s spectrum. The hydroxide peaks are most likely to be due to adventitious carbon, while lattice oxides are due to the $NiFe_2O_4$, further identified by the Ni 2p and Fe2p spectra.

The O 1s +1 V spectrum in figure 6.7 shows distinct differences. Firstly, the water/organic species shoulder peak is greatly reduced and the hydroxide/defect lattice oxide peak has increased in area. Secondly, the hydroxide/defect lattice oxide peak binding energy has shifted by +0.5 eV, which is significant in this spectrum.

The reduction of the water/organic species peak is attributed to the electrolysis of the water, which separates the oxygen from hydrogen. The electrolysis of water usually happens at +1.2 V, however it has recently been shown that NiO films can act as a catalyst in speeding up the electrolytic process[7]. This produces hydrogen and oxygen at the sample surface, which contributes to an increase in hydroxide species. The binding energy shift indicates a change in the hydroxide species; the binding energy increase indicates the photoelectron is more tightly bound to the nucleus due to the addition of an electron. This could be in the form of (OH) groups. Clearly there is an increase in the hydroxide species and possibly a change in the hydroxide species.
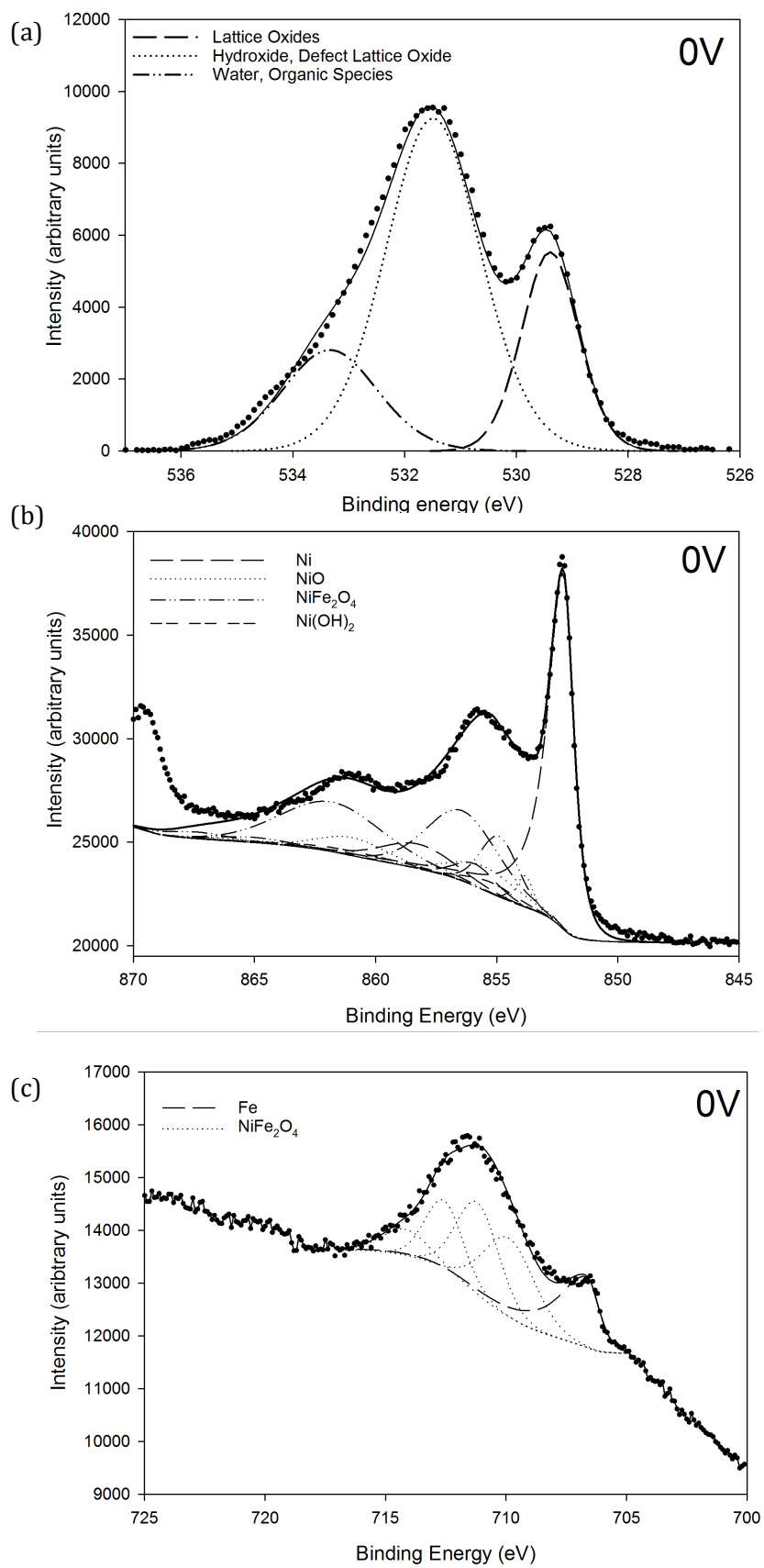
Figure 6.6: XPS spectrum for (a) O 1s, (b) Ni 2p and (c) Fe 2p at 0V with the components identified in the top left of the figures.
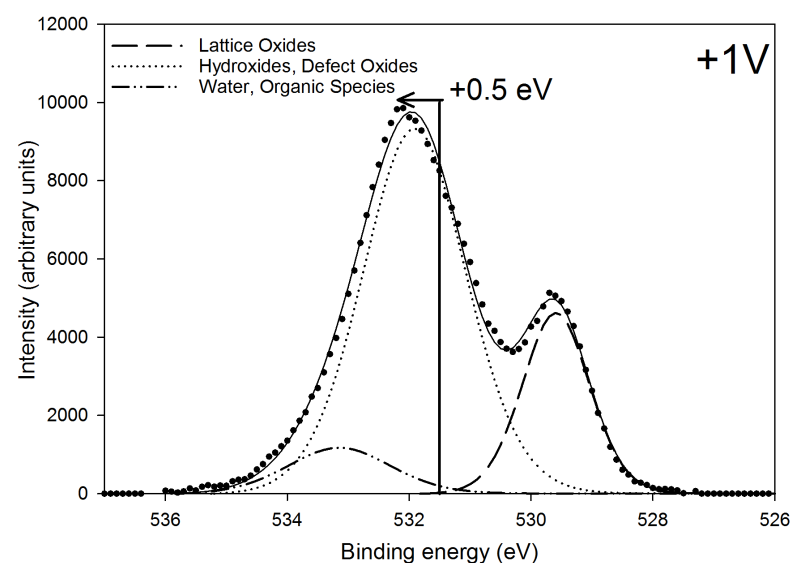
Figure 6.7: XPS spectrum for O 1s at +1 V with arrow to indicate +0.5 eV peak shift compare to the 0 V spectrum.

Further increasing the voltage to +3 V demonstrated very little change in the O 1s spectra (Figure A3.4). For the Ni 2p spectra however, there was a large decrease in the Ni peak, while the oxide and hydroxide grew in comparison (Figure 6.8a). The peak deconvolution of the secondary peak at 856.0 eV showed an increasing $NiFe_2O_4$ peak, with only small variation in the NiO and $Ni(OH)_2$. Upon increasing the voltage to +3 V the Fe peak decreases substantially (Figure 6.8b). There is a much larger peak at 711 eV, which corresponds to $NiFe_2O_4$ to agree with the Ni spectra. As the Fe peak decreased with increasing voltage the oxide peak increased in size.

These results suggest that the permalloy layer is becoming more oxidised with increasing voltage to form $NiFe_2O_4$. This suggests that the rate of growth of the $NiFe_2O_4$ is governed by the applied voltage magnitude. Thus thinning the permalloy layer and decreasing coercivity and magnetisation.
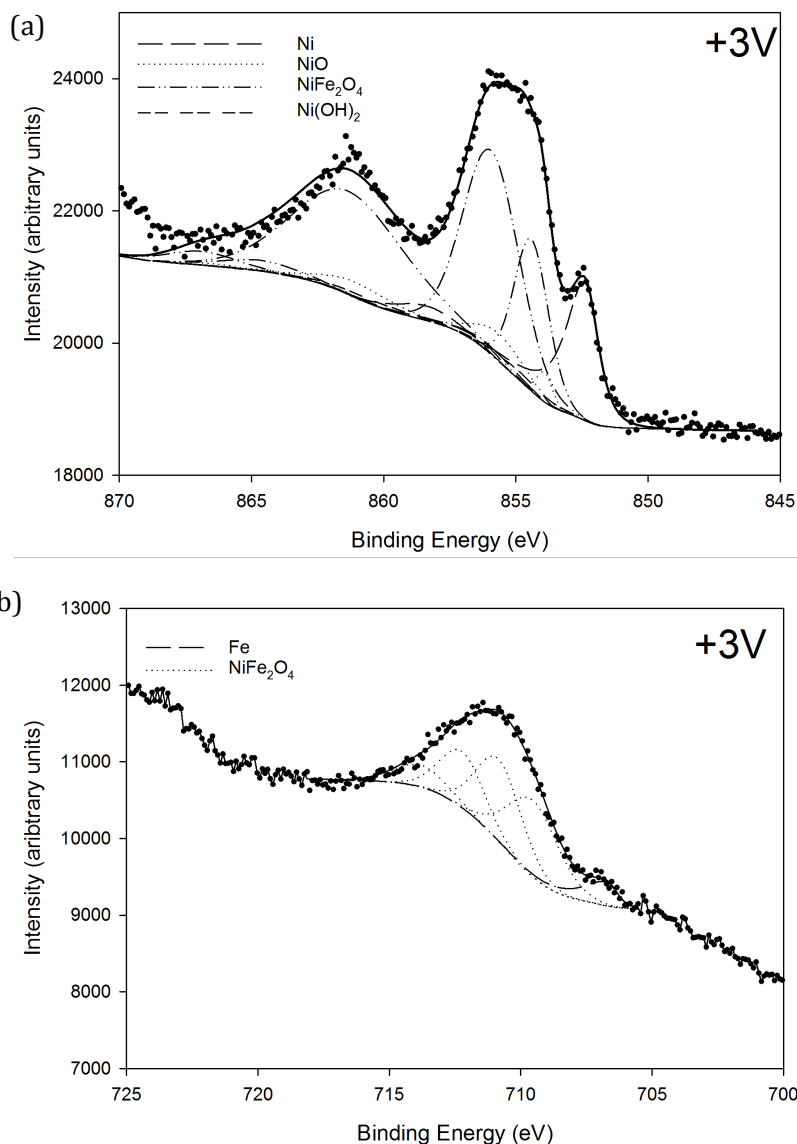
Figure 6.8: XPS spectra at 3 V for (a) Ni 2p energy range and (b) Fe 2p energy range with components identified in the top left corner.

The voltage subsequently switched to -1 V and -2 V demonstrated minimal change in the O 1s spectra (Figure A3.5 & 3.6). The Ni 2p spectra showed a slight increase in Ni metal peak at -1 V (Figure 6.9). This could be a sign that the reverse process is taking place and the permalloy layer is starting to increase and thus the oxide layer is decreasing. At -2 V the spectra remains almost unchanged from -1 V. The Fe 2p spectra show minimal change from the +3 V spectra at -1 V and -2 V (Figure A5.5 & 5.6).
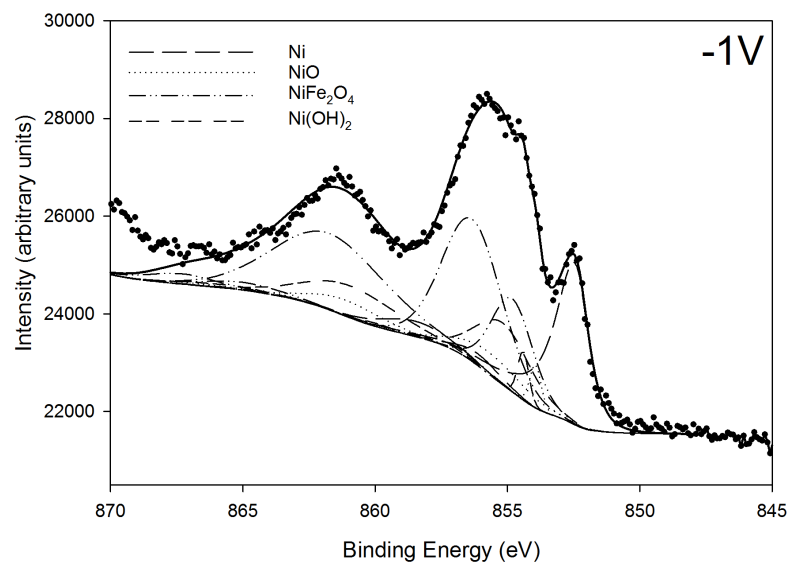
Figure 6.9: XPS spectra at -1 V for Ni 2p energy range previously exposed to +3 V.

Reducing the voltage further to -3 V and -4 V coincides with the deposition of In as shown in the survey spectra (Figure 6.3). In the O 1s spectra at -3 V the metallic oxide peak reduces substantially in size (Figure 6.10). At -3 V the In layer covers the surface of the permalloy film, increasing the distance required for the photoelectrons from the metallic oxide to escape. The unchanged hydroxide peak indicates that it is closer to the surface than the metallic oxide. This suggests the layered structure of the thin film is Si/$Ni_{80}Fe_{20}$/Metallic Oxide/Hydroxide (/In at -3V and -4V). This result is supported by Fitzsimmons et al.[4], who showed the growth of nickel and iron oxides and hydroxides at the expense of the metallic permalloy film.
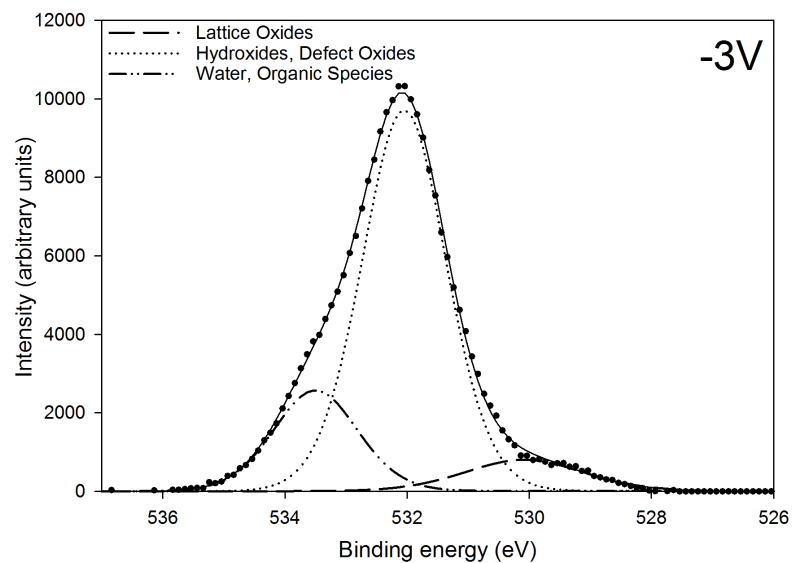
Figure 6.10: XPS spectra at -3 V for O 1s energy range previously exposed to +3 V displaying a much reduced lattice oxide peak.

The Ni 2p and Fe 2p spectra became very noisy at -3 V and -4 V due to the appearance of the In on the sample surface (Figure 6.11a & b). Unfortunately this makes fitting the spectra even more difficult and limits the information obtainable from the spectra. There is an observed increase in the oxide and hydroxide peak however this may be because the Ni is now further from the sample surface so is no longer detected.
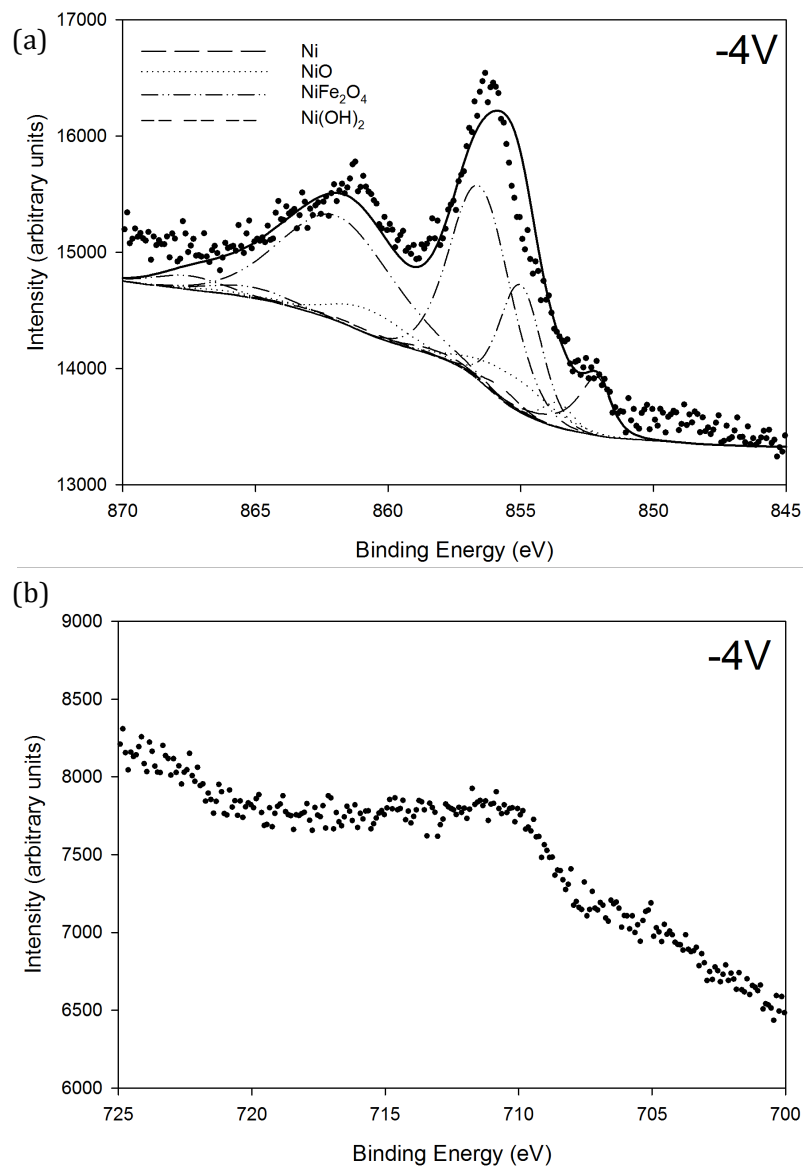
Figure 6.11: XPS spectra at -4 V for (a) Ni 2p energy range and (b) Fe 2p energy range previously exposed to +3 V.

In figure 6.12 the area percentage for the different peaks as a function of applied voltage for the O 1s spectra. This figure further demonstrates the decrease in water/organic species coinciding with an increase in hydroxide/lattice defect oxides at +1 V and above. The lattice oxide remains uniform until -3V and -4V, whereby the hydroxide/lattice defect oxide peak further increases, this is due to the In deposited on the surface. The error bars for this plot were calculated using a Monte Carlo approach

available within the CasaXPS software, which works by an iterative process of fitting the peak model data to synthetic data with noise. Therefore, the error bars presented here are related to the robustness of the peak model fit to the spectra.
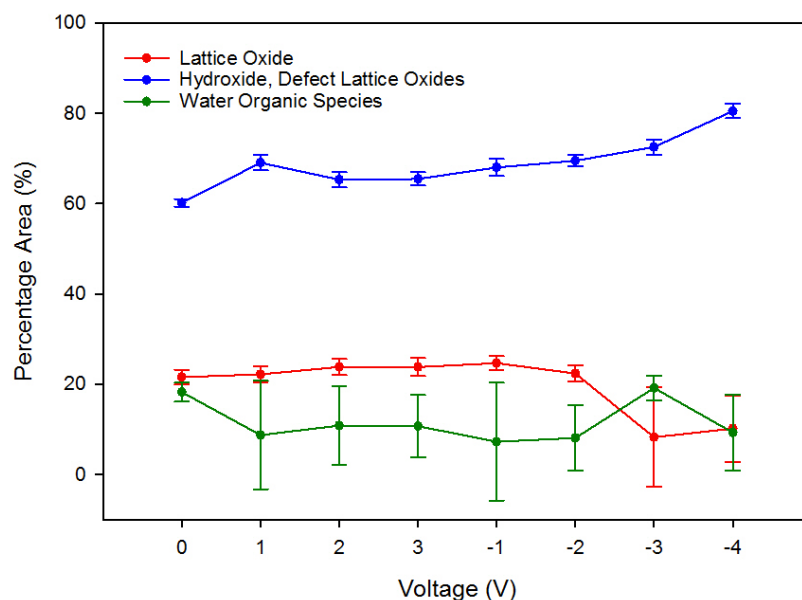
Figure 6.12: Percentage peak area of the O 1s for the lattice oxide, hydroxide/defect lattice oxides and water/organic species as a function of applied voltage with error bars calculated using a Monte Carlo approach from the CasaXPS software.

Plotting the peak area percentage as a function of voltage provides more quantitative analysis of the Ni 2p spectra (Figure 6.13). This data shows that there is a large decrease in Ni peak and a large increase in the $NiFe_2O_4$ peak. This demonstrates that the Ni containing permalloy layer is thinning due to a Ni-Fe oxide. The variation in metal and oxide presence is attributed to the voltage change. A thinner permalloy layer would reduce the coercivity and magnetic moment as described earlier in the chapter. Upon reversing the voltage polarity there is a large decrease in $NiFe_2O_4$, which could be a reversal of the effect seen for the positive voltage. The NiO and $Ni(OH)_2$ remain relatively constant throughout the voltage cycle. The -3 V and -4 V data was not included

in this plot due to concerns of the accuracy of the fit. Again the error bars were calculated using the Monte Carlo approach within the CasaXPS software.
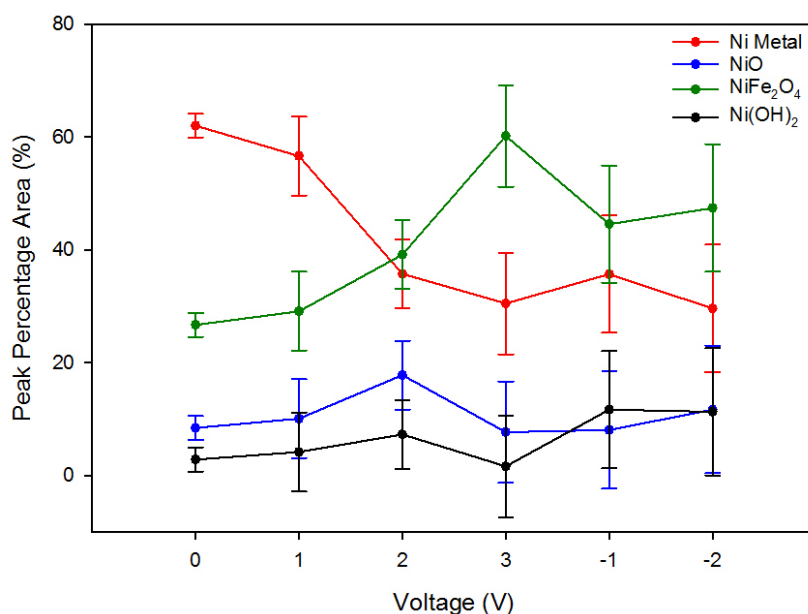
Figure 6.13: Percentage peak area of the Ni 2p energy range for Ni, NiO, NiFe$_2$O$_4$ and Ni(OH)$_2$ as a function of applied voltage with error bars calculated using a Monte Carlo approach from the CasaXPS software.

The data in figure 6.14 displays the percentage peak area for the Fe 2p energy range as a function of voltage. The data shows a clear correlation with a decrease in Fe to an increase in NiFe$_2$O$_4$. This conclusion agrees with the data shown in the Ni section. The -3 V and -4 V data have been left out because of the poor quality of the spectra. It is possible that at these voltages the Fe peak would increase and hence the permalloy thickness. Thus increasing the previously diminished magnetic properties. Again error bars were calculated using the Monte Carlo approach within the CasaXPS software.
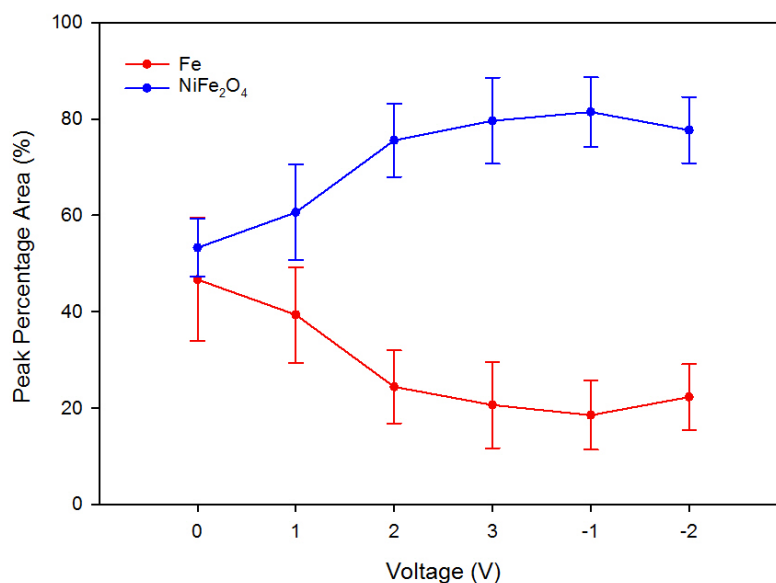
Figure 6.14: Percentage peak area of the Fe 2p energy range for Fe and NiFe$_2$O$_4$ as a function of applied voltage with error bars calculated using a Monte Carlo approach from the CasaXPS software.

6.5 Cyclic voltammetry of permalloy ionic liquid cell

Cyclic voltammetry measurements were carried out to investigate the electrochemical properties of the ionic liquid/permalloy cell. Due to experimental limitations the cell was composed of two copper disks coated in permalloy with the ionic liquid sandwiched in between. This differs from the previous cell as there is no ITO electrode.

The cyclic voltammogram shows that the cell is stable after cycling 5 times (Figure 6.15), which is important for potential applications. The first key points to notice are the peak and trough at ± 0.3V, which is indicating a minor oxidation (reduction) for the positive (negative) voltage. This result agrees well with the XPS data displayed in the previous section. Further at voltages of ± 2.5 V, the current density peaks are much higher indicating a much faster rate of oxidation/reduction. This also agrees well with the XPS and magnetic data, which displayed much-increased rates of oxidation and decrease of magnetic properties at higher voltage magnitudes.
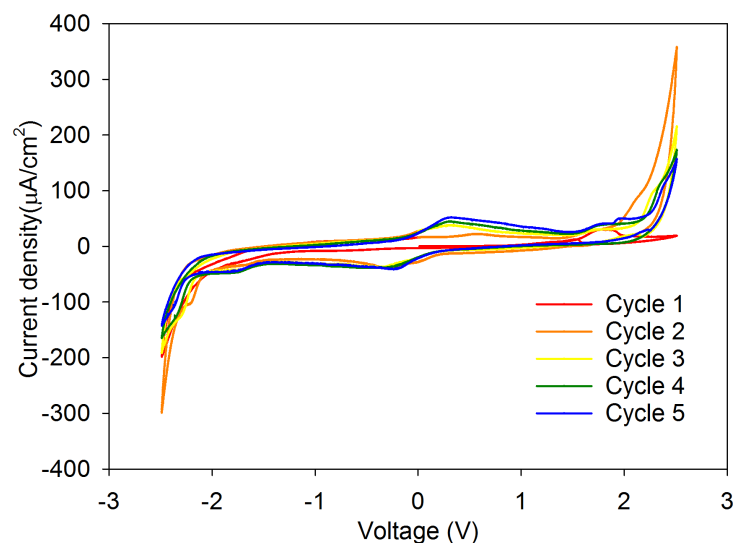
Figure 6.15: Cyclic voltammogram for permalloy/ionic liquid/permalloy cell over 5 cycles.

Cyclic voltammetry measurements were also carried out on the Ni/ionic liquid cell. The cell electrodes were both Ni coated copper disks, with no ITO present and sandwiched either side of apiece of filter paper soaked in the EMITSFI ionic liquid to form the electrochemical cell.

Figure 6.16 shows the current through the cell as a function of voltage for four voltammetry cycles. The small peaks at ± 0.3 V are indicative of minor oxidation (reduction) for the positive (negative) voltage. These peaks are also present in permalloy measurements (Figure 6.15), which may be due to Ni oxidation. For the Ni films, strong current density peaks at ± 2.5 V indicate a fast rate of oxidation/reduction. These values correlate with the sharp drops in magnetic properties observed for 5 nm Ni samples and indicate oxidation/reduction is the cause of the changes in magnetic properties (Figures 5.20- 5.25). The similarity in the four cycles shows that the effects are repeatable.
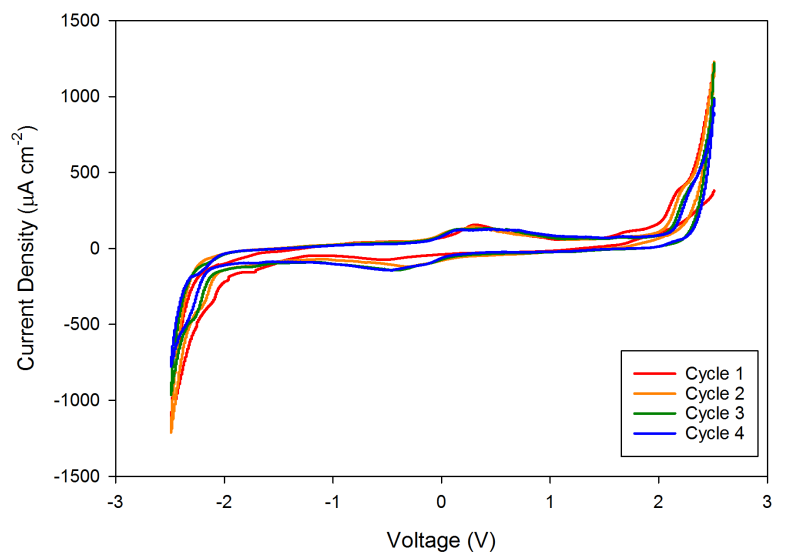
Figure 6.16: Cyclic voltammetry data for Ni/EMITSFI/Ni cell for four voltage cycles.

6.6 Conclusion

This chapter demonstrates the changes in surface chemistry of permalloy films and describes the electrochemical nature of the ferromagnetic ionic liquid cells upon application of a voltages. XPS showed the likely presence of a NiO layer above the permalloy film, which introduced an Fe rich species underneath that oxidised readily. This created a $NiFe_2O_4$ layer between the NiO and permalloy layer. The $NiFe_2O_4$ layer grew at the expense of the permalloy layer with increasing voltage, thus thinning the permalloy and causing the observed reduction of coercivity and magnetisation described in chapter 5.

XPS failed to show complete reversal of the oxidation due to the appearance of In on the film surface which blocked the XPS signal from the Ni and Fe regions. However, cyclic voltammetry revealed chemical reduction in the films at voltages below – 2.5V. This suggests the subsequent thickening of the permalloy film and thus the resurgence of the magnetic properties.

6.7 References

1. Biesinger, M. C. *et al.* Applied Surface Science Resolving surface chemical states in XPS analysis of first row transition metals , oxides and hydroxides : Cr , Mn , Fe , Co and Ni. *Appl. Surf. Sci.* **257,** 2717–2730 (2011).

2. Biesinger, M. C., Payne, B. P., Lau, L. W. M., St, R. & Smart, C. X-ray photoelectron spectroscopic chemical state quantification of mixed nickel metal , oxide and hydroxide systems. 324–332 (2009). doi:10.1002/sia.3026

3. Salou, M. *et al.* Initial oxidation of polycrystalline Permalloy surface. *Surf. Sci.* **602,** 2901–2906 (2008).

4. Fitzsimmons, M., Silva, T. & Crawford, T. Surface oxidation of Permalloy thin films. *Phys. Rev. B* **73,** 014420 (2006).

5. Briggs, D. & Seah, M. P. *Practical Surface Analsyis.* (Wiley, 1996).

6. Mangolini, F., McClimon, J. B., Rose, F. & Carpick, R. W. Accounting for nanometer-thick adventitious carbon contamination in X-ray absorption spectra of carbon-based materials. *Anal. Chem.* **86,** 12258–12265 (2014).

7. Gong, M. *et al.* Nanoscale nickel oxide/nickel heterostructures for active hydrogen evolution electrocatalysis. *Nat. Commun.* **5,** 4695 (2014).

7. Ferromagnetic resonance spectroscopy of permalloy (Ni$_{80}$Fe$_{20}$) films

7.1 Introduction

This chapter explores further the effects of voltage control of magnetic properties in thin films of permalloy (Ni$_{80}$Fe$_{20}$) using ferromagnetic resonance (FMR) spectroscopy. This work follows on from Chapters 5 & 6 and uses the same ionic liquid (EMITSFI)/permalloy cell described therein.

FMR occurs when all the magnetic moments precess with the same phase and amplitude over the whole volume of a material, an in-depth description of FMR theory and FMR spectroscopy is given in sections 2.5.2 and 4.3.3. FMR spectroscopy allows calculations to be made for magnetisation saturation (M$_s$)[1], surface anisotropy (K$_s$)[2] and Gilbert damping (α)[3]. Measuring these provides greater understanding of the variation in coercivity and magnetisation observed in earlier chapters. The first section of this chapter describes *ex situ* FMR spectroscopy measurements, while the second part describes *in situ* FMR spectroscopy measurements.

In situ and *ex situ* measurements demonstrated decreases in magnetisation in 5 nm thick permalloy films for increasing voltage magnitude, which subsequently increased upon reversal of voltage polarity. Upon measuring thick (10 nm - 50 nm) permalloy films the reverse effect was observed, i.e. increasing magnetisation for increasing voltage. Calculating M$_S$ for permalloy films gave a value 23% lower than that expected for permalloy films and calculations suggested a large surface anisotropy in the films. This suggests that the films are inhomogeneous and may contain regions that are not permalloy. This agrees well with the X-ray photoelectron spectroscopy (XPS) data in

chapter 6.

The results here demonstrate the voltage control of high frequency magnetic properties of permalloy films. This is of great interest in the field of high frequency tuneable magnetic devices.

7.2 Ex situ ferromagnetic spectroscopy of $Ni_{80}Fe_{20}$ films in the fundamental mode

First of all the samples were prepared for measurement by FMR spectroscopy. This required exposure of the permalloy films to the ionic liquid and voltage in an electrochemical cell, in the same method described in Chapter 6 for X-ray photoelectron spectroscopy (XPS). In these FMR spectroscopy measurements a fixed frequency was passed through a microwave stripline to create an excitation field, an in-plane DC magnetic field was swept and the microwave absorption detected using a lock-in amplifier. A detailed description of the FMR spectrometer apparatus is given in section 4.3.3.

In the *ex situ* experiments, previously exposed 5 nm permalloy samples were placed faced down on a microwave stripline to maximise the FMR signal obtained by the detector. FMR measurements were carried out on each sample at fixed frequencies of 8-15 GHz, while the magnetic field was swept. Figure 7.1 shows the shift in resonant magnetic field as a function of frequency for films previously exposed to various voltages within the electrochemical cell. The reader is reminded that the negative voltages had been previously exposed to +3 V, also in this experiment the 0 V sample had not seen the electrochemical cell.
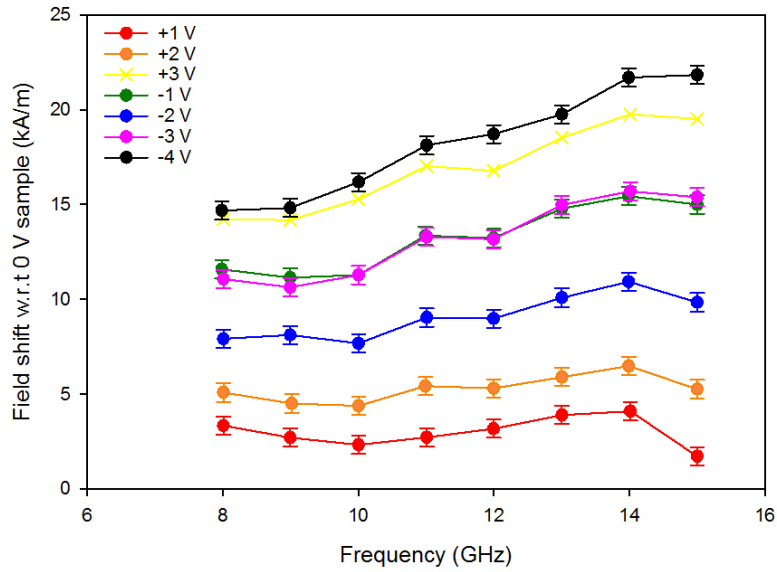
Figure 7.1: Shift in resonant FMR field with respect to 0 V, for samples previously exposed to a voltage within the electrochemical cell as a function of frequency.

These data show a steady increase in resonant field shift with increasing positive voltage, with a 14 kA/m shift in resonant field at +3 V. For samples that were subsequently exposed to -1 V and -2 V, the resonant field shift reduces closer to the value at 0 V. However, at -3 V and -4 V the resonant field shift increases again, reaching an overall maximum at -4 V.
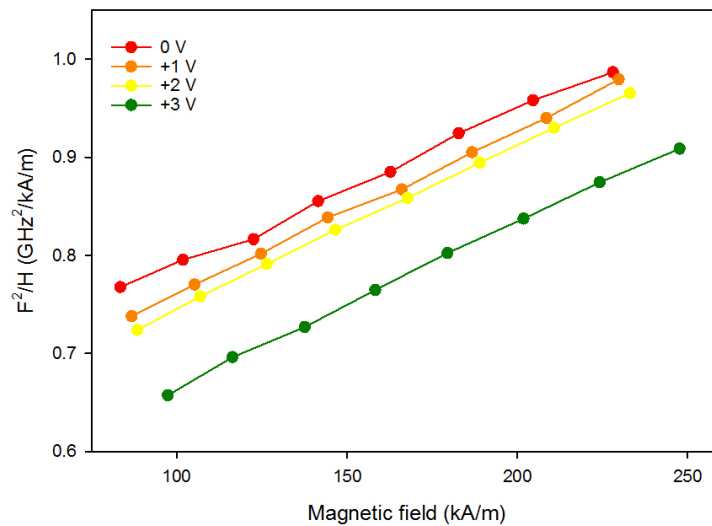
Figure 7.2: Plot of F^2/H vs magnetic field for 5 nm permalloy films previously exposed to a positive voltage and fitted to the Kittel equation.

Fitting these data with the Kittel equation for thin films magnetised in plane (4-7)(Figure 7.2) and calculating the gradient gives the gyromagnetic ratio. The gyromagnetic ratios measured here ranged from 2.33-2.45, which is approximately 10% higher than the report values of 2.10[4]. This difference from other reported values could be due to the low frequency range over which the measurement was made, which can induce significant errors[4]. Alternatively, the difference could be due to the quality of the film, which was shown to containing oxides in the previous chapter on XPS. The gyromagnetic ration can then be used to divide the y-intercept to give the effective magnetisation (Figure 7.3). This technique was used throughout this section to calculate magnetisation.
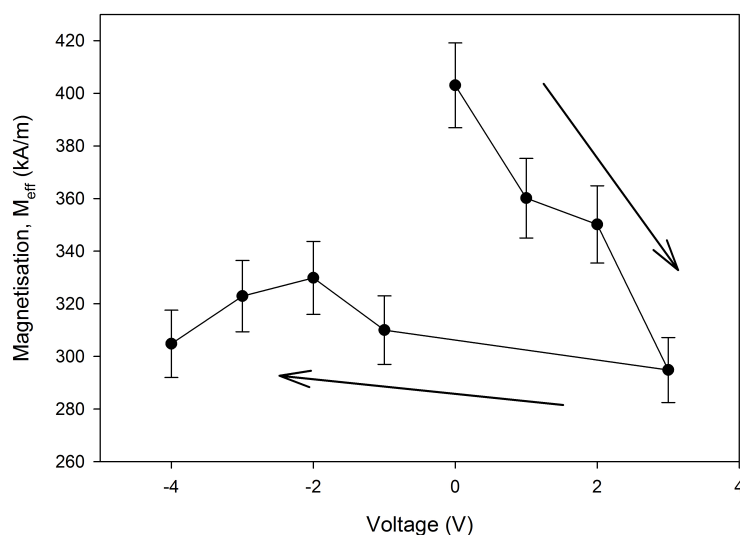
Figure 7.3: Magnetisation of 5 nm permalloy films from FMR measurement as a function of previously applied voltage to electrochemical cell.

A positive shift in resonant magnetic field results from a decrease in magnetisation, and a negative field shift an increase in magnetisation. Samples that were exposed to +3 V showed a decrease of approximately 25% in magnetisation from a value of 410 kA/m. This magnetisation value is significantly lower than bulk values of approximately 860 kA/m; however agrees well with values for ultrathin films[5]. This suggests that the films are thinner than 5 nm and therefore M_{eff} is reduced due to the

larger effect of the surface anisotropy (4-8) or there is a decrease in M_S. Reversing the voltage to -2 V subsequently increased the magnetisation by 12% of the value at +3 V. Further decreasing the voltage to -3 V and -4 V caused the magnetisation to decrease. At ultrathin thickness (<10 nm) there is a strong thickness dependence on magnetisation[5], therefore the changes in magnetisation are attributed a thinning/thickening of the permalloy film increasing the effect of surface anisotropy and thus reducing magnetisation. This agrees with the MOKE, VSM and XPS data presented in sections Chapters 5 & 6.
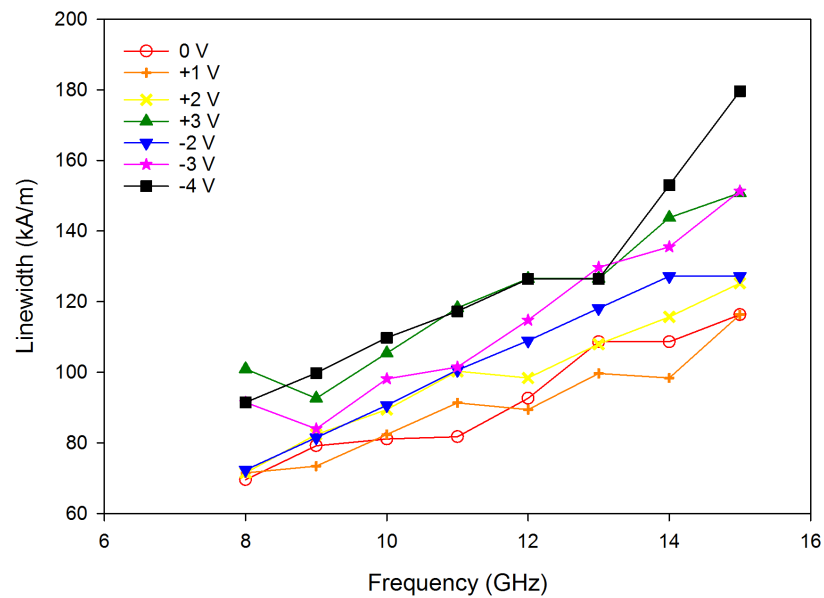
Figure 7.4: FMR linewidth as a function of frequency for calculation of Gilbert damping constant for 5 nm permalloy previously exposed to a sequence of voltages in electrochemical cell.

Plotting the linewidth against resonant frequency (Figure 7.4) and fitting to equation (4-9) it is possible to calculate the Gilbert damping, α, of the films by dividing the gradient by the gyromagnetic ratio (Figure 7.5), the same technique was used for future calculations. The Gilbert damping increased for increasing positive voltage and continued to increase after the voltage polarity had been switched. Similar to magnetisation, α is known to increase for decreasing film thickness[3], which further

suggests a voltage thinning effect of the ferromagnetic film. However, this could indicate deterioration in the quality of the film, leading to increased grain boundary contributions to damping.
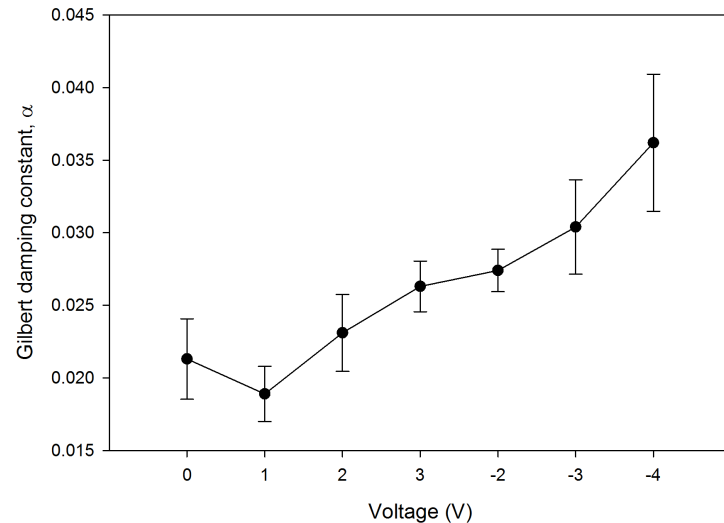
Figure 7.5: Gilbert damping for 5 nm permalloy films previously exposed to a sequence of voltages in electrochemical cell, where negative voltages had previously been exposed to +3 V.

7.3 In situ ferromagnetic spectroscopy of $Ni_{80}Fe_{20}$ films in the fundamental mode

This section describes *in situ* FMR spectroscopy measurements of 5 nm, 10 nm and 50 nm permalloy films. For these measurements the permalloy film was placed on the stripline and the cell arranged as described in Section 4.2.3. Similar to the *ex* situ measurements the excitation frequency was fixed and an in-plane DC magnetic field was swept, while a lock-in amplifier measured microwave absorption. However, in these measurements the sample was placed face-up i.e. stripline in contact with the underside of the Si substrate. This greatly reduced the signal compared to the *ex situ* measurements, however the signal generated was sufficient to obtain a clear FMR trace.
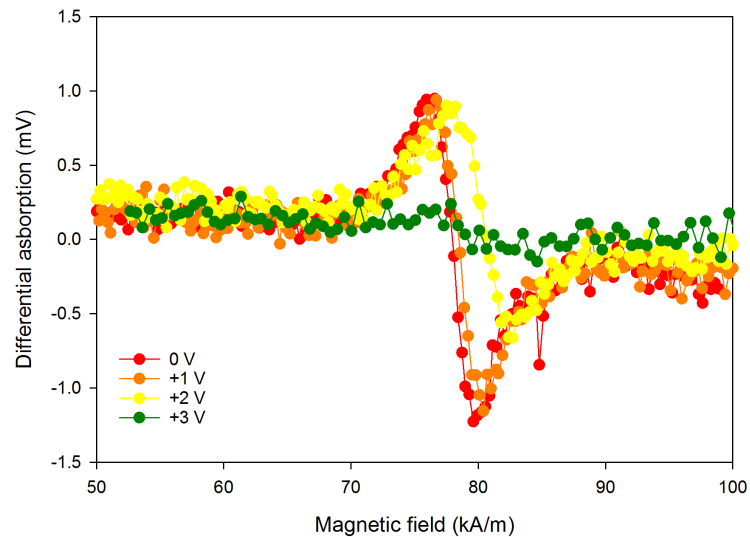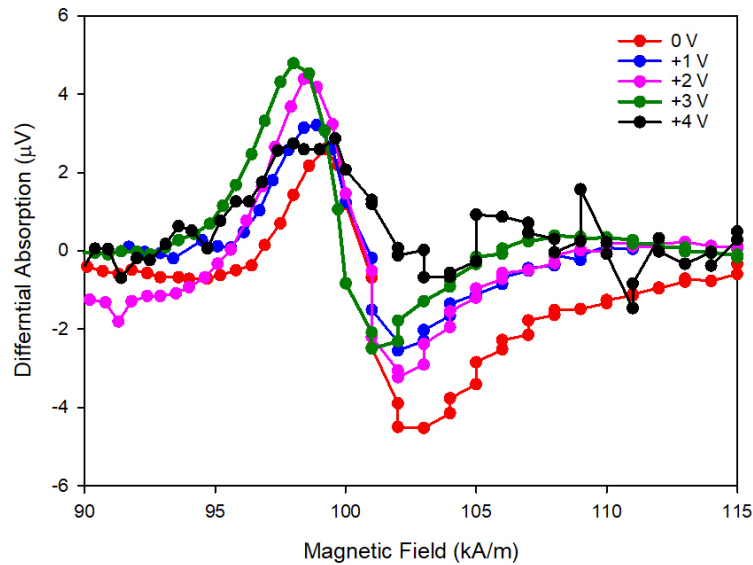
*Figure 7.6: Raw in situ FMR spectra at 8 GHz for 5 nm permalloy in electrochemical cell for a sequence of voltages.*

A 5 nm permalloy film in this arrangement was exposed to voltages of 0 V, +1 V, +2 V and +3 V and field sweeps taken at a frequencies of 4-12 GHz, Figure 7.6 shows data from the 8 GHz spectra. This gave values of the resonant field, which shifted by approximately +4 kA/m at +2 V when compared to 0 V (Figure 7.7), where +3 V showed a near zero FMR response suggesting the permalloy was fully oxidised. Fitting this data to the Kittel equation generated values for the magnetisation (Figure 7.8). Here the values of the magnetisation are higher than the previous section, which may be due to using fresher samples that were therefore less oxidised. The samples magnetisation remained relatively unchanged at +1 V but decreased by approximately 30% from the value at 0 V once +2 V was applied. FMR measurements at +3 V showed a rapid decrease in signal and made it impossible to calculate a reliable value for the magnetisation. This was due to the long duration of FMR sweeps (20 minutes) for each frequency and voltage. As described in Section 5.4, voltage exposure time has a strong effect on magnetic properties.

Plotting the linewidth against frequency and fitting to equation (4-9) again gave the Gilbert damping constant. Figure 7.8 shows an increasing Gilbert damping with increasing positive voltage, in agreement with the general trend seen in the *ex situ* measurements (Figure 7.3) and further supporting a voltage induced thinning of the permalloy film.
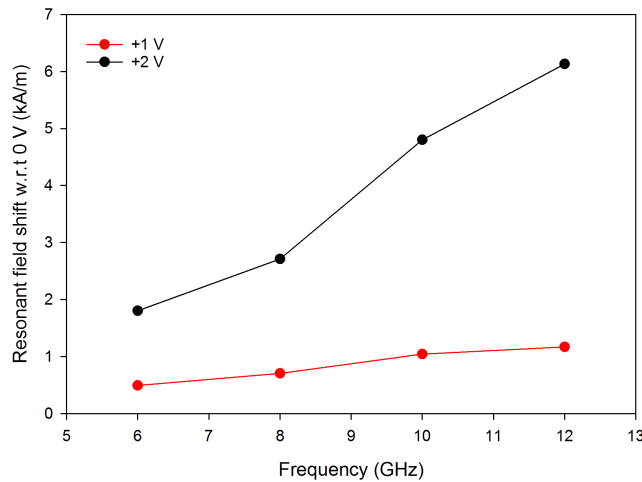
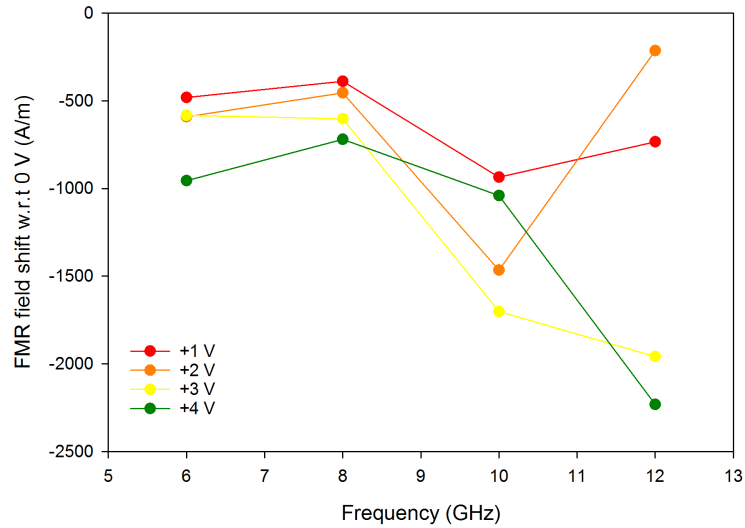*Figure 7.7: Resonant field shift with respect to 0 V sample as a function of frequency for 5 nm permalloy in electrochemical cell for a sequence of voltages*
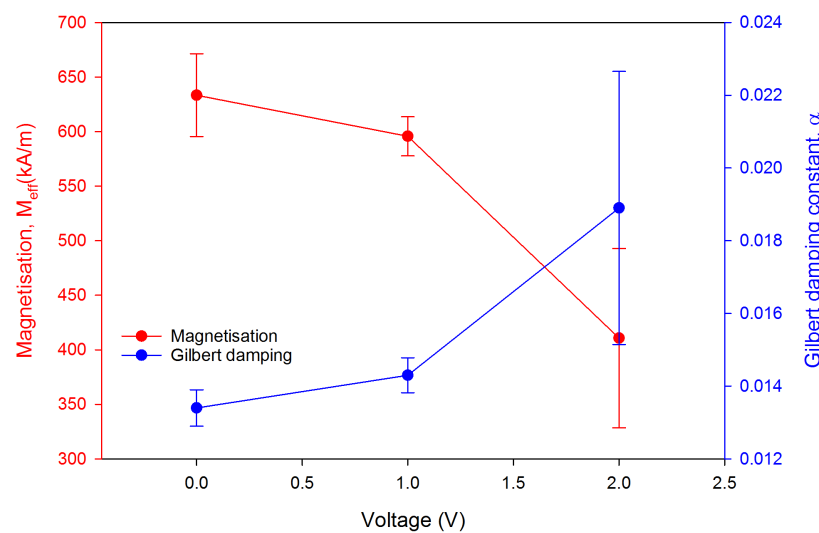
Figure 7.8: Magnetisation, M_{eff} and Gilbert damping constant as a function of applied voltage to a 5 nm permalloy film in an ionic liquid cell.

175

The measurement was repeated on a fresh 5 nm sample of permalloy with the maximum voltage magnitude capped at 2 V and field sweeps taken only at 8 GHz. This reduced the overall sample exposure time and allowed the negative voltage dependence on magnetisation to be explored. While this single frequency approach reduces the time, it unfortunately also removes the ability to calculate the magnetisation. As demonstrated in figures 7.1 & 7.7 it is possible to determine whether the magnetisation is increasing or decreasing depending on the direction of shift in resonant magnetic field. Figure 7.9 shows the raw data for the key voltage values and a clear shift in the resonant spectra is observed. Applying a Lorenztian fit to symmetricise the data adds further weight to this argument in figure 7.10, which shows a positive field shift for a positive voltage i.e. decrease in magnetisation, upon reversing to -2 V a negative field shift was observed (Figure 7.11). This suggests reversible control of magnetisation, agreeing with the MOKE and VSM data described in Chapter 5.
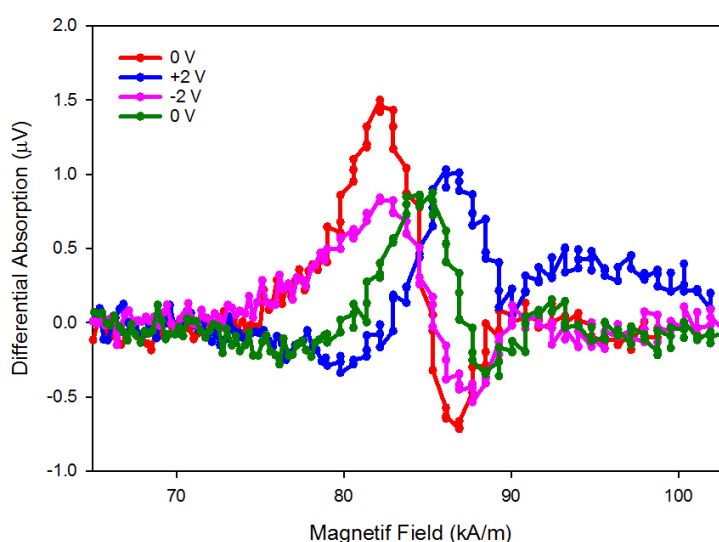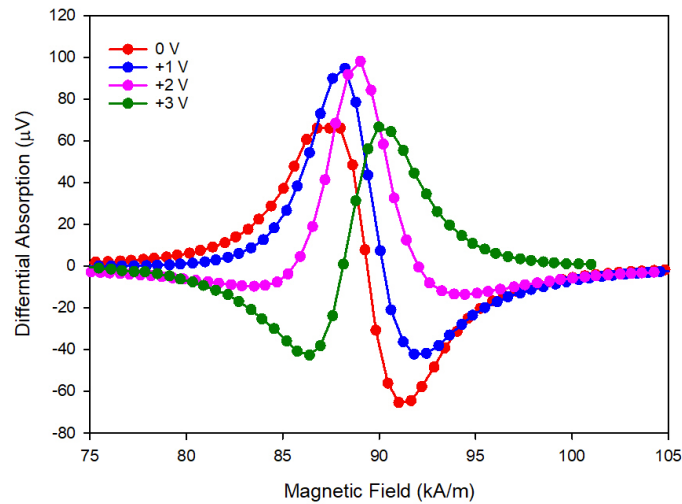

Figure 7.9: Raw in situ FMR spectra at 8 GHz for 5 nm permalloy in electrochemical cell for a sequence of voltages 0 V > +2 V > -2 V > 0V.
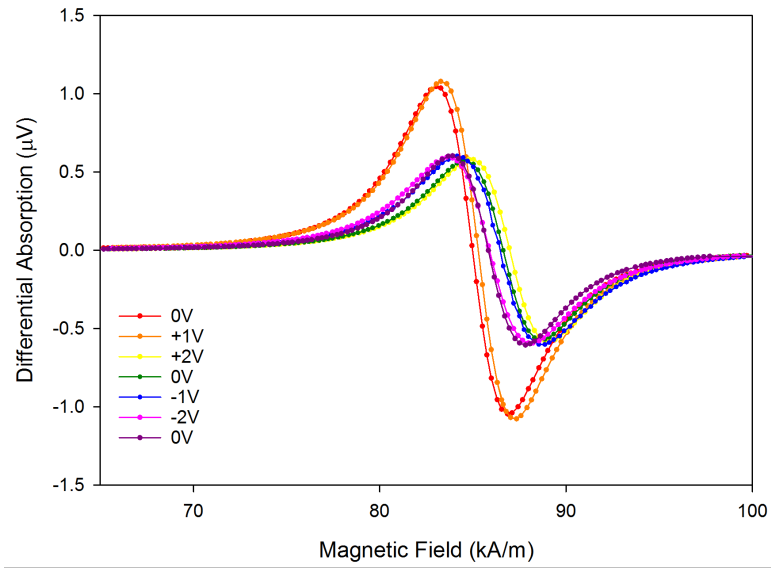
Figure 7.10: Processed (symmetricised and fit to a Lorentzian curve) in situ FMR spectra at 8 GHz for 5 nm permalloy in electrochemical cell for a sequence of voltages 0 V > +2 V > -2 V > 0V.
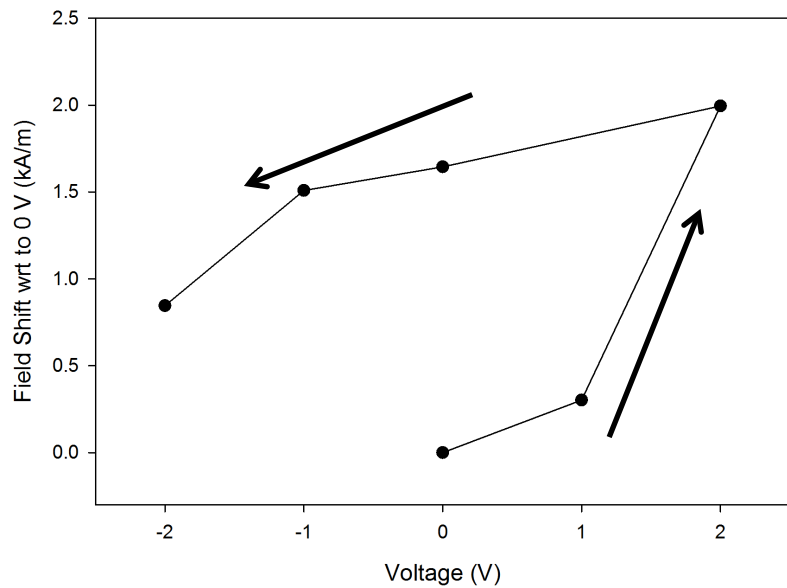
Figure 7.11: Shift in resonant field with respect to 0 V, as a function of voltage applied in situ to a 5 nm permalloy film within the electrochemical cell.

On a fresh 5 nm permalloy film the experiment was repeated but this time with a negative voltage applied first before switching the voltage polarity. The measurement

frequency was again kept at a constant 8 GHz while the magnetic field was swept for each voltage value. Figure 7.12 shows the raw FMR data, where a change in signal intensity and field shift was observed. Once again the data was symmetricised and fit to a Lorentzian curve, the processed data can be seen in Figure 7.13.
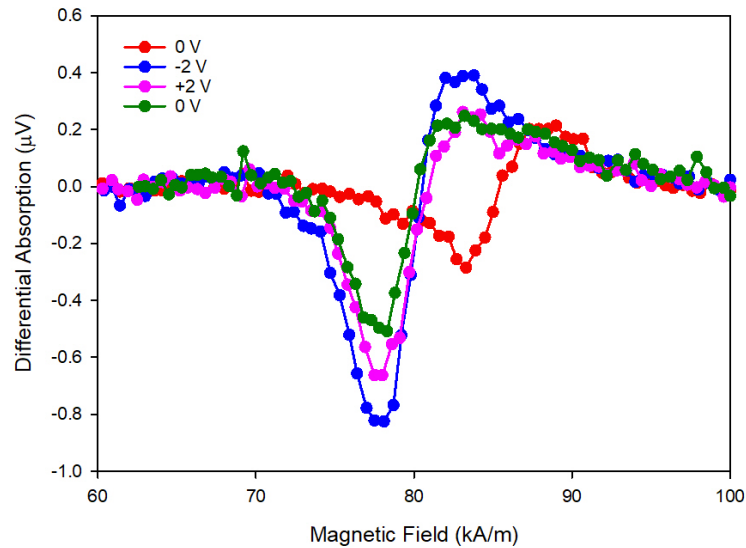
Figure 7.12: Raw in situ FMR spectra at 8 GHz for 5 nm permalloy in electrochemical cell for a sequence of voltages 0 V > -2 V > +2 V > 0V.
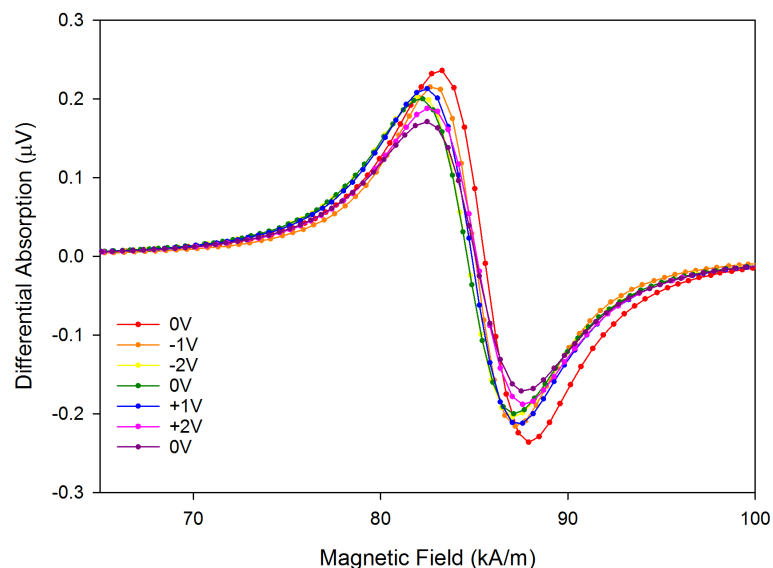
Figure 7.13: Processed (symmetricised and fit to a Lorentzian curve) in situ FMR spectra at 8 GHz for 5 nm permalloy in electrochemical cell for a sequence of voltages 0 V > -2 V > +2 V > 0V.

These data show a negative shift in resonant field when a negative voltage was applied (Figure 7.14). The resonant field shift subsequently increases from the value at -2 V. These data suggest that applying a negative voltage to the permalloy cell increased the film's magnetisation. This could be attributed to a negative voltage reducing oxidised material at the surface and thus increase interactions between magnetic moments.
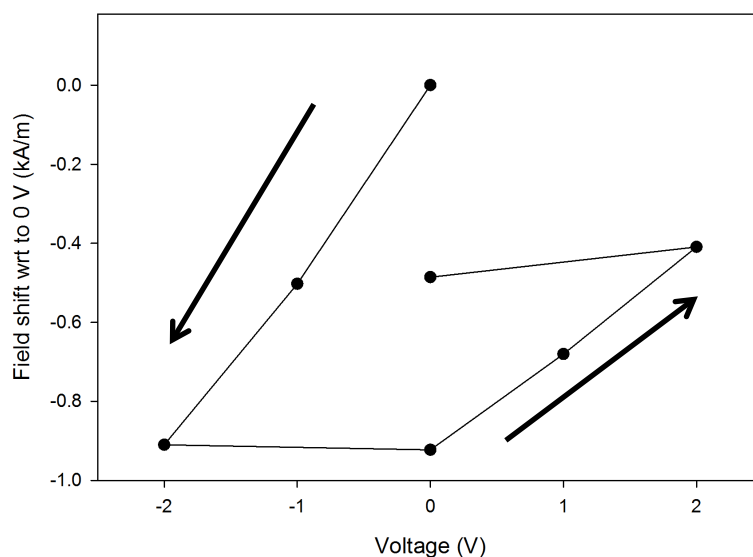
Figure 7.14: Shift in resonant field of a 5 nm permalloy film in an electrochemical cell with applied voltage with respect to 0 V sample.

The absorption by the film of the microwave excitations could be monitored over this period (Figure 7.15) and revealed changes in the absorption following a change in applied voltage. These abrupt changes in absorption suggest that initial changes take place quickly. These are likely to be surface changes and followed by the chemical changes at deeper levels that are responsible for the changes in magnetic behaviour seen over minutes of applied voltage described in Section 5.4.
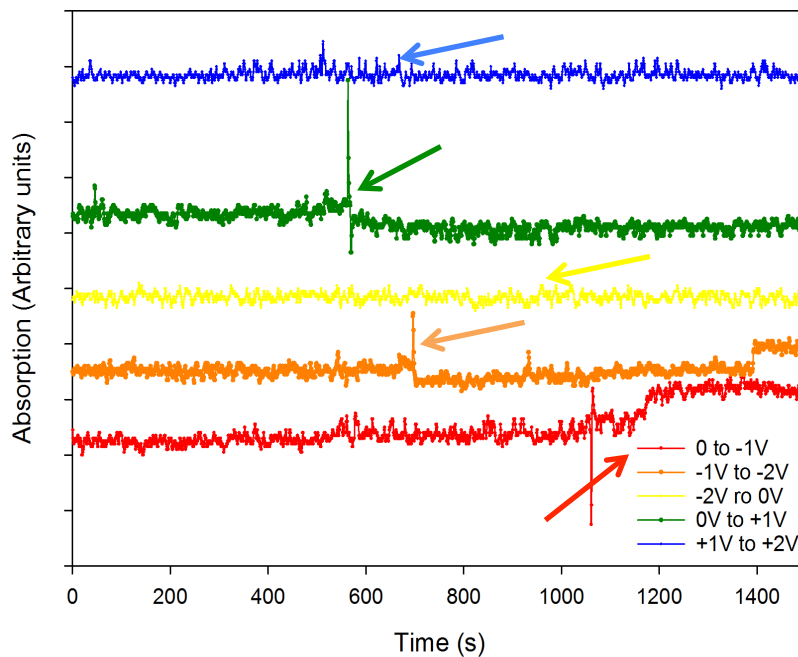
Figure 7.15: Change in microwave absorption as a function of time with voltages applied to 5 nm permalloy in electrochemical cell, with arrows indicating when voltage was applied.

To observe how thicker samples behaved under voltage exposure, 10 nm and 50 nm thick permalloy films were investigated. The 10 nm thick films were measured at multiple frequencies to enable the calculation of the magnetisation. Figure 7.16 shows the raw FMR data at 10 GHz, in these measurements there was significant drifting the absorption, this has been accounted for and removed from the spectra. However, in some cases the signal drift was more complicated and therefore there are differences for the baseline signal. At +4 V the FMR signal is significantly weakened due to severe oxidation of the permalloy film. The processed FMR traces showed a negative shift in resonant field of approximately -2 kA/m for a positive voltage up to +3 V (Figure 7.17 & 7.18). This is the opposite of the effect observed on the thinner, 5 nm permalloy samples (Figure 7.7). At +4 V the field shifts in the positive direction, suggesting a different interaction taking place or an oxidation similar to that in the 5 nm films. Calculating the

magnetisation for the 10 nm samples shows the magnetisation steadily increasing for increasing positive voltage, a 17% increase from the value at 0 V to approximately 680 kA/m (Figure 7.19). This increase in magnetisation could be due to an increase in ferromagnetic film thickness or the appearance of an Fe rich layer, which was suggested by XPS in chapter 6.2.

Figure 7.16: Raw in situ FMR spectra at 10 GHz for 10 nm permalloy in electrochemical cell for a sequence of voltages 0 V > +1 V > +2 V > +3 V > +4 V.
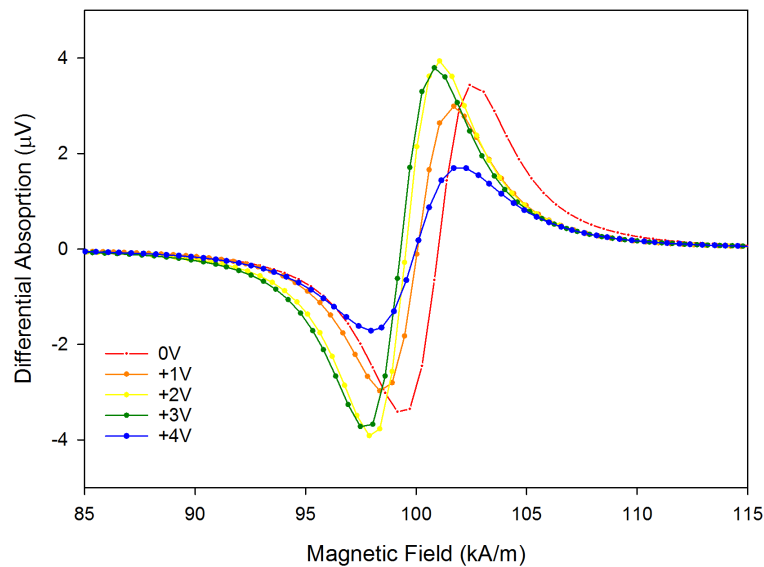
Figure 7.17: Processed (symmetricised and fit to a Lorentzian curve) in situ FMR spectra at 10 GHz for 10 nm permalloy in electrochemical cell for a sequence of voltages 0 V > +1 V > +2 V > +3 V > +4 V.

181

Figure 7.18: Shift in resonant field with respect to 0 V sample as a function of frequency, for 10 nm permalloy film in electrochemical cell for a sequence of voltages 0 V > +1 V > +2 V > +3 V > +4 V.
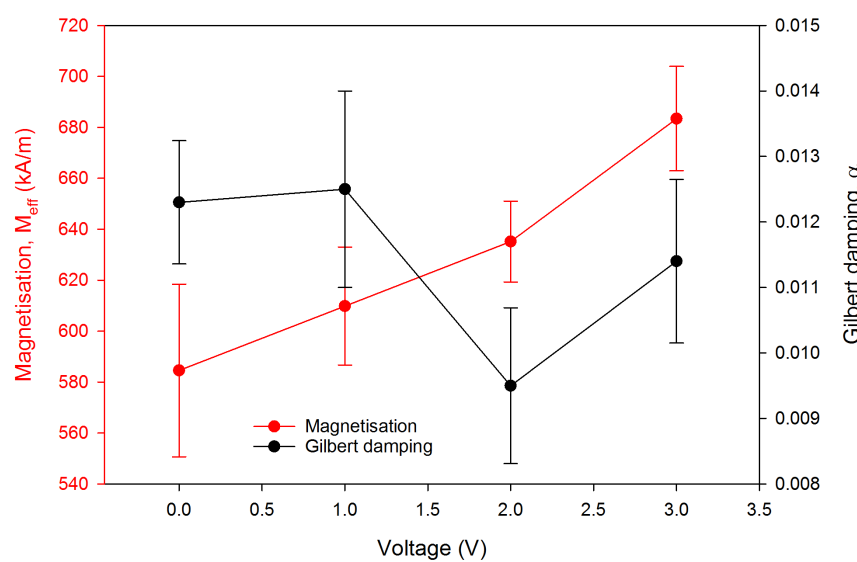
Figure 7.19: Magnetisation and Gilbert damping 10 nm film of permalloy in electrochemical cell for the sequence of voltages 0 V > +1 V > +2 V > +3 V > +4 V.

Calculated values of the Gilbert damping of the 10 nm films (Figure 7.19) shows a minor decrease at +2 V followed by a recovery at +3 V. Kobayashi *et al*[6]. have shown a similar thickness dependence of Gilbert damping in permalloy films, that attributed the changes at thinner films to lattice mismatch to the sample substrate.

182

Figure 7.20: Raw in situ FMR spectra at 9 GHz for 50 nm permalloy in electrochemical cell for a sequence of voltages 0 V > +1 V > +2 V > +3 V.

FMR measurements of the 50 nm thick permalloy films resulted in clear shifts in FMR field but also interesting changes in the absorption reading caused by signal mixing (Figure 7.20). Processing the data by symmetrising and fitting to a Lorentzian, it was possible to see a more accurate measure of the resonant field a in reduction in resonant fields with increasing positive voltages (Figure 7.21). This is accompanied by an increase in magnetisation (Figure 7.22), as with the 10 nm films. Also interesting to note is that the maximum resonant field shift and fractional changes in magnetisation were proportional to film thickness. This suggests the changes are a function of film thickness and may result from surface effects.
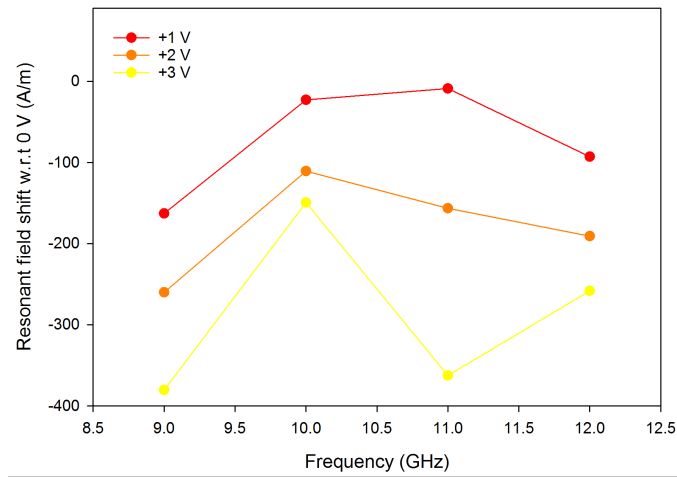
Figure 7.21: Resonant field shift for a range of frequencies for 50 nm permalloy film in the voltage sequence 0 V > +1 V > +2 V > +3 V

Using the data from the FMR spectra the magnetisation was calculated and is plotted against voltage (Figure 7.22). The magnetisation is shown to increase with increasing positive voltage, similar to the 10 nm sample. Plotting the magnitude of the percentage change in magnetisation against the inverse of the thickness (Figure 7.23) shows a linear response indicating the electrochemical effects are only effective at the surface.
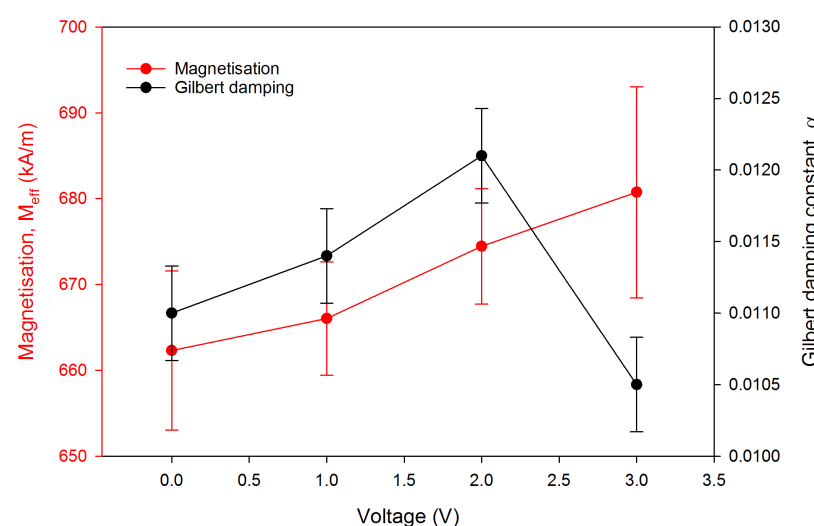
Figure 7.22: Magnetisation and Gilbert damping of 50 nm permalloy film in electrochemical cell under the voltage sequence 0 V > +1 V > +2 V > +3 V

Gilbert damping calculated from the fundamental FMR mode is shown to increase for a positive voltage for the 50 nm permalloy with a sharp drop at +3 V (Figure 7.22). This is contrary to the 10 nm data, and which along with the XPS data could suggest an oxidation-induced increase in damping.
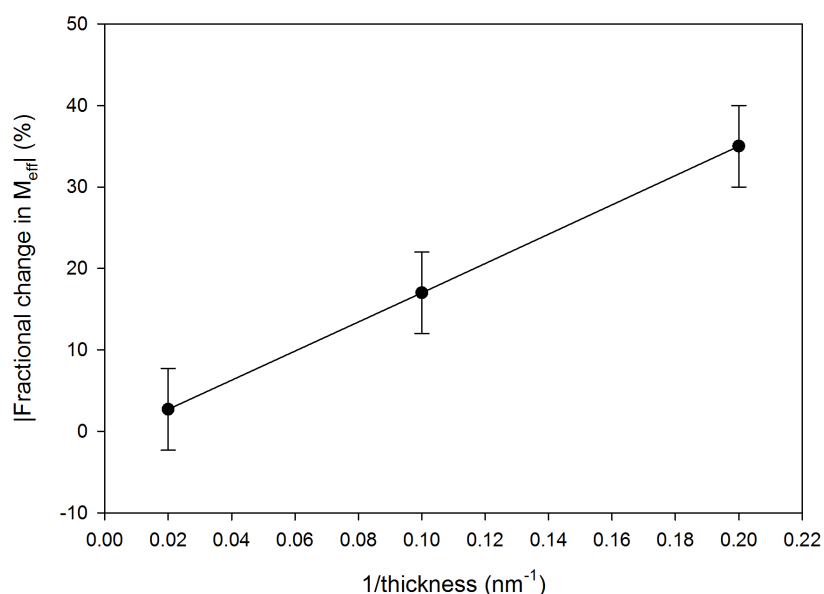
Figure 7.23: Magnitude of fractional change as a function of the inverse thickness of permalloy after exposure to a voltage in electrochemical cell

7.4 In situ ferromagnetic spectroscopy of $Ni_{80}Fe_{20}$ films for high order modes

Section 2.5.2 described how higher order spin waves can be observed at thicker film thicknesses. Modes corresponding to these could be observed from the 50 nm films at resonances greater than 9 GHz (Figure 7.24 & Figure 7.25), these are termed perpendicular standing spin wave modes. The higher order standing spin waves are more sensitive to surface effects than the normal ferromagnetic mode and have much lower resonant magnetic fields than bulk FMR. Figure 7.26 demonstrates the field shift in the first order standing spin wave with applied voltage, higher order modes could not be observed. The field shift is much larger than the fundamental mode; this is attributed to

the surface sensitivity of the first order mode. The large scatter of values at +3 V are attributed to a long exposure time damaging the film.
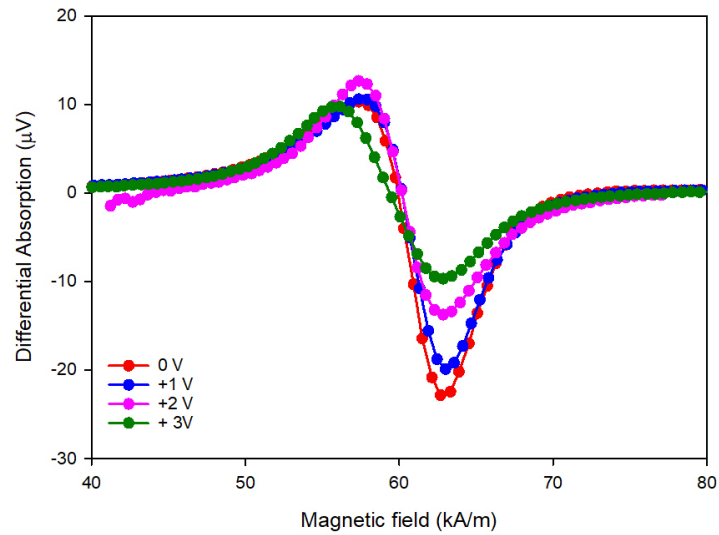
Figure 7.24: Raw in situ FMR spectra of the 1st order standing spin wave at 11 GHz for 50 nm permalloy in electrochemical cell for a sequence of voltages 0 V > +1 V > +2 V > +3 V.
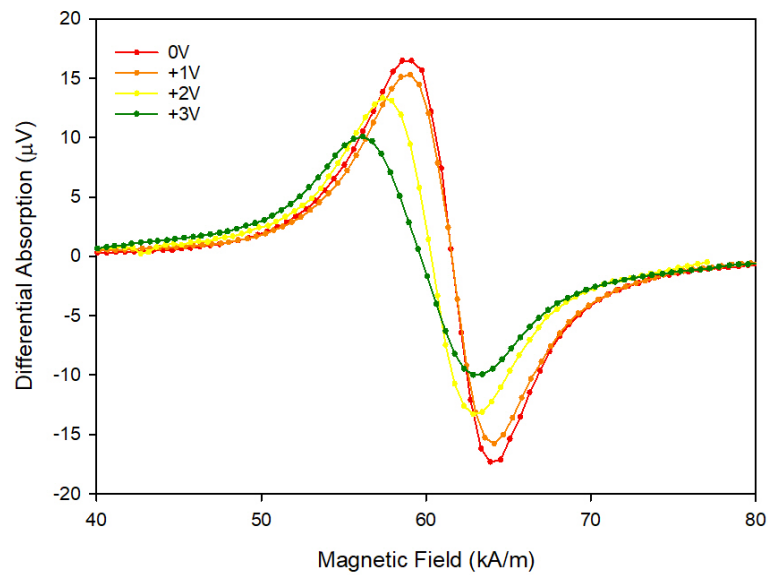
Figure 7.25: Processed (symmetricised and fit to a Lorentzian curve) in situ FMR spectra of the 1st order standing spin wave at 11 GHz for 50 nm permalloy in electrochemical cell for a sequence of voltages 0 V > +1 V > +2 V > +3 V.
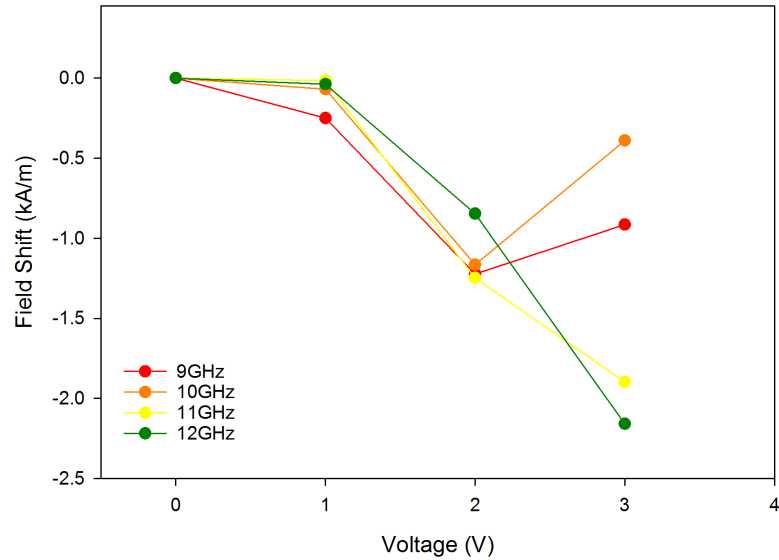
Figure 7.26: First order standing spin wave resonant field shift with increasing positive voltage for 50 nm permalloy film within electrochemical cell.

Using the Kittel equation for first order standing spin waves magnetised in plane (2-20) provides another route to calculating the magnetisation of the permalloy film. This was attempted using an exchange stiffness constant = 1.3×10^{-11} Jm^{-1}, mode number n =1 and film thickness d = 50 x 10^{-9} m. However the result did not fit the Kittel equation. By varying the film thickness in (2-21) the data was refit and the magnetisation calculated (Figure 7.27). Comparing the magnetisations to those calculated for the fundamental mode (Figure 7.27) suggest a permalloy thickness between 43-44 nm at 0 V. This is due to an oxidation of the film after removal of the film from the evaporation chamber, a thinner than expected film was also demonstrated using VSM for 5 nm films (Section 5.5). The large change in magnetisation for small changes in thickness make it unreliable for calculating thickness changes at increased voltages, however an increase in magnetisation suggests an increase in film thickness.
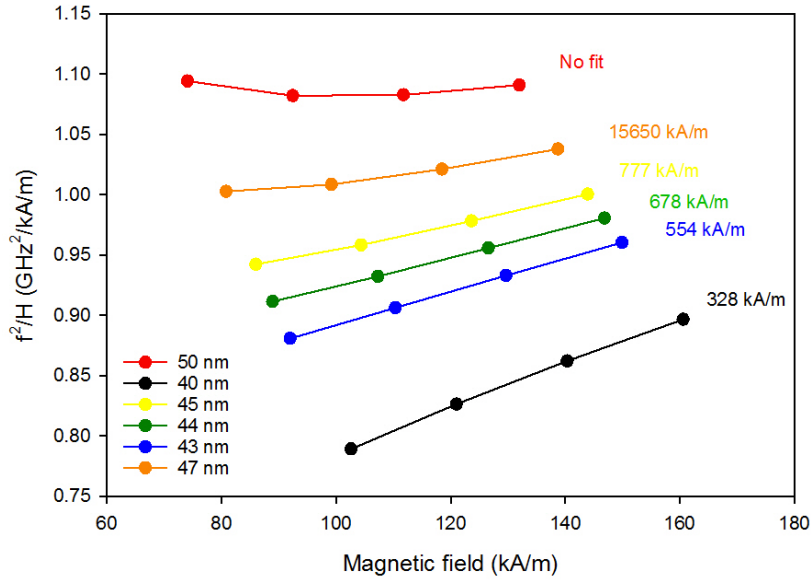
Figure 7.27: Kittel fits for first order SSWM for permalloy film in experimental cell, with varying film thicknesses and magnetisations calculated.

Using the 0 V data form the FMR spectra for the 5 nm, 10 nm and 50 nm it is possible to calculate the M_s and surface anisotropy of the films (7.28), from the gradient and y intercept using equation (4-8). Calculation showed that $M_S = 702.8 \pm 28.2$ kA/m and $K_S = 0.45 \pm 0.0675$ mJ/m^2. The magnetisation value here is much lower than that of permalloy, but agrees This suggests that the films are not $Ni_{80}Fe_{20}$ and may be richer in Ni, thus creating a reduced magnetisation in the films. The surface anisotropy is substantial and has a profound effect on the magnetic properties of the films. It is possible that the applied voltage is varying this term and thus generating the changes in M_{ef} observed throughout the FMR data.
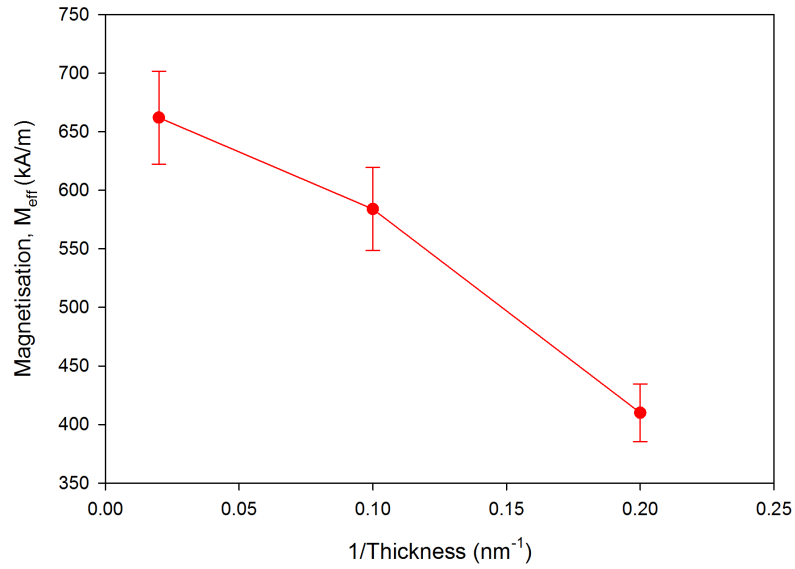
Figure 7.28: Effective magnetisation as function of the inverse of film thickness for calculation of saturation magnetisation.

The separate surface and bulk contributions from the surface and bulk to Gilbert damping can also be extracted from 0 V data (Figure 7.29) by using equation (4-10). Where these values are $\alpha_S = 0.0237 \pm 0.0009$ and $\alpha_B = 0.0108 \pm 0.0012$. This indicates again that surface has a large influence on the magnetic dynamics of thin films of permalloy. Unfortunately, it was not possible to obtain a measure of these values with voltage variation.
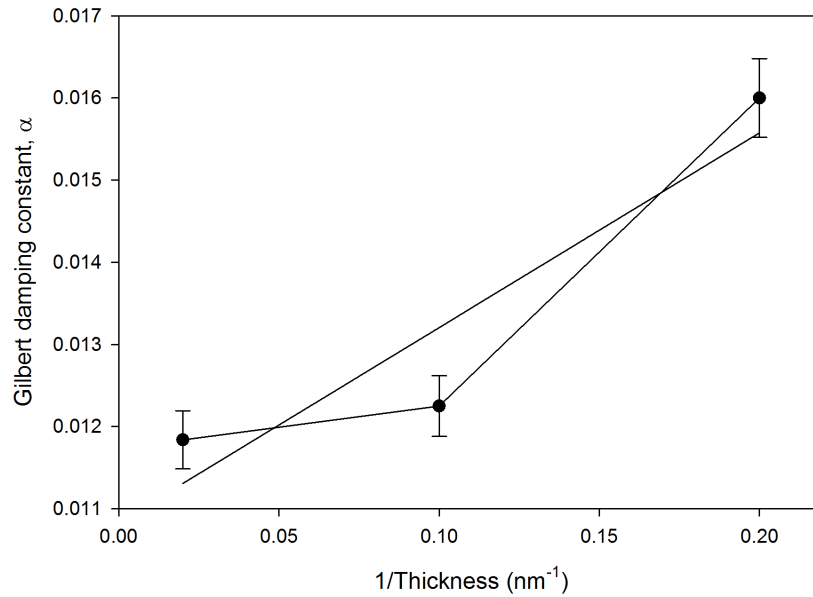
Figure 7.29: Gilbert damping constant vs. inverse of thickness for surface gilbert damping and bulk gilbert damping.

7.5 Conclusion

This chapter has demonstrated the effect of electrochemical voltage on FMR of permalloy films. Upon application of low voltages to a 5 nm permalloy film inside an electrochemical cell large decreases in magnetisation were demonstrated, these changes were then reversed by switching the voltage polarity applied to the film.

Investigating thicker permalloy films of 10 nm and 50 nm demonstrated an opposite change in magnetic properties with an applied voltage, i.e. an increase in magnetisation for increasing positive voltage. The changes in magnetisation also showed a thickness dependence of resonant field shift, suggesting that the surface of the film may play an important role in the magnetic properties. These increases in magnetisation are attributed to the production of an Fe rich layer in the film that is not possible in thinner films. The 50 nm thick films also demonstrated a decrease in expected thickness to values close to 44 nm.

The large control over the ferromagnetic resonance field and Gilbert damping factors show huge promise for low power tuneable high frequency magnetic devices.

7.6 References

1. Liu, X., Zhang, W., Carter, M. J. & Xiao, G. Ferromagnetic resonance and damping properties of CoFeB thin films as free layers in MgO-based magnetic tunnel junctions. *J. Appl. Phys.* **110,** (2011).

2. Chen, Y.-C. *et al.* Ferromagnetic resonance study of thickness-dependent magnetization precession in Ni80Fe20 films. *J. Appl. Phys.* **101,** 09C104 (2007).

3. Zhao, Y. *et al.* Experimental Investigation of Temperature-Dependent Gilbert Damping in Permalloy Thin Films. *Sci. Rep.* **6,** 22890 (2016).

4. Shaw, J. M., Nembach, H. T., Silva, T. J. & Boone, C. T. Precise determination of the spectroscopic g -factor by use of broadband ferromagnetic resonance spectroscopy. *J. Appl. Phys. 114,* **243906,** (2014).

5. Seavey, M. H. & Tannenwald, P. E. Ferromagnetic resonance in ultra-thin films. *J. Appl. Phys.* **29,** 292–293 (1958).

6. Kobayashi, K. *et al.* Damping constants for permalloy single-crystal thin films. *IEEE Trans. Magn.* **45,** 2541–2544 (2009).

8. Conclusion

This thesis investigates the voltage control of ferromagnetic properties in thin films of permalloy ($Ni_{80}Fe_{20}$) and Ni. In this research an electrochemical cell was constructed that consisted of a thermally evaporated ferromagnetic film and a commercially available indium-tin oxide (ITO) coated glass slide, these acted as the two electrodes of the cell. These two electrodes were separated by an ionic liquid, 1-Ethyl-3-methylimidazolium bis(trifluoromethylsulfonyl)imide (EMITSFI). Applying low voltages (< |4| V) to the cell generates extremely high-electric fields at the ferromagnet/ionic liquid interface via an electric double layer effect.

Carrying out magneto-optical Kerr effect (MOKE) magnetometry and ferromagnetic resonance (FMR) spectroscopy measurements while applying a voltage demonstrated controllability of coercivity and magnetisation as a function of voltage magnitude, voltage polarity and exposure time. Interestingly FMR spectroscopy of thicker films of permalloy (10 nm – 50 nm) demonstrated the converse magnetisation effect i.e. an increase in magnetisation for increasing voltage. Vibrating sample magnetometry (VSM) of exposed 5 nm permalloy samples demonstrated a decrease in magnetisation with increasing voltage exposure. These magnetic variations were all partially reversible upon switching the voltage polarity and the changes were non-volatile.

X-ray photoelectron spectroscopy (XPS) measurements of 5 nm permalloy films post voltage exposure displayed a voltage dependent oxidation of the films. An increasing voltage showed an increased oxidation signal that indicated the growth of various Ni & Fe oxides. Further, cyclic voltammetry measurements provided electrochemical information about the experimental cell, such as redox potentials and electrochemical window.

Combining these results together suggests a voltage induced thinning/thickening effect of the ferromagnetic film, where the 5 nm permalloy film becomes fully oxidised. In the thicker films it may be possible that an iron rich layer is produced giving rise to the larger magnetisation observed in FMR measurements.

This low power control of ferromagnetic properties shows great potential for applications in magnetic random access memory (MRAM) devices[1], magnetic sensors[2] and high frequency tuneable devices[3,4]. Further research is required to fully characterise these cells for a variety of different magnetic films and thicknesses in order to optimise the process for real life applications. It may be possible to develop prototypical devices to further the field.

8.1 References

1. Apalkov, D., Dieny, B. & Slaughter, J. M. Magnetoresistive Random Access Memory. *Proceedings of the IEEE* **104,** 1796–1830 (2016).

2. Freitas, P. P., Ferreira, R., Cardoso, S. & Cardoso, F. Magnetoresistive sensors. *J. PhysicsCondensed Matter* **19,** 165221 (2007).

3. Kiselev, S. V., Ozerov, R. P. & Zhdanov, G. S. Detection of Magnetic Order in Ferroelectric BiFeO3 by Neutron Diffraction. *Sov. Phys. Dokl.* **7,** 742 (1963).

4. Yao, J. J. RF MEMS from a device perspective. *J. Micromechanics Microengineering* **10,** 9–38 (2000).

Appendix

A1. Survey Spectra
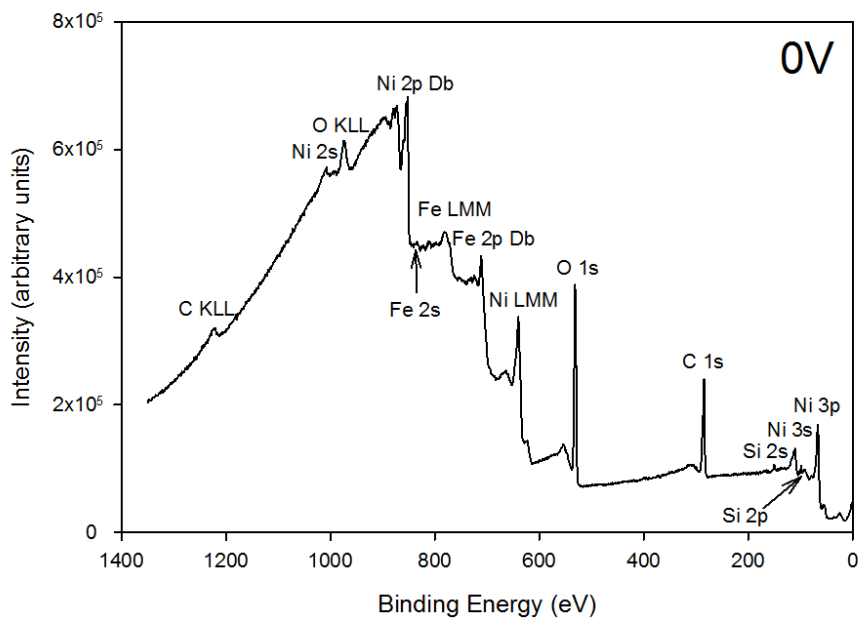
Figure A1.1: XPS survey spectra at 0 V
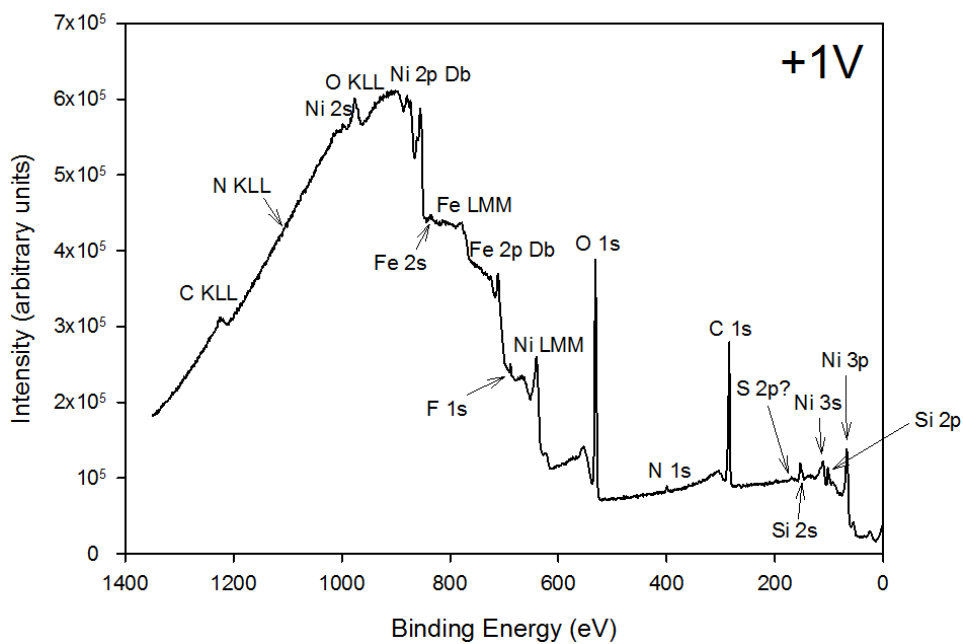
Figure A1.2: XPS survey spectra at +1 V
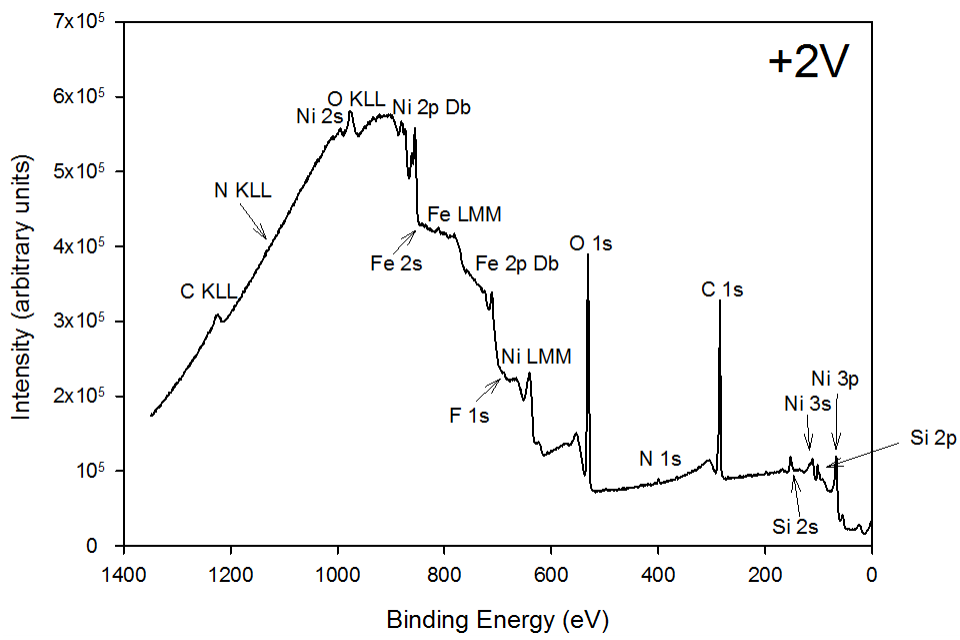
Figure A1.3: XPS survey spectra at +2
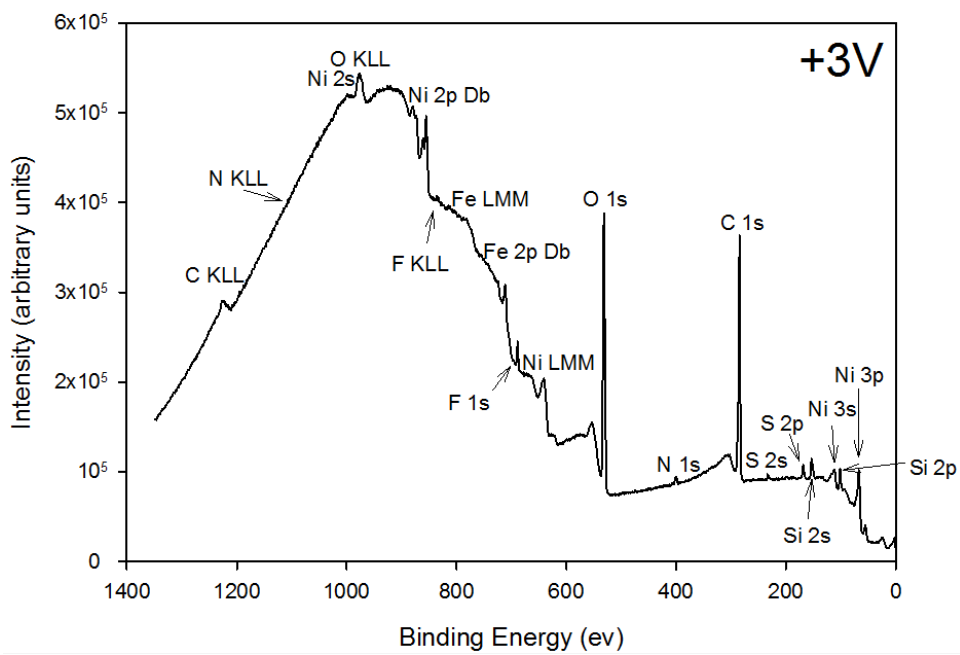
Figure A1.4: XPS survey spectra at +3 V
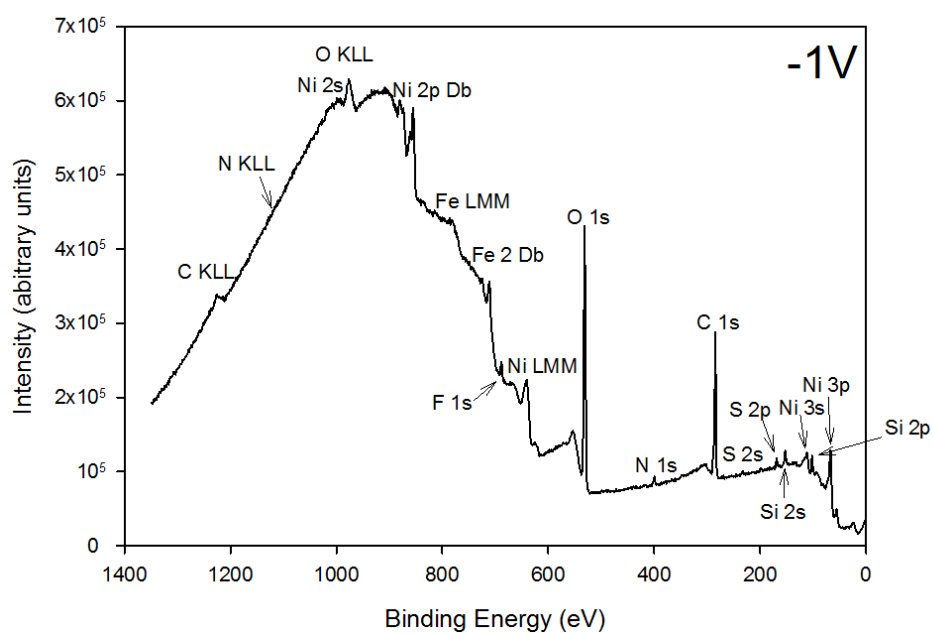
Figure A1.5: XPS survey spectra at -1 V after previous exposure to +3 V
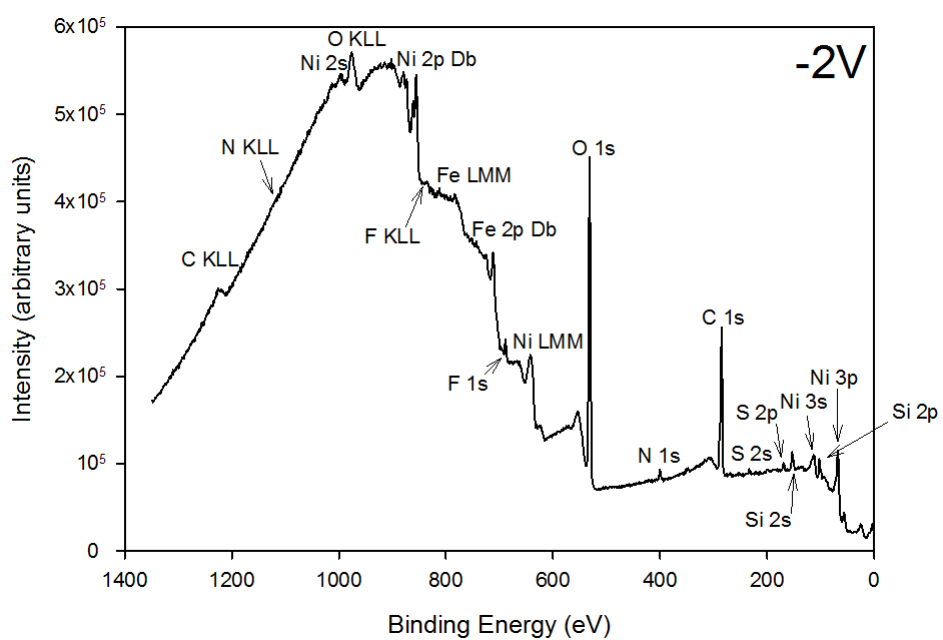
Figure A1.6: XPS survey spectra at -2 V after previous exposure to +3 V

196
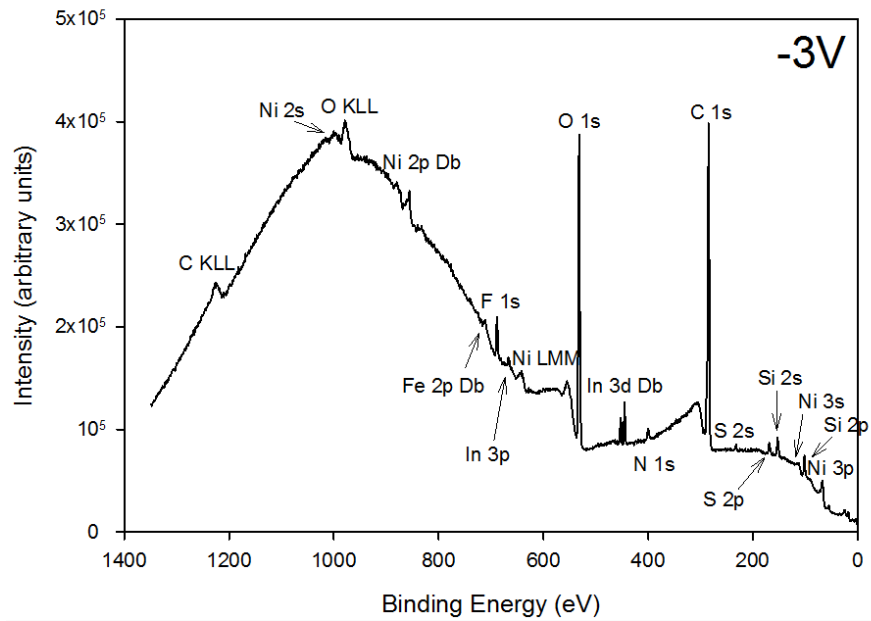
Figure A1.8: XPS survey spectra at -3 V after previous exposure to +3 V
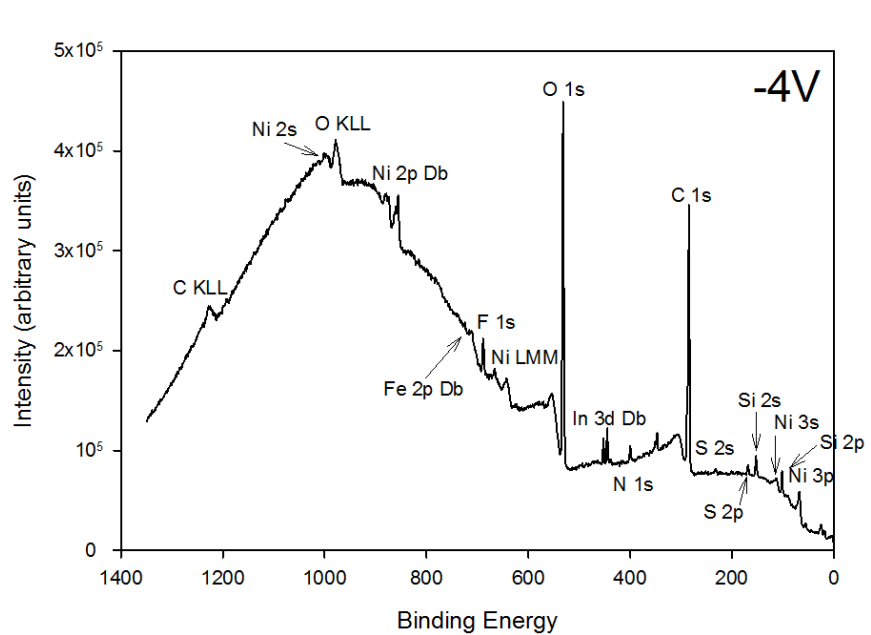
Figure A1.7: XPS survey spectra at -4 V after previous exposure to +3 V

197

A2. C 1s energy range spectra

The carbon 1s energy range spectra (Figure A2.1-2.8) showed stable carbon peaks, indicating that there is little change in the composition of C after voltage exposure. Carbon, therefore, was likely to only have had little or no effect on the change in magnetic properties observed in chapter 5. Figure A2.9 further demonstrates this by showing the relatively constant contribution of the different carbon bonds to the XPS peak.
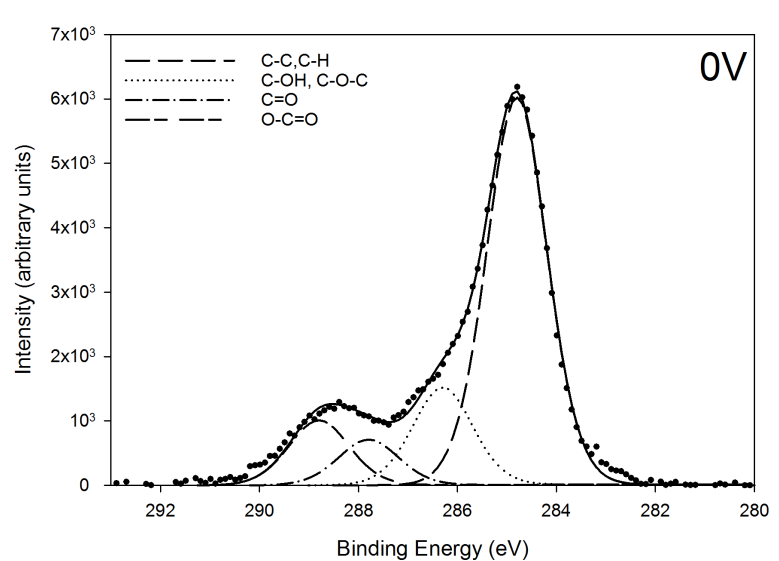
Figure A2.1: Carbon 1s high-resolution spectra at 0 V
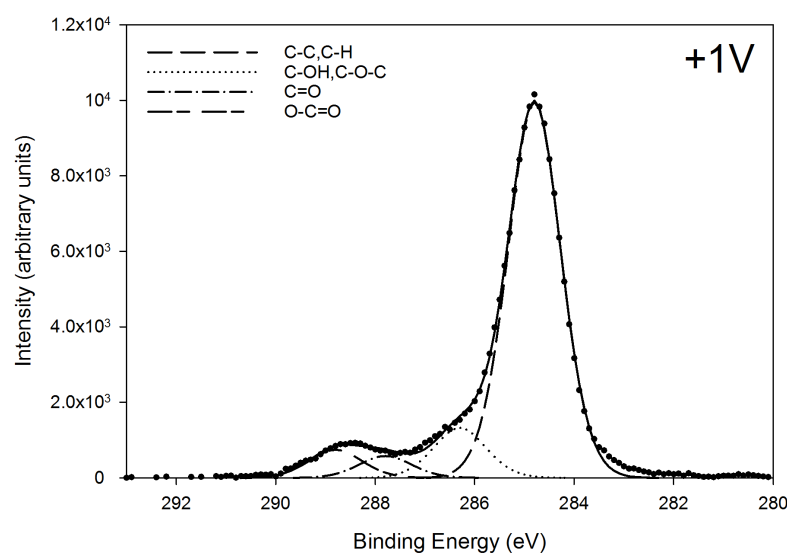
Figure A2.2: Carbon 1s high-resolution spectra at +1 V
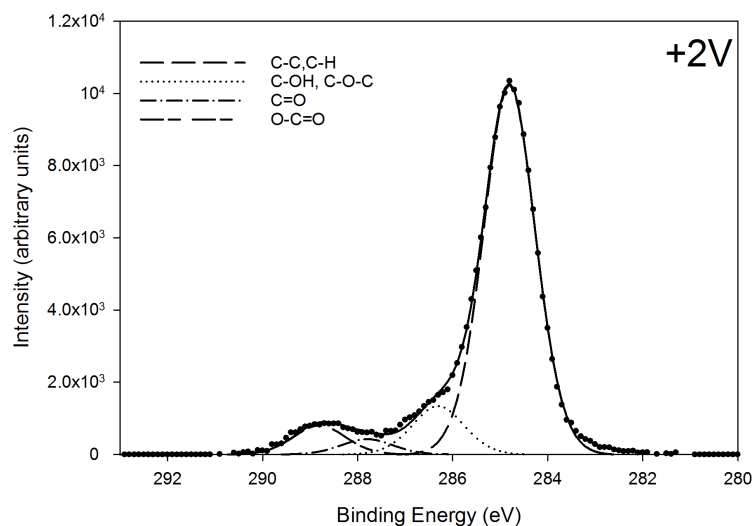
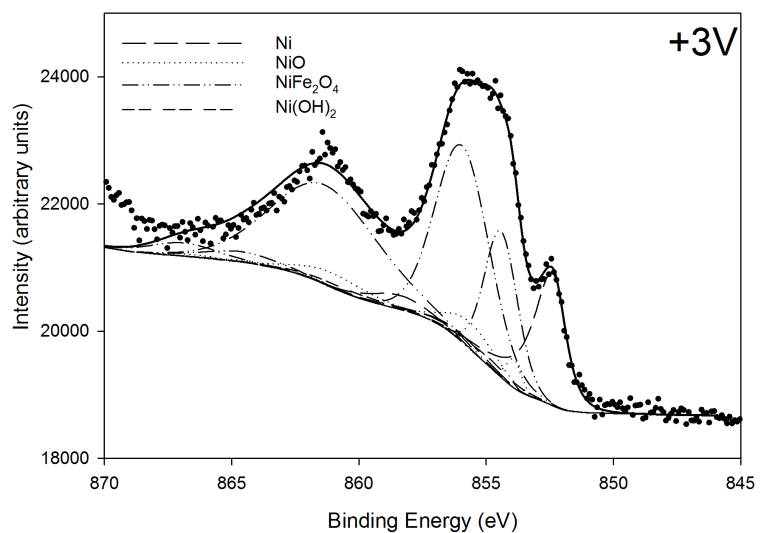*Figure A2.3: Carbon 1s high-resolution spectra at +2 V*
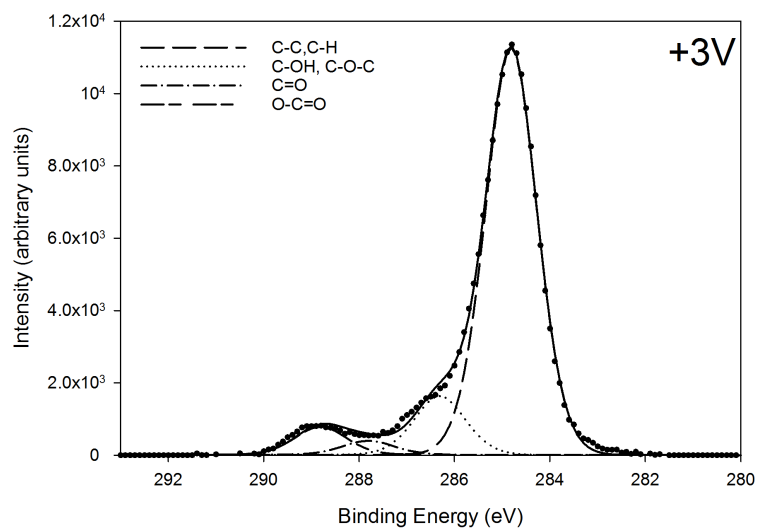
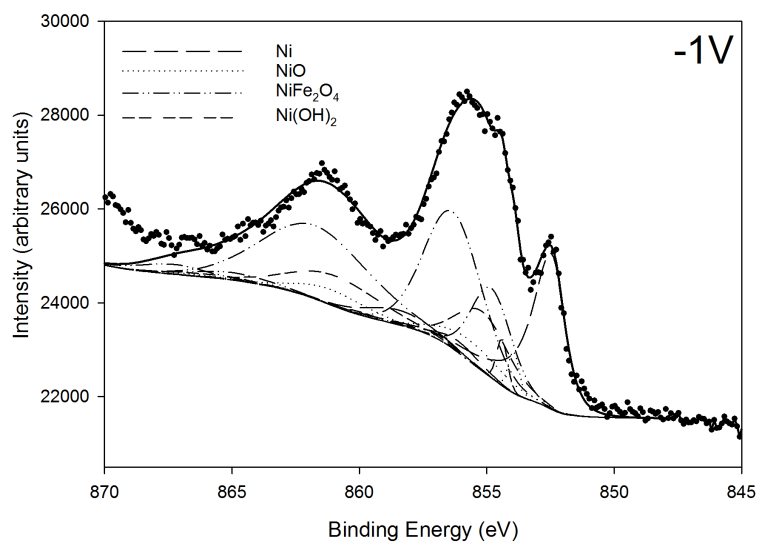*Figure A2.4: Carbon 1s high-resolution spectra at +3 V*
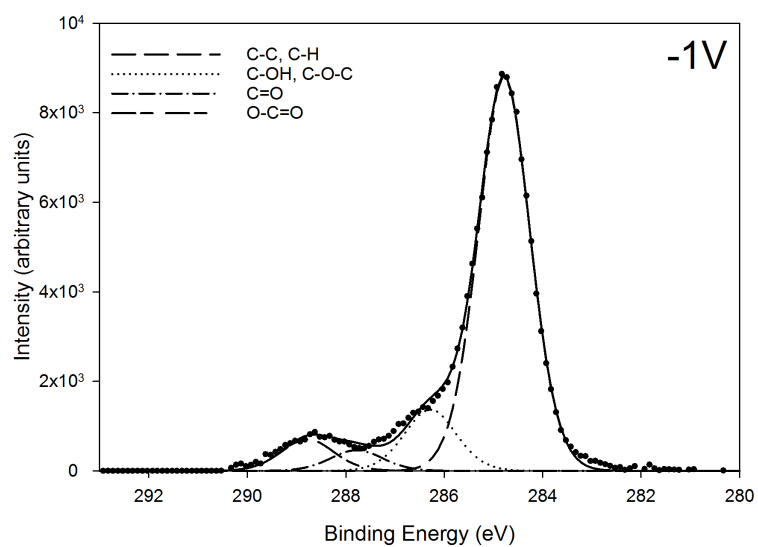
Figure A2.5: Carbon 1s high-resolution spectra at -1 V after previous exposure to +3 V
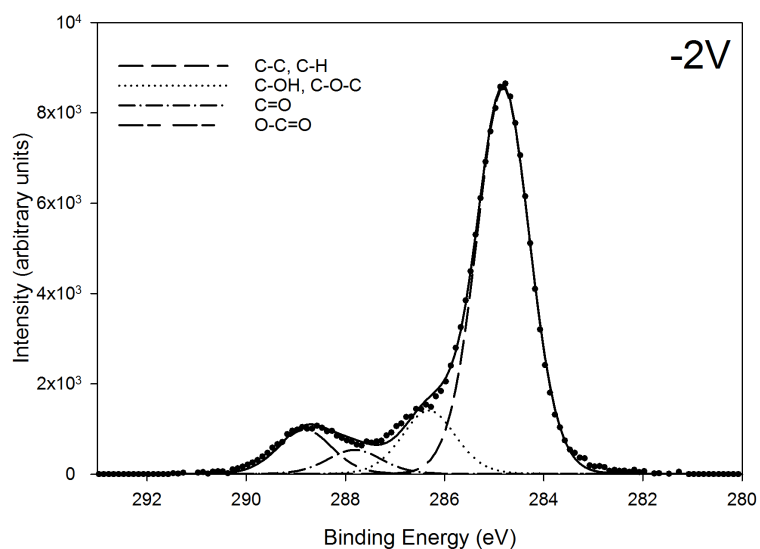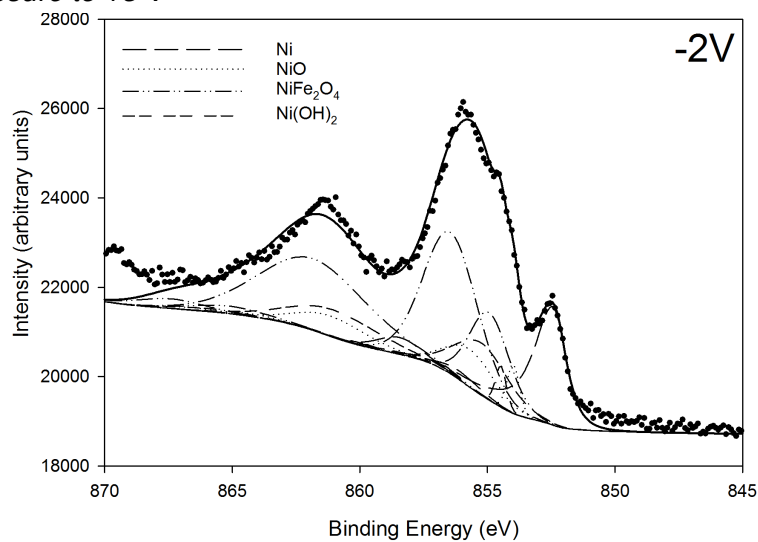
Figure A2.6: Carbon 1s high-resolution spectra at -2 V after previous exposure to +3 V
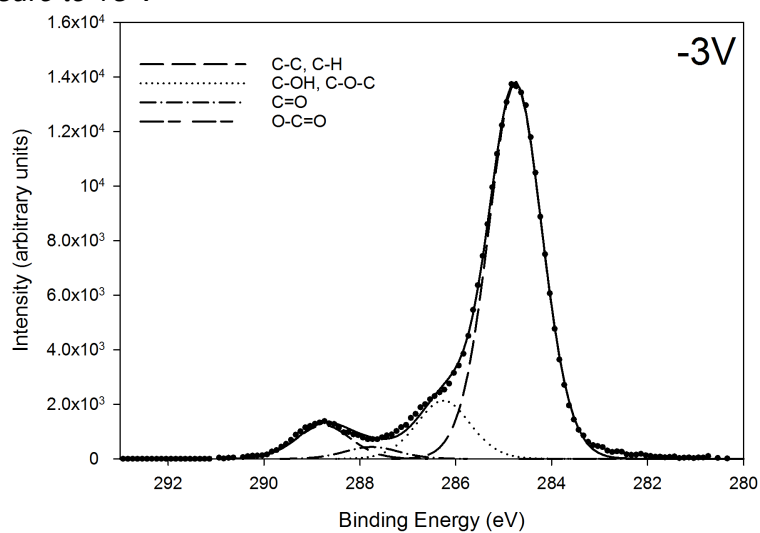
Figure A2.7: Carbon 1s high-resolution spectra at -3 V after previous exposure to +3 V
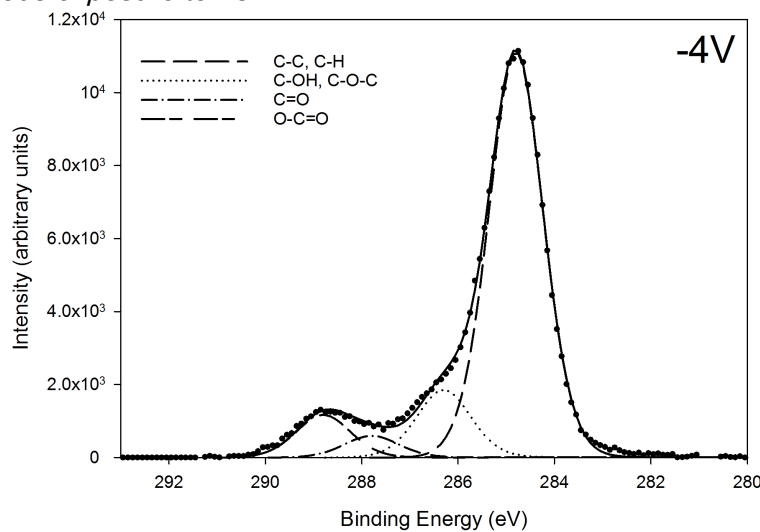
Figure A2.8: Carbon 1s high-resolution spectra at -4 V after previous exposure to +3 V
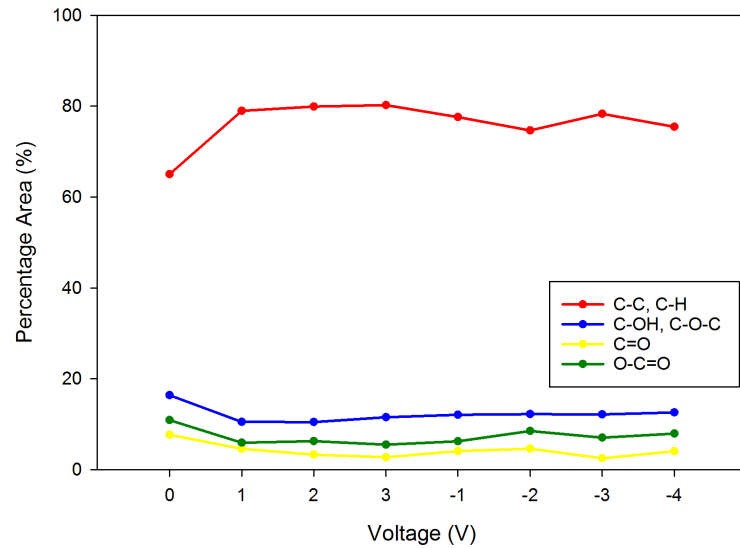
Figure A2.9: Percentage area for different carbon bonds after exposure to voltage sequence, 0 V → +3 V → -4V

A3. O 1s energy range spectra
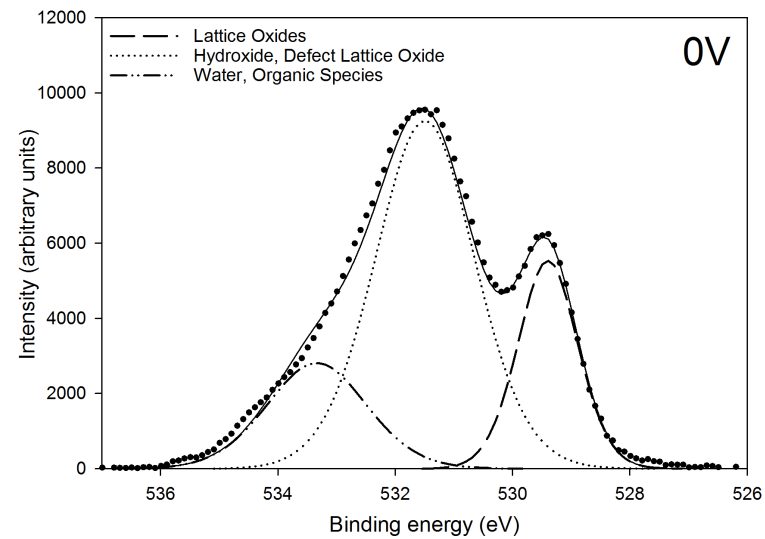
Figure A3.1: Oxygen 1s high-resolution spectra at 0 V
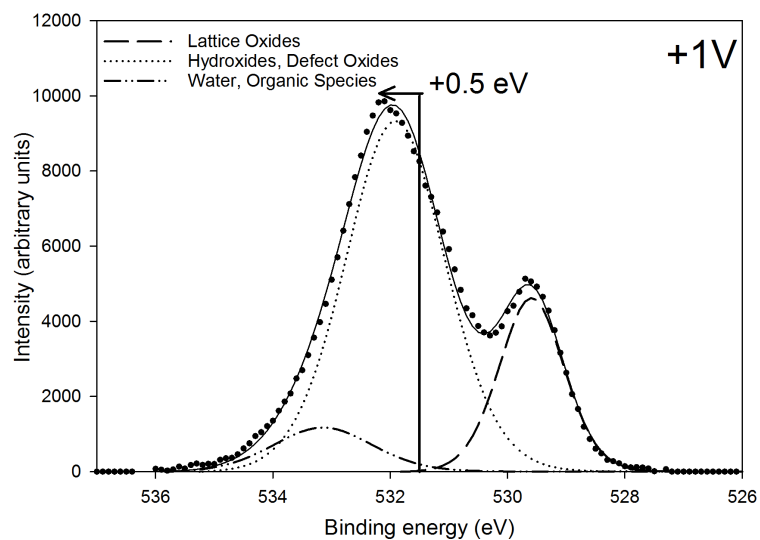
Figure A3.2: Oxygen 1s high-resolution spectra at +1 V
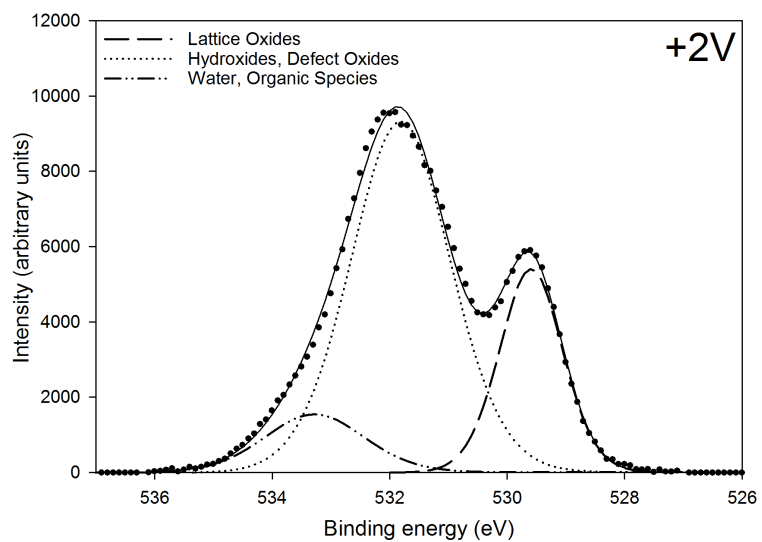
Figure A3.3: Oxygen 1s high-resolution spectra at +2 V
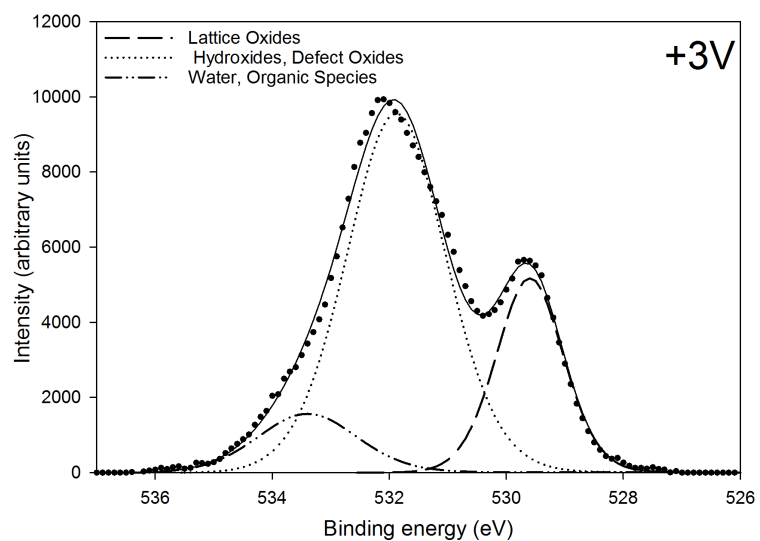
Figure A3.4: Oxygen 1s high-resolution spectra at +3 V
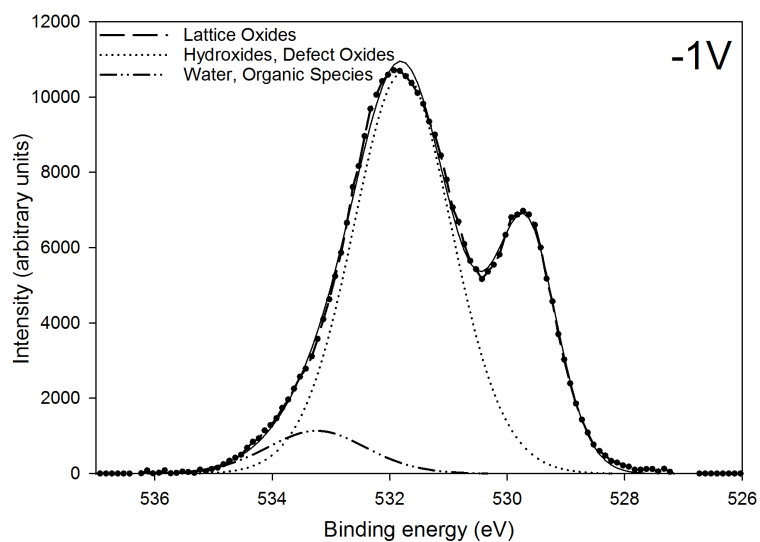
Figure A3.5: Oxygen 1s high-resolution spectra at -1 V, after previous exposure to +3 V
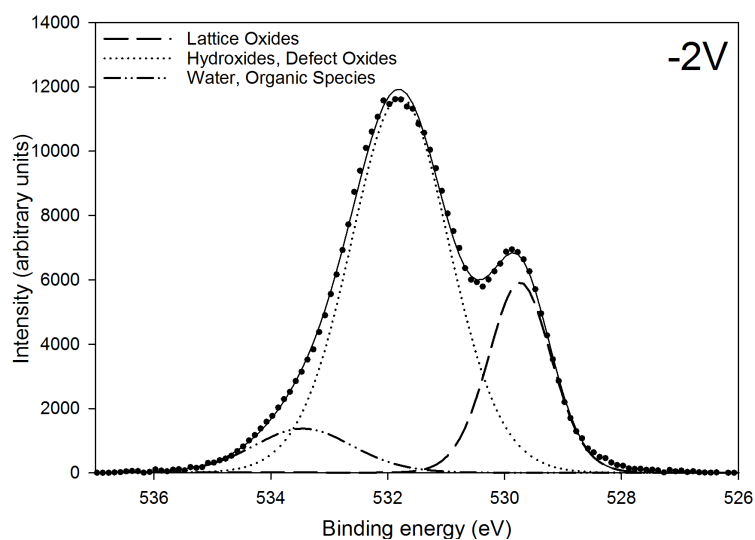
Figure A3.6: Oxygen 1s high-resolution spectra at -2 V, after previous exposure to +3 V
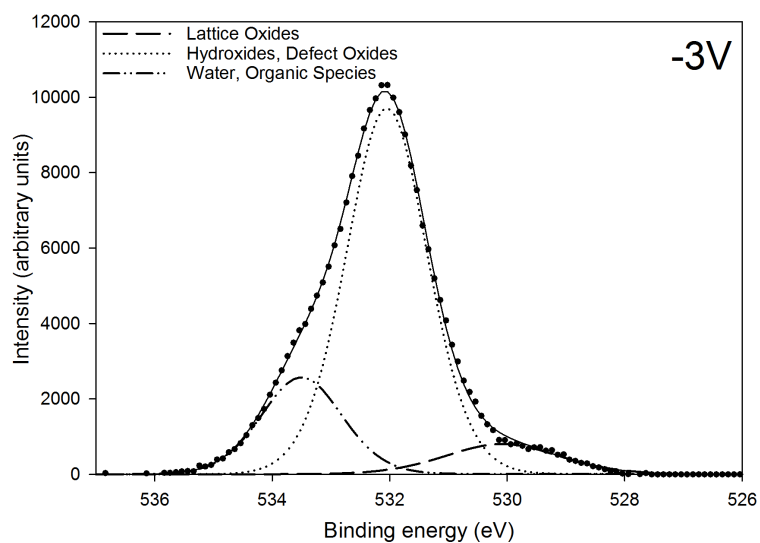
Figure A3.7: Oxygen 1s high-resolution spectra at -3 V, after previous exposure to +3 V
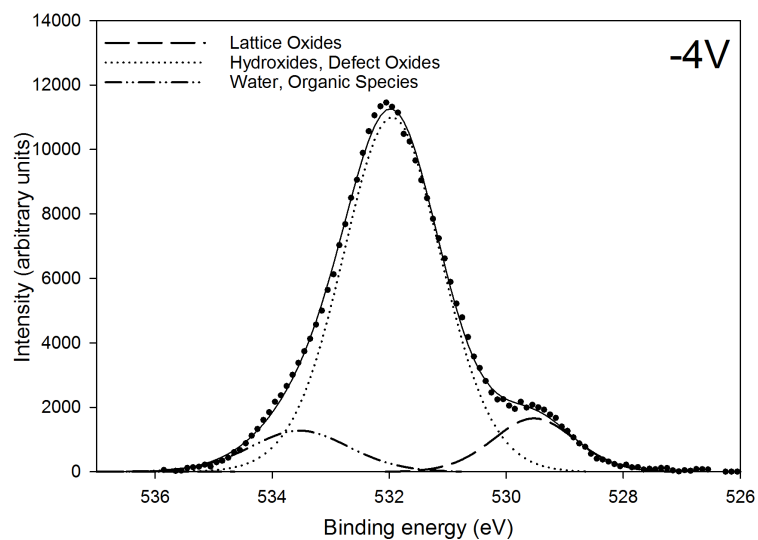
Figure A3.8: Oxygen 1s high-resolution spectra at -4 V, after previous exposure to +3 V
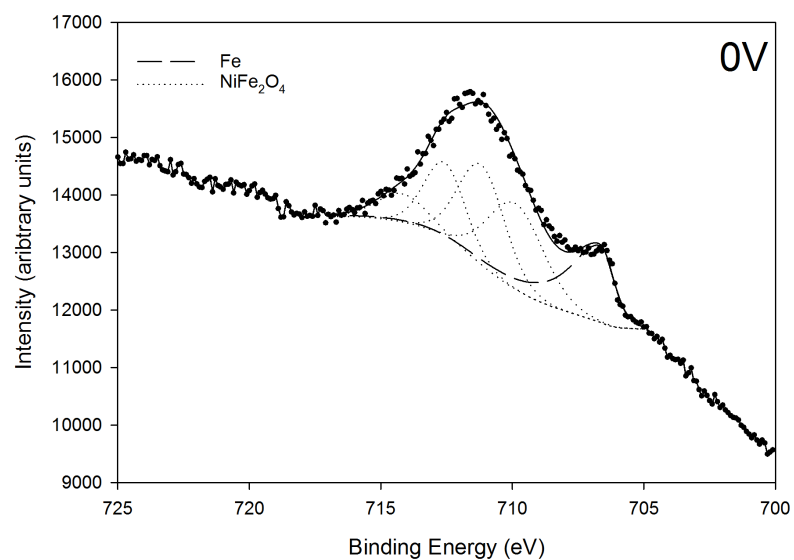
A4. Ni 2p high-resolution spectra
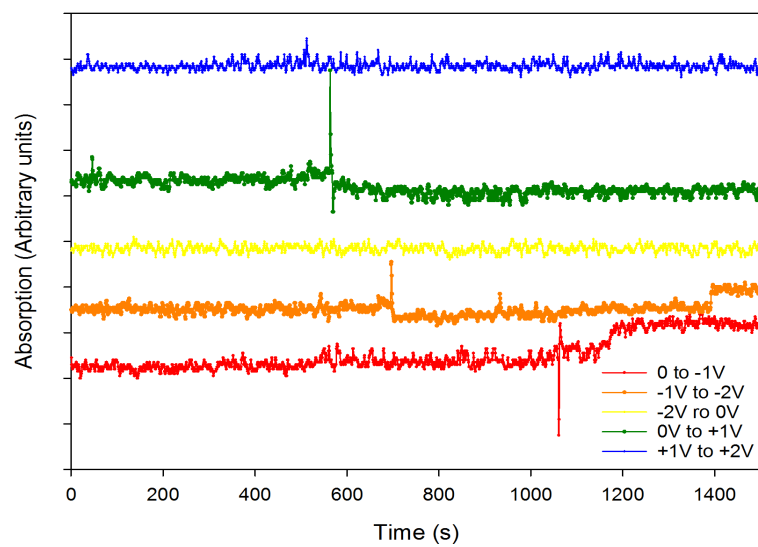
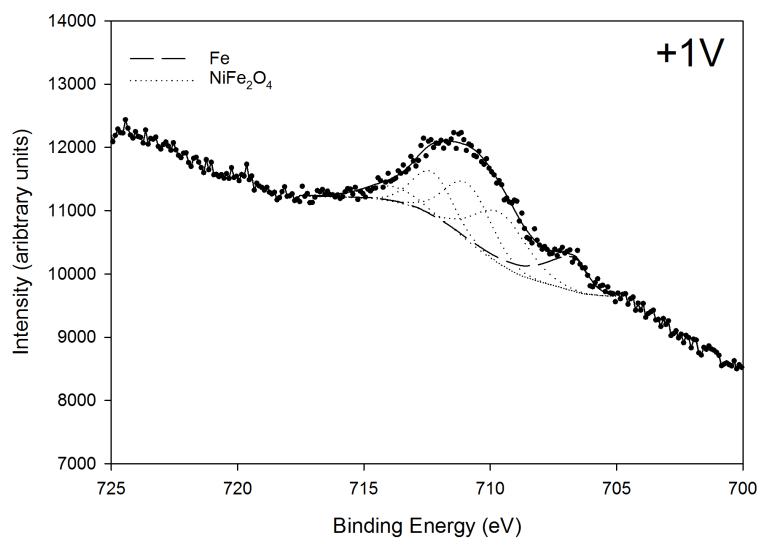*Figure A4.1: Nickel 2p high-resolution spectra at 0 V*
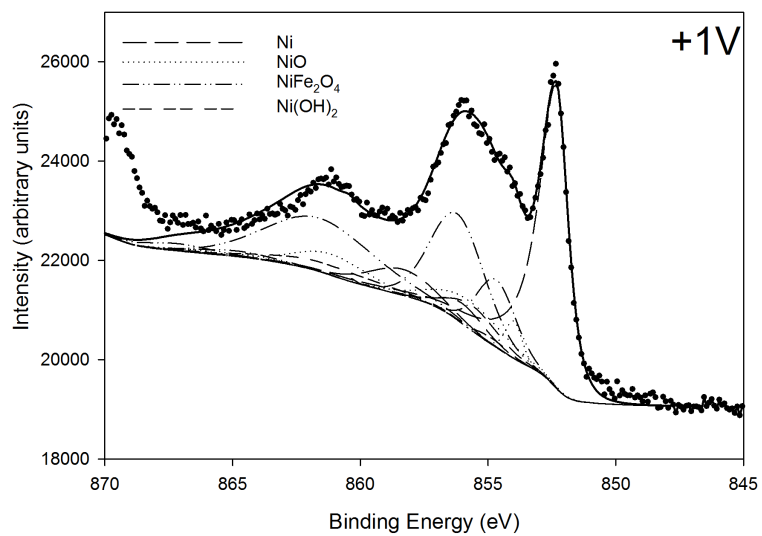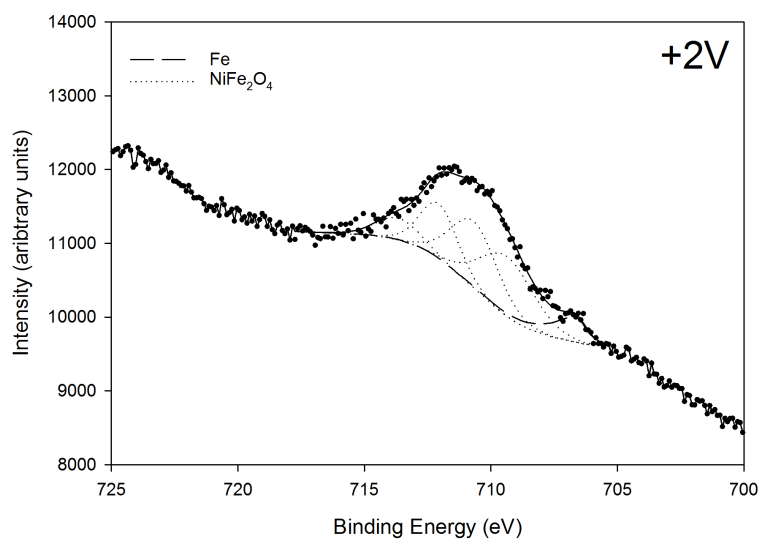
Figure A4.2: Nickel 2p high-resolution spectra at +1 V
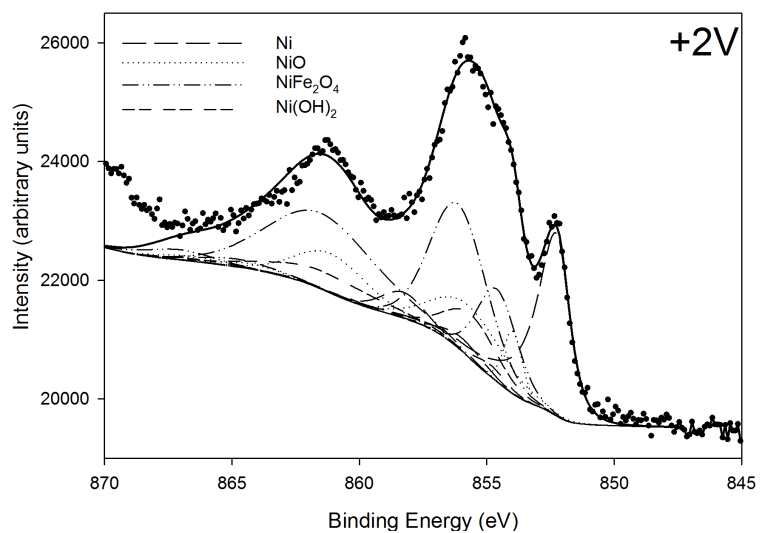
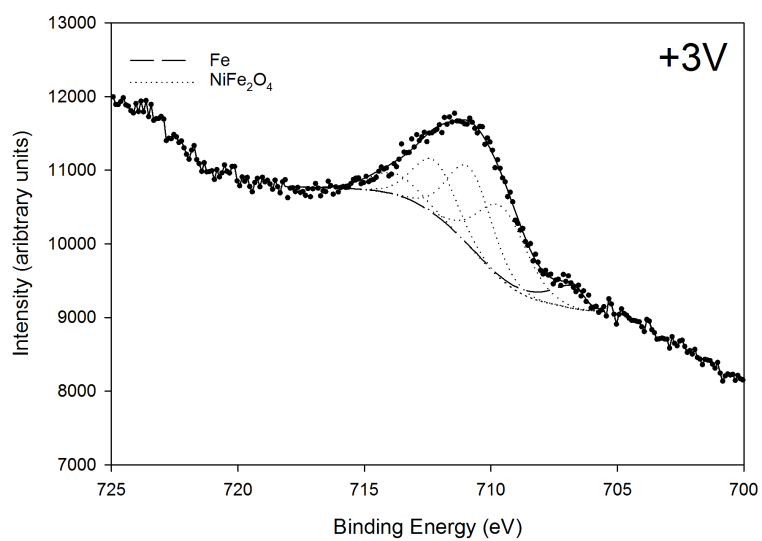*Figure A4.3: Nickel 2p high-resolution spectra at +2 V*

Figure A4.4: Nickel 2p high-resolution spectra at +3 V

Figure A4.5: Nickel 2p high-resolution spectra at -1 V, after previous exposure to +3 V

Figure A4.6: Nickel 2p high-resolution spectra at -2 V, after previous exposure to +3 V
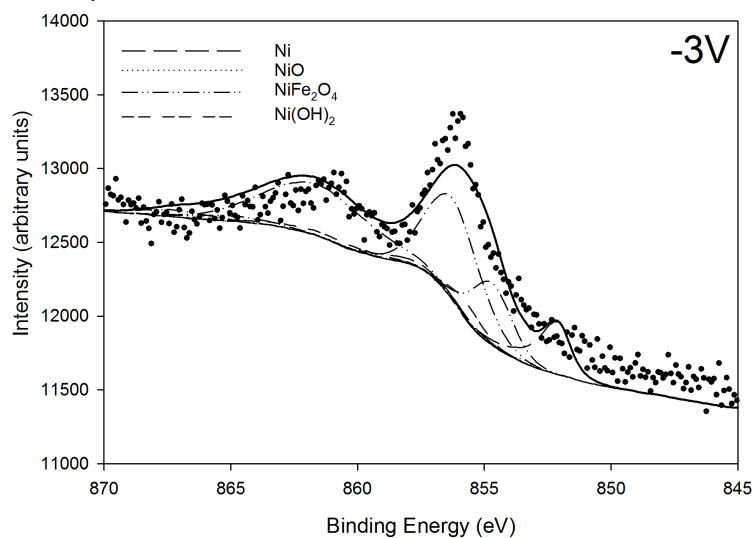
Figure A4.7: Nickel 2p high-resolution spectra at -3 V, after previous exposure to +3 V
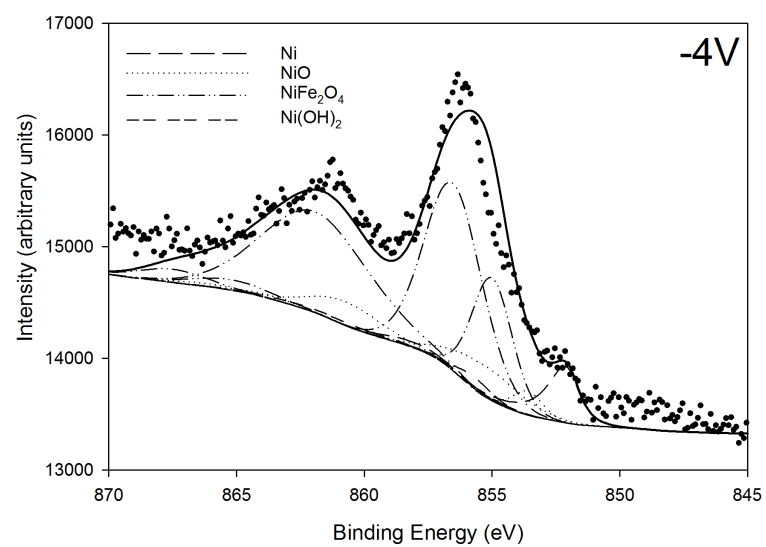
Figure A4.8: Nickel 2p high-resolution spectra at -4 V, after previous exposure to +3 V

A5. Fe 2p high-resolution spectra

Figure A5.1: Iron 2p high-resolution spectra at 0 V

Figure A5.2: Iron 2p high-resolution spectra at +1 V

Figure A5.3: Iron 2p high-resolution spectra at +2 V

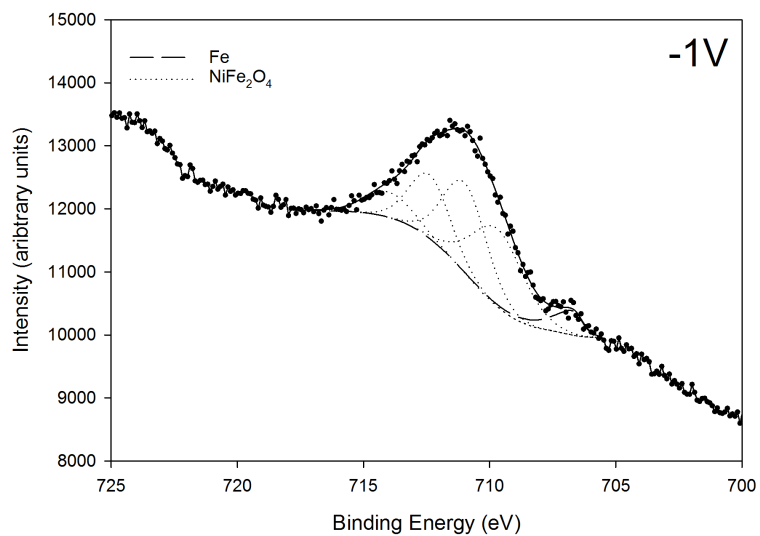*Figure A5.4: Iron 2p high-resolution spectra at +3 V*

*Figure A5.5: Iron 2p high-resolution spectra at -1 V after previous
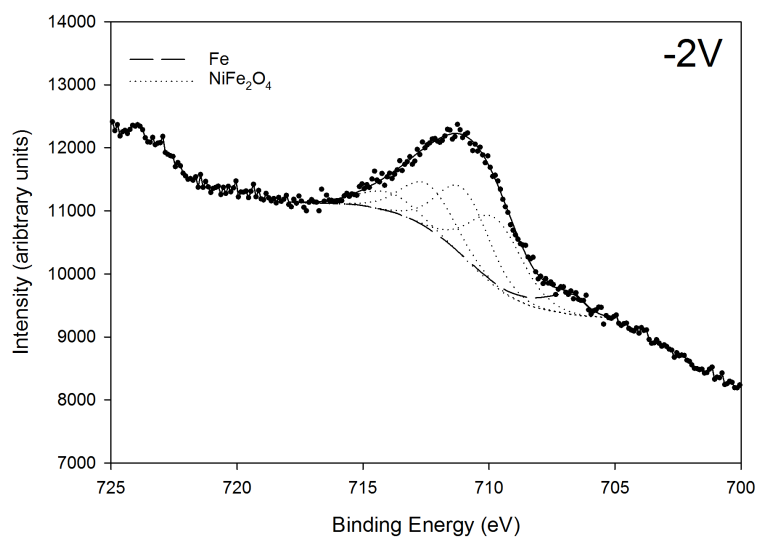exposure to +3 V*

*Figure A5.6: Iron 2p high-resolution spectra at -2 V after
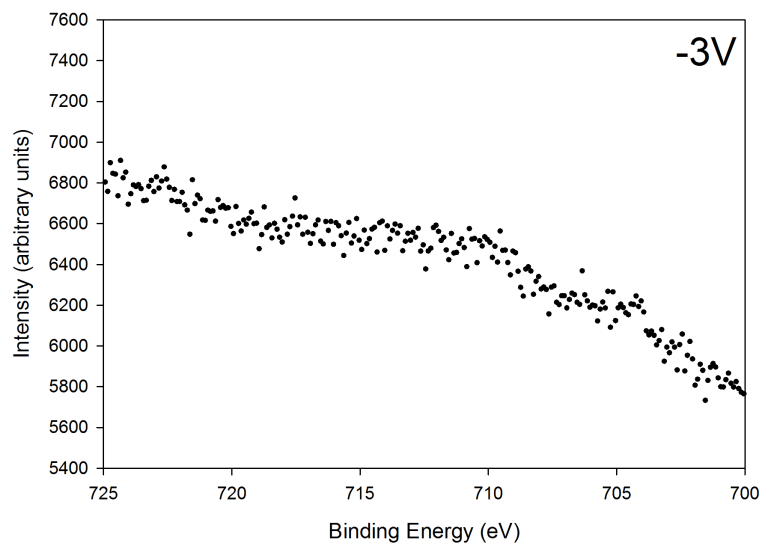previous exposure to +3 V*

Figure A5.7: Iron 2p high-resolution spectra at -3 V after previous exposure to +3 V
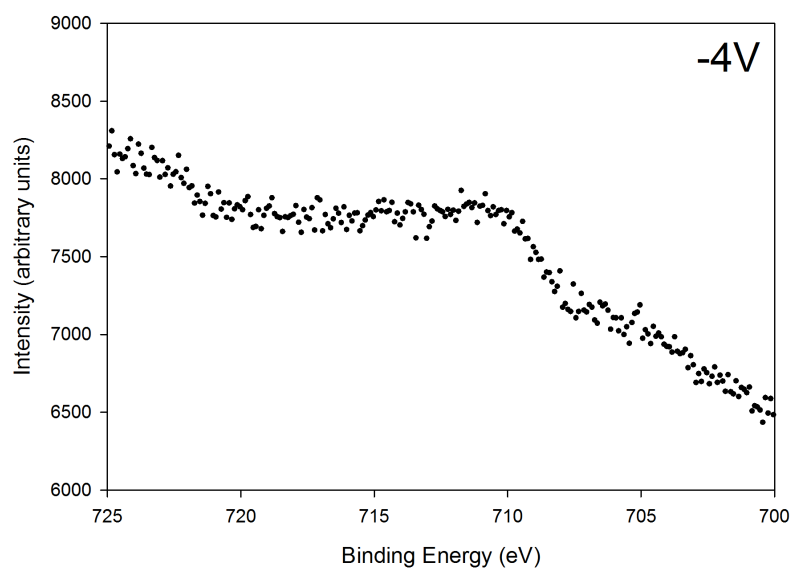

Figure A5.8: Iron 2p high-resolution spectra at -3 V after previous exposure to +3 V